Innovations in Spatial Response Assessment for Satellite Imagers

A thesis submitted in fulfillment of the requirements for the degree of

Doctor of Philosophy

Alvaro Valenzuela Quinteros

ORCID 0000-0002-5125-6722

BSc (Engineering Sciences – Electrical) University of Chile

Civil Electrical Engineer (Telecommunications) University of Chile

MSc with Distinction in Satellite Engineering - University of Surrey

School of Science

Science, Technology, Engineering and Maths (STEM) College

RMIT University

Australia

November 2024

Declaration

I certify that except where due acknowledgement has been made, this research is that of the author alone; the content of this research submission is the result of work which has been carried out since the official commencement date of the approved research program; any editorial work, paid or unpaid, carried out by a third party is acknowledged; and ethics procedures and guidelines have been followed.

In addition, I certify that this submission contains no material previously submitted for award of any qualification at any other university or institution, unless approved for a joint-award with another institution, and acknowledge that no part of this work will, in the future, be used in a submission in my name, for any other qualification in any university or other tertiary institution without the prior approval of the University, and where applicable, any partner institution responsible for the joint award of this degree.

I acknowledge that copyright of any published works contained within this thesis resides with the copyright holder(s) of those works.

I give permission for the digital version of my research submission to be made available on the web, via the University's digital research repository, unless permission has been granted by the University to restrict access for a period of time.

Alvaro Valenzuela Quinteros

20th November 2024.

"*A man may imagine things that are false,*

but he can only understand things that are true,

for if the things be false,

the apprehension of them is not understanding."

Sir Isaac Newton (1643 - 1727)

Acknowledgements

This work could not have been possible without the continuous help, support, guidance, and motivation provided by my two supervisors: Professor Simon Jones, and Associate Professor Karin Reinke. I was fortunate to have two supervisors which made me feel that I was part of a research team and that provided two complementary approaches to solve the various difficulties encountered on our quest for innovation on satellite images. I am indebted to both of them for achieving this goal.

Karin's interest on spatial data quality and her enthusiastic response to my preliminary research proposal were the keys that allowed me to gain access to RMIT University. During these last four years, her sensible and practical advice on academic and domestic issues has been the guideline in what for me were unfamiliar grounds. Thanks for making this research happen and for all your care, help, guidance, and encouragement during my stay at RMIT.

Simon has shown me that genuine research is the one that leads you to where you did not expect to go. His razor-sharp analytic skills have shaped and directed this research from the beaten track to unexplored territories. Thanks for taking the best out of me, for your technical help during my presentations, and for the professional development opportunities you gave me.

My warm thanks to the RMIT staff and to my fellow PhD candidates which in some way or another have provided help, encouragement, advice, or support during my stay at RMIT. Among these I would like to mention Brian Bai, Bryan Hally, Grace Leone, Jenni Tomkinson, Johan Tiede, Konstantinos Chatzopoulos, Lucas Holden, Mariela Soto-Berelov, Michael Meadows, Monica Wachowicz, Nur Trihantoro and Sven Huettermann.

I gratefully acknowledge the financial support received from RMIT University through my Stipend Research Scholarship and from SmartSat Cooperative Research Centre through my top-up scholarship. These two scholarships allowed me full dedication to my research during its initial period, without the hurdles of dealing with a part time job.

My special gratitude to the support received from my previous employer, the Chilean Air Force, which allowed me to initiate my research at RMIT. Among the support I received from the Chilean Air Force, I must acknowledge my commission at England to obtain a Master of Science in Satellite Engineering, the opportunity I was given to conduct in Chile some fundamental research on satellite image quality, and my commission to the Netherlands to present the results of this later research at the 2019 International Symposium on Spatial Data

Quality. The best paper award received at this symposium triggered my interest to pursuit a PhD in satellite images.

A grateful acknowledgment to the editors of the six journals where I have published my satellite image quality papers during this last six years, and to the reviewers that generously read, corrected, and commented the manuscripts. Innovations off the beaten track are difficult to explain; without the help of these reviewers the goal for clarity in the exposition would have not been accomplished.

My thanks to the Examination Team of the School of Graduate Research at RMIT University for their help in the thesis submission process and for correcting some typos in the original manuscript.

I acknowledge with appreciation the work of my two examiners in assessing the original manuscript. My special gratitude to Professor Clive Fraser for his encouraging assessment and for his meticulous correction of several blunders in my original manuscript.

At last, but not least, to my dear wife Evelyn my gratitude and admiration for her courage to leave a stable and secure financial position at Chile with the purpose to embark our family into a long journey with an unknown outcome. Your generous financial and emotional support to our Australian journey were essential to conduct this PhD research. Thanks for the multiple occasions in which you had to fill my absence and carry out by your own the demanding task of raising our two beloved children.

Table of Contents

Declaration……ii

Acknowledgements……...iv

Table of Contents……..…vi

List of Figures.....……..…….xiii

List of Tables……...xix

List of Acronyms…….....xxi

Abstract…….……1

Chapter 1:

Introduction 3

1.1. Overview…….……4

1.2. Background…….……4

1.2.1. Genesis of the problem……...…….……4

1.2.2. Imaging sensors……...…….……6

1.2.3. Spatial response of an imaging sensor……8

1.2.4. Satellite images…… 12

1.2.5. What's in a pixel?.....13

1.3. Knowledge Gaps, Aims and Research Questions…….15

1.3.1. Knowledge gaps……...……15

1.3.1.1. Spatial resolution metrics……..……15

1.3.1.2. Spatial response models……..……..16

1.3.1.3. Spatial response measurements…….17

1.3.1.4. Application of spatial response knowledge to image restoration…….……17

1.3.2. Aim…….……..18

1.3.3. Research Questions……...18

1.4. Thesis Structure…….……..19

Chapter Two:

A New Metric for the Assessment of Spatial Resolution in Satellite Imagers 21

2.1. Introduction……...22

2.2. Background……..24

2.2.1. Spatial resolution concepts……..……..24
2.2.2. A taxonomy for spatial resolution metrics……...26
2.2.2.1. Theoretic metrics…….……...…….……...……...27
2.2.2.2. Spatial Response metrics……29
2.2.2.3. Two-Point Source metrics……...32
2.3. Materials and Methods…….33
2.3.1. Basic equations…….33
2.3.1.1. Sampled image equation…….…….……...…...33
2.3.1.2. System point spread function computation…….…..…34
2.3.2. Spatial Resolution Function computation……38
2.3.2.1. Phasing condition……..38
2.3.2.2. Computational procedures……..……...40
2.3.2.3. Computation of ultimate resolution distance……42
2.3.2.4. Validation procedures……...42
2.3.3. Assessment of spatial resolution metrics…….43
2.3.3.1. Assessment procedure……..…….43
2.3.3.2. Computational range…….45
2.3.3.3. Metrics assessed…….46
2.4. Results…….…….46
2.4.1. Spatial resolution function of a perfect scanner……..……..…..……..49
2.4.2. High quality scanner spatial resolution function……...……...50
2.4.3. Medium quality scanner spatial resolution function…….……...50
2.4.4. Metrics assessment……...50
2.5. Discussion……...…….…….……52
2.5.1. Key results……..……...…….……52
2.5.2. Interpretation of results……..……..…….……52
2.5.3. Implication of results……..……...……54
2.5.4. Limitations and future work……..…….56
2.6. Conclusion……...…..……56
Abbreviations……..…..…58

Chapter Three:

A New Methodology to Assess Spatial Response Models for Satellite Imagers using the Optical Design Parameters of a Generic Sensor as Independent Variables 60

3.1. Introduction……...61

3.2. Materials and Methods……..63

3.2.1. Domain of interest in the (Q, ε) plane……..……..63

3.2.1.1. Optical factor - Obstruction ratio (Q, ε) plane……..……..63

3.2.1.2. Domain of optical factors……..……..……64

3.2.1.3. Domain of obstruction ratios...……..……..……64

3.2.2. Minimum point spread function level to be assessed…….……64

3.2.2.1. Basic equation…….64

3.2.2.2. Peak signal to background signal ratio……66

3.2.2.3. Background signal to noise ratio……66

3.2.2.4. Minimum point spread function's reference levels……...……..67

3.2.3. Point / line spread function computation….……...……67

3.2.3.1. Optics……..……68

3.2.3.2. Detector……..…….,……68

3.2.3.3. Scan speed……..…….,……69

3.2.3.4. System optical transfer function….…….……69

3.2.4. Assessment of separable point spread function model…….……..69

3.2.5. Validation methods……..…….……..69

3.3. Results…….…..70

3.4. Discussion……...…..72

3.4.1. Key results……..…….…….…..72

3.4.2. Interpretation of results……..72

3.4.3. Implications of results……..……..73

3.4.4. Limitations and future work……...…74

3.5. Conclusion……74

Chapter 4:

A New Method to Estimate the Point Spread Function of Satellite Imagers from Edge Measurements 76

4.1. Introduction……...77

4.2. Materials and Methods……...77

4.2.1. Edge measurements……...77
4.2.2. Point spread function models……79
4.2.2.1. Assessment Procedure……79
4.2.2.2. Point spread function models considered…...……80
4.2.2.3. Quadratic interpolation model…….…...……80
4.3. Results……...82
4.4. Discussion…….83
4.4.1. Key result……..…….83
4.4.2. Interpretation of results……..84
4.4.3. Implications of results……..……..84
4.4.4. Significance of results……..……..84
4.4.5. Limitations and future work……...85
4.5. Conclusion…….85

Chapter 5:

A New Procedure to Find the Optimum Deconvolution Kernel to Deblur Satellite Images 86
5.1. Introduction……...87
5.1.1. Basic concept of deblurring……87
5.1.2. Usual approach to image deblurring…….87
5.1.3. Need for an optimum deconvolution kernel…….88
5.1.4. Higher Resolution Satellite Images procedure…….89
5.1.5. Scope of this work……92
5.2. Materials and Methods……..……..93
5.2.1. Common stages and steps for both procedures…….93
5.2.1.1. First stage……...…93
5.2.1.2. Second stage……....96
5.2.1.3. Relationships between shrink factor and adjacency parameter…….……..97
5.2.2. Higher Resolution Satellite Image procedure…….……...…99
5.2.3. Synthetic Edge Images procedure……99
5.2.3.1. Ideal image model…….……100
5.2.3.2. Raw image model……..101
5.2.3.3. Deconvolved image model……102
5.2.3.4. Deblurring factor computation……..103

5.3. Results……104
5.4. Discussion……...106
5.4.1. Key result……..106
5.4.2. Interpretation of result…...……...…….107
5.4.3. Significance of result.…….……107
5.4.4. Limitations and future work……...108
5.5. Conclusion……..108

Chapter 6:
Assessing the Spatial Resolution Distance of Satellite Images: SuperDove versus Landsat 8 110
6.1. Introduction....…….…….111
6.2. Background……...…….……..113
6.2.1. Spatial response functions……..…….……..113
6.2.1.1. Two-dimensional functions…….…….……..113
6.2.1.2. One-dimensional functions……117
6.2.2. Spatial resolution metrics……..119
6.2.2.1. Theoretic metrics……...120
6.2.2.2. Spatial Response metrics……...121
6.2.2.3. Two-point source metrics……..122
6.3. Materials and Methods……126
6.3.1. Selection of imaging sensors and channels……126
6.3.2. Computation of the Spatial Response……...127
6.3.2.1. General procedure……..127
6.3.2.2. Optical Transfer Function model……128
6.3.2.3. General overview of the Green channels' OTF models……129
6.3.2.4. SuperDove's Green channel model……131
6.3.2.5. Landsat-8's Green channel model…….……131
6.3.3. Computation of Spatial Response Function……..132
6.3.4. Computation of Resolution Degradation Index……134
6.3.5. Instability of the spatial response……..134
6.3.5.1. Evidence of instability…….……..134
6.3.5.2. Atmospheric turbulence……135
6.3.5.3. Line of sight jitter……...135

6.4. Results……136
6.4.1. SuperDove……136
6.4.1.1. Case 1 (Baseline)……...138
6.4.1.2. Case 2 (Turbulence)……...139
6.4.1.3. Case 3 (Extra jitter)……138
6.4.1.4. Resolution Degradation Index……..139
6.4.1.5. Conclusion……139
6.4.2. Landsat 8……..……..140
6.4.3. Assessment of spatial resolution metrics……..140
6.5. Discussion……142
6.5.1. Key Findings……142
6.5.2. Spatial Resolution Distance……..……142
6.5.2.1. Confusion of GSD with SRD……142
6.5.2.2. Erroneous, biased and unbiased spatial resolution metrics……143
6.5.2.3. SuperDove's SRD is much larger than its GSD……143
6.5.2.4. Impact of results……144
6.5.3. Stability of the spatial response……144
6.5.3.1. Drawbacks of reducing the GSD……..144
6.5.3.2. Stability of SuperDove's images……145
6.5.3.3. Impact of results……145
6.5.4. Limitations and future work……..145
6.6. Conclusion……...146

Chapter 7:

Conclusion 148

7.1. Overview……...……..149
7.2. Summary of results……..149
7.2.1. How can we assess and improve current spatial resolution metrics for satellite imagers? ……..…149
7.2.2. How can we assess current spatial response models for satellite imagers?……..…150
7.2.3. How can we improve current spatial response models derived from edge measurements? ……..…..151
7.2.4. How can we exploit our knowledge on the spatial response of satellite imagers to upgrade current image processing algorithms?……..…152

7.3. Synthesis……..153
7.3.1. Overall significance of results……..153
7.3.2. A synergistic perspective……...156
7.4. Other results presented in the Appendices……156
7.5. Limitations of the Optical Transfer Function methodology……157
7.6. Future work……..157
7.7. Final remarks……...158

Bibliography……..……...160

Appendix 1: Spatial Resolution Function of Obstructed Apertures……178

Appendix 2: Impact of Modulation Transfer Function Compensation on the Spatial Resolution Function……..183

Appendix 3: Assessment of the bivariate Gaussian Point Spread Function model ……187

List of Figures

Figure 1.1: Production of an image by an imaging sensor. Electromagnetic energy radiated by the three-dimensional scene is captured through the optical aperture of the imaging sensor (imager). The imager produces a two-dimensional array of digital numbers which are visually represented in an image……6

Figure 1.2: Schematic cut view of the generation of digital numbers by an imaging sensor. Electromagnetic energy of wavelength λ, shown in red colour, is captured by an optical aperture of diameter *D* and then it is focused along a focal length *F* on the focal plane array or image plane. Each detecting element or "pixel" of this array converts the focused energy into an electrical signal whose intensity defines the pixel's digital number. Only one column of the array is represented in the figure…….7

Figure 1.3: Pictorial representation of the half-energy diameter in the image plane for three different optical factors. A section of 3×3 pixels in the image plane is represented by nine squares of width *p* and the half-energy diameter ϕ that contains 46 % of the energy focused into the image plane is represented by a black circle. The three figures assume that the geometrical projection of the point source in the scene lies in the center of the central pixel. The black circle contains almost half of the energy focused on the image plane, so when $Q = 0.1$ almost all this energy lies within the central pixel, when $Q = 1$ this energy distributes roughly evenly between the central pixel and its surrounding pixels, and when $Q = 2$ the greatest portion of this energy spreads into adjacent pixels……..8

Figure 1.4: Point Spread Function of a perfect imager with an optical factor $Q = 0$……...10

Figure 1.5: Point Spread Function of a perfect imager with an optical factor $Q = 0.05$…....11

Figure 1.6: Point Spread Function of a perfect imager with an optical factor $Q = 0.5$……....11

Figure 1.7: Point Spread Function of a perfect imager with an optical factor $Q = 3$..….....12

Figure 1.8: Mapping of the Earth's surface by a satellite sensor. Each square pixel of width *p* in the mage represents a square area of width GSD in the ground plane. The scene has three point sources A, B, and C. Sources B and C can be resolved in the ideal image, but they cannot be resolved in the actual image…….…..……..13

Figure 2.1: Image plane response to point sources. The figures show in one dimension the response in the image plane to: a) Single point source located at the centre of a pixel. b) Two-point sources located symmetrically with respect to the later centre, separated at a distance of one pixel. c) Two-point sources located symmetrically with respect to the later centre, separated at a distance of two pixels. Vertical axes represent the intensity of the responses normalized to a maximum value of 1 and horizontal axes represent distance measured in pixels. The positions of the geometrical projection of the point sources on the image plane are represented by arrows……..…25

Figure 2.2: Taxonomy of spatial resolution metrics for satellite imagers. This taxonomy is based on a previous classification for optical systems (Ramsay et al. 1941) adapted to include current satellite metrics. The three types of metrics differ in their criterion to define spatial resolution as follows. "Theoretic": A single value function of imager parameters. "Spatial Response": A single value obtained as a property of the imager's

spatial response to a single source. “Two-Point Source”: Either a single value or a function, computed in terms of the contrast achieved in the image plane when imaging two closely spaced point sources……..…...27

Figure 2.3: System Point Spread Function examples. System PSF cuts are shown in along scan (red curves) and cross scan (blue curves) directions, in the case of the Perfect Scanner, for two different optical factors. Vertical axes represent the PSF intensity and horizontal axes represent the distance measured in pixels widths from the point of maximum intensity……...38

Figure 2.4: Phasing condition. Three possible measures of spatial resolution are shown for an ideal imager considering different phasing conditions. To measure resolution, the two-point sources are gradually separated along a straight trajectory, with respect to an equidistant point of symmetry. The projection of the point sources in the image plane, when resolution is declared, is represented by a black dot, their trajectory is shown as a dashed line and its point of symmetry is depicted by an encircled “plus” symbol ⊕. Resolution is declared when sources are separated at such a distance that at least one empty pixel appears between the two pixels occupied by these sources. As the separation trajectory and point of symmetry are arbitrary, there are an infinite number of ways to measure resolution. The phasing condition with centre symmetry and a movement parallel to the pixel grid (2.4.a) is selected because it yields an angular resolution α equal to the Instantaneous Field Of View (IFOV). Figures 2.4.b and 2.4.c. with edge and corner symmetry, respectively, yield angular resolutions larger than the IFOV……....39

Figure 2.5: Flowchart of the procedure used to compute the Spatial Resolution Function. This procedure involves: the definition of the Point Spread Function; the gradual separation of the two point sources according to the phasing condition of Figure 2.4.a; the computation of the pre-sampled response; the computation of the sampled response in all pixels; the computation of contrast “*C*” in the image plane as a function of source separation “s”; the inversion of the function *C*(*s*); and the final presentation of resolution distance “*s*” as a function of contrast “*C*”……....41

Figure 2.6: Spatial Resolution Function for Perfect Scanner (PS – top figures), High Quality scanner (HQ – middle figures) and Medium Quality scanner (MQ – bottom figures). The Spatial Resolution Function is presented in along scan (left figures) and cross scan (right figures) directions for five values of contrast *C*. Vertical axes represent resolution distance R in pixels and horizontal axes represent the optical factor *Q*……..47

Figure 2.7: Associated Contrast of Soft Metrics. Associated contrast C_a of soft metrics is presented as a function of optical factor *Q*, for a Perfect Scanner, in along scan (left figures) and cross scan (right figures) directions. Vertical axes represent C_a, and horizontal axes represent *Q*. C_a is computed assuming that a metric agrees with the Spatial Resolution Function at a given *Q*. When a soft metric predicts a resolution distance lower than Sparrow limit no data is shown, being this the reason why GSD metric is not presented. All metrics are biased because their C_a depends on *Q*, erring when comparing imagers with different optical factors……..…48

Figure 2.8: Contours of Constant Spatial Resolution Function in Cross Scan direction. Contours of constant $R_y(C, Q)$ measured in pixels are drawn for a High Quality scanner in the resolving contrast *C* versus optical factor *Q* plane. The GSD metric postulates $r(Q) = 1$ pixel, so the contours can be used to assess its error for a given combination of *C* and *Q*

values. For example, with relation to Figure 2.8.b, $R_y(0, 0.1) = 1.05$, thus, if the GSD metric is used to predict Sparrow limit ($C = 0$) for an HQ imager with $Q = 0.1$, then its prediction error is $100 \cdot (1-1/1.05) = 4.8$ %.....48

Figure 3.1: One dimensional illustration of the PSF adjacency effect. A single point source's position represented at pixel 10 generates a peak signal P in this pixel and also increases the signal level in adjacent pixels 6 to 9 and 11 to 14. The signal increase ΔS in adjacent pixels 8 and 12 will be detected only if it is substantially larger than the background signal fluctuations due to image noise……65

Figure 3.2: Flowchart of the procedure to assess the separable PSF model. For a given optical factor Q and obstruction ratio ε, the Point Spread Function (PSF) estimated by the model defined by equation (1) is compared with the actual PSF. The Mean Absolute Percentage Error of this model is computed considering all PSF values larger or equal than the minimum PSF level that is relevant to the application (PSF_{min}). An analogous procedure (actual versus estimated PSF or LSF) can be used to assess other spatial response models……70

Figure 3.3: Mean Absolute Percentage Error (MAPE) of separable PSF model for $PSF_{min} = 0.1$. Contours of constant MAPE are drawn for the Separable Point Spread Function model in the optical factor Q - obstruction ratio ε plane. This model has smallest errors for smallest values of Q and ε, and largest errors for highest values of Q and ε……..71

Figure 3.4: Mean Absolute Percentage Error (MAPE) of separable PSF model for $PSF_{min} = 0.01$. Contours of constant MAPE are drawn for the Separable Point Spread Function model in the optical factor Q - obstruction ratio ε plane. This model has small errors for very small values of Q and large errors elsewhere……71

Figure 4.1: Four steps of the edge measurement procedure. Its input is an image of a straight edge, and its output is a one-dimensional cut of the Optical Transfer Function (OTF1D) in a direction perpendicular to this edge. The steps are: 1) a slanted edge in the image is identified and modelled; 2) the Edge Spread Function (ESF) is found from the image pixel counts as a function of the distance to the edge; 3) the Line Spread Function (LSF) is obtained as the derivative of the ESF; and 4) the inverse Fourier transform of the LSF yields the OTF1D……..……..78

Figure 4.2**:** Flowchart of the procedure to assess a Point Spread Function (PSF) model. A generic sensor system is defined and used to compute the actual two-dimensional Optical Transfer Function (OTF) and the actual PSF for a given optical factor Q and obstruction ratio ε. The data required to build the PSF model under assessment is computed and the PSF predicted by this model is calculated as a function of Q and ε. The PSF predicted by the PSF model is compared with the actual PSF to compute the Mean Absolute Percentage Error (MAPE) of this model as a function of Q and ε. The MAPE is computed in the (x, y) plane considering all actual PSF values larger or equal than the minimum PSF level that is relevant to the application (PSF_{min})……..79

Figure 4.3: Mean Absolute Percentage Error (MAPE) of the Quadratic Interpolation Point Spread Function (PSF) model for $PSF_{min} = 0.1$. Contours of constant MAPE are drawn for the Quadratic Interpolation model in the optical factor Q - obstruction ratio ε plane, for the case of the generic sensor defined in the text. The domain where MAPE ≤ 10 % is approximately $Q \geq -0.08 \cdot \varepsilon + 0.10$……..82

Figure 4.4: Mean Absolute Percentage Error (MAPE) of Quadratic Interpolation Point Spread Function (PSF) model for $PSF_{min} = 0.01$. Contours of constant MAPE are drawn for the Quadratic Interpolation PSF model in the optical factor Q - obstruction ratio ε plane, for the case of the generic sensor defined in the text. The domain where MAPE ≤ 10 % is approximately $Q \geq -0.36 \cdot \varepsilon + 0.49$……..83

Figure 5.1: Flowchart of the first stage of the procedure to find the optimum deconvolution kernel to restore the images that will be acquired by a Sensor Of Interest (SOI). In this stage the following data required to compute the Deblurring factor Δ are found: a) Pre-sampled Point Spread Function (PSF) of the SOI. b) Images required to produce the Ideal Image Model (IIM) and the Raw Image Model (RIM) of the SOI. c) Ideal Image Model of the SOI. d) Raw Image Model of the SOI. e) Mean Absolute Difference between the ideal and the raw image models (MAD_{RAW}) of the SOI…….……..…..94

Figure 5.2: Flowchart of the second stage of the procedure to find the optimum deconvolution kernel to deblur the images that will be acquired by a Sensor Of Interest (SOI). In this stage the deblurring factor Δ is computed for different values of the PSF's shrink factor β and the shrunk deconvolution kernel $\boldsymbol{K}$ that maximizes the deblurring factor is selected as the optimum deconvolution kernel……..95

Figure 5.3: Example of a scene assumed by the Synthetic Edge Image procedure, for the case that the slope of the edge is an integer number $P = 11$. The straight edge separates a dark zone from a bright zone…….……100

Figure 5.4: Images obtained by applying the Synthetic Edge Image procedure to the example scene depicted in Figure 5.3. The left panel shows the ideal image computed by equation (16). The centre panel shows the raw image computed by equations (17) and (20). The right panel shows the restored image computed by deconvolving the raw image with the kernel defined by equation (22) for the case of optimum restoration ($\alpha = 0.105$)…….101

Figure 5.5: The deblurring factor Δ computed for a triangular PSF using the Synthetic Edge Images (SEI) procedure is plotted against the adjacency parameter α defined by Huang et al. (1998). The figure shows as a blue curve the average of five computations considering edges with slopes 9, 11, 13, 15 and 17. The maximum and minimum values of the deblurring factor Δ computed with these five slopes, are shown as dotted and dashed curves, respectively. The value of the maximum deblurring factor Δ and the optimum adjacency parameter obtained by Huang et al. (1998) with the Higher Resolution Satellite Images (HRSI) procedure is depicted as a red dot. The optimum adjacency parameter α predicted by the SEI procedure is in the domain 0.12 to 0.14, showing very good agreement with the optimum value $\alpha = 0.14$ obtained by the HRSI procedure for six Landsat TM spectral bands..……104

Figure 5.6: The deblurring factor Δ computed for a Gaussian PSF using the Synthetic Edge Images (SEI) procedure is plotted against the adjacency parameter α defined by Huang et al. (2002). The figure shows as a blue curve the average of five computations considering edges with slopes 9, 11, 13, 15 and 17. The maximum and minimum values of the deblurring factor Δ computed with these five slopes, are shown as dotted and dashed curves, respectively. The values of the deblurring factor Δ versus the adjacency parameter α obtained by Huang et al. (2002, figure 3.a) with the Higher Resolution Satellite Images (HRSI) procedure, for a red band image of a landscape in Egypt, are

depicted as red dots. The optimum adjacency parameter α predicted by the SEI is in the domain 0.10 to 0.11, showing excellent agreement with the optimum values α = 0.105 ± 0.005 obtained with the HRSI procedure, for the red and near infrared bands images over four landscapes (Huang et al. 2002, figure 3)……..….105

Figure 6.1: Point Spread Function (PSF) of three imaging channels. The two-dimensional PSF is represented in the image plane over an extent of 10×10 pixels, for three imaging channels: (*a*) an ideal imaging channel with no adjacency effect; (*b*) Landsat 8's Green channel; and (*c*) SuperDove's Green channel……114-115

Figure 6.2: Procedures used to obtain the different spatial response functions. The five spatial response functions of interest are displayed in rectangular boxes. The mathematical procedures used to derive a spatial response function from another spatial response function are displayed as arrows that connect these two spatial response functions. These mathematical procedures are labelled with the letter "M" and a correlative number. The image used to measure the spatial response is displayed in an oval shape. The empirical procedure that uses this image to obtain the Edge Spread Function (ESF) is labelled as E1 and displayed as an arrow that connects the image with the ESF……116

Figure 6.3: One-dimensional spatial response functions computed in this work for Landsat 8's Green channel in Along Scan (AS) direction. The spatial response functions represented as blue curves are: (a) the Edge Spread Function (ESF); (b) the Line Spread Function (LSF); and (c) the Optical Transfer Function cut (OTF-1D). For each function the magnitude of the parameter of interest for the respective spatial resolution metric is represented with red arrows……...……118

Figure 6.4: Pictorial representation of the parameters involved in the definition of Ground Sampling Distance (GSD) and Ground Spot Size (GSS) for a satellite imaging sensor. The upper figure represents the GSD as the projection of the Instantaneous Field Of View (IFOV) on the ground plane. The lower figure represents the GSS as the projection of the Optical Field Of View (OFOV) on the ground plane…….120

Figure 6.5: Example of resolving contrast computation. Two point sources of identical strength in the scene are projected in the image plane on pixels 4 and 6, being separated in this plane at a distance of 1.8 pixels. The maximum signal level I_{max} is produced in pixels 4 and 6, where the projections of the sources are located. Due to the adjacency effect, signal is generated in pixels 2 to 8. The minimum signal level I_{min} between the two pixels with maximum signal occurs at pixel N° 5. The resolving contrast is defined as the difference between I_{max} and I_{min} divided by I_{max}…….……..……...123

Figure 6.6: Two examples of the computation of image resolving contrast C versus separation distance s between two-point sources. The red lines show the $C(s)$ function for the ideal imager, which changes from $C = 0$ to $C = 1$ at $s = 1$ pixel. The green curve shows the $C(s)$ function for Landsat 8's Green channel in AS direction, in which the contrast starts to gradually increase from $C = 0$ when the separation s is greater than 1.27 pixels…….……124

Figure 6.7: Example of the computation of spatial resolution metrics for Landsat 8's Green channel in AS direction. The green curve shows the Spatial resolution Function (SRF), the blue dot on this curve at $C = 0.25$ represents the prediction of the Generalized

Rayleigh Criterion (GRC) which is identical to the SRD predicted by the SRF for this same value of contrast. The dashed horizontal lines show, from bottom to top, the SRD predicted by the following metrics: Rayleigh Diffraction Limit (RDL); Ground Sampling Distance (GSD); Full Width at Half Maximum (FWHM) of the Line Spread Function (LSF); Effective Instantaneous Field Of View (EIFOV); and Relative Edge Response (RER). Only the RER metric predicts an SRD that allows some resolving contrast to be obtained in the image, the RDL, GSD, LSF's FWHM and EIFOV metric fail because they predict an SRD at which it is not possible to resolve the two sources…….125

Figure 6.8: Line Spread Functions for Landsat 8's Green Channel in Along Scan (AS) and Cross Scan (CS) directions. The Line Spread Function (LSF) predicted by the OTF model is presented as a blue line, the values measured for the LSF are presented as red circles. The unknown parameters of the OTF model were adjusted to provide the best possible match in both directions……130

Figure 6.9: Conditions required to compute the Spatial Resolutions Function (SRF) in horizontal direction. The projections of the two point sources in the image plane are represented as black dots. These two projections are symmetrical with respect to the centre of Pixel 0 depicted by the symbol "⊕". The two point sources are separated at a variable distance "s" by moving along the dashed horizontal straight line that passes through the centre of Pixel 0……..……132

Figure 6.10: Spatial Resolution Function of SuperDove's Green ii channel (upper figures a and b) and Landsat 8's Green channel (lower figures c and d) in Along Scan (AS) direction (left figures a and c) and Cross Scan (CS) direction (right figures b and d) for three cases. Case 1 (blue line) has moderate jitter and no turbulence. Case 2 (red line) has moderate jitter and strong turbulence. Case 3 (slashed magenta line) has high jitter and no turbulence……..……137

Figure 7.1: Innovations developed in this thesis to answer the four research questions. From left to right, these innovations are described in Chapters 2, 3, 4 and 5, respectively…155

List of Tables

Table 1.1: Parameters of the spatial response for a perfect staring imager…….……10

Table 2.1: Detector metrics. These Theoretic metrics compute spatial resolution in terms of the ratio between pixel pitch *p* and focal length *f*.……..…28

Table 2.2: Optics metrics. These Theoretic metrics compute the spatial resolution of sensors comprising a single optical aperture. The angular resolution is $\alpha = K \cdot \lambda / D$, where *K* is a constant, *D* is the aperture diameter and λ is the mean wavelength. *C* is the contrast achieved in the combined response when the two-point sources are separated at an angle α.……...……...……28

Table 2.3: System metrics. These Theoretic metrics assume that the angular resolution of the imaging sensors is $\alpha = \text{IFOV} \cdot [1 + (K \cdot Q)^k]^{1/k}$, where *K* and *k* are constants, IFOV is the detector's instantaneous field of view and Q is the imager's optical factor……....29

Table 2.4: Modulation Transfer Function (MTF) Point metrics. These metrics are based on fixed threshold values MTFmin for the system MTF. The limiting spatial frequency at which the system MTF achieves the threshold value is ξ_{max} so $MTF_{min} = MTF(\xi = \xi_{max})$. Angular resolution is proportional to the cycle $1/\xi_{max}$ of the limiting spatial frequency……...……..…31

Table 2.5: Range of Optical Factors for Satellite Imagers. For each imager shown, the optical factor *Q* is computed for all its imaging channels, presenting the minimum Q and maximum *Q* in the table. Abbreviations are defined at the end of this chapter……...35

Table 2.6: Scanning Imagers Quality Types. The parameters shown are assumed to model three quality types of satellite imagers: Perfect Scanner (PS), High Quality scanner (HQ) and Medium Quality scanner. Root mean square wavefront error "WFE" models optical aberrations, jitter standard deviation "σ" models the line of sight stability and effective diffusion length "*L*" models charge diffusion in detectors. Values assigned to parameters for HQ and MQ imagers are based on published data…….38

Table 2.7: Analytic approximations to Sparrow limits. Equations shown approximate the Spatial Resolution Function of a Perfect Scanner for zero contrast (Sparrow limit) in AC (*x*) and CS (y) directions. The bounds for the Mean Average Percentual Error (MAPE) and the maximum error (Max.) within domain $0.001 \leq Q \leq 2$ are indicated……49

Table 2.8: Soft metrics bias errors and average associated contrasts. For the soft metrics indicated in column 1, their Maximum Prediction Errors are presented in columns 2, 3 and 4, for three quality types of imagers (PS: Perfect Scanner, HQ: High Quality Scanner, MQ: Medium Quality Scanner). Columns 5, 6 and 7 present average associated contrast $\langle C_a \rangle$ for these same quality types of imagers. $\langle C_a \rangle = 0$ indicates that metric predicts a resolution distance smaller than Sparrow limit. All values in per cent. A perfect soft metric should have zero bias error and its $\langle C_a \rangle$ should not depend on imager type, none of the metrics assessed fulfills these conditions……51

Table 2.9: Example of resolution distance computation. The Spatial Resolution Function is used to compute the resolution distances of two hypothetical High Quality (HQ) imagers in Along Scan (x) and Cross Scan (y). directions. The GSD metric incorrectly predicts that Sensor 1 has the best (smallest) resolution distance, whereas actually it has the worst (largest) resolution distance……..…55

Table 3.1: Optical factor *Q* and linear obstruction ratio ε data for satellite imagers……64

Table 3.2: Examples of extreme radiances ratio "*R*" for satellite imagers……...66

Table 3.3: Examples of signal to noise ratio requirements for satellite imagers……..67

Table 3.4: Comparison of signal to noise ratio metrics for five satellite imaging channels…67

Table 4.1: Point spread function models for edge measurements……80

Table 4.2: Domain of validity of point spread function models……...83

Table 5.1: Description of the three real case scenarios for which the optimum deconvolution kernel for MODIS images was found by using Landsat Thematic images. The reduction of land cover characterization errors due to optimum deconvolution, was computed by comparing the predictions of the linear mixture model for the different classes considered, with ground truth data obtained through field work conducted in Maryland, USA…...91

Table 5. 2: Improvement in deblurring performance due to optimum kernel. Increase in average deblurring factor Δ according to the Synthetic Edge Images procedure implemented with Wiener filtering deconvolution, due to the use of the optimum shrunk PSF kernel as compared with the usual unshrunk PSF kernel……106

Table 6.1: Spatial response functions considered in this work……...117

Table 6.2: Spatial resolution metrics used in this study……119

Table 6.3: Parameters of SuperDove and Landsat-8 satellites, their remote sensing instruments, and their green channels……..……..127

Table 6.4: Spatial response parameters measured for SuperDove's L3B Green ii channel images……..…….129

Table 6.5: Values assumed for the unknown OTF parameters of the Green channels. The jitter parameter σ represents low jitter, so it is not applicable to Case 3…….130

Table 6.6: Spatial resolution metrics for (*a*) SuperDove's Green ii channel and (*b*) Landsat 8's Green channel, in three different cases……..…138

Table 7.1: Remote sensing tasks that benefit by improving the accuracy of the sensor's spatial response data The execution of these tasks requires previous knowledge of the sensor's Point Spread Function (PSF) and their final result will improve if this PSF is known with greater accuracy.……...…….154

List of Acronyms

ABI: Advanced Baseline Imager

AHI: Advanced Himawari Imager

AMI: Advanced Meteorological Imager

AS: Along Scan

AVHRR: Advanced Very High Resolution Radiometer

CS: Cross Scan

DIM: Deconvolved Image Model

DN: Digital Number

EIFOV: Effective Instantaneous Field Of View

ESA: European Space Agency

ESF: Edge Spread Function

FFT: Fast Fourier Transform

FWHM: Full Width at Half Maximum

FWhM: Full Width at hundredth Maximum

FWTM: Full Width at Tenth Maximum

GIQE: General Image Quality Equation

GK-2: Geostationary Kompsat 2 satellite

GOES: Geostationary Operational Environmental Satellite

GRC: Generalized Rayleigh Criterion

GSD: Ground Sampling Distance

GSS: Ground Spot Size

HQ: High Quality satellite scanner

HRS: Higher Resolution Sensor

HRSI: Higher Resolution Satellite Images

H-8: Himawari 8 satellite

IFOV: Instantaneous Field Of View

IFT: Inverse Fourier Transform

IIM: Ideal Image Model

LEO: Low Earth Orbit

LOS: Line Of Sight

LSF: Line Spread Function

MAD: Mean Absolute Difference

MAPD: Mean Average Percentual Difference

MAPE: Mean Average Percentual Error

MODIS: Moderate Resolution Imaging Spectroradiometer

MPE: Maximum Prediction Error

MS: Multispectral

MSG: Meteosat Second Generation (satellite)

MSI: Multispectral Instrument

MSS: Multispectral Scanner

MQ: Medium Quality satellite scanner

MTF: Modulation Transfer Function

MTFC: Modulation Transfer Function Compensation

NASA: National Aeronautics and Space Administration

NIR: Near Infra Red

NRC: National Research Council

OFOV: Optical Field Of View

OLCI: Ocean and Land Colour Instrument

OLI: Operational Land Imager

OTF: Optical Transfer Function

PAN: Panchromatic

PE: Prediction Error

POTF: Polychromatic Optical Transfer Function

PPE: Percentage of Pixel Energy

PS: Perfect satellite Scanner

PSF: Point Spread Function

RAIFOV: Radiometrically Accurate Instantaneous Field Of View

RDL: Rayleigh Diffraction Limit

RER: Relative Edge Response

RIM: Raw Image Model

RMS: Root Mean Square

SEI: Synthetic Edge Images

SEP: Schade's Equivalent Passband

SEVIRI: Spinning Enhanced Visible and InfraRed Imager

SLSTR: Sea and Land Surface Temperature Radiometer

SNR: Signal to Noise Ratio

SOI: Sensor Of Interest

SPOT: Satellite Pour l'Observation de la Terre

SRD: Spatial Resolution Distance

SRF: Spatial Resolution Function

TIRS: Thermal Infrared Sensor

TM: Thematic Mapper

USA: United States of America

USAF: United States Air Force

USGS: United States Geological Service

WFE: Wave Front Error

Abstract

All satellite imaging sensors suffer from a fundamental limitation; the Digital Number (DN) recorded by a pixel does not only measure radiance originating from the area of the Earth's surface represented by this pixel, but it also measures radiance originating from surrounding areas represented by adjacent pixels.

This adjacency effect impacts image processing algorithms that characterize the Earth's surface on a per-pixel basis. These algorithms usually neglect the adjacency effect and assume an ideal pixel for which 100 % of its DN originates from the area represented by this pixel. This "ideal pixel" assumption is equivalent to stating that the spatial resolution of the image is equal to the ground pixel size or Ground Sampling Distance (GSD).

The ideal pixel assumption generates moderate errors for satellite imagers in which the spatial response of the sensor is limited by the spatial response of its detector, but it generates gross errors for satellite imagers in which the spatial response of the imaging sensor is limited by the spatial response of its optical aperture.

Traditional large remote sensing satellites (few tons in weight) deployed by space agencies, such as Landsat, provide images that usually have a detector-limited response, whereas the more recent small CubeSat satellites (few kilograms in weight) deployed by commercial vendors, such as Planet's SuperDove, provide images that usually have an optics limited response.

As demonstrated in the sixth chapter, in a Landsat image about 70 % of a pixel's DN originates from the area represented by this pixel, and its average spatial resolution distance is about 1.5 times larger than its GSD. In a SuperDove image about 10 % of a pixel's DN originates from the area represented by this pixel, and the average spatial resolution distance is about five times larger than its GSD.

The early satellite images had a detector-limited response, so the moderate errors of the ideal pixel assumption were almost unnoticeable, being mostly masked by image noise. The models (metrics, methods, and algorithms) associated with this assumption were adopted as axioms, and although some works warned about the errors involved in using these models to describe optics-limited images, these warnings went unnoticed by most of the remote sensing community.

The aim of this research is to advance the assessment of the spatial response of satellite images by developing four innovations applicable to detector-limited and optics-limited images: (1) a metric to gauge spatial resolution distance, (2) a method to assess spatial response models, (3) a model to estimate spatial response from edge measurements, and (4) a procedure to improve the spatial response of satellite images.

The first chapter of this thesis presents the genesis of the problem, introduces some key technical terms that will be used in the next chapters, and gives an overall view of my research.

The second chapter presents an upgraded taxonomy of spatial resolution metrics and develops a new metric that computes the spatial resolution distance as a function the image's resolving contrast. This new metric allows current spatial resolution metrics to be assessed using an unbiased framework, showing that most current metrics are either incorrect or biased.

The third chapter shows that the current methodology to assess spatial response models is biased since it uses as a benchmark a specific sensor with a given spatial response, so the model's assessment is only applicable to this specific spatial response. This chapter develops a new methodology that uses the optical design parameters - which define the spatial response - as independent variables, so the assessment is applicable to a wide variety of spatial responses. This methodology is applied to assess the two-edge Separable Point Spread Function (PSF) model that estimates the spatial response of a satellite image by measuring this response along two perpendicular edges. It is shown that this popular two-edge model is only applicable to low optical factors (detector-limited images) and that it gives incorrect results for the higher optical factors (optic-limited images) employed by most types of current satellite images.

The fourth chapter develops a new spatial response model that uses three edge measurements and that is applicable to the higher optical factors not covered by the Separable PSF model. This new three-edge model is developed and assessed with the same methodology developed in the third chapter, showing that it complements the two-edge model, so that both models together enable the estimation of the spatial response through edge measurement for all optical factors.

The adjacency errors of the ideal pixel assumption can be reduced by "restoration", an image processing technique that approximates the actual image to the ideal image. The usual restoration technique deconvolves the raw image with a deconvolution kernel defined by the sensor's spatial response. It has been shown that this usual kernel is not optimal and an empirical method to find the optimum kernel has been proposed, but this method is cumbersome and is not applicable to all satellite imagers. In response to this limitation, the fifth chapter develops a new alternative method to find the optimum kernel by using synthetic edge images. This new method is validated by showing that its predictions agree with the results of the previous empirical method. The new method is more accurate and simpler to apply, opening new research paths on image restoration.

The sixth chapter demonstrates the practical application of the metric developed in the second chapter, by computing the spatial resolution distance of the green channels' images captured by SuperDove and Landsat 8 satellites, under three different conditions: (1) negligible atmospheric turbulence and moderate spacecraft jitter, (2) strong atmospheric turbulence and moderate spacecraft jitter, (3) negligible atmospheric turbulence and high spacecraft jitter. An original procedure is developed to estimate the spatial response model of the imaging channels, by using a combination of spatial response measurements, known sensor parameters, and unknown sensor parameters.

The seventh chapter synthetizes the results, illustrating new applications for the innovations presented in the previous chapters and giving examples how they can be used altogether as tools to improve the assessment and the quality of satellite images.

Chapter One

Introduction

1.1. Overview

Section 1.2 provides the background material required to understand the statement of the problem and the corresponding research questions.

Section 1.2.1 provides a qualitative description of how the technical development of satellite imaging sensors has currently generated a problem regarding the assessment of their spatial response.

Section 1.2.2 introduces the parameters of an imaging sensor that are required to compute its optical factor and section 1.2.3 graphically illustrates the spatial response for different values of the optical factor.

Section 1.2.4 contrasts the concept of an ideal satellite image with the concept of an actual satellite image, and section 1.2.5 discusses how the conflict between these two concepts paves the way to the statement of the problem that will be presented in section 1.3.

Section 1.3 identifies the research gaps and the corresponding research questions.

Section 1.4 outlines the structure of this thesis.

1.2. Background

1.2.1. Genesis of the problem

This research addresses the assessment of the spatial response of imaging sensors on board satellite platforms, named satellite imagers for short. The spatial response of an imaging sensor (imager) is one of its most important features, because it defines the level of detail of the scene that can be captured in the image. The assessment of the spatial response of imagers considers several issues: the metrics used to characterize the properties of the spatial response, the mathematical models used to predict the shape of the spatial response, the methods used to measure the spatial response when the imager is already in orbit, and the image processing procedures used to improve the spatial response of the image once it is captured. In this section, the previous metrics, models, methods, and procedures are collectively described as “models”.

Since the launch of Landsat 1 in 1972, the design concept of satellite remote sensing instruments has experienced some important changes. Until 1999 satellite imagers were high quality instruments, designed to achieve a spatial response limited by the size of the detector elements (Markham 1985). This “detector-limited” design allowed the spatial response of the instruments to be successfully assessed by using some simple models. The small errors of these models were almost unnoticeable because the images were relatively noisy, so model’s errors were masked by image noise (Mika 1997). Thus, the practical utility of these detector-limited spatial response models was firmly established in the remote sensing community, and so in many publications they were presented – and are still presented nowadays - as axioms.

In 1999 the Ikonos satellite was launched, becoming the first commercial high-resolution satellite imager to provide a 1-meter ground pixel size. To achieve this small ground pixel, the Ikonos sensor deviated from the detector-limited design and used instead a new type of "optics-limited" design in in which the spatial response is mainly limited by the size of the optical aperture.

The models that are useful to assess the spatial response of detector-limited imagers are not applicable to optics-limited imagers. Several publications have warned the remote sensing community of the high errors incurred by using detector-limited models to assess optics-limited sensors (Townshend 1981, 32; NRC 2000, 29; Thompson 2009, 1; Verhoeven 2018, 25), but the number of these "model-warning" publications is insignificant when compared to the overwhelming number of publications which present the detector-limited models as axioms.

Space agencies are still deploying instruments with detector-limited designs; this is the case of some imaging channels on board Landsat 9 and Sentinel 2 satellites. But, considering the overall number of remote sensing satellites currently in orbit, optics-limited designs are by far the most prevalent trend. This trend has been exacerbated by the hundreds of CubeSat imaging sensors in orbit, which use an optics-limited design to achieve a small ground pixel size.

Nowadays, most satellite images used in remote sensing applications are captured by optics-limited sensors, However, most users are unaware of the errors incurred by applying detector-limited models to assess the spatial response of optics-limited images. This lack of awareness is due to a combination of three main factors: the success of detector-limited models to characterize the first satellite imaging sensors, the current presentation of detector-limited models as axioms in the remote sensing literature, and the lack of suitable models to replace the former models outside their range of validity.

The need to provide more accurate spatial response models is exacerbated not only by the trend for higher optical factors, but also due to the improved electronics of current detector technologies which have reduced by more than one order of magnitude the noise level of satellite images. For example, it is illustrative to compare the radiometric performance of the Multi Spectral Scanner (MSS) on board Landsat 1, launched in 1972, with the performance of the Ocean and Land Colour Instrument (OLCI) on board Sentinel 3B, launched in 2018. For this purpose, band 4 of the MSS, which covered wavelengths from 500 to 600 nm will be compared with band 12 of OLCI which is centred at 560 nm.

The parameters of interest for this comparison are the Signal to Noise Ratio (SNR) measured in orbit and the number of bits per pixel in which the Digital Number (DN) recorded by each pixel is encoded. For Landsat 1 the SNR was 113 and the DN was coded in six bits (Mika 1997, Table 2), whereas for Sentinel 3B the SNR was 1822 and its DN is coded in twelve bits (S3MPC 2021, Table 5). The noise level has decreased 16 times and the number of DN levels has increased 64 times, this means that more accurate spatial response models are required to fully exploit the radiometric performance of current satellite images.

The evolution of satellite sensors has generated the need to develop new spatial response models applicable to optics-limited and detector-limited designs. These new models should allow a more accurate characterization and a more efficient exploitation of the spatial response of optics-limited satellite images. These new models could also be used to quantify the huge errors of the current detector-limited models, contributing to raise awareness in the remote sensing community about the fundamental limitations of these later models and the need to replace them when dealing with optics-limited images.

1.2.2. Imaging sensors

An imaging sensor, known as imager for short, is an electrooptical device that produces a two-dimensional visual representation of a three-dimensional scene. This representation, known as "image", is a rectangular array of many picture elements named "pixels".

The production of the image is schematically illustrated in Figure 1.1; the imager captures through its optical aperture some electromagnetic energy radiated from the scene and transforms it into an array of digital numbers which are represented visually as an image. In this schematic figure the image is simplified by assuming that it has only 11×11 pixels, whereas in practice it may have more than one million pixels.

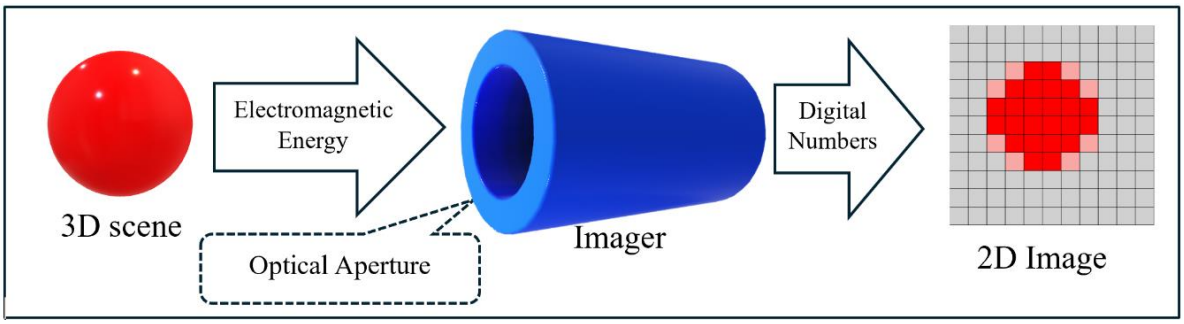

Figure 1.1: Production of an image by an imaging sensor. Electromagnetic energy radiated by the three-dimensional scene is captured through the optical aperture of the imaging sensor (imager). The imager produces a two-dimensional array of digital numbers which are visually represented in an image.

Once the electromagnetic energy enters the optical aperture, the optical elements of the sensor channelize this energy, focusing it on a two-dimensional array of detector elements, also known as focal plane array or image plane. Each element of this array, also known as a "pixel", generates an electrical signal that is proportional to electromagnetic energy that was focused on its detecting surface. The intensity of this signal is measured, and the recorded result is the pixel's Digital Number (DN).

Therefore, the term "pixel" may refer to the physical detector elements of the focal plane array or to the picture elements of the image that visually represents the DNs measured by the detector elements. For a given image, each detector element generates a single DN which uniquely defines the picture element, thus there is a one-to-one correspondence between these two elements. The possible ambiguity between these two meanings of "pixel" is not an issue, being resolved by the context.

Figure 1.2 provides a schematic cut-view illustration of this focusing process, showing the four dimensions that are most relevant to the image obtained: the wavelength λ of the electromagnetic energy, the diameter D of the optical aperture, the focal length distance F between this aperture and the image plane, and the pixel pitch p of the detector elements. In what follows it is assumed that the optical aperture is circular and that detector elements have a square shape.

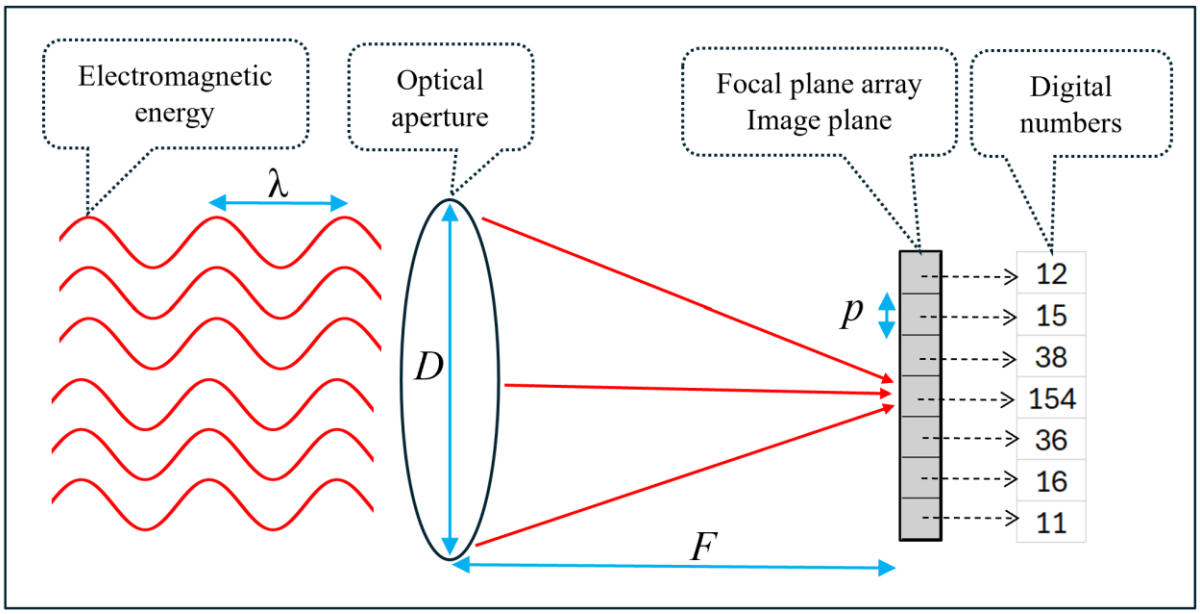

Figure 1.2: Schematic cut view of the generation of digital numbers by an imaging sensor. Electromagnetic energy of wavelength λ, shown in red colour, is captured by an optical aperture of diameter D and then it is focused along a focal length F on the focal plane array or image plane. Each detecting element or "pixel" of this array converts the focused energy into an electrical signal whose intensity defines the pixel's digital number. Only one column of the array is represented in the figure.

One of the most important design parameters of an imaging sensor, is the optical factor Q defined as (Fiete 2010, Chapter 8):

$$Q = \frac{\lambda}{D}\frac{F}{p} \tag{1.1}$$

Where λ is the central wavelength of the detected radiation, D is the diameter of the optical aperture, p is the pixel pitch of the detector elements, and F is the focal length of the optical system. As will be discussed in what follows, the optical factor defines the shape and the extent of the sensor's spatial response.

One illustrative definition of the optical factor is to consider the focusing on the image plane of the energy generated by a scene in which there is single point source; a practical case is the astronomical observation of a single star surrounded by dark space. In this case, about half of the energy focused by the circular optical aperture on the focal plane array is contained within a circle of diameter $\phi = \lambda \cdot F/D$ (Tschunko 1974), thus the optical factor can also be defined as the ratio between the half-energy diameter ϕ and the pixel pitch p:

$$Q = \frac{\phi}{p} \tag{1.2}$$

Although almost half of the energy (actually 46 %) is focused within a circle of diameter ϕ, the remainder energy spreads into a much larger diameter. For example, 83 % of the energy is contained within a diameter 2·ϕ and 96 % of the energy is contained within a diameter 10·ϕ (Tschunko 1974).

Figure 1.3 presents a plan view of nine pixels in the image plane, depicting as a black circle the half-energy diameter for three values of the optical factor. For Q = 0.1 (left panel of Figure 1.3) 97 % of the energy focused into the image plane is detected by the central pixel (Andersen 2015). For Q = 1 (central panel of Figure 1.3) 54 % of the energy focused into the image plane is detected by the central pixel (Andersen 2015). For Q = 2 (right panel of Figure 1.3) 18 % of the energy focused into the image plane is detected by the central pixel (Andersen 2015).

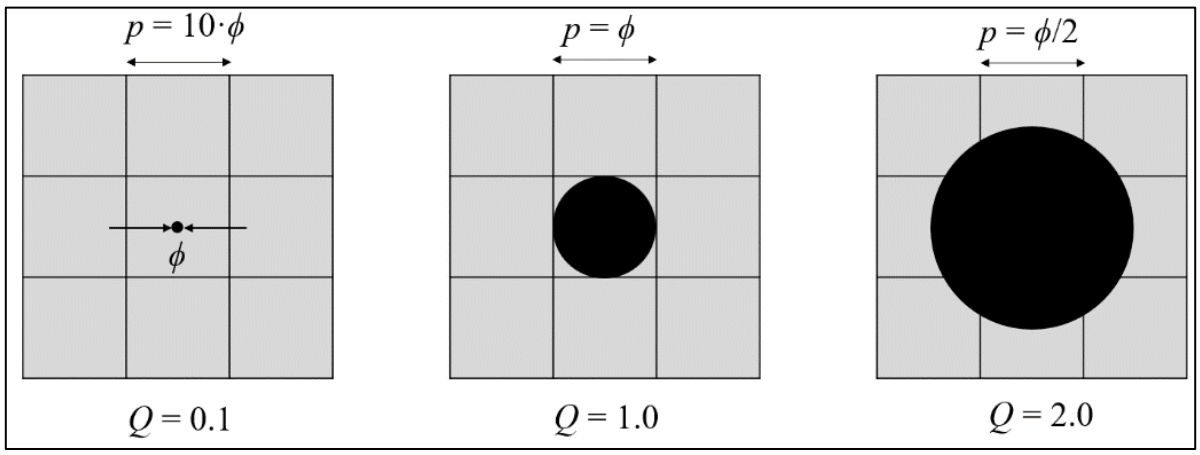

Figure 1.3: Pictorial representation of the half-energy diameter in the image plane for three different optical factors. A section of 3×3 pixels in the image plane is represented by nine squares of width p and the half-energy diameter ϕ that contains 46 % of the energy focused into the image plane is represented by a black circle. The three figures assume that the geometrical projection of the point source in the scene lies in the centre of the central pixel. The black circle contains almost half of the energy focused on the image plane, so when Q = 0.1 almost all this energy lies within the central pixel, when Q =1 this energy distributes roughly evenly between the central pixel and its surrounding pixels, and when Q = 2 the greatest portion of this energy spreads into adjacent pixels.

1.2.3. Spatial response of an imaging sensor

The spatial response of an imaging sensor, known as the Point Spread Function (PSF), determines the image that will be produced for a given scene. The PSF is a two-dimensional function, defined as the response of the imager to a single point-source in the scene. The shape and the extent of this function depends mainly on the optical factor Q, some examples of spatial response will be graphically presented for a perfect staring imager.

A perfect imager has an ideal optical system, without any type of imperfection (no optical aberrations), and an ideal detector array, in which the DN measured by each pixel does not affect the DN measured by adjacent pixels (no pixel crosstalk due to charge diffusion between detector elements). A staring imager does not scan its field of view while capturing the image.

As described in sections 2.3.1.2, 3.2.3 and 4.2.2.1, all imagers have imperfections, and most satellite imagers scan their field of view to produce the image. But, to introduce the concept of spatial response, it is convenient to leave imperfections and scanning aside, to consider only the impact of the optical factor on the spatial response. Under these conditions, the one-dimensional cuts of the spatial response are identical along the columns and lines of the detector array. Four examples of these response will be graphically and numerically illustrated.

In all these examples there is only a single point source in the scene whose geometrical projection in the image plane is located at the centre of the central pixel. For convenience only a small area of 10×10 pixels in the image plane is presented. The spatial response is normalized to a maximum value of 1, which always occurs at the centre of the central pixel. To quantify the spatial response to single point source in the scene the following parameters are presented at Table 1.1:

1. The Full Width at Half Maximum (FWHM) of the PSF along the columns or lines of the detector array. This parameter measures the distance (in pixel pitch units) between the points where PSF = 0.5, and so it gives a measure of the space in the image plane where about half of the energy detected is distributed.

2. The Full Width at one-hundredth Maximum (FWhM) of the PSF along the columns or lines of the detector array. This parameter measures the distance (in pixel pitch units) between the points where PSF = 0.01, and so it gives a measure of the spread of the spatial response into adjacent pixels. The spread of the PSF into adjacent pixels is quantified by (FWhM-1)/2.

3. The Percentage of Pixel Energy (PPE). This parameter measures the percentage of energy focused into the image plane that is detected by the central pixel, the remainder of this energy distributes throughout the surrounding pixels. Ideally 100 % of this energy should be detected by the central pixel, but this occurs only when $Q = 0$.

If the optical factor is zero ($Q = 0$) the shape of the PSF has a perfect square cross section and extends over one pixel. Figure 1.4 illustrates the PSF for $Q = 0$, in this case the central pixel detects 100 % of the energy that was focused on the image plane, and the PSF does not spread into adjacent pixels. This case is impossible to achieve in practice because it requires an infinitely large diameter of the optical aperture ($D \rightarrow \infty$) or infinitely large pixels ($p \rightarrow \infty$).

If the optical factor is much smaller than one ($Q << 1$) the shape of the PSF is mainly defined by the detector elements; it has a square cross section. Figure 1.5 illustrates the PSF for $Q = 0.05$, the spatial response spreads about one fifth of a pixel into the adjacent pixels and the central pixel detects 98 % of the energy focused on the image plane (Andersen 2015).

If the optical factor is about one half ($Q \approx 0.5$) the shape of the PSF is defined by the detector elements and by the optical aperture, it has a square cross section with rounded corners. Figure 1.6 illustrates the PSF for $Q = 0.5$. The PSF spreads about 0.8 pixels into the adjacent pixels and the central pixel detects 84 % of the energy focused on the image plane (Andersen 2015).

If the optical factor is larger than one ($Q > 1$) the shape of the PSF is defined by the optical aperture: it has a circular cross section. Figure 1.7 illustrates the PSF for $Q = 3$. The

PSF spreads about 2.9 pixels into the adjacent pixels and the central pixel detects only 7 % of the energy focused on the image plane.

Table 1.1: Parameters of the spatial response for a perfect staring imager

Q	FWHM (pixels)	FWhM (pixels)	PPE (%)
0	1.00.	1.00	100.0
0.05	1.00	1.42	98
0.5	1.02	2.68	84
3	3.14	6.84	7

Figures 1.4 to 1.7 and Table 1.1 illustrate how the shape and extent of the spatial response varies as the optical factor Q increases. The main impact of an increase in Q is an increase in the spread of the spatial response into adjacent pixels and consequentially a decrease in the fraction of the energy detected by the central pixel. In practice, satellite imagers have imperfections, and they need to scan their field of view to produce the image. These two issues will broaden the spatial response, increasing the FWHM and the FWhM and decreasing the PPE values indicated in Table 1.1.

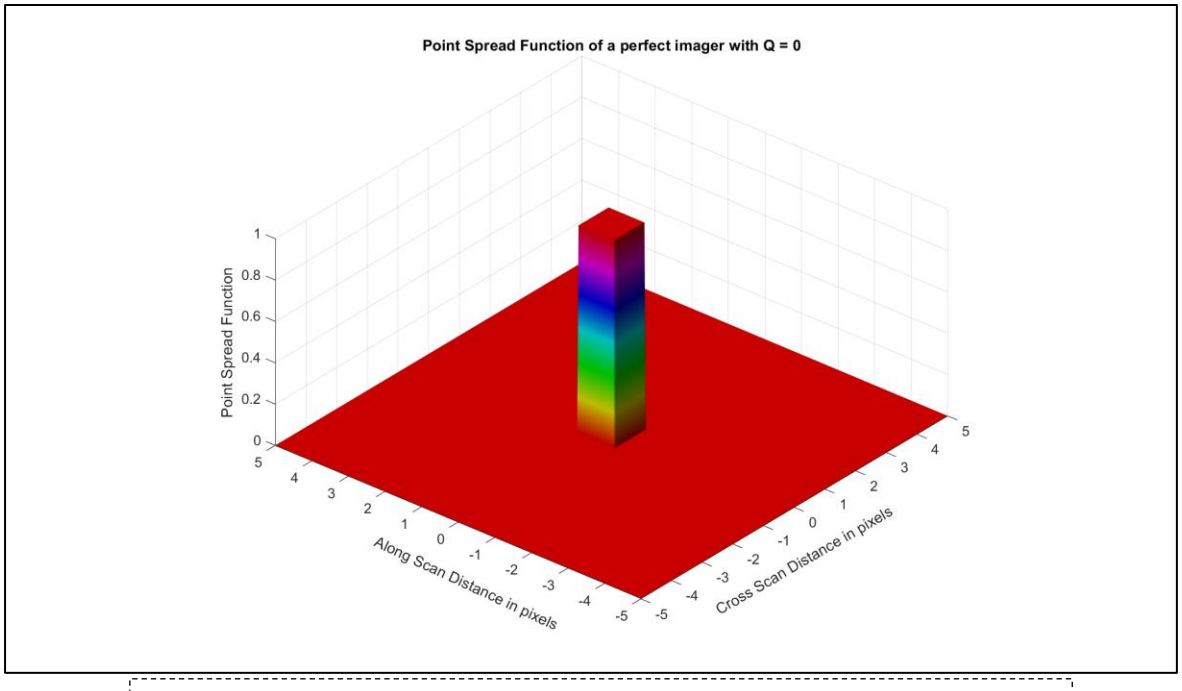

Figure 1.4: Point Spread Function of a perfect imager with an optical factor $Q = 0$.

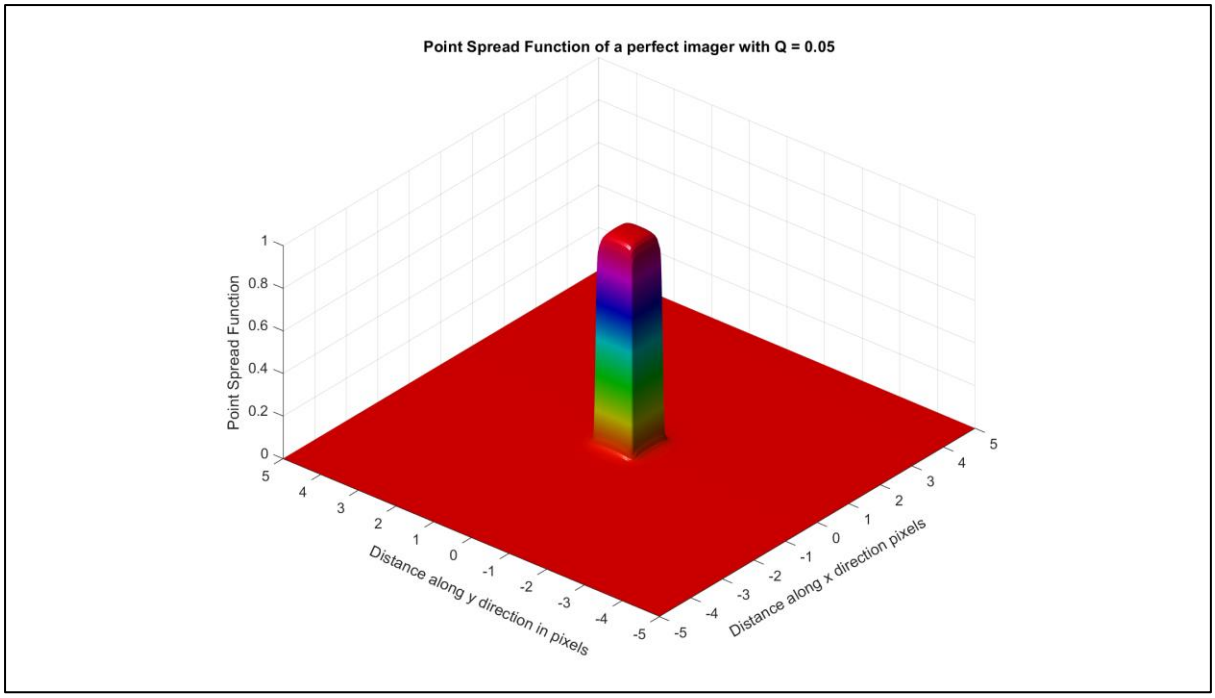

Figure 1.5: Point Spread Function of a perfect imager with an optical factor $Q = 0.05$.

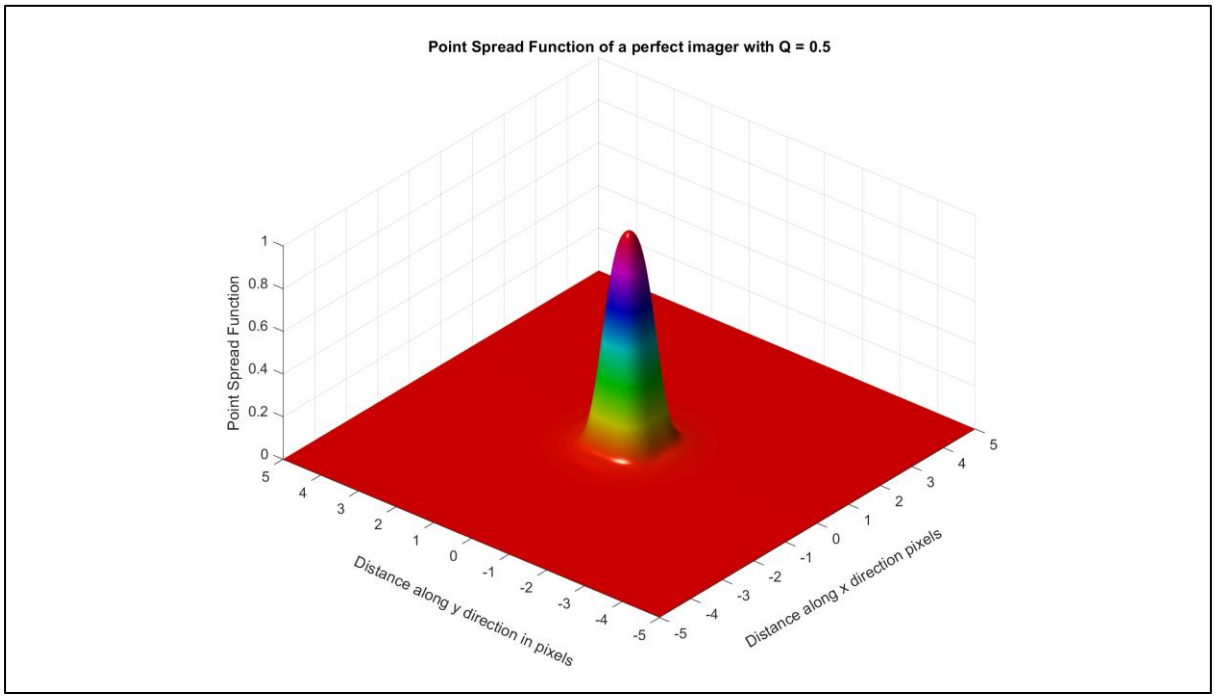

Figure 1.6: Point Spread Function of a perfect imager with an optical factor $Q = 0.5$.

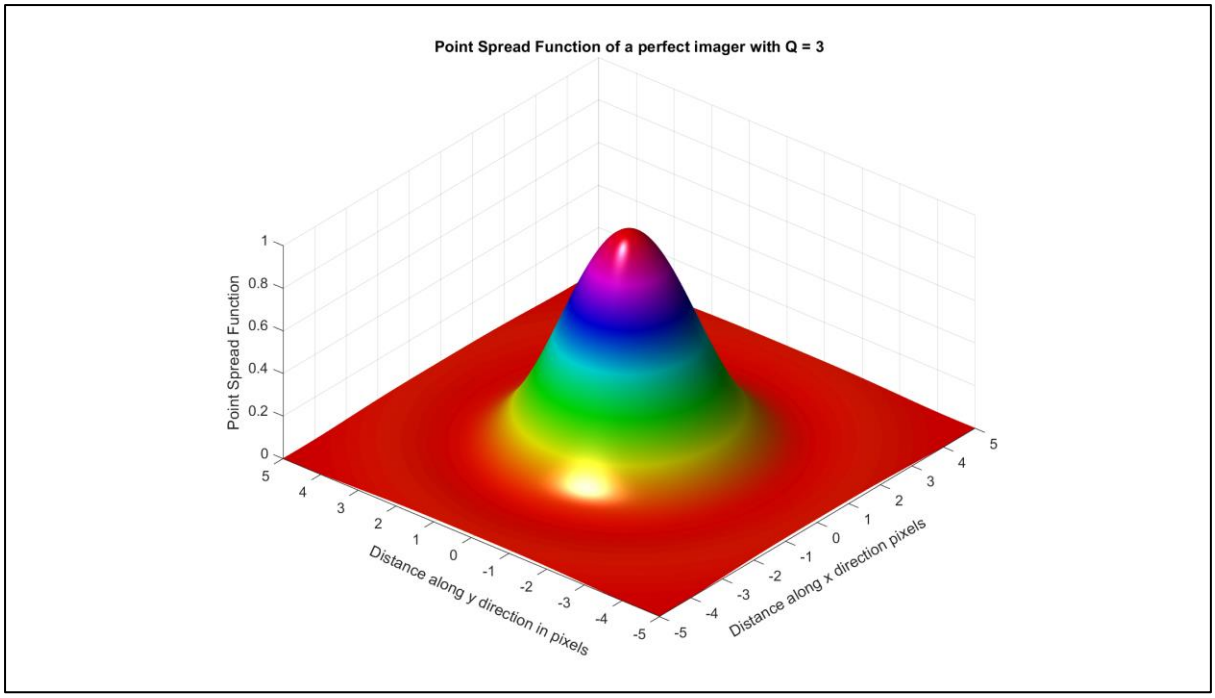

Figure 1.7: Point Spread Function of a perfect imager with an optical factor $Q = 3$.

1.2.4. Satellite images

The imaging sensors on board Earth observing satellites are currently one of the most powerful tools to monitor our planet. The number of satellites that capture images from the ground surface has grown exponentially in the past decade due to the launch of hundreds of small CubeSat satellites. For example, the PlanetScope constellation has more than 430 CubeSats that provide daily images over most of the Earth's surface (ESA Earth Online 2024).

The number of applications of satellite images has also increased, the most common usages are found in the fields of air quality, agriculture, cartography, defence, disaster management, fire monitoring, hydrology, meteorology, oceanography, and water quality.

A satellite imager can be modelled as a device that maps the ground surface onto an image composed of an array of pixels, as illustrated in Figure 1.8. Although pixels may have different shapes, they are typically square, as will be assumed in what follows. For a nadir looking satellite imager, each pixel of width p represents a square area of width GSD on the Earth's surface, where GSD stands for Ground Sampling Distance. In satellite imagers the pixel pitch p varies between a few microns (μm) to several tens of microns, whereas the GSD varies between 30 cm and several kilometres.

Figure 1.8 presents the ideal image and the actual image for a scene composed of three point sources of equal strength, named A, B, and C, which are located over a homogeneous background. The ideal satellite imager has the perfect spatial response presented in Figure 1.4 which spreads uniformly through one pixel. The actual satellite imager assumed in Figure 1.8 has a spatial response that spreads over adjacent pixels, like the response shown in Figure 1.6.

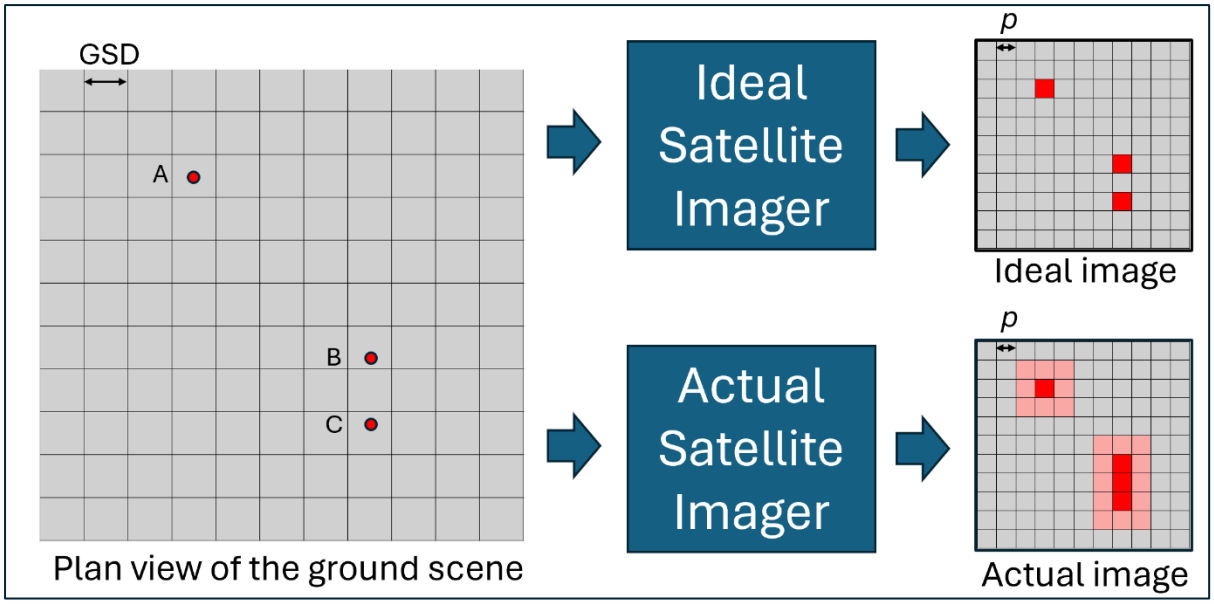

Figure 1.8: Mapping of the Earth's surface by a satellite sensor. Each square pixel of width *p* in the image represents a square area of width GSD in the ground plane. The scene has three point sources A, B, and C. Sources B and C can be resolved in the ideal image, but they cannot be resolved in the actual image.

In the ideal image, the DN measured by each pixel is proportional to the average radiance originating from the ground area represented by the pixel. The three pixels that contain the point sources have the same DN, regardless of the position of the point sources within the areas represented by these pixels. Sources B and C are separated at a distance larger than a pixel so they can be resolved, that is, they can be identified in the image as two separate sources.

In the actual image, the DN measured by each pixel is proportional to a weighted average of the radiance originating from the ground area represented by the pixel and its adjacent pixels. The DNs measured by three pixels that contain the point sources are dependent on the position of the point sources within the areas represented by these pixels. Sources B and C are separated at a distance only slightly larger than a pixel so they cannot be resolved, that is, they appear in the image as one single extended source.

1.2.5. What's in a pixel?

In the ideal image a pixel is a sharply defined entity because there is an exact correspondence between the DN it measures and the ground area it represents. In the actual image a pixel is a fuzzy entity since the DN it measures also contains some information from ground areas represented by adjacent pixels. In theory, if the scene and the spatial response of the sensor are known, the DNs of the actual image can be found. But, in practice, the image is usually captured because the scene is not fully known, so in this case the adjacency effect cannot be rigorously characterized. As stated by Cracknell (1998, 2025):

"*There is no simple answer to the question `what exactly gives rise to the signal detected and recorded in a pixel in a remotely-sensed image?' The main point to be made is to try to ensure that it is realised that there is a problem and to give some indication of the nature of that problem.*"

The problem indicated by Cracknell (1998) does not yet have an exact and unique solution. If the sensor's spatial response is known, a technique to alleviate this problem is to "restore" the actual image so that it approximates the ideal image, but this restoration is completely successful only when the scene is known beforehand (Huang et al. 2002).

In practice, the remote sensing user is usually forced to assume that an actual image can be approximated to an ideal image. This is the key assumption behind all image processing algorithms that characterize the properties of the Earth's surface on a pixel-to-pixel basis. Although this assumption is incorrect from a physical point of view, it is highly convenient from a mathematical point of view, because it greatly simplifies the image processing algorithms by assigning to each pixel a representation of a well-defined area on the Earth's surface.

The errors behind this ideal image assumption were relatively small for the first types of satellite imagers that had a low optical factor, because in this case more than half of the energy detected by a pixel originates from the ground area represented by this pixel. But these same errors are very large for the current CubeSat imagers that have a high optical factor, because in this case less than one tenth of the energy detected by a pixel originates from the ground area represented by this pixel. Thus, it may be surprising that in some remote sensing textbooks this assumption is presented as a fact without acknowledging that, in the best case, it is only a rough approximation:

"*The intensity of each pixel corresponds to the average brightness, or radiance, measured electronically over the ground area corresponding to each pixel*." (Lillesand et al. 2015, 31).

If this ideal image assumption is accepted as valid, then it readily follows that the spatial resolution distance of the image is exactly one pixel, because if two sources are separated at a distance slightly larger than one pixel, as depicted for sources B and C in the left plan view of Figure 1.8, they can be resolved in an ideal image as two distinct objects, as shown in the upper right image of Figure 1.8.

The identification of GSD with spatial resolution distance is an assumption deep-rooted in the remote sensing community. This assumption is an acceptable approximation for high quality imagers with low optical factors ($Q << 1$), but it grossly underestimates the spatial resolution distance of imagers with high optical factors ($Q > 1$). For example, NASA and ESA have independently concluded that the spatial resolution distance of Planet's CubeSat imagers is about five times larger than their GSD (NASA 2020, 12; Saunier and Cocevar 2022, 28).

Thus, the assumption that a pixel from an actual image can be approximated to a pixel from an ideal image generates two errors that are usually neglected by the remote sensing community: the pixel adjacency error and the spatial resolution distance error. These errors were small for the early satellite imagers with low optical factors, and they were masked by the relatively high noise in the early images. These errors are high for the current satellite imagers with high optical factors, and they are no longer masked by the relatively low noise in the current images.

1.3. Knowledge Gaps, Aims and Research Questions

1.3.1. Knowledge gaps

During the literature review, several knowledge gaps were found regarding the assessment of the spatial response of satellite imagers. Subsequently, the following four knowledge gaps were identified as the most relevant for defining my four research questions.

1.3.1.1. *Spatial resolution metrics*

Spatial resolution is a highly popular concept, that in most remote sensing publications has a clear and unambiguous definition: it is equal to the GSD of the image. The fact that the spatial resolution of imaging sensors is always larger than the GSD and that it is an elusive and difficult concept to manage, has been noted in a few scattered publications since the advent of satellite imagers. It is illustrative to quote some warnings of the difficulties encountered when dealing with the concept of spatial resolution:

"*Throughout the history of imagery the concept of* [spatial] *resolution has been poorly defined, misused, and confused. Recently raster (sample data) systems have added further confusion. Accordingly, a closer look at the concept of* [spatial] *resolution is in order*." (NASA 1973, 104)

"In practice the capabilities of such future [high spatial resolution satellites] *systems, and even current ones, are poorly comprehended by many earth scientists including geographers. In large part this arises because users do not properly understand the significance of resolution figures which are quoted."* (Townshend 1981, 32)

"*Spatial resolution is one of the sensor parameters often mentioned but, in my opinion, also one that is least understood."* (Joseph 2000, 9)

"*No property of images is more widely quoted, and simultaneously misused, than resolution. It is a term that conveys a strong intuitive meaning, but is difficult to define quantitatively.*" (Schowengerdt 2007, 76)

"*The smallest sized detail on the ground actually recorded by an airborne or satellite camera system can be different to that expected by an applications scientist or image analyst. When this misconception occurs, it may be due to the method used in determining the spatial resolution of the camera system concerned.*" (Thomson 2009, 1)

"*It is thus fair to say that the technical concept of resolution – or more specifically spatial resolution – and all its implications are commonly poorly understood, which leads to many popular, accepted but completely wrong statements."* (Verhoeven 2018, 25)

By comparing the statement of Verhoeven (2018) with the one of NASA (1973) it is appreciated that although more than five decades of research have elapsed, the concept of spatial resolution is still considered by the technical literature as a source of confusion and

misunderstanding. The fact that more than thirty spatial resolution metrics have been proposed to compute the spatial resolution distance of satellite images, and that all these metrics give different results, shows the need of a fundamental review to the concept of spatial resolution distance.

Thus, there is a clear knowledge gap regarding the concept of spatial resolution itself and consequentially in the metric that mut be used to compute the spatial resolution distance of satellite images. Chapter 2 is an attempt to clarify this subject by defining a new spatial resolution metric which computes the spatial resolution distance as a function of the resolving contrast in the image, instead of assuming that it is a single number as other metrics usually do. This new metric allows current metrics to be assessed under a common framework, showing that the most popular metrics are either erroneous or biased.

1.3.1.2. *Spatial response models*

A review of 91 remote sensing publications that employ analytic models for the spatial response of an imaging sensor, indicated that the most popular model by far is the Gaussian function which is used in 59 of these works. The Fermi function model came second, being used in 29 of these works. The results of this review suggest that most researchers assume, either tacitly or explicitly, that the spatial response of imaging sensors has a standard shape defined by a given analytic function (Gaussian, Fermi, Cauchy, and others), and that what varies from one sensor to the other is only the width of this shape.

The current methodology to assess spatial response models tacitly follows the previous assumption, as the accuracy of competing models is assessed by comparing their predicted response with the actual response of a specific imaging sensor. If all imaging sensors would have the same shape for their spatial response and will differ only on the width of this response, then this methodology would be adequate, but the fact is that the spatial response has an infinite variety of shapes, some of them triangular or rectangular (Schowengerdt 2007, Section 3.4), which differ markedly from the Gaussian and Fermi functions usually assumed.

The limitations of the current methodology are vividly illustrated by comparing the results of five key publications in which different imagers have been used to assess several analytic models of the spatial response, with the purpose of selecting the most accurate model (Smith 2006, Claxton and Stauton 2008, Li et al. 2009, Li et al. 2011, Peng et al. 2015). The results indicate that the most accurate model of the spatial response is a Cauchy function (Smith 2006), a generalized Gaussian function (Claxton and Stauton 2008), a Fermi function (Li et al. 2009), a sine integral function (Li et al. 2011), and a Gaussian function (Peng et al. 2015). These five disparate contradictory conclusions are expected because in each case a different imager (and so a different actual spatial response shape) has been considered.

Thus, there is a knowledge gap regarding the methodology that must be employed to assess the spatial response models of satellite imagers. Chapter 3 addresses this issue by developing a new methodology that considers the parameters that define the shape of the spatial response as independent variables. Thus, instead of assessing a model against a specific spatial

response, the model is assessed in a plane of possible imager designs, where each point in this plane represents a different spatial response.

To illustrate the application of this new methodology, the popular Separable PSF model was assessed, showing that it is only valid for $Q \leq 0.35$. Thus, this model works well for the early satellite imagers that had $Q << 1$ but fails for most of the satellite imagers currently in orbit which have $Q > 0.35$. This finding generated the following knowledge gap.

1.3.1.3. *Spatial response measurements*

The Separable PSF model is used to estimate the two-dimensional spatial response of satellite sensors by measuring two one-dimensional spatial responses, generated at two straight edges orientated at perpendicular directions in the image. In Chapter 3 it was demonstrated that this two-edge model is valid only for $Q \leq 0.35$, thus the need was generated to provide a new model that is valid for $Q > 0.35$.

A new model to estimate the spatial response of satellite imagers by measuring three edges is developed and assessed in Chapter 4, using the same assessment methodology developed in Chapter 3. The new three-edge model is applicable for $Q > 0.35$ so it closes the gap regarding the estimation of the two-dimensional spatial response from edge measurements.

1.3.1.4. *Application of spatial response knowledge to image restoration*

Once the imager's spatial response has been found, this knowledge can be applied in several techniques that improve or exploit the image product. For example: calibration (Du and Voss 2004), image fusion (Zhou et al. 2020), super resolution (Lv et al. 2017), and restoration (Ngo et al. 2021).

Restoration is an attempt to approximate an actual image to the ideal image. The usual technique to restore an image is to deconvolve it with a kernel derived from the imager's PSF (Gonzalez and Woods 2017), although it has been demonstrated that this is not the optimum kernel, as deconvolution with a kernel derived from a shrunk version of this later PSF gives the best results (Huang et al. 2002).

The procedure to find the optimum PSF shrink factor kernel for restoration is quite involved because it requires suitable satellite images acquired by an auxiliary imager which has a GSD much smaller than the GSD of the images that will be restored. Moreover, the GSD of the images to be restored must be an integer multiple of the GSD of the auxiliary imager.

The difficulties of the current procedure to find the optimum PSF shrink factor for restoration, have precluded its application and consequentially the remote sensing community has overlooked the existence of an optimum restoration kernel.

Chapter 5 proposes a new simpler procedure to find the optimum restoration kernel., by using synthetic edge images. The new procedure is validated by showing that it gives the same results as the current procedure.

1.3.2. Aim

The aim of this research is to advance the knowledge regarding the assessment of the spatial response of satellite imagers, by developing the following four innovations: (1) a metric to gauge spatial resolution distance, (2) a method to assess spatial response models, (3) a model to estimate spatial response from edge measurements, and (4) a procedure to use spatial response knowledge to improve image processing algorithms.

1.3.3. Research Questions

To address the knowledge gaps identified in section 1.3.1, the following research questions have been formulated:

RQ1: How can we assess and improve current spatial resolution metrics for satellite imagers?

The remote sensing community uses spatial resolution metrics that are easy to compute but that are either incorrect or biased. The aim in addressing this question is to develop a new metric that provides a comprehensive definition of spatial resolution distance and that allows a quantitative assessment of the deficiencies and biases of current metrics.

RQ2: How can we assess current spatial response models for satellite imagers?

The current methodology to assess spatial response models is biased because it uses as a benchmark a specific sensor with given spatial response. The limitation of this approach is that the models' assessment is only applicable to a specific spatial response. The aim in addressing this question is to develop a new methodology that uses the optical design parameters which define the spatial response as independent variables, so the assessment is applicable to a wide variety of spatial responses.

The new methodology is used to assess the two-edge Separable PSF model that estimates the two-dimensional spatial response of a satellite image by measuring the one-dimensional spatial responses along two perpendicular edges. It is shown that this model is only applicable to low optical factors and that it gives wrong results for the higher optical factors representative of most types of current satellite images.

RQ3: How can we improve current spatial response models derived from edge measurements?

The usual model to estimate the spatial response of satellite imagers from edge measurements, is the Separable PSF model which uses two perpendicular edges. In RQ2 it is shown that the Separable PSF model is only applicable to low optical factors and that it gives wrong results for higher optical factors.

The aim of RQ3 is to develop a new spatial response model that uses three edges, and that is applicable to the higher optical factors not covered by the Separable PSF model. This

new three-edge model is assessed with the same methodology developed on RQ2, showing that it complements the two-edge model, so that both models altogether allow the estimation of the spatial response through edge measurements for all optical factors.

RQ4: How can we exploit our knowledge on the spatial response of satellite imagers to upgrade current image processing algorithms?

Image processing algorithms assume an ideal image in which the DN measured by a pixel, is only due to the radiance originating in the ground area represented by this pixel. In an actual satellite image, the DN is also due to the radiance originating in the surrounding ground areas represented by adjacent pixels. This adjacency effect generates errors in image processing algorithms which characterize the ground surface in a per pixel basis. These errors can be reduced by "restoration", an image processing technique that approximates the actual image to the ideal image (Huang et al. 2002).

The usual restoration technique deconvolves the raw image with a deconvolution kernel defined by the sensor's spatial response. It has been shown that this usual kernel is not optimum and an empirical method to find the optimum kernel has been proposed (Huang et al. 2002). This empirical method is cumbersome and has several drawbacks that have inhibited its application.

The aim in addressing this question is to develop a new simpler method to find the optimum kernel by using synthetic edge images. This new method is validated by showing that its predictions agree with the results of a previous empirical method. The new method is more accurate and simpler to apply than this empirical method, opening new research paths on satellite image restoration.

1.4. Thesis Structure

This thesis has five research chapters numbered as Chapter 2 to Chapter 6. Chapters 2, 3, 4 and 5 provide the corresponding answers to the four research questions presented in this Chapter. Chapter 6 applies the metric developed in Chapter 2 to some cases of practical interest.

The structure of the thesis is by publication, so chapters 2, 3, 4, 5 and 6 are reformatted copies of technical papers which have been published in peer-reviewed journals . To integrate these five papers as chapters of this thesis, they have been reformatted in the numbering of the sections, tables, and figures, and in the referencing style to match the one used in this thesis.

Chapter 2 presents an upgraded taxonomy of spatial resolution metrics and develops from first principles the Spatial Resolution Function, a new metric that computes the spatial resolution distance as a function the image's resolving contrast, allowing all current spatial resolution metrics to be assessed under an unbiased framework.

Chapter 3 develops a new method to assess spatial response models and applies this method to assess the Separable Point Spread Function model, showing that is only valid for low optical factors.

Chapter 4 develops a new model to estimate the spatial response from edge measurements and assesses this model using the same method developed in Chapter 3, showing that the new model is valid for those optical factors for which the Separable Point Spread Function model fails.

Chapter 5 develops a new procedure to find the optimum restoration kernel for satellite imagers by using synthetic edge images, showing that this synthetic image procedure gives the same results as the more complex procedure that uses actual satellite images.

Chapter 6 computes the Spatial Resolution Function of two specific remote sensing satellites under different conditions, presenting three original contributions: (1) an empirical procedure to estimate the spatial response from sensor parameters and spatial response measurements, (2) a metric to gauge the degradation of spatial resolution due to sensor imperfections, and (3) a quantitative analysis of the instability of the spatial response of imaging sensors on board CubeSat satellites.

Chapter 7 opens with a summary and synthesis of the outcomes of the thesis in the context of the research questions formulated. It then outlines some additional applications of the outcomes that are included in the appendices. Finally, it discusses some limitations of the methodology employed and sketches some options for future research.

Chapter Two

A New Metric for the Assessment of Spatial Resolution in Satellite Imagers*

* This chapter was published on 27th October 2022 as:

Valenzuela A, Reinke K, Jones S (2022). A new metric for the assessment of spatial resolution in satellite imagers. *International Journal of Applied Earth Observation and Geoinformation* **114**, 1-19. https://doi.org/10.1016/j.jag.2022.103051.

2.1. Introduction

Spatial resolution is one of the key properties of satellite imagers because it determines the smallest object or feature in the real world that can be captured within the resultant two-dimensional image and, therefore, the corresponding applications for which this product is suitable. Despite the fundamental importance of spatial resolution, confusions surrounding its definition and assessment for satellite imagers have been a recurring topic of concern during the last five decades.

This confusion is first documented with the advent of digital images on Earth observation satellites. "*Throughout the history of imagery the concept of resolution has been poorly defined, misused, and confused. Recently raster (sample data) systems have added further confusion. Accordingly, a closer look at the concept of resolution is in order"* (NASA[1] 1973, 104). Decades later, the issue remains with Schowengerdt (2007, 76) stating "*No property of images is more widely quoted, and simultaneously misused, than resolution. It is a term that conveys a strong intuitive meaning, but is difficult to define quantitatively."* and more recently with other authors including Thomson (2009), Joseph (2015) and Verhoeven (2018), raising similar concerns.

The main source of confusion regarding spatial resolution is the lack of consensus on which criterion should be used to define it, and once this criterion is settled, which metric should then be employed to compute it. In this study, my literature survey shows that several criteria have been defined and more than thirty metrics have been proposed for satellite imagers.

Agreement on the defining parameters for spatial resolution is needed, as the use of satellite imagery and its integration with other data sources becomes ubiquitous in remote sensing applications across disciplines. If a biased metric is used to select an imager with the best spatial resolution for a certain application, a wrong decision can be taken.

One of the most popular criteria for digital imagers identifies spatial resolution with pixel size, regardless of image quality. The associated metric for satellite imagers is the popular Ground Sampling Distance (GSD), computed as the geometrical projection of a pixel's width on the ground plane (Fiete 1999, Schowengerdt 2007, Verhoeven 2018).

The GSD is equal to the resolution distance for an ideal pixel which represents only the radiance collected from an area on the Earth's surface that corresponds to its geometrical projection. Some satellite imagers approximately fulfil this ideal pixel requirement, but on most imagers the actual pixel also collects radiance from surrounding areas represented by adjacent pixels, in this later case the spatial resolution distance is larger than the GSD.

The ideal pixel assumption can lead to several types of errors, for example:

1. Errors in land cover characterization were assessed to be 11 % (Townshend et al. 2000).

2. Errors in fire brightness temperature were estimated at 20 K (Calle et al. 2009).

3. The actual resolution distance of a sensor was valued as twice its GSD (Just 2000).

Although the fundamental limitations of the GSD as a resolution metric are well known (Townshend 1981, Fisher 1997, Cracknell 1998, Townshend et al 2000, Thomson 2010,

[1] Abbreviations used in this paper are defined at the end of this chapter in page 58.

Valenzuela and Reyes 2019a), this simple parameter is usually identified with spatial resolution, due to its simplicity and the lack of consensus on which one of the tens of alternative metrics available should be used to replace it. Each metric predicts a different resolution distance, for example, the "*radiometrically accurate*" metric (Joseph 2000, 10) predicts resolution distances roughly twenty times larger than the GSD (Joseph 2015).

Another common approach to spatial resolution is the two-point source criterion, which defines resolution as the smallest distance between two-point sources in the scene that allows them to be detected as two separate objects in the image (Goodman 1996, Boreman 2001, Reulke et al. 2006, Fiete 2010, Cremer 2012).

The two-point sources are considered to be resolved in the image when a certain minimum amplitude dip or contrast is achieved between them, as illustrated in Figure 2.1.c. This criterion has been used to compute (Jahn and Reulke 2000) and measure (Conran et al. 2021) the resolution distance of satellite imagers and remains a popular approach to provide a more general definition of spatial resolution beyond the basic pixel size criterion.

While the two-point source criterion is generally accepted, it is somewhat ambiguous because it does not specify the minimum resolving contrast that must be achieved to declare resolution.

For the case of spatial resolution metrics that consider only an ideal optical aperture, different contrast requirements lead to dissimilar metrics, which diverge up to a factor of 2.5 in the computation of resolution distance (Chesley et al. 1999, Fiete 2010).

In response to this divergence, image resolution was defined as the distance between two-point sources for which a certain contrast is achieved in the image, computing this contrast for an ideal optical aperture as a function of the separation distance between sources, noting that some metrics are particular points along this contrast function (Stelzer 1998).

For satellite imagers, it was noted that is not possible to characterize spatial resolution by a single parameter (Joseph 2015) and that a comprehensive study of resolution should consider the computation of resolution distance as a function of contrast (Valenzuela and Reyes 2019a).

Following these lines of thought, this work develops a general metric called "Spatial Resolution Function", based on the two-point source criterion, computing the spatial resolution distance as a function of the contrast achieved in the image plane.

The Spatial Resolution Function is defined in a such a way that it is equal to the GSD when the pixel size is the only relevant spatial resolution factor, showing that the pixel size criterion is a particular case of the two-point source criterion.

The Spatial Resolution Function computes resolution distance for any type of satellite imager, using as input the imaging system's pre-sampled spatial response to a single point source. A property of this same response is used as spatial resolution criterion for the most common alternative metrics to the GSD, herein called "Spatial Response" metrics.

To compute the Spatial Resolution Function, the sampled image equation (Park et al. 1984) is applied to the case of two-point sources in the scene, computing the contrast in the

image plane for a wide range of given separation distances. The results of this computation illustrate that resolution distance is a function of the contrast in the sampled image rather than a single distance as usually assumed by Spatial Response metrics. These results also show that these later metrics are biased, giving erroneous predictions when used to compare different types of satellite imagers.

The computation of the Spatial Resolution Function requires the same input data used by Spatial Response metrics, thus rendering them obsolete, generating a paradigm shift in the assessment of the spatial resolution for satellite imagers.

2.2. Background

2.2.1. Spatial resolution concepts

Since the onset of satellite imagers, the assessment of their spatial resolution has been a regular research subject (NASA 1973, Townshend 1981, Wang and Li 1999, Thomson 2009, Valenzuela and Reyes 2019a, Stankevich 2021). Beyond pixel size, there is consensus that this matter is related to the spatial response of the sensor, quantified either in the spatial domain, by its system Point Spread Function (PSF), or in the frequency domain, by its system Optical Transfer Function (OTF).

The computations of OTF and PSF are mature subjects (Boreman 2001, Cota et al. 2010, Fiete and Paul 2014), but once these functions are known, there remains no consensus on how to compute spatial resolution.

This lack of consensus has led to the predominance of the GSD metric, a simple geometrical concept that is easy to grasp, compute and measure. A plethora of alternative metrics have been defined, but none of them has achieved the popularity of the GSD (Townshend 1981, Joseph 2000, Thomson 2009, Valenzuela and Reyes 2019a, Stankevich 2021).

When the GSD is identified with spatial resolution, it is tacitly assumed that the sensor is an ideal detector, so each pixel in the image plane represents only the area on the Earth's surface that corresponds to its geometrical projection.

The fragility of this later assumption was highlighted during the late 1990's in three key works with attention-grabbing titles, which noted that a pixel collects radiance not only from the area defined by its projection on the Earth's surface, but also from surrounding areas represented by adjacent pixels, introducing the concepts of PSF and OTF to quantify this adjacency effect (Fisher 1997, Cracknell 1998, Townshend et al. 2000).

Later, the "*fundamental flaw*" (Thomson 2010, 42) of the GSD as a spatial resolution metric was illustrated for satellite and airborne sensors in which resolution is limited by the spatial response of the optics.

Spatial resolution is usually defined as the smallest distance between two-point sources in the scene that allows them to be detected as separate objects in the image (Goodman 1996, Boreman 2001, Reulke et al. 2006, Fiete 2010, Cremer 2012).

Point sources are typically more amenable to a rigorous theoretical treatment than areal objects such as circles (Helstrom 1969) or bars (Boreman and Yang 1995). In practice, point sources provide good models for high-radiance objects that subtend an angle much smaller than the one subtended by the GSD; for example, distant stars used for satellite calibration (Greslou et al. 2012), convex mirrors that simulate ground based point sources to measure the PSF of satellite imagers (Helder et al. 2005), and small fires detected from geostationary orbits (Engel et al. 2021).

The new Point Pair Resolution Technique (Conran et al 2021) has further extended the use of convex mirrors to measure the spatial resolution of satellite imagers, successfully verifying the contrast predictions of two-point source metrics against in-orbit *PSF* measurements. Thus, a theory of spatial resolution based on two-point sources has direct practical utility and can be experimentally verified.

Figure 2.1 illustrates the concepts of PSF, spatial resolution and resolving contrast, depicting in one dimension the PSF and the spatial resolution of two-point sources in the image plane. Three cases are shown: a) Response to single point source in the scene whose geometrical projection is located at the centre of a pixel. b) Combined response to two-point sources in the scene whose geometrical projections are separated at a distance of one pixel width and located at the edges of a pixel. c) Combined response to two-point sources in the scene whose geometrical projections are separated at a distance of two pixels widths and located at the centres of two pixels.

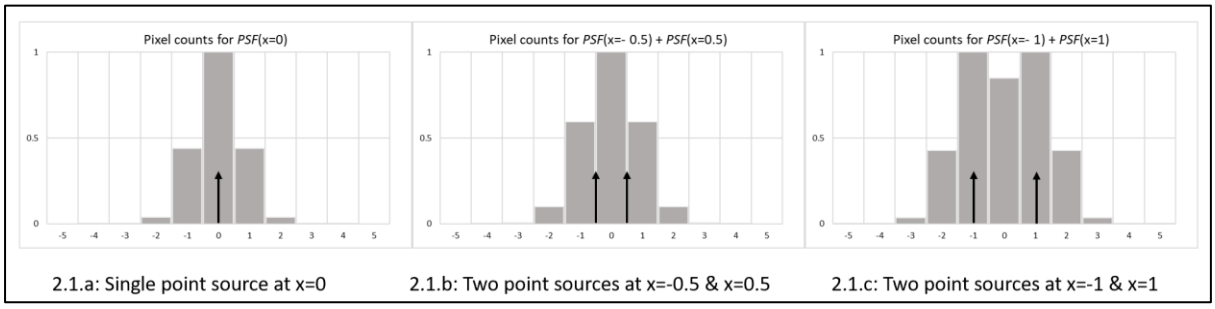

Figure 2.1: Image plane response to point sources. The figures show in one dimension the response in the image plane to: a) Single point source located at the centre of a pixel. b) Two-point sources located symmetrically with respect to the later centre, separated at a distance of one pixel. c) Two-point sources located symmetrically with respect to the later centre, separated at a distance of two pixels. Vertical axes represent the intensity of the responses normalized to a maximum value of 1 and horizontal axes represent distance measured in pixels. The positions of the geometrical projection of the point sources on the image plane are represented by arrows.

Figure 2.1.a illustrates the adjacency effect of the PSF, by showing that a single point source generates not only a strong signal in the pixel where its projection is located, but also lower signals in four adjacent pixels.

Figure 2.1.b illustrates the case of two-point sources separated at a relatively small distance, which cannot be resolved as there is no resolving dip in the image. The two-point source criterion states that in this case the two sources are unresolved, regardless of the resolution metric.

Figure 2.1.c illustrates the case of two-point sources separated at a relatively large distance, which can be resolved as there is a small resolving dip between the two sources in the image. The two-point source criterion states that in this case the two sources can be declared resolved or unresolved, depending on the minimum resolving contrast specified by the resolution metric used to implement this criterion.

With relation to Figure 2.1.c, let I_{min} be the value of the combined response at its centre and I_{max} the maximum value at each side. Resolving contrast is defined as $C = (I_{max} - I_{min})/I_{max}$ (Stelzer 1998, Reulke et al 2006). C ranges from 0 (minimum contrast) to 1 (maximum contrast).

The two sources are considered resolved when contrast reaches a minimum value or threshold $C_{min} \geq 0$. This threshold is a characteristic of the two-point source resolution metric, for example, the generalized Sparrow limit metric requires that the central pixel has the same signal as the adjacent pixels ($I_{max} = I_{min}$), that is, $C_{min} = 0$, whereas the generalized Rayleigh criterion metric requires $C_{min} = 0.265$.

In Figure 2.1.c, $I_{max}= 1$, $I_{min}= 0.84$ and $C = 0.16$. Thus, case 2.1.c is declared resolved according to Sparrow metric ($0.16 > C_{min} = 0$) and unresolved according to Rayleigh metric ($0.16 < C_{min} = 0.265$). Case 2.1.b (no contrast) is declared unresolved regardless of the metric.

The disparate conclusions of the two metrics applied to Figure 2.1.c show that spatial resolution cannot be dissociated from contrast (Stelzer 1998); different contrast thresholds lead to different resolution metrics (Fiete 2010, Verhoeven 2019).

In practice the choice of threshold is conditioned by the Signal to Noise Ratio (SNR), as to detect the central dip its amplitude must be higher than signal fluctuations due to noise, so the higher the noise the higher the useful threshold (Steltzer 1998).

For example, if in Figure 2.1.c, SNR = 5, then signal amplitudes will mostly fluctuate in a range $I_{max} = 1 \pm 0.2$ and $I_{min}= 0.84 \pm 0.17$, so the resolving dip may be lost in noise when $I_{max} < I_{min}$.

Sparrow limit defines the minimum theoretical spatial resolution distance without considering noise limitations, but actual images are noisy so in practice a threshold $C_{min} > 0$ will always be required. An estimate of this threshold is presented at section 2.3.2.3.

2.2.2. A taxonomy for spatial resolution metrics

A taxonomy that classifies spatial resolution metrics into one of three types according to the criterion used to define spatial resolution is proposed, offering a comprehensive view of the metrics that have been applied to satellite imagers.

This taxonomy is based on a three-type taxonomy of optical instruments (Ramsay et al 1941) which was adapted to consider satellite imagers (Valenzuela and Reyes 2019a). As a

result of our literature review on spatial resolution metrics for satellite imagers, this later taxonomy was further developed by defining subtypes under each type, extending it to include the imager's response in the spatial frequency domain and empirical metrics.

With these developments the new taxonomy was able to encompass most resolution metrics encountered in our review, classifying them under one of three types of resolution criteria which were given new self-explanatory titles (previously A, B and C types). This new taxonomy is illustrated in Figure 2.2.

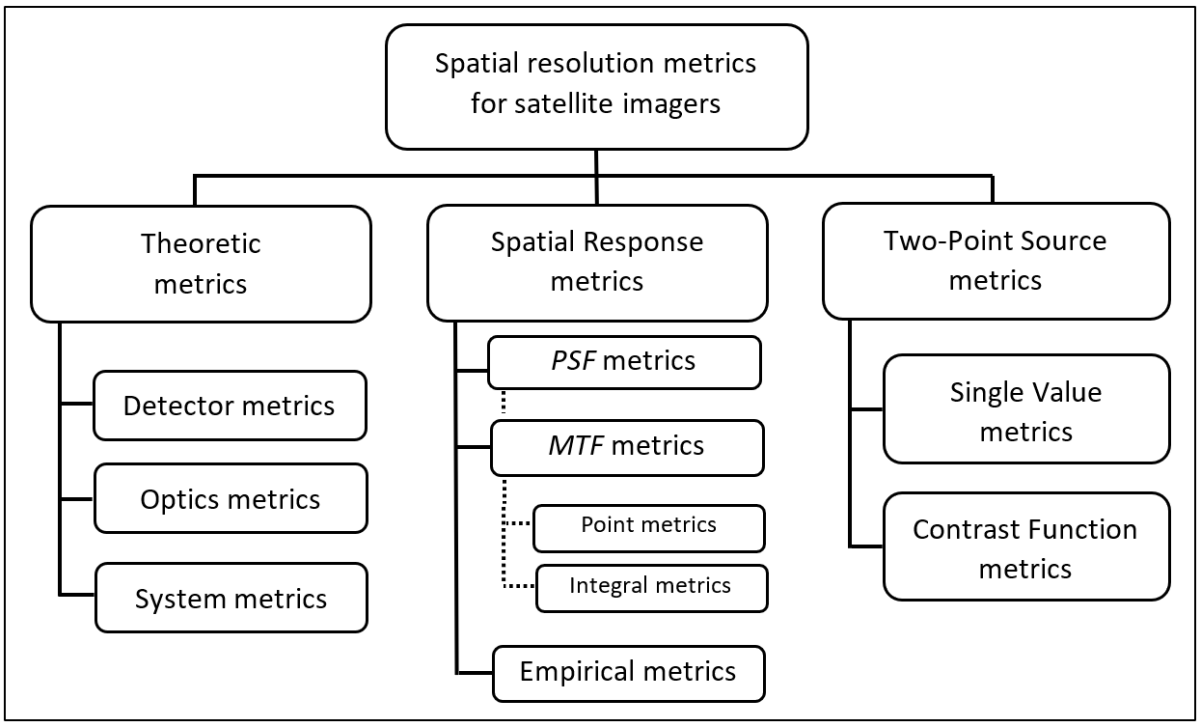

Figure 2.2: Taxonomy of spatial resolution metrics for satellite imagers. This taxonomy is based on a previous classification for optical systems (Ramsay et al. 1941) adapted to include current satellite metrics. The three types of metrics differ in their criterion to define spatial resolution as follows. "Theoretic": A single value function of imager parameters. "Spatial Response": A single value obtained as a property of the imager's spatial response to a single source. "Two-Point Source": Either a single value or a function, computed in terms of the contrast achieved in the image plane when imaging two closely spaced point sources.

To describe the spatial resolution distance predicted by different metrics, instead of specifying the resolution distance measured in the ground plane, which is a function of the satellite height and the off nadir view angle, it is more convenient to specify the angular resolution α measured at the imager.

The nadir-looking resolution distance measured in the ground plane is $\alpha \cdot H$, where H is the satellite height.

2.2.2.1. *Theoretic metrics*

Theoretic metrics assume that spatial resolution is a single value computed as a function of imager parameters. These metrics are divided into Detector, Optics, and System metrics, when their parameters describe the detector, the optics or both, respectively.

Assuming square pixels and a circular optical aperture, usual parameters include pixel pitch p, focal length f, aperture diameter D and mean wavelength λ.

Detector metrics predict spatial resolution in terms of pixel pitch and focal length. The *GSD* is the most common Detector metric, it assumes $\alpha = \text{IFOV} = p/f$, where IFOV stands for Instantaneous Field Of View (Fiete 1999).

A variation of this metric replaces the physical pixel pitch p along scan direction with an equivalent pitch p_{eff} (Cota et al 2010) to consider over-sampling or under-sampling (Fiete and Tantalo 1999).

Other Detector metrics acknowledge that pixel size underestimates resolution distance, so they assume instead $\alpha = 2 \cdot \text{IFOV}$ (Lomheim and Kalman1992, Lillesand et al 2015) or $\alpha = 3 \cdot \text{IFOV}$ (Verhoeven 2018). Detector metrics are summarized in Table 2.1.

Table 2.1: Detector metrics. These Theoretic metrics compute spatial resolution in terms of the ratio between pixel pitch p and focal length f.

Detector metrics	Angular resolution α	References
GSD	p/f	Fiete 1999
Effective GSD	p_{eff}/f	Cota et al. 2010
Twice GSD	$2 \cdot p/f$	Lomheim and Kalman1992, Lillesand et al. 2015
Triple GSD	$3 \cdot p/f$	Verhoeven 2018

Optics metrics assume that spatial resolution is directly proportional to the ratio between mean wavelength and the diameter of the optical aperture. The constant of proportionality K follows from the application of two-point resolution criteria to ideal circular apertures, defining resolution as $\alpha = K \cdot (\lambda/D)$. Each metric is characterized by the contrast C of the combined response (Fiete 2010, Verhoeven 2019). Table 2.2 presents some Optics metrics used for satellite imagers.

Table 2.2: Optics metrics. These Theoretic metrics compute the spatial resolution of sensors comprising a single optical aperture. The angular resolution is $\alpha = K \cdot \lambda / D$, where K is a constant, D is the aperture diameter and λ is the mean wavelength. C is the contrast achieved in the combined response when the two-point sources are separated at an angle α.

Optics metrics	K	C	References
Sparrow limit, Sparrow criterion	0.947	0.000	Fiete 2010, Verhoeven 2019
Ground Spot Size, Abbe criterion	1.000	0.017	Fiete 1999, Verhoeven 2019
FWHM, Houston criterion	1.029	0.038	Auelmann 2012, Verhoeven 2019
Rayleigh criterion	1.220	0.265	Townshend 1981, Light 2004
Schade (and Sendall) criterion	1.854	0.830	Light 2004, Holts 2007
Schuster criterion, Airy disk diameter	2.439	1.000	Den Dekker and Van den Bos 1997, Chesley et al. 1999

System metrics combine detector and optics metrics. The angular resolution can be written as a function of the imager's optical factor $Q = (\lambda/D)\cdot(f/p)$ (Fiete 2010), so that when $Q \rightarrow 0$ (infinitely large aperture) resolution is described by a Detector metric and when $Q \rightarrow \infty$ (infinitely small pixels) it is described by an Optics metric.

We found that five System metrics in the literature are particular cases of the general equation $\alpha = \text{IFOV}\cdot[1 + (K\cdot Q)^k]^{1/k}$, where K and k are numerical constants. This equation is a generalization of an equation with $K = 1$ (Auelmann 2012). If $Q \rightarrow 0$ then $\alpha = \text{IFOV}$ and if $Q \rightarrow \infty$ then $\alpha = K\cdot(\lambda/D)$. System metrics are shown in Table 2.3.

Table 2.3: System metrics. These Theoretic metrics assume that the angular resolution of the imaging sensors is $\alpha = \text{IFOV}\cdot[1 + (K\cdot Q)^k]^{1/k}$, where K and k are constants, *IFOV* is the detector's instantaneous field of view and Q is the imager's optical factor.

System metric	*K*	*k*	References
Fuji model	1.000	1.00	Auelmann 2012
GIQE based "truth" model	1.000	1.35	Auelmann 2012
Kodak model	1.000	2.00	Auelmann 2012
Composite resolution	2.440	2.00	Holts 2000
Equivalent system resolution	1.854	2.00	Holts 2007

Auelmann (2012) studied three System metrics with K=1: Fuji model (k = 1), Kodak model (k = 2) and his new metric (k = 1.35) based on the General Image Quality Equation (GIQE) (Leachtenauer et al. 1997). He showed that his metric correlated better with GIQE predictions and used it to compute resolution for eight satellite imagers (Auelmann 2012).

Holts proposed two System metrics with k = 2. His "Composite" metric (Holts 2000) uses Schuster criterion (Table 2.2) as Optics metric whereas his "Equivalent" metric (Holts 2007) uses Schade criterion (Table 2.2). The Equivalent metric has an additional display term, which was not included in Table 2.3 to assimilate it to the other System metrics.

2.2.2.2. *Spatial Response metrics*

Spatial Response metrics are based on a property of the actual spatial response of the imaging sensor to a single point source. This response is characterized by the system PSF or by its Fourier transform, the system OTF. Some examples of system PSF are shown in Figure 2.3.

Although in-orbit system PSF can be directly measured by an array of convex mirrors (Helder et al. 2005), due to SNR considerations and target availability, the most common procedure to measure the spatial response of satellite imagers is the edge method, in which the one-dimensional Line Spread Function (LSF) and a one-dimensional cut of the system OTF,

are measured in a direction perpendicular to the edge (Helder et al. 2005, Viallefont-Robinet et al. 2018).

The LSF is the line integral of the PSF along a certain direction, so if the LSF is known in several directions the system PSF can be found (Marchand 1965, Reichenbach et al. 1991).

Spatial Response metrics are divided into: PSF metrics, based on the pre-sampled system PSF; OTF metrics, based on the pre-sampled system OTF; and Empirical metrics, based on the analysis of an actual image. PSF and OTF metrics are further divided into Point metrics, based on a single value of these functions, and Integral metrics, based on an integral of these functions.

Most common PSF Point metrics are the Full Widths at Half Maximum (FWHM) and at Tenth Maximum (FWTM) of the pre-sampled system PSF.

After the GSD, the most popular resolution metric for satellite imagers is the FWHM of the pre-sampled system PSF or LSF (Salomonson et al. 1998, Ryan et al. 2003, Kerekes 2009, Pagnutti et al. 2010, Campagnolo and Montano 2014). Half of the FWHM has also been used as resolution metric (Jacobsen 2011).

In medical imaging the FWTM of system PSF or LSF is used as a metric together with the FWHM (Wang and Li 1999, Bugby et al. 2016). FWTM metric has also been proposed for satellite imagers, as an alternative to the FWHM when the sidelobe level of the LSF is of the order of half its peak response (Valenzuela and Reyes 2019a).

PSF Point metrics define resolution considering a single point of the PSF or LSF. PSF Integral metrics consider instead a range of the PSF or LSF. An LSF Integral metric used for a geostationary imager, defined the in-orbit "IFOV size" as the angular sector containing half the total integrated LSF (Okuyama et al. 2015).

Other Integral PSF metrics, infrequent for satellite imagers, are the standard deviation of the PSF (Wang and Li 1999) and the "Encircled Energy Diameter" of the PSF (McLean 2008, Mori et al. 2018) which is popular in astronomy.

MTF metrics are based on the Modulation Transfer Function (MTF) defined as the absolute value of the OTF. MTF(ξ) curves represent a one-dimensional cut of MTF versus spatial frequency ξ, measured in cycles per unit of distance, along a certain direction.

MTF curves are usually monotonic, starting from unit value at zero frequency; $MTF(\xi=0) = 1$, and decreasing steadily with increasing frequency; $MTF(\xi \rightarrow \infty) = 0$.

MTF Point metrics define resolution in terms of the limiting spatial frequency ξ_{max} at which a minimum useful MTF value or threshold is obtained; $MTF_{min} = MTF(\xi = \xi_{max})$. There is no consensus on this threshold; as shown in Table 2.4 its values range between 0.05 and 0.95.

Table 2.4: Modulation Transfer Function (MTF) Point metrics. These metrics are based on fixed threshold values MTF_{min} for the system MTF. The limiting spatial frequency at which the system MTF achieves the threshold value is ξ_{max} so $MTF_{min} = MTF(\xi = \xi_{max})$. Angular resolution is proportional to the cycle $1/\xi_{max}$ of the limiting spatial frequency.

Denomination or features of MTF threshold	MTF_{min}	References
Rule of thumb for minimum useful MTF value	0.05	Maidment 2014
Empirical design threshold for Pleiades satellite	0.07	Rosak et al. 2004
Value associated to Rayleigh resolution criterion	0.09	Cremer 2012
Rule of thumb for typical MTF threshold value	0.10	Koretsky et al. 2013
Lower end of MTF range for some satellite imagers	0.15	Stankevich 2021
Higher end of MTF range for some satellite imagers	0.30	Stankevich 2021
Effective IFOV (EIFOV) spatial resolution metric	0.50	Markham 1985
Radiometrically accurate IFOV (RAIFOV) metric	0.95	Joseph 2015

"Intersection Threshold" MTF Point metrics, define resolution at the spatial frequency ξ_{max} where the system MTF curve intersects a threshold function that predicts MTF_{min} versus spatial frequency, considering SNR (Lomheim and Kalman 1992, Boreman 2001). These metrics are uncommon because the threshold function is usually unknown.

Two dissimilar approaches are used by MTF metrics to compute angular resolution in terms of the spatial frequency cycle $1/\xi_{max}$. First approach assumes $\alpha = 1/(f \cdot \xi_{max})$ considering full cycle, while second approach assumes $\alpha = 1/(2 \cdot f \cdot \xi_{max})$ using half cycle. Full cycle is used for $MTF_{min} \leq 0.3$ (Lomheim and Kalman 1992, Stankevich 2021) while half cycle is used for $MTF_{min} \geq 0.5$ (Park et al. 1984, Markham 1985).

Two MTF Integral metrics used for satellite imagers are Schade's Equivalent Passband (SEP) and the Relative Edge Response (RER). The SEP metric along a given spatial direction is (Torshina and Yakushenkov 2015):

$$\alpha = \frac{1}{2 \cdot f \cdot \int_0^\infty MTF^2(\xi) \cdot d\xi}$$

The RER is the slope of the normalized edge response along a given spatial direction (Fiete 2010). Analytically, it has the following integral form (Fiete 2010):

$$RER = 2 \cdot \int_0^\infty \left[\frac{sin(\pi\xi)}{\pi\xi}\right] \cdot OTF(\xi) \cdot d\xi$$

Based on version 3 of the GIQE, the angular resolution associated to the RER has been defined as $\alpha = IFOV/RER$ (Auelmann 2012).

Empirical metrics identify resolution with the size of the smallest elements that can be distinguished or resolved in actual images, without computing the system PSF or OTF. They are classified under Spatial Response metrics only for convenience.

A variety of targets are used to implement Empirical metrics, one of the most common being arrays of bars, as the ones used in the popular USAF 1951 test chart (Orych 2015). In this chart the distance between bars is equal to their width w so the element's width is $W = 2 \cdot w$. Angular resolution is computed as $\alpha = W_{min}/f$ where W_{min} is the width (full cycle) of the smallest element resolved.

To declare an element resolved, Campbell and Wynne (2011) require bars to be "*completely separated along their entire length*" (p. 289) whereas Silverfast (2024) requires that space between bars is "*barely still detectable*". Thus, the lack of consensus on the minimum contrast to declare resolution is also present in Empirical metrics.

The "*true GSD*" (Thomson 2010, 44) is an Empirical metric defined as the average size of the smallest observable patches in a suitable image, found by examining with microscopy an enlarged hard copy (Thomson 2009).

2.2.2.3. *Two-Point Source metrics*

Spatial Response metrics base their prediction on the response to a single point source, so they do not quantify the contrast achieved when two-point sources are separated at the predicted resolution distance.

Two-Point Source metrics fill this gap by computing the response to two-point sources separated at a given distance to find the corresponding resolving contrast.

These later metrics are classified into Single Value metrics, which compute the separation distance required to achieve a given contrast, and Contrast Function metrics, which compute resolution distance as a function of contrast.

Single Value metrics define resolution as the distance between sources which allows a given contrast to be achieved. These metrics generalize the classical two-point source criteria, only applicable to ideal apertures, to any type of imaging sensor (Ramsay et al. 1941, Den Dekker and Van den Bos 1997).

Jahn and Reulke (2000) used a Single Value metric to compute the spatial resolution of staggered line arrays detectors for spaceborne and airborne imagers. To compute the sampled response, they integrated the pre-sampled optics response to two-point sources over each pixel, and then found the resolution distance using the generalized Rayleigh criterion. Their results predicted that staggered arrays had twice better (smaller) resolution than conventional arrays and their laboratory tests ratified these predictions.

Stelzer (1998) computed contrast as a function of separation between two-point sources, emphasizing the futility of computing resolution independently of contrast and illustrating the degradations of contrast and resolution by noise and "pixelation".

Within the context of satellite imagers, Valenzuela and Reyes (2019a) defined the Resolution Function and emphasized the advantages of Two-Point Source metrics over Theoretic and Spatial Response metrics.

Conran et al. 2021 provided an empirical foundation for Two-Point Source metrics by using convex mirrors to simulate point sources for satellite imagers. They performed in-orbit along scan and cross scan measurements of image contrast, using two-point-sources separated at distances between 1 and 2 pixels. They successfully compared these empirical results with contrasts predicted by simulated images based on previous PSF knowledge.

2.3. Materials and Methods

In this section we describe procedures to compute the Spatial Resolution Function and to assess Theoretic and Spatial Response metrics against this function.

The Spatial Resolution Function gives the distance at which two-point sources can be resolved as a function of the actual resolving contrast in the image plane. To compute this later function, the sampled image equation is applied to the case of two-point sources in the scene. To apply this equation, the system PSF is required, so section 2.3.1 reviews the image equation and the method to compute this PSF.

The resolving contrast depends on the relative position or "phasing" between the two-point sources in the scene and the pixels in the detector's grid. A key element of the computation of the Spatial Resolution Function is the selection of the specific phasing condition that allows the GSD metric to be obtained as a limiting case.

Section 2.3.2 specifies the "GSD limit" phasing condition, presents the procedure to compute the Spatial Resolution Function and proposes a method to compute the smallest practical resolution distance in the presence of noise.

Once the Spatial Resolution Function is known, the metrics that describe spatial resolution as a single distance can be assessed. Section 2.3.3 describes this assessment procedure.

2.3.1 Basic Equations

2.3.1.1. *Sampled image equation*

The following sampled image equation (Park et al. 1984) is used to translate the continuous distribution of scene radiance into a discrete representation of pixel intensities in the image plane:

$$g(x,y) = [f(x,y) * PSF(x,y)] \cdot comb(x,y)$$

Where $g(x,y)$ is the sampled raw image (before reconstruction), $f(x,y)$ is the scene radiance, PSF(x,y) is the system pre-sampled PSF, the symbol $*$ denotes two-dimensional convolution and *comb*(x,y) is the two-dimensional *comb* function.

System PSF(x,y) is a pre-sampled (shift invariant) response, computed as the convolution between individuals PSFs of all the elements contributing to image formation; optics, detector, scanning and others (Choi and Helder 2005, Schowengerdt 2007, Fiete and Paul 2014).

Alternatively, system PSF is computed as the inverse Fourier transform of the system OTF, which is equal to the product of the individual OTFs of these same elements (Markham 1985, Boreman 2001, Fiete 2010, Cota et al. 2010).

Although the imaging equation assumes point sampling through the *comb*(x,y) function (Wittenstein et al. 1982, Park et al. 1984, Fiete 2010), the sampled image $g(x,y)$ is actually obtained by integral sampling, in which the "intermediate image" focused by the optics on the image plane is integrated over the pixel area (Wittenstein et al. 1982).

This integration is mathematically equivalent to a convolution between the optics PSF and the detector PSF, followed by point sampling at a pixel centre (Schneider and Fink 1976, Wittenstein et al. 1982, Fiete 2010).

This later equivalence may lead to confusion about the applicability of the imaging equation: Luca and Cardonne (1991) stated that it only considers point ("*spot*") sampling whereas it can consider either integral or point sampling as long as the proper detector PSF is used to derive the system PSF.

For a scene with only two identical point sources, the imaging equation predicts that the signal intensity at a pixel is obtained by sampling at its centre, the sum of the two correspondent system PSF (Fiete 2010).

2.3.1.2. *System point spread function computation*

Comparisons between theoretical predictions and measurements of system PSF have given satisfactory results in the laboratory (Reichenbach et al. 1991) and in-orbit (Markham 1985). Thus, a fair prediction of actual performance can be obtained by using a suitable theoretical model for the system PSF.

This later model is peculiar to the specific type of imager being considered; we will assume a model considered representative of a generic satellite imager (Choi and Helder 2005, Fiete 2007). The following assumptions and procedure will be used to compute the system PSF of this model.

Assume a scanning imager with an unobstructed circular optical aperture of diameter D, focal length f, square pixels with pitch and width p (100 % fill factor) detecting monochromatic radiation at wavelength λ. This sensor is modelled as follows:

1. Spatial frequencies

   ξ_x and ξ_y are spatial frequencies measured in cycles per unit of length, in Along Scan (AS) and Cross Scan (CS) directions, respectively. Normalized frequencies measured in cycles per pixel pitch are $\eta_x = \xi_x/\xi_{dc}$ and $\eta_y = \xi_y/\xi_{dc}$, where $\xi_{dc} = 1/p$ is the detector cut-off frequency.

   Optical cut-off frequency of a circular aperture is $\xi_{oc} = D/(f\cdot\lambda)$. Normalized radial frequency is defined as $\rho = [\sqrt{(\xi_x^2+\xi_y^2)}]/\xi_{oc} = Q\cdot\sqrt{(\eta_x^2+\eta_y^2)}$. For $\rho > 1$, system OTF = 0, so only the range $0 \le \rho \le 1$ is considered.

2. Optical factor

   Table 2.5 shows the range of optical factors computed from published data, for the channels of some Earth observation satellite imagers. When pixel pitch or focal length were not available, Q was estimated as $(\lambda/D)\cdot(H/\mathrm{GSD})$.

   Table 2.5: Range of Optical Factors for Satellite Imagers. For each imager shown, the optical factor Q is computed for all its imaging channels, presenting the minimum Q and maximum Q in the table. Abbreviations are defined at the end of this chapter.

Satellite	Imager	Optical Factor Q		References
		Minimum	Maximum	
Sentinel 3	SLSTR	0.020	0.40	Coppo et al. 2020 Nieke and Mavrocordatos 2017
MSG	SEVIRI	0.024	0.50	Schmetz et al. 2002, Schmid 2000
Sentinel 2	MSI	0.039	0.45	Sentinel-2 2024
GOES 16, H-8 & GK-2	ABI, AHI & AMI	0.076	1.44	Geo-Kompsat-2 2022, NASA 2019
Landsat 8	OLI & TIRS	0.077	0.78	Figoski et al. 2009, Reuter et al. 2015
Pleiades	PAN & MS	0.19	0.99	Pleiades 2024
Pleiades Neo	PAN & MS	0.24	1.42	Pleiades Neo 2024
SpaceView 50	450 nm & 950 nm	0.90	1.90	SpaceView 2024

   These results indicate that a range $0.01 \le Q \le 2.0$ is representative of Earth observation satellite imagers. For purposes of numerical validation, a computational range $0.001 \le Q \le 2.0$ will be selected.

3. Optics

   Circular aperture's OTF is (Boreman 2001, Fiete and Paul 2014):

$$OTF_{aperture} = (2/\pi)\cdot[cos^{-1}(\rho)-\rho\cdot(1-\rho^2)^{-1/2}]$$

A model that describes optical aberrations is (Fiete 2010):

$$OTF_{aberrations}(\rho, WFE) = 1- (WFE/0.18)^2\cdot[1 - 4\cdot(\rho-0.5)^2]$$

Where WFE is the Root Mean Square (RMS) value of the Wave Front Error measured in wavelengths.

Line Of Sight (LOS) vibrations are modelled as (Fiete 2010):

$$OTF_{jitter}(\rho, \sigma) = exp[-2\cdot(\pi\cdot\rho\cdot\sigma)^2]$$

Where σ is the jitter standard deviation measured in pixel widths.

As ρ depends on Q, η_x and η_y:

$$OTF_{optics}(Q, \eta_x, \eta_y, WFE, \sigma) = OTF_{aperture}\cdot OTF_{aberrations}\cdot OTF_{jitter}$$

For imaging sensors, WFE varies typically between 0.1 and 0.25, with values below 0.15 considered as "*nearly perfect*" (Shannon 2010, 4.4). WFE = 0.1 is usually assumed as a representative value in image quality studies (Fiete and Tantalo 1999, Fiete 1999, Cota et al. 2010).

For satellite imagers, σ varies between 0.05 and 5 pixels (Ye et al. 2020). For GOES 16's imagers σ ≈ 1 μrad was calculated (Chapel et al. 2014), so we obtain σ ≈ 0.1 pixel for its channel with the smallest IFOV (NASA 2019).

4. Detector

"Pixel" OTF, usually called detector aperture OTF or detector footprint OTF, is (Fiete and Paul 2014):

$$OTF_{pixel}(\eta_x, \eta_y) = sinc(\eta_x)\cdot sinc(\eta_y)$$

With $sinc(x) = [sin(\pi\cdot x)]/(\pi\cdot x)$.

A model that predicts charge diffusion effects in imaging detectors is (Davis et al. 1998, Rafol et al. 2019):

$$OTF_{diffusion}(\rho, L) = 1/[1+(2\cdot\pi\cdot\rho\cdot L)^2]$$

Where L is the effective diffusion length measured in pixel widths.

Thus: $OTF_{detector}(Q, \eta_x, \eta_y, L) = OTF_{pixel} \cdot OTF_{diffusion}$

For five types of imaging detectors, ten measurements performed along vertical and horizontal directions yielded $L \approx 0.2 \pm 0.1$ pixels (Rafol et al. 2019).

For Sentinel 4 imaging detectors, measurements at four wavelengths, showed that MTF at Nyquist frequency was 0.89 ± 0.02 times the MTF of a perfect detector (Reulke et al. 2017). Processing this result, we obtain $L \approx 0.11 \pm 0.01$ pixels.

5. Scanning

Assuming that the LOS moves one IFOV in x direction during integration time, scanning OTF is (Fiete and Paul 2014):

$$OTF_{scanning}(\eta_x) = sinc(\eta_x)$$

This models Low Earth Orbit (LEO) push broom scanners and Geostationary Orbit raster scanners. It also approximately models LEO whiskbroom scanners whose LOS speed along track is much slower than its LOS speed along scan.

6. System Functions

System OTF is:

$$OTF(Q, \eta_x, \eta_y, WFE, \sigma, L) = OTF_{optics} \cdot OTF_{detector} \cdot OTF_{scanning}$$

To compute system OTF, η_x and η_y are varied with intervals $\delta\eta = F_S/N_S$ where F_S is the sampling frequency in cycles per pixel and N_S is the number of samples, in x and y directions, used to compute the inverse fast Fourier transform.

System PSF is the two-dimensional Inverse Fourier Transform (IFT) of system OTF:

$$PSF(x,y) = IFT\{OTF(\eta_x, \eta_y)\}$$

The resultant system PSF is defined at intervals $\delta x = \delta y = p/F_S$ where p is the pixel width.

7. Scanning Imagers Quality Types

System PSF is computed as a function of the optical factor for three quality types of satellite imagers: Perfect Scanner (PS), High Quality scanner (HQ) and Medium Quality scanner (MQ). These scanners are defined in Table 2.6, considering the empirical data previously quoted for WFE, L and σ.

Table 2.6: Scanning Imagers Quality Types. The parameters shown are assumed to model three quality types of satellite imagers: Perfect Scanner (PS), High Quality scanner (HQ) and Medium Quality scanner. Root mean square wavefront error "WFE" models optical aberrations, jitter standard deviation "σ" models the line of sight stability and effective diffusion length "*L*" models charge diffusion in detectors. Values assigned to parameters for HQ and MQ imagers are based on published data.

Parameters	Units	Satellite Imager Quality Types		
		PS	HQ	MQ
WFE	RMS wavelengths	0.0	0.1	0.2
σ	pixels	0.0	0.1 *Q*	0.5 *Q*
L	pixels	0.0	0.1 *Q*	0.3 *Q*

To illustrate the system PSF obtained, Figure 2.3 shows two graphical examples for a PS imager in AS and CS directions. The low *Q* imager in the left has very different cuts in both directions due to scanning OTF, whereas for the high *Q* imager in the right, these differences are reduced due to the prevalence of the axially symmetric optics OTF.

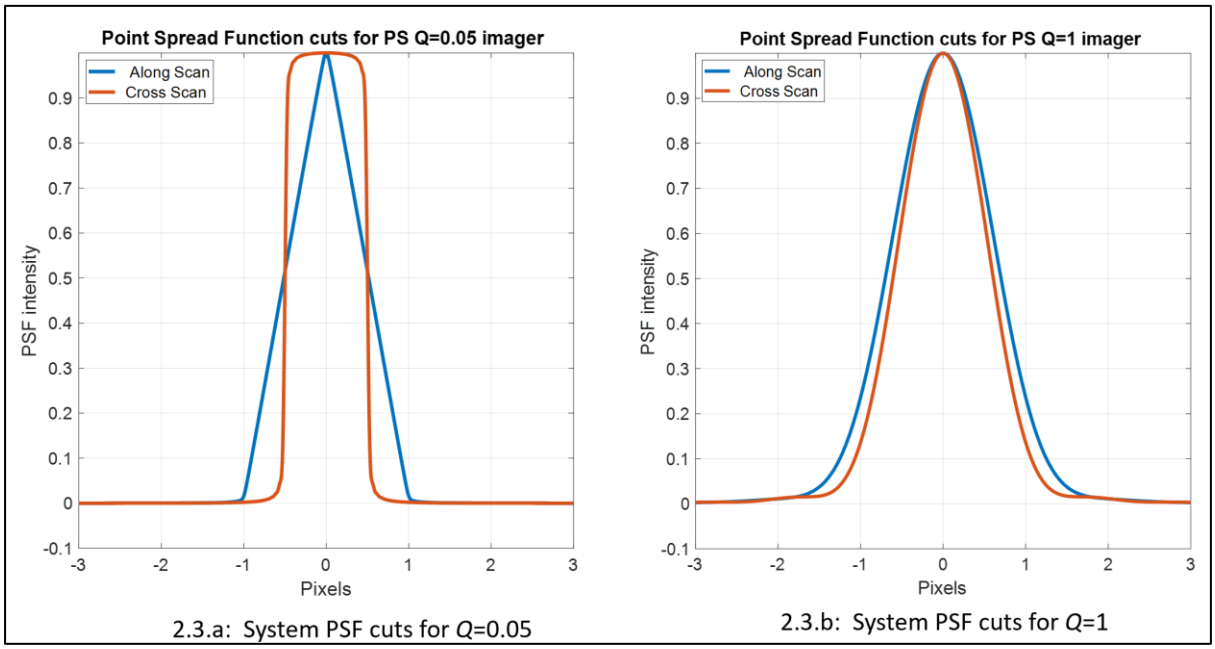

Figure 2.3: System Point Spread Function examples. System PSF cuts are shown in along scan (red curves) and cross scan (blue curves) directions, in the case of the Perfect Scanner, for two different optical factors. Vertical axes represent the PSF intensity and horizontal axes represent the distance measured in pixels widths from the point of maximum intensity.

2.3.2. Spatial Resolution Function computation

2.3.2.1. *Phasing condition*

Spatial resolution computation depends on the phasing, or relative position, between point sources and sampling grid. Among all phasing conditions the one that yields α = IFOV

for an ideal staring imager with $Q = 0$ will be selected, so the GSD metric prediction is obtained in this particular case.

An ideal staring imager ($Q = 0$) represents a point source in the scene as a geometrical point on the image plane; its optics PSF is an impulse. This ideal impulse excites signal in a single pixel leaving all other pixels empty of signal. Thus, for two-point sources, at most two pixels have signal, and resolution is declared when one empty (no signal) pixel appears between these two pixels.

Figure 2.4 shows three image plane's plan views for an ideal staring imager. Spatial resolution will be computed for a phasing that yields α = IFOV in this ideal case. As illustrated in Figure 2.4, this occurs when sources move parallel to pixel edges and are located equidistant to a pixel centre; all other possibilities give higher (worse) resolution values.

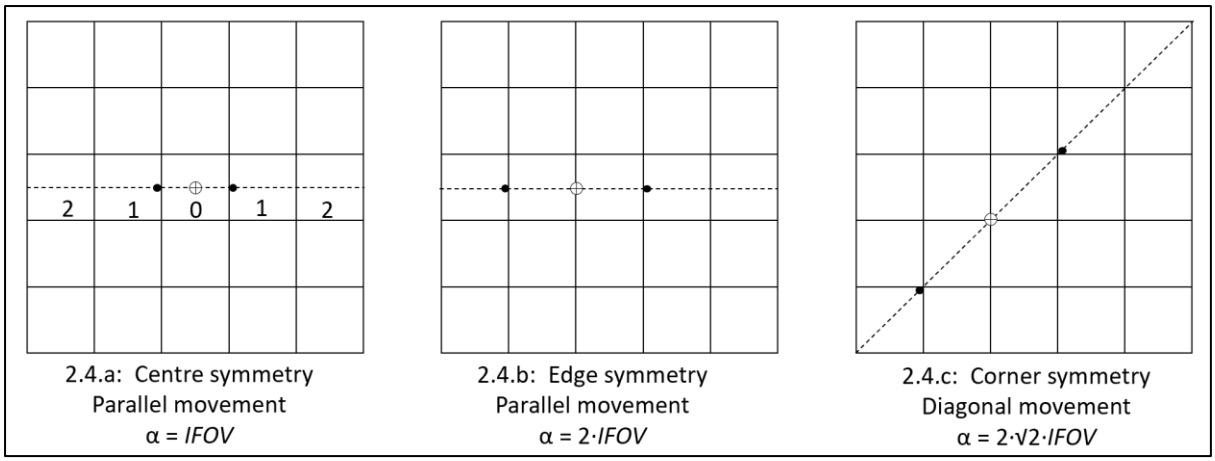

Figure 2.4: Phasing condition. Three possible measures of spatial resolution are shown for an ideal imager considering different phasing conditions. To measure resolution, the two-point sources are gradually separated along a straight trajectory, with respect to an equidistant point of symmetry. The projection of the point sources in the image plane, when resolution is declared, is represented by a black dot, their trajectory is shown as a dashed line and its point of symmetry is depicted by an encircled "plus" symbol ⊕. Resolution is declared when sources are separated at such a distance that at least one empty pixel appears between the two pixels occupied by these sources. As the separation trajectory and point of symmetry are arbitrary, there are an infinite number of ways to measure resolution. The phasing condition with centre symmetry and a movement parallel to the pixel grid (2.4.a) is selected because it yields an angular resolution α equal to the Instantaneous Field Of View (IFOV). Figures 2.4.b and 2.4.c. with edge and corner symmetry, respectively, yield angular resolutions larger than the IFOV.

Thus, spatial resolution function is computed for the phasing depicted in Figure 2.4.a, which assumes sources located symmetrically with respect to a pixel centre, moving along a trajectory parallel and equidistant to pixel edges. This last equidistant condition is not necessary to obtain α = IFOV, but it is a reasonable assumption for actual imagers, as it maximizes the signal measured by the pixels involved in the computation of contrast.

With this assumption, the Spatial Resolution Function is computed for the most favourable phasing condition that gives a minimum resolution distance and which yields the

GSD metric as a limiting case. This later metric will be shown to be useful for low optical factors in cross scan direction.

Other phasing conditions are possible, for example 2.4.b, but the resultant Contrast Function metric would then predict that the GSD and other popular metrics, like the FWHM of the PSF or the EIFOV, are completely useless for not being applicable to any range of optical factors.

2.3.2.2. *Computational procedures*

The procedure to compute the Spatial Resolution Function from the system PSF is now presented. Assume that the projections of the two-point sources on the image plane are separated at a given distance s, according to the phasing condition of Figure 2.4.a.

Resolution distance on the image plane is measured in pixels and computed at intervals $\delta s = 2 \cdot p/F_S$ in AS and CS directions, as a function of resolving contrast, using the following procedure:

1. Assume an initial separation s slightly smaller than pixel pitch p to assure that it is less than Sparrow limit. As result of the IFT, the system *PSF* is computed at intervals p/F_S. Thus, to compute the sum of two system PSFs without using interpolation, s must be a multiple of $\delta s = 2 \cdot p/F_S$.

2. Compute pre-sampled system response $f(x,y) * \mathrm{PSF}(x,y)$ as sum of two system PSFs corresponding to sources projections located at distances $\pm s/2$ from centre of central pixel ("Pixel 0" in Figure 2.4.a).

3. Compute intensities of sampled responses I in each one of the pixels by point-sampling $f(x,y) * \mathrm{PSF}(x,y)$ at their centres.

4. Define Pixel 0's signal as I_{min}. Find the pixel in the image, different from Pixel 0, with maximum signal I_{max}. Compute contrast as $C(s) = (I_{max} - I_{min})/I_{max}$. If Pixel 0 has the maximum signal, then a negative value for $C(s)$ is obtained.

5. Increase separation s by $\delta s = 2 \cdot p/F_S$ and repeat steps 2 to 4, until $C \geq C_{max}$, where $C_{max} < 1$ is the maximum contrast value for which the resolution function will be computed.

6. Examine computed values of C versus s and apply linear interpolation to find separation s_o such that $C(s_o) = 0$ and $C > 0$ for $s > s_o$. The separation s_o is the imager's Sparrow limit.

7. Present s/p values versus C, for $s \geq s_o$, this set of values is the Spatial Resolution Function $R(C) = s(C)/p$ defined in domain $0 \leq C \leq C_{max}$. This function gives the resolution distance - normalized to the pixel width - versus the resolving contrast in the image plane, for any type of imaging sensor. The maximum contrast value C_{max} is selected according to the application, in this paper $C_{max} = 0.95$ was assumed.

The general procedure to compute the Spatial Resolution Function is presented in the flowchart of Figure 2.5.

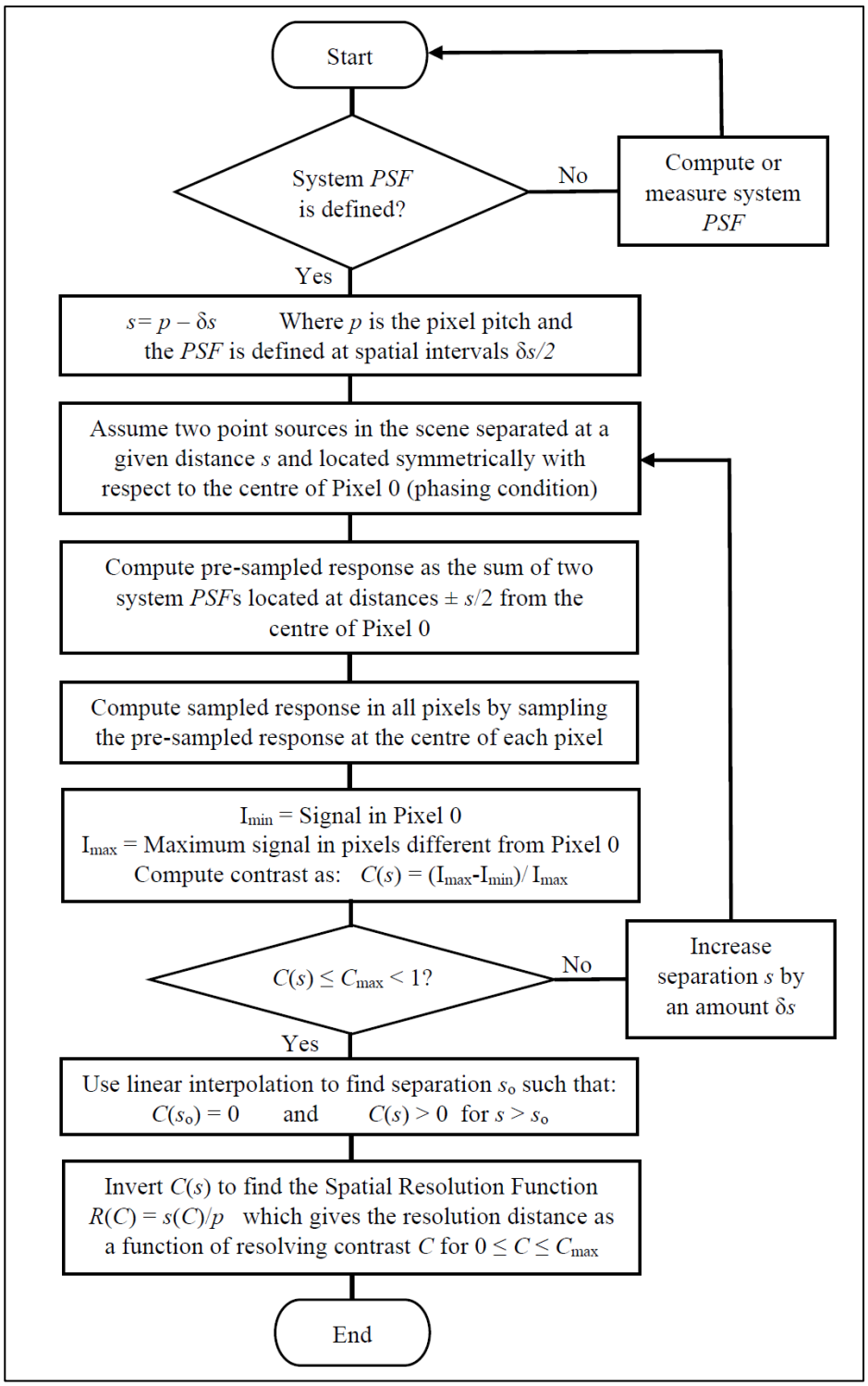

Figure 2.5: Flowchart of the procedure used to compute the Spatial Resolution Function. This procedure involves: the definition of the Point Spread Function; the gradual separation of the two point sources according to the phasing condition of Figure 2.4.a; the computation of the pre-sampled response; the computation of the sampled response in all pixels; the computation of contrast "*C*" in the image plane as a function of source separation "*s*"; the inversion of the function *C*(*s*); and the final presentation of resolution distance "*s*" as a function of contrast "*C*".

Previous procedure uses the system PSF, an alternative procedure using the optics PSF was also implemented for code validation purposes, by replacing steps 2 and 3 as follows:

2. Compute pre-sampled "intermediate" response as sum of two optics PSF corresponding to sources projections located at distances ± s/2 from centre of central pixel.

3. Compute intensities of sampled responses I in each one of the pixels by integrating the pre-sampled intermediate response over their active areas. Approximate this integration by the sum of all optics PSF samples within the pixel's active area (equal to the pixel's area for 100 % fill factor).

2.3.2.3. *Computation of ultimate resolution distance*

Noise degrades spatial resolution by limiting the minimum detectable contrast. We define the "ultimate" resolution distance as the minimum resolution distance R_{min} that can be obtained for a given image SNR, corresponding to the effective Sparrow limit in the presence of noise. (Stelzer 1998).

We estimate this ultimate distance using Rose criterion, which states that the contrast $C = (I_{max} - I_{min})/I_{max} = \Delta I/I_{max}$ between two adjacent pixels with signals I_{max} and I_{min} is detectable if their signal difference ΔI is at least 5 times larger than image's noise N. That is, if $\Delta I \geq 5 \cdot N$ (Maidment 2014). Although this criterion has limitations (Burgess 1999), it is a useful tool for spatial resolution assessment (Lifschin et al. 2013).

If the SNR at the maximum of the combined response is $SNR_{max} = I_{max}/N_{max}$, then Rose criterion requires that $C = \Delta I/I_{max} \geq 5 \cdot N_{max}/I_{max} = 5/SNR_{max}$. Thus, the minimum detectable contrast for two-point sources is $C_{min} = 5/SNR_{max}$ and $R_{min} = R(C_{min})$ is the ultimate spatial resolution distance considering image noise limitations.

2.3.2.4. *Validation procedures*

The system PSF was found as the fast IFT of the system OTF, using $N_S = 30000$ samples. Codes were developed to compute the Spatial Resolution Function using the system PSF procedure (Section 2.3.2.2).

These codes were validated for optical factors between 0.001 and infinity, by comparing their results with the ones obtained by the following alternative procedures:

1. Analytic equations for $Q = 0$

   Analytic equations for the Spatial Resolution Function when $Q = 0$, are presented in section 2.4.1 for a Perfect Scanner. The system PSF results obtained for $Q = 0.001$ were compared with these equations. For the 20 values computed in each direction, the Mean Absolute Percentual Difference (MAPD) is 0.007 % in AS direction and 0.11 % in CS direction. As expected, these differences increase as Q increases, for example, when $Q = 0.01$, the MAPD is 0.07 % in AS direction and 1.1 % in CS direction.

2. Integration of optics point spread function

   The Spatial Resolution Function was computed for a Perfect Scanner in AS direction, using the two procedures defined in section 2.3.2.2 (point sampling of system PSF and integration of optics PSF). A sampling frequency $F_S = 601$ samples per pixel was used to compute $R_x(C, Q)$ using these two procedures, for 44 optical factors within domain $0.05 \leq Q \leq 2$ and for 20 resolving contrasts within domain $0.0 \leq C \leq 0.95$. The MAPD for the $44 \times 20 = 880$ values compared was 0.00003 %.

3. Analytic equation for $Q \rightarrow \infty$

   The PSF of an ideal optical aperture ($Q \rightarrow \infty$), computed with the first-order Bessel function (Fiete 2014), was compared with the results obtained with the system PSF procedure. Using a sampling frequency $F_S = 101$, the MAPD was 0.0003 % for the 315 data points for which $PSF \geq 0.001$.

2.3.3. Assessment of spatial resolution metrics

2.3.3.1 *Assessment procedure*

We denominate Theoretic and Spatial Response metrics as “soft” metrics because they predict a single hypothetical spatial resolution distance without considering the contrast achieved in the image plane when two-point sources are separated at this distance.

We claim the Spatial Resolution Function $R(C, Q)$ to be a “hard” metric because it defines the resolution distance in terms of the actual contrast in the image plane, computed for the most favourable phasing condition.

We assess soft metrics by comparing their predictions with the resolution distance computed by the Spatial Resolution Function metric. $R(C, Q)$ is a function of contrast C and optical factor Q, but soft metrics predict a resolution distance $r(Q)$ that depends only on Q.

To assess soft metrics, we initially assume that for a given value of Q their prediction agrees with to the Spatial Resolution Function and compute the contrast $C_a(Q)$ associated to this prediction, such that the predicted distance $r(Q)$ is equal to the resolution distance $R(C, Q)$:

$$r(Q) = R(C_a, Q)$$

Resolution distance is a function of contrast, the higher the contrast the higher this distance (see for example Table 2.2). Thus, to compare the resolution of two imagers with different Q factors, this comparison must be performed at the same contrast.

A perfect soft metric has a constant $C_a(Q)$, so its prediction $r(Q)$ is always associated to the same contrast. This perfect metric would be easier to compute than the Spatial Resolution Function and would be "hardened" by its association to a known value of contrast.

The associated contrast $C_a(Q)$ of actual soft metrics depends on Q, so they systematically err when comparing the resolution of two imagers with different optical factors. We qualify a spatial resolution metric as "biased" when its associated contrast depends on the optical factor.

When a biased metric is used to compare the spatial resolution of two imagers with different optical factors, it will either overestimate the spatial resolution of the imager with the smaller associated contrast or underestimate the spatial resolution of the imager with the higher associated contrast.

An unbiased metric should compute resolution at the same contrast or at a given known contrast. As will be shown in section 2,4, all soft metrics have bias errors because their associated contrast depends on the optical factor. This error is generated because soft metrics predict *a priori* a single resolution distance, without considering the actual contrast that is achieved in the image plane when two point sources are separated at this distance. Thus, it is not unusual that soft metrics predict resolution distances well below Sparrow limit, that is, they declare resolution when there is actually no resolving contrast in the image plane.

Two-Point Source metrics are by definition perfectly unbiased metrics, because they predict a single spatial resolution distance at a specific value of contrast (Single Value metrics) or, more generally, they compute the spatial resolution distance as a function of contrast (Contrast Function metrics).

The Spatial Resolution Function is a Contrast Function metric that is preferred over any Single Value metric, because it predicts resolution for all values of contrast, a crucial advantage when image noise (see Section 2.3.2.3) and the different contrast requirements for image processing applications are considered. The Spatial Resolution Function can also be used to gauge the errors incurred by biased metrics, a task beyond the capability of Single Value metrics.

To illustrate how the bias error is gauged by the Spatial Resolution Function, assume that a soft metric predicts that two imagers called 1 and 2, with different optical factors Q_1 and Q_2, respectively, have equal resolution: $r(Q_1) = r(Q_2)$. These "soft" predictions are made without considering the actual contrasts associated to these resolution distances.

Further assume that the Spatial Resolution Function indicates that the associated contrast $C_a(Q_1)$ of Imager 1 is larger than the associated contrast $C_a(Q_2)$ of Imager 2: $C_1 = C_a(Q_1) > C_2 = C_a(Q_2)$.

To compare resolution distances at the same contrast, either C_1 or C_2 can be selected. If C_1 is selected, then $r(Q_1) = R(C_1, Q_1)$ is a correct prediction, but $r(Q_2) < R(C_1, Q_2)$ is not, because

a larger separation is needed for Imager 2 to increase contrast from C_2 to C_1. Thus, in this case the soft metric underestimates the resolution distance of Imager 2.

If C_2 is selected, then $r(Q_2) = R(C_2, Q_2)$ is a correct prediction, but $r(Q_1) > R(C_2, Q_1)$ is not, because a smaller separation is needed to decrease contrast from C_1 to C_2. Thus, in this case the soft metric overestimates the resolution distance of the Imager 1.

Thus, the soft metric errs in equating the resolution of both imagers because, for both associated contrasts, Imager 1 has smaller resolution distance than Imager 2.

To assess the bias error incurred by a soft metric, the average value $<C_a>$ of its associated contrast is computed in the domain of optical factors of interest, and then its prediction $r(Q)$ is compared with the Spatial Resolution Function $R_o(Q) = R(<C_a>, Q)$ evaluated at a contrast equal to this average value.

The Prediction Error (PE) is defined as $PE(Q) = 1 - r(Q)/R_o(Q)$. A perfect soft metric with constant $C_a(Q)$ is assigned zero prediction error if $0 \leq C_a \leq 1$. A soft metric with variable C_a has $PE \approx 0$ if $C_a(Q) \approx <C_a>$.

In principle, any soft metric with $0 \leq C_a \leq 1$ can have small bias errors if applied on a sufficiently narrow range of optical factors. In practice, all known soft metrics display large bias errors when assessed in the range $0.001 \leq Q \leq 2.0$.

For scanning imagers, $r(Q)$ and $R_o(Q)$ are dependent on direction, so $PE_x(Q)$ and $PE_y(Q)$ are separately computed. Maximum Prediction Error (MPE) is defined as the maximum absolute value of *PE* considering both directions:

$$MPE = maximum\{|PE_x(Q)|, |PE_y(Q)|\}.$$

MPE and $<C_a>$ are finally multiplied by 100 to be expressed in per cent.

2.3.3.2. *Computational range*

For each one of the three quality types of satellite imagers defined by Table 2.6 we compute:

1. Resolution function $R(C, Q)$ in AS ($R_x(C, Q)$) and CS ($R_y(C, Q)$) directions

   $R(C, Q)$ was computed in AS and CS directions within domain $0.001 \leq Q \leq 2$ and within domain $0 \leq C \leq 0.95$ at intervals $\delta C = 0.05$, thus, 20 values of C were considered. For $Q < 0.01$; $\delta Q = 0.001$, for $Q > 0.1$; $\delta Q = 0.05$ and for $0.01 \leq Q \leq 0.1$; $\delta Q = 0.01$. Thus, 57 values of Q were considered. Consequently, $2 \times 20 \times 57 = 2280$ $R(C, Q)$ values are computed for each imager.

N_S = 30000 samples were used for the IFT, with F_S = 7501 samples per pixel for $Q < 0.05$ and F_S = 601 samples per pixel for $Q \geq 0.05$.

2. Soft metrics prediction $r(Q)$

For each soft metric $r(Q)$ was computed in AS and CS directions within domain $0.001 \leq Q \leq 2$, with the same δQ intervals used for $R(C, Q)$. Thus, 2×57 = 114 values for $r(Q)$ were computed for each metric.

3. Associated contrast

For each $r(Q)$ value, the associated contrast $C_a(Q)$ is computed by the following procedure:

- If $R(0, Q) \leq r(Q) \leq R(0.95, Q)$ then $C_a(Q)$ is found by linear interpolation between the nearest $R(C,Q)$ curves.
- If $r(Q) < R(0, Q)$ then $C_a = 0$ is assumed.
- If $r(Q) > R(0.95, Q)$ then $C_a = 1$ is assumed.

For each soft metric, the average associated contrast $\langle C_a \rangle$ is the average of the 114 $C_a(Q)$ values.

2.3.3.3 *Metrics assessed*

Twelve metrics are assessed:

1. GSD metric: $r(Q) = 1$.
2. Theoretic System metrics: Fuji, Kodak, GIQE, Composite and Equivalent.
3. PSF Point metrics: FWHM and FWTM .
4. MTF Point metrics: EIFOV and MTF = 0.1 metric (MTF.1)
5. MTF Integral metrics: RER and SEP.

2.4. Results

Figure 2.6 presents the Spatial Resolution Function in AS and CS directions, $R_x(C, Q)$ and $R_y(C, Q)$, respectively, for the three quality types of imagers defined in Table 2.6, as a function of the optical factor Q for five values of contrast C (0.0, 0.3, 0.5, 0.7 and 0.9).

Figure 2.7 presents the associated contrast C_a for the twelve soft metrics assessed, in AC and CS directions, as a function of Q for a Perfect Scanner. The GSD metric is not displayed in Figure 7, because the resolution distance it predicts is always smaller than Sparrow limit, so its associated contrast is defined as zero.

Although the GSD metric displays the largest errors when assessed over the whole range of optical factors, it is still a useful approximation to the resolution distance in cross scan

direction for low optical factors. To illustrate the range of optical factors and resolving contrasts where the GSD metric is applicable, contours of constant $R_y(C, Q)$ have been drawn in Figure 2.8 for a High Quality scanner, using contrast intervals $\delta C = 0.01$.

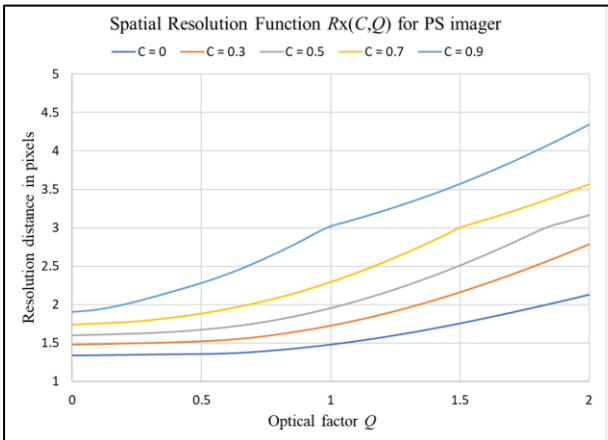

2.6.a: PS Along Scan Spatial Resolution Function

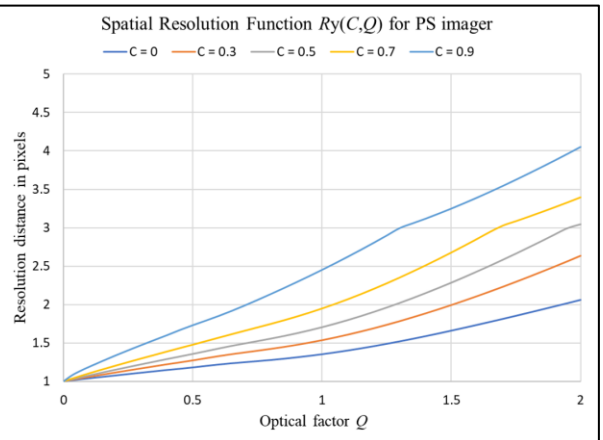

2.6.b: PS Cross Scan Spatial Resolution Function

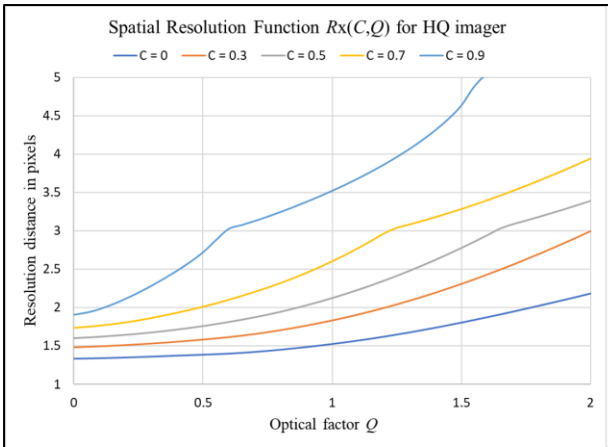

2.6.c: HQ Along Scan Spatial Resolution Function

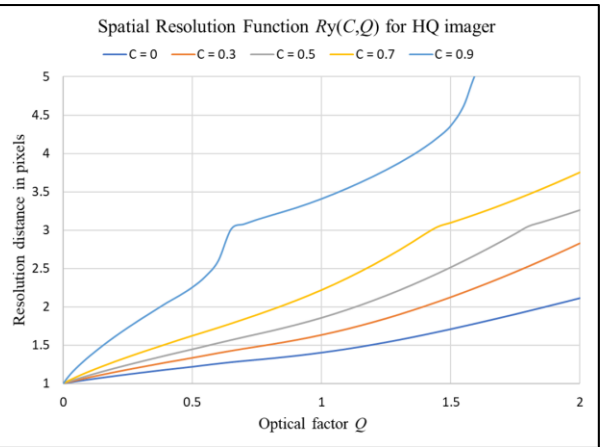

2.6.d: HQ Cross Scan Spatial Resolution Function

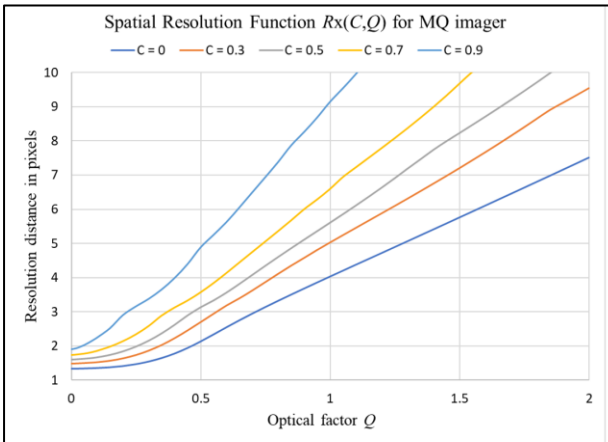

2.6.e: MQ Along Scan Spatial Resolution Function

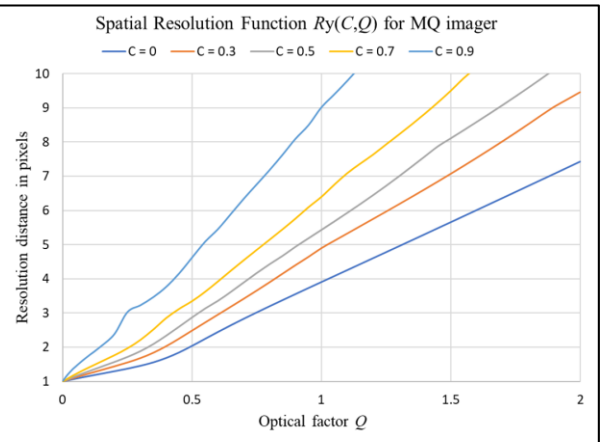

2.6.f: MQ Cross Scan Spatial Resolution Function

Figure 2.6: Spatial Resolution Function for Perfect Scanner (PS – top figures), High Quality scanner (HQ – middle figures) and Medium Quality scanner (MQ – bottom figures). The Spatial Resolution Function is presented in along scan (left figures) and cross scan (right figures) directions for five values of contrast *C*. Vertical axes represent resolution distance *R* in pixels and horizontal axes represent the optical factor *Q*.

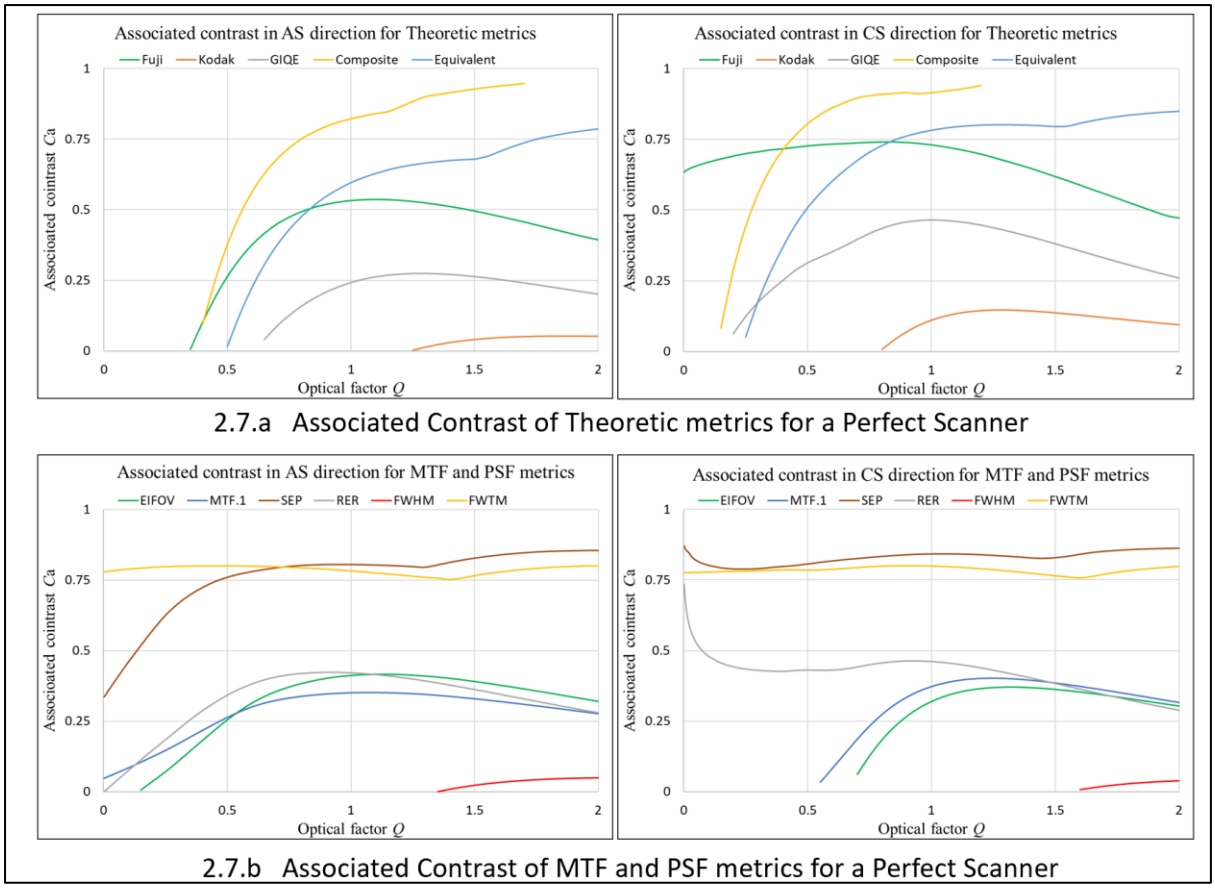

Figure 2.7: Associated Contrast of Soft Metrics. Associated contrast C_a of soft metrics is presented as a function of optical factor Q, for a Perfect Scanner, in along scan (left figures) and cross scan (right figures) directions. Vertical axes represent C_a, and horizontal axes represent Q. C_a is computed assuming that a metric agrees with the Spatial Resolution Function at a given Q. When a soft metric predicts a resolution distance lower than Sparrow limit no data is shown, being this the reason why GSD metric is not presented. All metrics are biased because their C_a depends on Q, erring when comparing imagers with different optical factors.

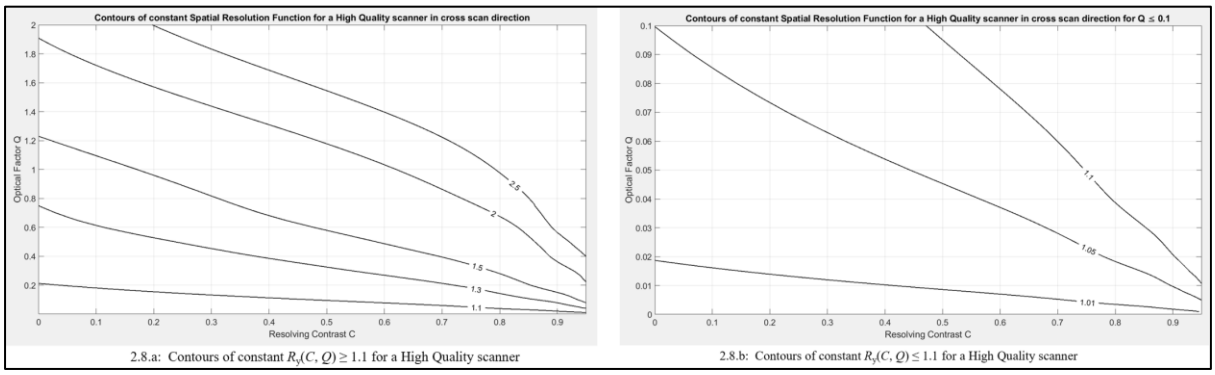

Figure 2.8*:* Contours of Constant Spatial Resolution Function in Cross Scan direction. Contours of constant $R_y(C, Q)$ measured in pixels are drawn for a High Quality scanner in the resolving contrast C versus optical factor Q plane. The GSD metric postulates $r(Q) = 1$ pixel, so the contours can be used to assess its error for a given combination of C and Q values. For example, with relation to Figure 2.8.b, $R_y(0,0.1) = 1.05$, thus, if the GSD metric is used to predict Sparrow limit ($C = 0$) for a HQ imager with $Q = 0.1$, then its prediction error is $100 \cdot (1\text{-}1/1.05) = 4.8$ %.

2.4.1. Spatial resolution function of a perfect scanner

As depicted in Figures 2.6.a and 2.6.b, the resolution distance increases monotonically with contrast and optical factor, showing inflection points near $R = 3$, when maximum intensity I_{max} shifts from Pixel 1 to Pixel 2 (pixel numbers defined in Figure 2.4.a).

When $Q = 0$ the system PSF cut for the Perfect Scanner has the well-known triangular and rectangular shapes in along and cross scan directions, respectively (Schowengerdt 2007). In this case, the Spatial Resolution Function has simple analytic expressions:

$$R_x(C, 0) = 4/(3\text{-}C) \qquad R_y(C, 0) = 1$$

Due to scan, AS resolution is always worse (larger) than CS resolution: $R_x(C, Q) > R_y(C, Q)$. Main difference between AS and CS resolution distances is that for $Q << 1$ and $C = 0$, the GSD metric fails in AS direction, because $R_x(0, Q) \approx 4/3$ instead of $R_y(0, Q) \approx 1$.

This difference is congruent with the differences observed for low Q imagers, between their system PSF cuts in AS (triangular shape) and CS (rectangular shape) directions. These PSF shapes, illustrated in Figure 2.3.a, are characteristic of low optical factor imagers like AVHRR, MSS and MODIS (Schowengerdt 2007).

The 4/3 factor appears due to scanning because in AS direction the optics PSF cut is spread into a square pulse of width p instead of an impulse as in CS direction. Sparrow criterion ($C = 0$) is fulfilled when the central pixel and its two adjacent pixels have equal signal, so this square shape increases resolution distance from 1 to 4/3 pixels, as the following line of reasoning shows.

Assume the phasing condition of Figure 2.4.a and that the optics PSF is spread on the image plane into a square pulse of width p. If sources are separated by a distance $s = p$ then the central pixel has twice the signal of its two adjacent pixels (central pixel has 1/2 of each source, making a total of 1, and adjacent pixels have 1/2 of a source), whereas if sources are separated by $s = 4/3 \cdot p$ then central and adjacent pixels have equal signal (central pixel has 1/3 of each source, making a total of 2/3, and adjacent pixels have 2/3 of a source).

Analytic approximations to $R(C, Q)$ curves for Sparrow limit ($C = 0$) are presented in Table 2.7.

Table 2.7: Analytic approximations to Sparrow limits. Equations shown approximate the Spatial Resolution Function of a Perfect Scanner for zero contrast (Sparrow limit) in AC (x) and CS (y) directions. The bounds for the Mean Average Percentual Error (MAPE) and the maximum error (Max.) within domain $0.001 \le Q \le 2$ are indicated.

Approximations for Sparrow limits	Errors (%)	
	MAPE	Max.
$R_x(0, Q) = (4/3)\cdot[1 + (0.74\cdot Q)^{3.2}]^{1/3.2}$	0.2	0.7
$R_x(0, Q) = Q^2/4 - Q/10 + 4/3$	0.5	2
$R_y(0, Q) = Q^2\cdot 0.15 + Q\cdot 0.23 + 1$	1	3
$R_y(0, Q) = [1 + (0.8\cdot Q)^{1.6}]^{1/1.6}$	2	5
$R_y(0, Q) = 1 + Q/2$	4	11

Without scanning, resolution functions in AS and CS directions would be identical and very similar to the curves displayed in Figure 2.6.b. The MAPD and maximum differences between $R_y(C,Q)$ of a Perfect Scanner and the Spatial Resolution Function $R(C, Q)$ of a Perfect Starer are smaller than 0.4 and 1.5 %, respectively, within domains $0 \leq C \leq 0.9$ and $0.001 \leq Q \leq 2$. Thus, approximations for $R_y(0, Q)$ in Table 2.7, are also applicable to a Perfect Starer.

2.4.2. High quality scanner spatial resolution function

Figures 2.6.c and 2.6.d present the Spatial Resolution Function for a High Quality scanner. Comparing with Figures 2.6.a and 2.6.b, respectively, the curves for $C = 0$ are very similar but the ones for $C = 0.9$ are strikingly different, indicating that although minor imperfections do not affect Sparrow limit, they significantly degrade resolution at high contrast values.

Degradation of resolution distance due to minor imperfections is more pronounced for high optical factors, being almost unnoticeable for $Q << 1$. For example, $R_x(0.9, 1.5)$ is significantly degraded from 3.6 (PS) to 4.7 (HQ) pixels whereas $R_x(0.9, 0.05)$ is barely degraded from 1.92 (PS) to 1.93 (HQ) pixels.

The constant $R_y(C, Q)$ contours of Figure 2.8 are useful to define the range of validity of the *GSD* metric in CS direction. For example, assuming that errors smaller than 10 % are tolerated, if $C = 0$ is required, the GSD metric is valid for $Q < 0.2$, but if $C = 0.9$ is required, then the GSD metric is valid only for $Q < 0.02$.

2.4.3. Medium quality scanner spatial resolution function

Figures 2.6.e and 2.6.f present the resolution function for a medium quality scanner. Comparing with Figures 2.6.c and 2.6.d, respectively, all curves are shifted upwards, indicating that medium imperfections significantly degrade resolution distance at all contrast values.

For $Q > 0.5$ the AC and CS curves are very similar, indicating that the asymmetry due to scan has been obliterated by the effect of symmetrical imperfections.

The resolution degradation due to medium imperfections is more pronounced for high optical factors, being small for $Q << 1$. For example, $R_x(0.9, 1.5)$ is strongly degraded from 4.7 (HQ) to 13.5 (MQ) pixels whereas $R_x(0.9, 0.05)$ is slightly degraded from 1.93 (HQ) to 2.03 (MQ) pixels.

We conclude that, regarding spatial resolution, sensors with $Q << 1$ are highly resistant to degradations in the performance of system components, whereas sensors with $Q \approx 1$ are highly susceptible to these same degradations.

2.4.4. Metrics assessment

Figure 2.7 shows associated contrast curves $C_a(Q)$ for a perfect scanner in AS and CS directions for the twelve soft metrics indicated in section 2.3.3.3. GSD metric is not shown because its predictions are always smaller than Sparrow limit. Similar curves are obtained for HQ and MQ scanners, main difference being that curves for Theoretic System metrics disappear for MQ scanner as their predictions are then below Sparrow limit.

Due to the dependence of their associated contrast on Q, all soft metrics show bias when used to compare imagers with different optical factors, incorrectly disregarding the dependence of resolution on contrast.

Table 2.8 presents MPE and average associated contrast $<C_a>$ of assessed metrics for the three quality types of imagers.

Table 2.8: Soft metrics bias errors and average associated contrasts. For the soft metrics indicated in column 1, their Maximum Prediction Errors are presented in columns 2, 3 and 4, for three quality types of imagers (PS: Perfect Scanner, HQ: High Quality Scanner, MQ: Medium Quality Scanner). Columns 5, 6 and 7 present average associated contrast $<C_a>$ for these same quality types of imagers. $<C_a> = 0$ indicates that metric predicts a resolution distance smaller than Sparrow limit. All values in per cent. A perfect soft metric should have zero bias error and its $<C_a>$ should not depend on imager type, none of the metrics assessed fulfills these conditions.

	Maximum Prediction Error (%)			Average Associated Contrast (%)		
Metric	**PS**	**HQ**	**MQ**	**PS**	**HQ**	**MQ**
IFOV	53	54	87	0	0	0
Fuji	36	34	60	46	35	0
Kodak	26	25	70	3	1	0
GIQE	29	28	66	17	11	0
Composite	64	59	35	52	44	0
Equivalent	40	38	49	38	31	0
EIFOV	16	36	16	19	39	38
MTF.1	10	12	10	36	41	36
SEP	15	40	17	74	79	80
RER	12	16	14	36	49	42
FWHM	25	25	26	1	2	6
FWTM	3	6	6	78	78	79

A perfect soft metric has MPE = 0 and $<C_a>$ = constant for all quality types of imagers; none of the assessed metrics fulfills this requirement. We conclude:

1. IFOV has the largest errors with MPE ≥ 53 %, due to its inadequacy to predict resolution distance for the higher optical factors.

2. All Theoretic System metrics have large errors with MPE ≥ 25 %, exhibiting a large variation of $<C_a>$ with imager quality type.

3. FWHM metric has large errors with MPE ≥ 25 % and with a systematic dependence of $<C_a>$ on imager quality type.

4. MTF.1 metric has smallest errors within MTF metrics with a moderate variation of $<C_a>$ with imager quality type.

5. Best metric is FWTM with MPE ≤ 6 % and almost constant $<C_a>$ with imager type.

2.5. Discussion

2.5.1. Key results

A new spatial resolution metric for satellite imagers, designated Spatial Resolution Function, is developed by applying the classical two-point source resolution criteria to digital images with the following innovations:

- Resolution distance R is computed as a function of sampled image contrast C.
- Phasing between two-point source scene and image plane's pixels is defined so the GSD metric (r =1) is valid for a non-scanning imager when $Q \rightarrow 0$.
- Ultimate resolution distance is computed as function of image SNR using Rose criterion.

A scanning satellite imager model, with circular aperture and square pixels, is selected to apply this metric. The Optical Transfer Function (OTF) approach is used to compute the system Point Spread Function (PSF) of this model.

Spatial Resolution Function $R(C, Q)$ is computed for perfect, high quality and medium quality types of scanning imagers, in along and cross scan directions, within domain $0.001 \leq Q \leq 2$.

Current "soft" metrics that predict resolution as a single distance r, without considering the actual resolving contrast, are assessed by finding their "associated contrast" C_a for which their predicted resolution $r(Q)$ is equal to $R(C_a, Q)$.

An unbiased resolution comparison between two imagers must be performed at the same contrast, but as the C_a of soft metrics depends on Q, all of them are biased. To gauge a metric bias error within the range of optical factors of interest, its predicted resolution distances are compared with the Spatial Resolution Function computed at a contrast equal to the average value of its associated contrast $<C_a>$ within this range.

Metrics are assessed by computing their Maximum Prediction Error (MPE). All metrics assessed show MPE ≥ 6 %. The most popular metric, the Ground Sampled Distance (GSD) has the largest errors with MPE ≥ 53 %. The popular Full Width at Half Maximum (FWHM) of the PSF metric has MPE ≥ 25 %.

2.5.2. Interpretation of results

If resolution is defined in the sampled image according to the two-point source criterion and the GSD is the resolution distance in cross scan direction when $Q = 0$, then the Spatial Resolution Function $R(C, Q)$ is the actual resolution distance of satellite imagers.

The two-point source criterion has a sound empirical and theoretical basis, so currently, as the popular pixel size GSD criterion has been shown to be a particular case, there seems to be no other criterion to challenge it.

The Spatial Resolution Function allows the assessment of "soft" metrics. These later metrics define resolution as a single distance without considering the actual contrast in the sampled image. We have shown that soft metrics are biased, as - for example - they may predict that two imagers with different optical factors have the same resolution when in fact they don't.

The limitations of the GSD metric ($r = 1$) were previously known, our results define its application domain; it should be used to estimate Sparrow limit in cross scan direction for $Q << 1$, outside this domain large errors are expected, especially for high optical factors.

The large errors of all other Theoretic metrics were also expected, as they attempt to predict resolution of actual imagers assuming ideal imagers.

An unexpected result are the large errors of the PSF's Full Width at Half Maximum (FWHM) metric. Its widespread usage in the validation and calibration community suggested smaller errors, but although it is a main descriptor of the PSF's shape, it is inadequate as resolution metric for the full range of optical factors considered. A much better Spatial Response metric is the PSF's Full Width at Tenth Maximum (FWTM).

The high bias errors of the FWHM metric and the low bias errors of the FWTM metric are now interpreted using the analytic expressions presented in section 2.4.1 for the Spatial Resolution Function when $Q = 0$.

Assume that a PSF metric based on its full width at a certain relative level "ε" of response is required, with $0 \leq \varepsilon \leq 1$ so that, at least for $Q \approx 0$, this PSF width metric predicts the correct resolution distance in both AS (x) and CS (y) directions.

For $Q = 0$ the system *PSF* is similar to the one illustrated in Figure 2.3.a.

The system PSF's Full Width in CS direction is $FW_y = 1$ pixel, independently of ε, so for this direction any response level ε will suffice as $FW_y = R_y(C,0) = 1$ pixel is always satisfied.

In AS direction, the Full Width of the PSF is:

$$FW_x(\varepsilon) = 2 \cdot (1 - \varepsilon) \text{ pixels}$$

This width varies from 0 to 2 pixels when the response level ε varies from 1 to 0.

For the PSF width metric to correctly predict resolution in AS direction, the following equality must hold:

$$FW_x(\varepsilon) = 2 \cdot (1 - \varepsilon) = R_x(C,0) = 4/(3-C)$$

Thus, the required relation between response level and resolving contrast is:

$$\varepsilon = 1 - 2/(3-C)$$

The response level ε varies from 0.33 to 0 as the contrast C varies from 0 to 1. Thus, under the restriction $0 \leq \varepsilon \leq 0.33$ the PSF width metric will work at $Q \approx 0$ for a contrast:

$$C = 3 - 2/(1 - \varepsilon)$$

Finally, we conclude that the FWTM metric ($\varepsilon = 0.1 < 0.33$) satisfies this later restriction for a contrast $C \approx 0.78$ whereas the FWHM metric ($\varepsilon = 0.5 > 0.33$) does not.

Very good agreement is obtained for the FWTM metric between this later value of C, derived through the analytic approximations of the Spatial Resolution Function, and the average associated contrast values presented in the bottom line of Table 2.8.

The overall inadequacy of Spatial Response metrics is interpreted by considering the following facts:

1. Spatial Response metrics predict resolution distance of digital images without considering the contrast achieved in the image plane when two-point sources are separated at this distance. If the system PSF and OTF would always have the same shapes a single property of them could suffice to define resolution for a given contrast, but as the PSF and OTF shapes depends on imager type, scan direction and optical factor, there is no easy substitute to the computation of resolution distance versus resolving contrast in a case by case basis.

2. Spatial Response metrics are based on a property of the pre-sampled spatial response without considering the dependence of resolution distance on pixel sampling and scene phasing. Spatial resolution occurs in the sampled image and is highly dependent on scene phasing, as illustrated in Figure 2.24. Thus, metrics that do not explicitly consider sampling and phasing cannot be expected to give an accurate estimation of resolution distance.

2.5.3. Implications of results

The Spatial Resolution Function $R(C, Q)$ allows an unbiased assessment of resolution for any type of satellite imager, using as input the same system PSF or OTF whose properties are employed by Spatial Response metrics. Whereas these later metrics define resolution as a single distance $r(Q)$ computed from the pre-sampled system PSF or OTF, the $R(C, Q)$ approach computes the resolution distance of two-point sources as a function of the actual resolving contrast in the sampled image.

The advantage of Spatial Response metrics is that resolution is estimated directly from the system PSF or OTF, without applying the computational procedure described in section 2.3.2.2. Considering the large bias errors of Spatial Response metrics and the widespread availability of computational resources, it does not seem wise to sacrifice accuracy due to an economy in calculation effort, especially when the required system PSF is already available.

The main implication of our results is that Theoretic and Spatial Response metrics are unsuitable to compare the resolution distance of different types of satellite imagers, as they may give erroneous conclusions. To gauge spatial resolution with an unbiased metric, the Spatial Resolution Function can be employed.

As an example of the errors due to biased metrics, consider the task to select between two HQ satellite sensors, “Sensor 1” and “Sensor 2”, the one with the best spatial resolution. Sensor 1 has $Q = 0.4$ and GSD = 250 m. Sensor 2 has $Q = 1.5$ and GSD = 200 m.

According to the GSD metric, Sensor 2 has better (smaller) resolution than Sensor 1, in AS and CS directions, independently of the resolving contrast.

Consider now the use of the Spatial Resolution Function for this same task, assuming that a contrast $C = 0.3$ is required to declare resolution. The results are shown in Table 2.9.

When the resolution distance of both sensors is measured at the same contrast level, the Spatial Resolution Function indicates that Sensor 1 has better (smaller) resolution than Sensor 2 in both directions.

Table 2.9: Example of resolution distance computation. The Spatial Resolution Function is used to compute the resolution distances of two hypothetical High Quality (HQ) imagers in Along Scan (x) and Cross Scan (y). directions. The GSD metric incorrectly predicts that Sensor 1 has the best (smallest) resolution distance, whereas actually it has the worst (largest) resolution distance.

Sensor	GSD (metres)	Q (scalar)	C (scalar)	$R_x(C,Q)$ (pixels)	GSD·R_x (meters)	$R_y(C,Q)$ (pixels)	GSD·R_y (meters)
Sensor 1	250	0.4	0.3	1.554	388.6	1.275	318.7
Sensor 2	200	1.5	0.3	2.306	461.3	2.127	425.4

This example illustrates the use of the Spatial Resolution Function in a practical case, and also highlights the following general implications that must be considered when assessing the spatial resolution distance of satellite imagers:

1. Spatial resolution distance is a function of the contrast that is required in the image to declare that the two point sources have been resolved (separated).

2. To compare the spatial resolution distance of different satellite imagers, this comparison must be performed at the same image contrast.

3. Spatial resolution metrics which do not explicitly consider image contrast must not be employed to compare different types of imagers.

4. The spatial resolution distance is usually different in along scan and cross scan directions, being always larger than the GSD.

Even for the same satellite imager, soft metrics err when resolutions distances in AS and CS directions are compared. For example, in the case of a low Q imager illustrated in Figure 2.3.a, the GSD and the PSF FWHM metrics predict that the resolution distance in both AC and CS directions is 1 pixel. If zero contrast is assumed, both metrics are approximately correct in CS direction, but both metrics err by a 4/3 factor in AS direction.

In practice, instead of the Spatial Resolution Function, a single figure of merit to assess resolution may sometimes be needed. The PSF's FWTM could be an alternative if a contrast $C \approx 0.78$ is relevant, but this metric's errors have only been assessed for the specific types of imagers herein considered. More general figures of merit are obtained by computing $R(C)$ for the specific type of imager and optical factor Q of interest and extracting from this function a single value suitable to the application. For example:

- When minimum resolution distance is of interest, the ultimate resolution $R(C_{min})$ limited by SNR can be employed.

- In image processing applications where a given contrast threshold $C_{thr} > C_{min}$ must be exceeded, $R(C_{thr})$ is a suitable resolution parameter.

- If radiometric accuracy is critical, $R(0.95)$ can be used to estimate at which distances the measurements are uncontaminated by PSF's adjacency effect.

- If overall image quality for a certain domain of contrasts is of interest, then average value of $R(C)$ in this domain can be used.

2.5.4. Limitations and future work

The procedure to compute the Spatial Resolution Function is general, but as its computation depends on the system PSF, the results presented and the conclusions regarding the assessment of current metrics are strictly valid only for imagers satisfying the assumptions stated in section 2.3.1.2.

Although these later assumptions are representative of satellite imagers, the OTFs of section 2.3.1.2 must be modified when considering: obstructed optical apertures (Cota et al. 2010); partial pixel fill factors (Boreman 2001); square optical apertures (Boreman 2001); different pixel geometries (Fliegel 2004); time delay and integration (Fiete 2010); atmospheric propagation effects (Boreman 2001); pixel over-sampling (Fiete and Tantalo 1999); pixel under-sampling (Boreman 2001); and clock-phasing techniques (Fiete 2010).

Optics and detector responses are wavelength dependent, but monochromatic radiation was assumed. If $\Delta\lambda$ is the extent of the sensor's spectral response and λ_o is its central wavelength, the monochromatic OTF computed at λ_o is a good approximation to the Polychromatic OTF (POTF) when $\Delta\lambda/\lambda_o << 1$.

Some panchromatic imagers have spectral responses between 450 and 900 nm ($\Delta\lambda/\lambda_o = 2/3$), in these cases the POTF is required to accurately assess their spatial resolution (Wetherell 1980, Cota et al 2010).

The implementation of previous modifications is straightforward, but as their treatment will significantly extend the length of this paper, they are left aside as future work.

Due to optics PSF's sidelobes, the spatial resolution function may be multi valued for a contrast C larger than a certain contrast C_o. The multiple valued property of $R(C)$ is not an issue for a clear aperture for which $C_o > 0.95$, so it has not been here addressed, but it should be considered when $C_o < 0.95$ due to obstructed apertures or other factors. For this purpose, an adaptive sliding average may be defined, so the averaged resolution function is always continuous and monotonic.

2.6. Conclusion

Although spatial resolution is one of the key parameters of satellite imagers, the most popular metrics to measure it are biased, leading to incorrect conclusions when comparing the spatial resolution of different types of imagers. The aim of this research is to develop an unbiased metric.

To achieve this aim, the classical optical criteria of angular resolution, is applied to satellite imagers, in such a way that the popular Ground Sampling Distance metric is obtained as a particular case of a more general Spatial Resolution Function metric. This new metric computes resolution distance versus the contrast achieved in the image plane when imaging two closely spaced point sources.

The procedure to compute the Spatial Resolution Function can be applied to any type of satellite imager providing its system Point Spread Function (PSF) is known. Once the Spatial

Resolution Function is found, the effect of noise can be assessed through the computation of an ultimate resolution distance based on Rose criterion.

Only the system PSF is required as input to compute the Spatial Resolution Function, so in this respect, this new metric does not differ from metrics that define resolution as a property of the system PSF or of its Fourier transform, the system Optical Transfer Function (OTF).

In this study it was shown that Theoretic and Spatial Response metrics err when predicting the resolution distance of imagers with different optical factor Q, because the contrast associated to their prediction is a function of Q.

Metrics errors were assessed by comparing their predictions with the Spatial Resolution Function computed at a reference value of contrast. For a given quality type of imager, this reference was defined as the average value of associated contrast within the range of optical factors of interest, but other definitions are also possible.

The performance of twelve metrics was assessed by computing their prediction errors for three quality types of imagers. All metrics assessed show large bias errors with the exception of a lesser used metric (FWTM of the PSF) whose smaller errors were demonstrated, but only for the specific types of imagers here considered.

The impact of our findings is that the most popular spatial resolution metrics are biased and may lead to gross errors when comparing different types of imagers. Our work defines a general procedure to compute the Spatial Resolution Function, an unbiased metric that can be used to compute the spatial resolution distance of any satellite imager.

The advantages of this new Spatial Resolution Function metric over current metrics are:

1. It is a Two-Point Source metric, so it can be used to compare the spatial resolution of different types of imagers without the bias errors that are characteristic of Theoretic and Spatial Response metrics.

2. It can be applied to any satellite imager to compute its spatial resolution distance for any value of contrast selected as a resolution threshold. Current metrics either disregard the dependence of spatial resolution on image contrast (Theoretic and Spatial Response metrics) or assume a fixed value of contrast (Two-Point Source Single Value metrics).

3. It provides a unified approach to spatial resolution by choosing a phasing condition that allows the popular Ground Sampling Distance (GSD) metric to be obtained as a limiting case.

4. It allows a quantitative estimation of how image noise degrades spatial resolution, through the definition of a minimum detectable contrast via Rose criterion.

5. It can be used to compute the bias errors of Theoretic and Spatial Response metrics, a task beyond the capability of Single Value metrics.

The Spatial Resolution Function can be used for multiple purposes, for example, to comprehensively assess the impact of image processing algorithms on image resolution. Results based on biased Spatial Response metrics, which state that some algorithms like MTF

compensation provide a twofold increase in spatial resolution (Blonski et al. 2002), can now be reassessed under an unbiased framework.

In the light of the new Spatial Resolution Function and the overall limitations of Spatial Response metrics, the interest on these later metrics seems more a tribute to our historical legacy in spatial resolution assessment rather than a practical need. This paper poses the question: Why dedicate efforts to study Spatial Response metrics, that approximately predict spatial resolution as a property of system PSF, when by using this same PSF, the exact Spatial Resolution Function can be found?

Abbreviations

ABI: Advanced Baseline Imager

AHI: Advanced Himawari Imager

AMI: Advanced Meteorological Imager

AS: Along Scan

AVHRR: Advanced Very High Resolution Radiometer

CS: Cross Scan

EIFOV: Effective Instantaneous Field Of View

FWHM: Full Width at Half Maximum

FWTM: Full Width at Tenth Maximum

GIQE: General Image Quality Equation

GOES: Geostationary Operational Environmental Satellite

GK-2: Geostationary Kompsat 2 satellite

GSD: Ground Sampling Distance

HQ: High Quality satellite scanner

H-8: Himawari 8 satellite

IFOV: Instantaneous Field Of View

IFT: Inverse Fourier Transform

LEO: Low Earth Orbit

LOS: Line Of Sight

LSF: Line Spread Function

MAPD: Mean Average Percentual Difference

MAPE: Mean Average Percentual Error

MODIS: Moderate Resolution Imaging Spectroradiometer

MPE: Maximum Prediction Error

MS: Multispectral

MSG: Meteosat Second Generation (satellite)

MSI: Multispectral Instrument

MSS: Multispectral Scanner

MQ: Medium Quality satellite scanner

MTF: Modulation Transfer Function

NASA: National Aeronautics and Space Administration

nm: nanometre

OLI: Operational Land Imager

OTF: Optical Transfer Function

PAN: Panchromatic

POTF: Polychromatic Optical Transfer Function

PS: Perfect satellite Scanner

PSF: Point Spread Function

RAIFOV: Radiometrically Accurate Instantaneous Field Of View

RER: Relative Edge Response

RMS: Root Mean Square

SEP: Schade's Equivalent Passband

SEVIRI: Spinning Enhanced Visible and InfraRed Imager

SLSTR: Sea and Land Surface Temperature Radiometer

SNR: Signal to Noise Ratio

TIRS: Thermal Infrared Sensor

USAF: United States Air Force

WFE: Wave Front Error

Chapter Three

A New Methodology to Assess Spatial Response Models for Satellite Imagers using the Optical Design Parameters of a Generic Sensor as Independent Variables*

* This chapter was published on 26th April 2023 as:

Valenzuela AQ, Reinke K, Jones SD. A new methodology to assess spatial response models for satellite imagers using the optical design parameters of a generic sensor as independent variables. *IEEE Transactions on Geoscience and Remote Sensing* **61**, 1-10. https://doi.org/10.1109/TGRS.2023.3270433.

3.1. Introduction

The Point Spread Function (PSF) is a two-dimensional (2D) function that describes the spatial response of an imaging sensor to a single point source in the scene. If the sensor's *PSF* is known, then the image produced by this sensor can be computed in terms of the known scene radiance (Schowengerdt 2007).

Several analytic models are used to estimate (approximate) the actual PSF, either as part of a measurement process or in theoretical studies in which a given PSF is assumed. The following models are used for imaging sensors:

1. Analytic PSF models (Wang et al. 2020, Bendinelli et al. 1998, Helder et al. 2005, Zhang et al. 2006, Peng et al. 2015).

2. Line Spread Function (LSF) models (Helder et al. 2005, Smith 2006, Claxton and Staunton 2008, Li et al. 2009, Li et al. 2011, Khetkeeree and Liangrocapart 2018).

3. Separable PSF model: this model estimates the PSF from two perpendicular edge measurements, assuming that the PSF equals the product of the two measured LSFs (Craknell 1998):

$$\mathrm{PSF}(x,y) = \mathrm{LSF}_x(x) \cdot \mathrm{LSF}_y(y) \tag{1}$$

4. One-dimensional Hankel transform (Calle et al. 2009).

Considering the plethora of spatial response models, it is of interest to assess them to select the most accurate for a given sensor and application. The assessment of these models is complicated by the fact that PSF shape is dependent on the optical design of the imaging sensor, so any assessment that considers only a specific kind of optical design is inherently biased as its results will not be valid for other designs.

For example, specific imagers have been used to assess analytic PSF and LSF models to select the most accurate. The results indicate that the most accurate functions are Gaussian (Peng et al. 2015), generalized Gaussian (Claxton and Staunton 2008), Cauchy (Smith 2006), Fermi (Li et al. 2009), and sine integral (Li et al. 2011). These disparate contradictory conclusions are expected because in each case a different imager (and so a different actual PSF shape) has been considered.

To properly assess a spatial response model, in a way that is meaningful to a large number of potential users, its accuracy must be computed as a function of the optical design, so the end user can select the model that is best suited for the specific sensor type and intended application.

If actual sensors are used, it is not practical to consider a broad variety of optical designs, but if a generic sensor model is employed as a yardstick, then this theoretical model can be formulated in such a way that its PSF shape depends only on a few key parameters that characterize the optical design. If only two key parameters are defined, then the accuracy of any spatial response model can be conveniently represented as constant error curves in a plane of possible optical designs.

The definition of the key parameters of the optical design is dependent on the geometries of the optical aperture and the detector elements. In this work we assume a generic model whose geometries are representative of the most common types of satellite imagers: an annular optical aperture with square detector elements.

A main optical design parameter is the optical factor *Q*, a non-dimensional number that gauges the relative importance of the optics and the detector in the spatial response of the sensor (Fiete 2010). For an annular optical aperture of external diameter *D*, detecting radiation of wavelength λ, which is focused through a focal length *F*, into a detector array of square pixels with pitch *p*, the optical factor is:

$$Q = \frac{\lambda}{D} \frac{F}{p} \tag{2}$$

Another optical design parameter that influences the shape and extension of the PSF is the central obstruction of the optical aperture. For an annular optical aperture with internal diameter *d* and external diameter *D*, the linear obstruction ratio ε is:

$$\varepsilon = \frac{d}{D} \tag{3}$$

The annular geometry is representative of several "folded optics" telescope designs like the Cassegrain, Ritchey-Chrétien and Newtonian types.

Q and ε are selected as key optical design parameters, so spatial response models can be assessed in the (*Q*, ε) plane.

To illustrate the application of this methodology we assess the separable PSF model. The following types of arguments to validate the usage of (1) are found in the literature:

1. Present it as a property of the PSF (Cracknell 1998, Zhang et al. 2014, Peng et al. 2015, Pahlevan et al. 2016, Zhu et al. 2021).

2. Identify it as a suitable approximation or assumption (Markham 1985, Forster and Best 1994, Shea 1999, Chen et al. 2011, Ruiz and Lopez 2012, Radoux et al. 2016).

3. Cite works in which it has been already employed (Guo et al. 2010, Chen et al. 2011, Li et al. 2011, Rongjun and Jianya 2011, Stankevich 2021).

4. Justify its use with technical arguments (Khetkeeree and Liangrocapart 2018, Lin et al. 2013, Campagnolo and Montano 2014, Luo et al. 2014).

Despite the widespread use of (1), there is no rigorous assessment of its validity or accuracy. It has been stated that "*its errors usually turn out to be small*" (Chen et al. 2011, 7182), but this claim is based on a single case study (Vollmerhausen and Driggers 2000). In this study, the authors considered an ideal optical sensor with square pixels and an unobstructed circular optical aperture ($Q = 0.71$, $\varepsilon = 0$), concluding that the maximum error of the following equation was less than 1 % (Vollmerhausen and Driggers 2000):

$$\mathrm{PSF}(x, y) = \mathrm{PSF}(x, 0) \cdot \mathrm{PSF}(y, 0) \tag{4}$$

If the same single case study of (Vollmerhausen and Driggers 2000) is used to assess (1), the maximum error is now 95 %.

The literature provides evidence that the utility of (1) needs to be further assessed. The recommendation to verify the validity of (1) before using it, was stressed in a work that lay the foundations of the slanted edge method (Reichenbach et al. 1991). By way of example, the use of (1) to estimate the PSF was shown to yield poor image restoration results for SPOT satellite, so the separable PSF model was empirically modified to improve them (Ruiz and Lopez 2012). The striking differences between the PSF measured before launch and the PSF estimated by (1) has also been graphically illustrated (Ando and Tanaka 2019). Finally, the need of future research to study the domain of validity of (1) for different optical systems has been identified (Skauli and Torkildsen 2019) but, to the best of the authors' knowledge, such a study has not been performed.

Therefore, the objective of this paper is to propose a new methodology to assess spatial response models by assuming a generic sensor that allows the computation of the error of these models as a function of the key optical design parameters. This methodology is illustrated by assessing the separable PSF model (1), assuming a generic satellite imager with annular optical aperture and square pixels, and computing the error of this model as a function of Q and ε.

Section 3.2 presents the relevant data and procedures required to assess spatial response models for Earth viewing satellite imagers. Section 3.3 exemplifies the results of the application of the previous procedures to the assessment of the separable PSF model (1). Section 3.4 discusses the relevance and limitations of our study.

3.2. Materials and Methods

3.2.1. Domain of interest in the (Q, ε) plane

Assuming a generic sensor with annular optical aperture and square pixels, the accuracy of spatial response models can be assessed as a function of the optical factor Q and the obstruction ratio ε. To consider a broad domain of optical designs, Q and ε are treated as continuous independent variables. This section defines the domain of interest of Q and ε for satellite imagers.

3.2.1.1. *Optical factor - Obstruction ratio (Q, ε) plane*

Table 3.1 presents (Q, ε) data for some representative spaceborne imagers for Earth observation, each imager has the number of channels or bands indicated in the third column. The optical factor was computed for each one of these channels. Table 3.1 indicates the minimum and maximum Q values computed for each imager.

Optical factors were computed from data given in the references cited in Table 3.1, assuming that the wavelength λ of (2) is the center wavelength of the channel's spectral response. For rectangular pixels, the pitch p of (2) is assumed to be the square root of the pixel's area.

Obstruction ratios were computed as the ratio of the secondary and primary (focusing) mirrors' diameters. If these diameters were not available, they were estimated analyzing photographs of the optical aperture.

Table 3.1: Optical factor *Q* and linear obstruction ratio ε data for satellite imagers

Satellite	Imager	N° of channels	*Q*		ε	References
			Min.	Max.		
AlSat 2	NAOMI	5	0.17	0.81	0.31	Luquet et al. 2008
GaoFen 2	PAN & MS	5	0.18	1.01	0.25	Cheng et al. 2017, Huang et al. 2018
Global 4	SpaceView 24	4	0.97	1.30	0.25	Saunier 2021, SpaceView 2024
GOES 16	ABI	16	0.076	1.36	0.00	Geo-Kompsat-2 2024, NASA 2019
KompSat 3	PAN & MS	5	0.17	0.93	0.28	SESO 2024, Kompsat-3 2024
Landsat 1	MSS	4	0.029	0.048	0.44	Slater 1979, Mika 1997
Landsat 9	OLI	8	0.077	0.38	0.00	Figoski et al. 2009, Morfitt et al. 2015
Pleiades	HiRI	5	0.19	0.99	0.26	Lamard et al. 2004, Pleiades-HR 2024
Satellogic	MS	4	0.71	1.22	0.36	Satellogic 2024
Sentinel 2	MSI	12	0.068	0.42	0.00	Sentinel-2 2024
SSOT	NAOMI	5	0.21	1.28	0.31	Luquet et al. 2008
SuperDove	PSD.SD	8	0.80	1.57	0.43	Kim et al. 2021

3.2.1.2. *Domain of optical factors*

The optical factor of Earth observation satellites is usually smaller than 1.5 due to spatial resolution and Signal to Noise Ratio (SNR) considerations (Fiete 2010, 118). Based on Table 3.1, a domain $0.01 \leq Q \leq 2$ will be selected to assess the spatial response models for satellite imagers.

3.2.1.3. *Domain of obstruction ratios*

Obstructed apertures are popular because they allow more compact designs than unobstructed apertures. A maximum obstruction ratio $\varepsilon = 0.5$ has been estimated as convenient (Lin et al. 2020) and, as Table 3.1 suggests, satellite imagers seem to follow this guideline. Based on the previous data and considerations, a domain $0.0 \leq \varepsilon \leq 0.5$ will be selected for our purposes.

3.2.2. Minimum point spread function level to be assessed

3.2.2.1. *Basic equation*

It is necessary to define until what minimum PSF level, named PSF_{min}, will the spatial response models be assessed.

The PSF should only be modelled until a minimum level that has practical significance; PSF model's errors which generate image signal errors smaller than the random signal fluctuations due to image noise are irrelevant.

To estimate PSF_{min} we initially assume a scene with a uniform background which generates a signal *B* on the image. If the background signal to noise ratio is SNR_B and a Gaussian noise distribution is assumed, the background signal will fluctuate with a standard deviation (Fiete and Tantalo 2001):

$$N = \frac{B}{\mathrm{SNR}_B} \tag{5}$$

We now assume that a single point source in the scene generates a peak signal *P* in the image's pixel where the position of this source is represented. This is illustrated in Figure 3.1

for a point source's position presented at pixel 10. The contribution of the point source to the peak signal is:

$$\Delta S_P = P - B \tag{6}$$

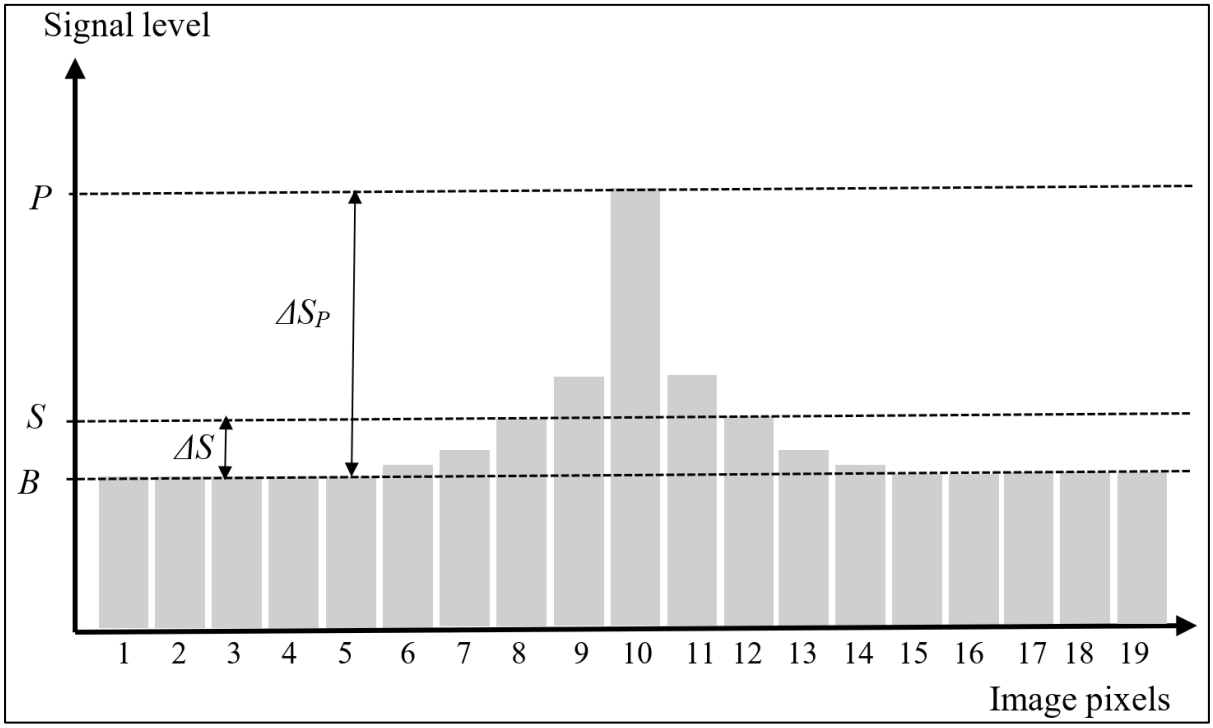

Figure 3.1: One dimensional illustration of the PSF adjacency effect. A single point source's position represented at pixel 10 generates a peak signal *P* in this pixel and also increases the signal level in adjacent pixels 6 to 9 and 11 to 14. The signal increase Δ*S* in adjacent pixels 8 and 12 will be detected only if it is substantially larger than the background signal fluctuations due to image noise.

The PSF usually extends through more than one pixel, so the point source will also increase the signal in adjacent pixels, in direct proportion to the PSF intensity at these pixels. If the point source's position is represented at the center of a pixel with coordinates (0,0) and the center of an adjacent pixel is at coordinates (*x*, *y*), the signal increase at this later pixel is:

$$\Delta S(x,y) = \Delta S_P(0,0)\ \frac{PSF(x,y)}{PSF(0,0)} \tag{7}$$

The signal increase Δ*S* will be detected only if it is substantially larger than the fluctuations of the background signal due to image noise. The minimum signal increase that can be observed will be associated to the minimum PSF level of interest. Assuming PSF(0,0) = 1, equations (6) and (7) yield:

$$\Delta S_{min} = \Delta S_P \cdot \mathrm{PSF}_{min} = (P - B)\ \mathrm{PSF}_{min} \tag{8}$$

For simplicity we apply Rose criterion, which states that the minimum detectable *ΔS* should be five times greater than the standard deviation of the background noise (Maidment 2014):

$$\Delta S_{min} = 5\,N = 5\ \frac{B}{\mathrm{SNR}_B} \tag{9}$$

Equating the rightmost members of equations (8) and (9), we obtain:

$$\mathrm{PSF}_{min} = \frac{5}{(R - 1)\,\mathrm{SNR}_B} \tag{10}$$

Where $R = P/B$ is the peak signal to background signal ratio.

The possible ranges of variation for R and $\mathrm{SNR_B}$ are now analyzed.

3.2.2.2. *Peak signal to background signal ratio*

The relevant peak signal to background signal ratio R is application dependent. Assuming that the signal is proportional to the radiance, the maximum ratio R, cannot exceed the extreme radiances ratio of the sensor, defined as the ratio between the maximum and minimum measurable radiances. Some examples of this ratio, which can be considered a measure of the dynamic range of the sensor, are presented in Table 3.2.

Table 3.2: Examples of extreme radiances ratio "*R*" for satellite imagers

Satellite	Imager	N° of channels	Extreme radiances ratio		References
			Minimum	Maximum	
Landsat 4	TM	6	4	16	Mika 1997
Landsat 8	OLI	9	14	540	Ren et al. 2014
Pleiades	HiRI	5	26	45	Kubik and Pascal 2004
Sentinel 2	MSI	13	37	900	Sentinel-2 2004

In practice R will rarely achieve the extreme radiances ratio. An example with high R values is fire detection at infrared wavelengths, in this case measured R ratios were 50 and 1.5 for the 3.9 and 11.3 μm channels, respectively (Wu et al. 2020).

We conclude that the evolution of satellite sensor's dynamic range has allowed the peak to background signal ratio R to exceed 1000, but that in practice this ratio will be usually less than 100.

3.2.2.3. *Background signal to noise ratio*

Several metrics are used to compute SNR, but for our purposes we consider only sensor-based and image-based metrics (Fiete and Tantalo 2001). Table 3.3 shows some examples of sensor-based SNR requirements for satellite imagers and Table 3.4 compares, the sensor-based requirements and measurements with the image-based SNR values provided in (Radoux et al. 2016) for five satellite channels. Although measured sensor-based SNR is higher than the specification, the image-based SNR is always smaller than this same specification.

We conclude that the evolution of sensor performance has allowed the maximum possible background (sensor-based) signal to noise ratio to exceed 1000, but that in practice this (image-based) ratio will be usually less than 100.

Table 3.3: Examples of signal to noise ratio requirements for satellite imagers

Satellite	Imager	N° of channels	Required Sensor SNR		References
			Minimum	Maximum	
Aqua	MODIS	19	57	1087	Barnes et al. 1998
Landsat 1	MSS	4	38	77	Mika 1997
Landsat 7	ETM+	7	16	41	Iron et al. 2012
Landsat 8	OLI	7	80	130	Iron et al. 2012
Pleiades	HiRI	5	90	90	Lamard et al. 2004
Sentinel 2	MSI	13	50	174	Sentinel 2 2004
Sentinel 3	OLCI	20	203	2188	S3MPC 2021

Table 3.4: Comparison of signal to noise ratio metrics for five satellite imaging channels

Satellite	Channel N° (Name)	Sensor-based SNR		Image-based SNR	References
		Required	Measured		
Landsat 8	4 (Red)	100	227	21	Irons et al. 2012, Morfitt et al. 2015, Radoux et al. 2016
SPOT 5	2 (Red)	100	166	57	CNES 2013, Radoux et al. 2016
Sentinel 2	4 (Red)	142	230	88	Radoux et al. 2016, Gascon et al. 2017
Sentinel 2	5 (Red edge)	117	253	50	Radoux et al. 2016, Gascon et al. 2017
Sentinel 2	11 (SWIR1)	100	158	31	Radoux et al. 2016, Gascon et al. 2017

3.2.2.4. *Minimum point spread function's reference levels*

The evolution of sensor performance has increased the dynamic range, the signal to noise ratio and the optical factor of satellite imagers, so the probability that images are affected by the *PSF* adjacency effect has also increased. The exact requirement for the minimum PSF value of interest must be established in a case-by-case basis, using equation (10) as a guideline.

For our purposes we will select two PSF_{min} reference values: 0.1 and 0.01. For example, if $SNR_B = 50$, the $PSF_{min} = 0.1$ value is applicable for $R = 2$ and the $PSF_{min} = 0.01$ value is applicable for $R = 11$. Although in some cases smaller PSF_{min} values may be required, it will be shown that equation (1) has high errors already for $PSF_{min} = 0.01$, thus, there is no need to consider smaller PSF_{min} values to assess its domain of validity.

3.2.3. Point / line spread function computation

To assess spatial response models in the (Q, ε) plane, we employ the same generic sensor used in (Valenzuela et al. 2022) to represent a High-Quality (HQ) satellite imager with the purpose to assess spatial resolution metrics. Instead of the circular (unobstructed) aperture ($\varepsilon = 0$) used by (Valenzuela et al. 2022) we study the more general case of an annular aperture ($\varepsilon \geq 0$). This section describes the procedures and assumptions used to compute the PSF and the *LSF* of this model as a function of Q and ε.

The system PSF is computed as the inverse Fourier transform of the two-dimensional system Optical Transfer Function (OTF). The system OTF is computed versus the spatial frequencies in Along Scan (AS) and Cross Scan (CS) directions, in what follows denominated

f_x and f_y, respectively, using the procedure described below. Once the OTF is known, the PSF is computed as the 2D Inverse Fourier Transform (IFT) of the OTF:

$$\mathrm{PSF}(x,y) = \mathrm{IFT}[\mathrm{OTF}(f_x, f_y)] \tag{11}$$

A real-valued OTF is assumed so PSF(x,y) = PSF(-x,-y) and LSF(x) = LSF(-x) (Williams and Becklund 2002, 204-208). The OTF must be considered instead of its absolute value (MTF) as negative OTF values are encountered for $Q < 1$.

The system LSFs are computed as the IFT of a one-dimensional cut of the system OTF:

$$\mathrm{LSF_x}(x) = \mathrm{IFT}[\mathrm{OTF}(f_x, 0)] \tag{12}$$

$$\mathrm{LSF_y}(y) = \mathrm{IFT}[\mathrm{OTF}(0, f_y)] \tag{13}$$

The system OTF is computed as the product of all factors that contribute to the spatial response of the sensor. Among these factors the most important are: 1) optics; 2) detector; 3) line of sight scan; 4) atmosphere; and 5) image reconstruction. For our purpose we consider only the first three factors as described below. We assume that Q is varied at a given wavelength by changing the pixel pitch p as it is usual when a given volume is assigned to an imager on board a satellite platform (optical aperture and focal length are fixed).

3.2.3.1. *Optics*

An annular aperture affected by random optical aberrations and line of sight jitter (high frequency random oscillations) is assumed. The OTF of an annular aperture is well known (Fiete 2010, equation 5.35); when $\varepsilon = 0$ it reduces to the OTF of a circular aperture. We assume well-focused optics and neglect defocusing effects (Boreman 2021, 27).

Random wavefront errors are modeled through Shannon's empirical OTF equation (Fiete 2010, equation 5.49), assuming that the root mean square error of the wavefront error is 0.1 wavelength, a value characteristic of a high-quality optical system (Shannon 2010).

A Gaussian OTF model is assumed for the random Line Of Sight (LOS) jitter (Fiete 2010, equation 7.11) with a standard deviation of 0.1 pixel for $Q = 1$, a value representative of a high-quality line of sight attitude control (Ye et al. 2020). To consider that higher Q sensors are more susceptible to motion blur (Fiete 2010, 122), a constant jitter is assumed so its standard deviation in pixel units is proportional to Q.

3.2.3.2. *Detector*

A focal plane array of square pixels with 100 % fill factor is assumed. The OTF of this detector array is well known (Boreman 2021, equation 2.2). Charge diffusion is modelled with a Lorentz function (Davis et al. 1998) using an effective diffusion length parameter of 0.1 pixel for $Q = 1$, a value representative of a high-quality detector (Rafol et al. 2018). To consider that smaller pixels are more affected by diffusion effects (Davis et al. 1998), a constant diffusion length is assumed so in pixels units this length is proportional to Q.

3.2.3.3. *Scan speed*

A constant scan speed in *x* direction with "exact" sampling is assumed. In this case the effective pixel sampling width is equal to the physical pixel pitch (Cota e al. 2010, equation 27) and the corresponding scan OTF is well-known (Fiete 2010, equation 7.6). This scan OTF is applicable to Low Earth Orbit (LEO) push broom scanners, LEO push frame scanners, and Geostationary Orbit raster scanners. It also approximately applicable to LEO whiskbroom scanners whose LOS speed along track is much slower than its LOS speed along scan.

3.2.3.4. *System optical transfer function*

The previous assumptions allow the system OTF to be computed as a function of the optical factor Q and the obstruction ratio ε. This computation is performed for each combination of Q and ε values by varying the spatial frequencies in *x* and *y* directions at intervals:

$$\delta f_x = \delta f_y = \frac{F_S}{N_S} \tag{14}$$

Where δf_x and δf_y are the spatial frequency resolution of the fast IFT in in *x* and *y* directions, respectively, F_S is the sampling frequency employed for the IFT in cycles per pixel and N_S is the number of IFT samples in both directions.

3.2.4. Assessment of separable point spread function model

The flowchart to assess the separable PSF model is presented in Figure 3.2. For given values of Q and ε, the actual PSF is compared with the PSF estimated by the separable PSF model of equation (1). The errors of equation (1) are computed for PSF_{min} = 0.1 and PSF_{min} = 0.01, within the sector of interest in the (Q, ε) plane, using the Mean Absolute Percentage Error (MAPE) metric.

The optical factor Q was varied between 0.01 and 2, at intervals δQ = 0.01, and the obstruction ratio ε was varied between 0.0 and 0.5, at intervals δε = 0.01, totaling 10200 channel points. This high number of points allows constant MAPE contours to be drawn in the (Q, ε) plane.

A value MAPE = 10 % was selected as the boundary of the domain of validity for the model defined by equation (1), considering that the maximum error is usually two to four times larger than the MAPE. As shown in the results, the MAPE = 10 % contours of equation (1) in the (Q, ε) plane, are roughly parallel to the obstruction ratio axis. Thus, to simplify the definition of the validity region, the domain of validity of equation (1) was defined as the maximum Q value for which MAPE < 10 % for any value of $\varepsilon \leq 0.5$.

3.2.5. Validation methods

The fast Inverse Fourier Transform (IFT) algorithms used to compute the PSF and LSFs have numerical errors due to the finite number of samples and the floating-point arithmetic. These errors are reduced by decreasing the spatial frequency resolution at the expense of an increase in computer time.

To validate the IFT algorithms their errors were estimated by using the analytic PSF and LSF for a circular aperture (Tschunko 1978) and the LSF computed via the Edge Spread Function integrals (Fiete 2010, equations 11.11 – 11.12). F_S and N_S were selected so that the maximum IFT error was below 0.1 %.

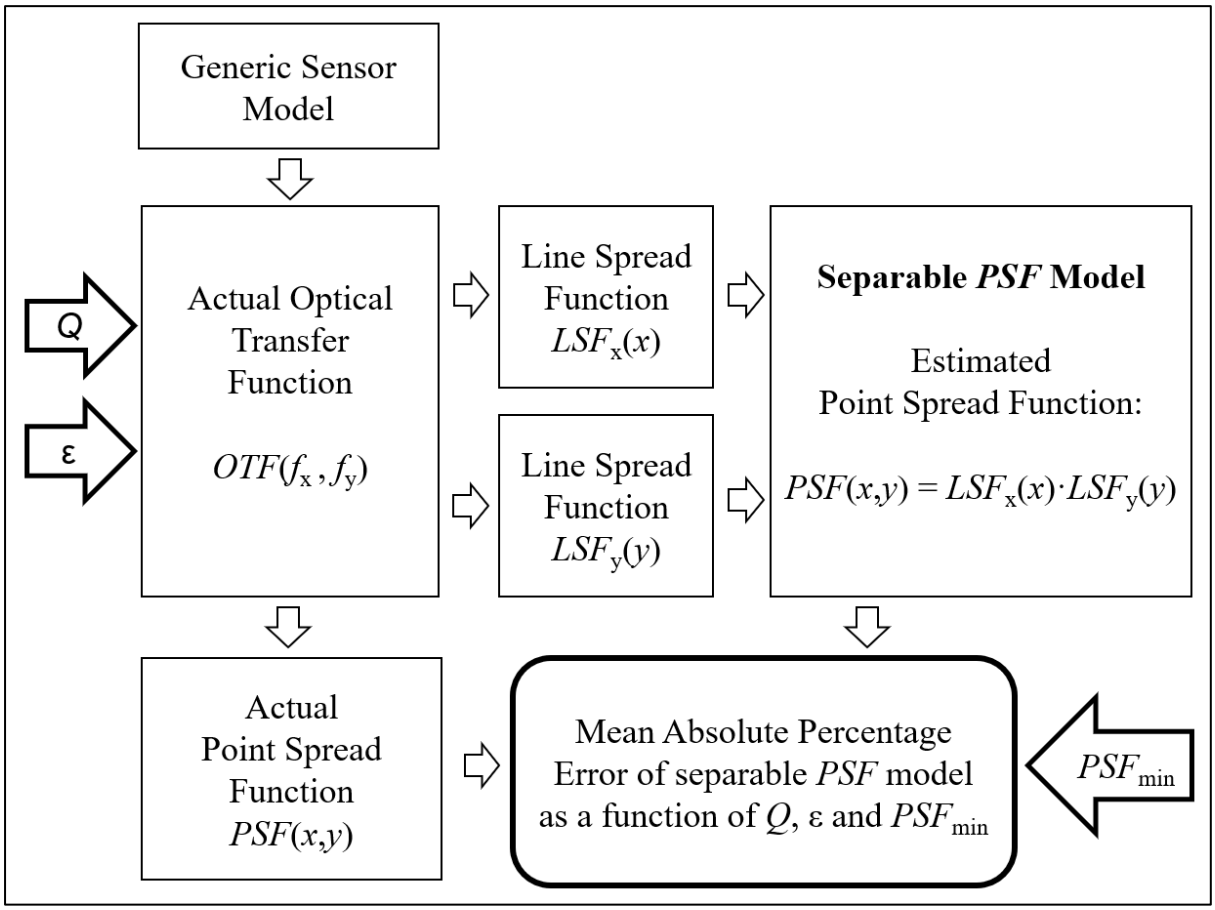

Figure 3.2: Flowchart of the procedure to assess the separable PSF model. For a given optical factor Q and obstruction ratio ε, the Point Spread Function (PSF) estimated by the model defined by equation (1) is compared with the actual PSF. The Mean Absolute Percentage Error of this model is computed considering all PSF values larger or equal than the minimum PSF level that is relevant to the application (PSF_{min}). An analogous procedure (actual versus estimated PSF or LSF) can be used to assess other spatial response models.

3.3. Results

Seven contours of constant MAPE for the separable PSF model defined by equation (1) are shown in Figure 3.3 for $PSF_{min} = 0.1$. The conclusions are: 1) errors below 1 % are obtained for $Q \leq 0.03$; 2) errors below 5 % are obtained for $Q \leq 0.16$; and 3) errors below 10 % are obtained for $Q \leq 0.35$. The maximum error in the upper right corner of the (Q, ε) plane is 64 %. The domain of validity of equation (1) is $Q \leq 0.35$.

Seven contours of constant MAPE for the separable PSF model defined by equation (1) are shown in Figure 3.4 for $PSF_{min} = 0.01$. The conclusions are: 1) errors below 10 % are obtained for $Q \leq 0.04$; and 2) errors above 40 % are obtained for $Q \geq 0.42$. The maximum error in the upper right corner of the (Q, ε) plane is 73 %. The domain of validity of equation (1) is $Q \leq 0.04$.

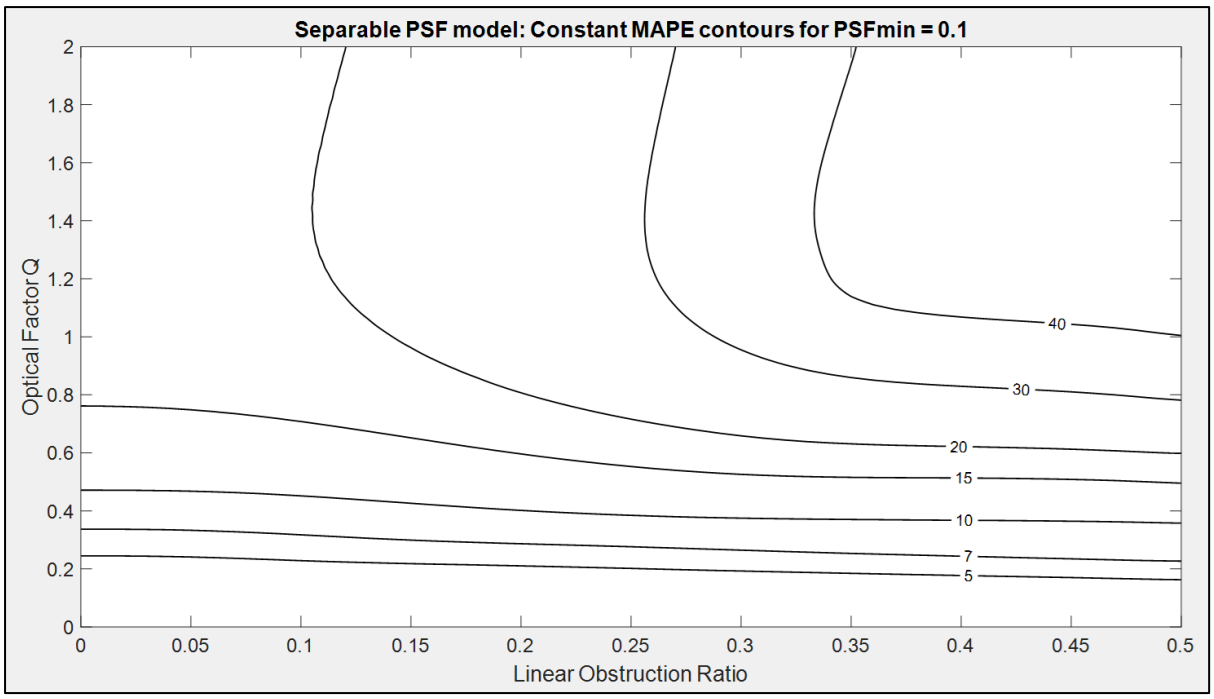

Figure 3.3: Mean Absolute Percentage Error (MAPE) of separable PSF model for PSF_{min} = 0.1. Contours of constant MAPE are drawn for the Separable Point Spread Function model in the optical factor *Q* - obstruction ratio ε plane. This model has smallest errors for smallest values of *Q* and ε, and largest errors for highest values of *Q* and ε.

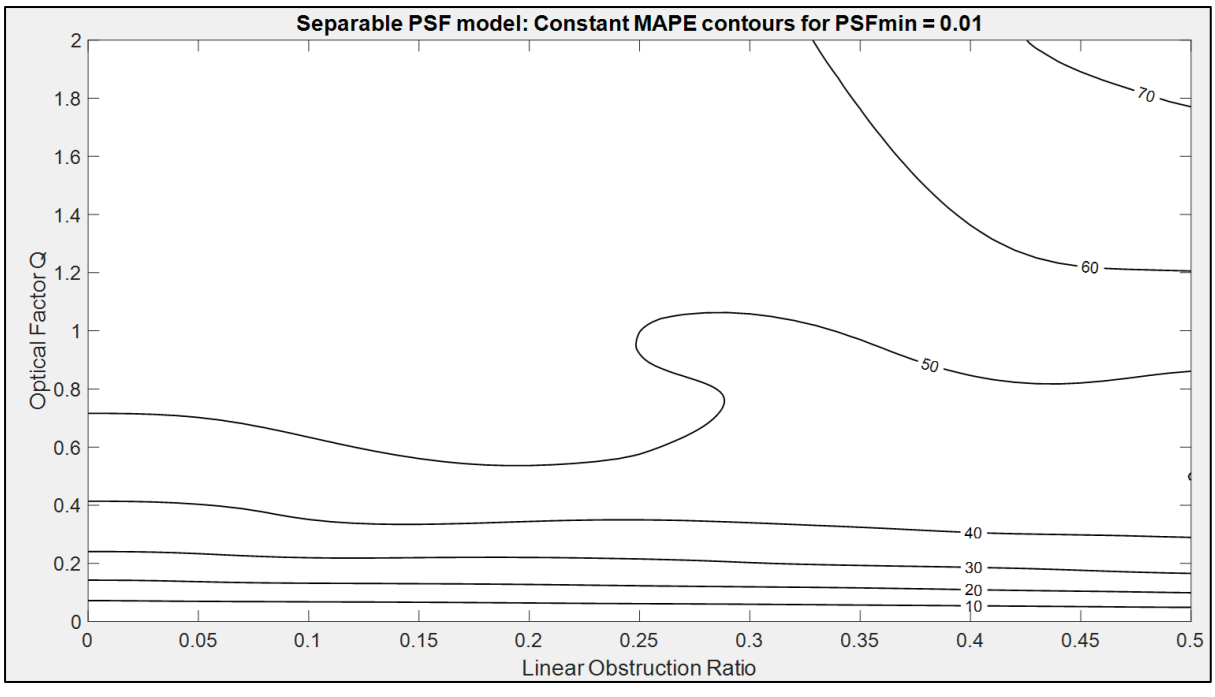

Figure 3.4: Mean Absolute Percentage Error (MAPE) of separable PSF model for PSF_{min} = 0.01. Contours of constant MAPE are drawn for the Separable Point Spread Function model in the optical factor *Q* - obstruction ratio ε plane. This model has small errors for very small values of *Q* and large errors elsewhere.

3.4. Discussion

3.4.1. Key Results

1. A new methodology to assess spatial response models.

A new methodology is proposed to assess spatial response models for satellite imagers, it is based on a generic theoretical sensor whose PSF is fully characterized by a few key optical design's parameters. The Mean Absolute Percentage Error (MAPE) of the spatial response model under assessment, is computed as a function of these key parameters for all PSF values larger or equal than a minimum PSF level of interest named PSF_{min}.

A generic sensor with square pixels and annular optical aperture was used to implement this methodology, selecting the optical factor Q and the obstruction ratio ε of the optical aperture as key design parameters. This approach allows constant MAPE contours of the model under assessment to be represented in the (Q, ε) plane.

The detection of a point source over a homogeneous background is used to estimate PSF_{min}. Minimum PSF levels at one ($PSF_{min} = 0.1$) and two ($PSF_{min} = 0.01$) orders of magnitude below the PSF's peak level were selected for assessment purposes.

2. Separable PSF model is only useful for low optical factors.

The previous methodology was applied to a generic High-Quality (small imperfections) imager with square pixels and annular optical aperture. The sensor's imperfections (optical aberrations, charge diffusion and line of sight jitter) were modelled in such a way that its PSF depends only on Q and ε.

The MAPE of the separable PSF model was computed at more than ten thousand points in the (Q, ε) plane, for minimum PSF levels at one and two orders of magnitude below peak level, yielding domains of validity (MAPE < 10 %) of $Q \leq 0.35$ and $Q \leq 0.04$ respectively. Thus, even in the best case ($PSF_{min} = 0.1$), the separable model is only useful for relatively low optical factors.

3.4.2. Interpretation of results

Equation (1) is valid if the system OTF is separable, this requires that all OTF factors are separable (Gaskill 1978, 307). Although the scan OTF is separable, the only optics and detector geometries with a separable OTF are the square and the rectangle. In our case the detector elements are square, so the detector OTF is separable, but the optical aperture is annular, so the optics OTF is non-separable. The three imperfection factors are radially symmetric, so they are non-separable, but these imperfections are small for a high-quality imager, so they have a relatively minor impact in the overall separability of the system OTF.

For a given obstruction ratio ε, the errors of equation (1) increase as the optical factor Q increases. This is to be expected, as for a low Q the system OTF is dominated by the OTF of the square detector, which has a separable OTF, whereas for a high Q the system OTF is dominated by the OTF of the annular optical aperture, which has a non-separable OTF.

For a given optical factor Q, the errors of equation (1) increase as the obstruction ratio ε increases. This is due to the fact that as ε increases, the LSF deviates further from the PSF cut at a given PSF level. This property is inherent to the annular aperture (Tschunko 1978), so it is more evident in Figures 3.3 and 3.4 for the higher optical factors in which the non-separable OTF of the optical aperture predominates over the separable OTF of the detector elements.

3.4.3. Implications of Results

1. Procedures that assess spatial response models considering a specific type of optical design are biased.

   The procedures that assess spatial response models by assuming a specific type of imager or optical design are biased because they neglect the strong dependence of the model's errors on the optical design.

2. New methodology allows different spatial response models to be assessed.

   The assessment methodology proposed in this work uses a generic imager to compare the actual spatial response with the model's estimated spatial response. The parameters of the optical design are treated as independent variables to compute the MAPE of the model as a function of these parameters. This methodology allows an assessment of different types of spatial response models for a broad domain of optical designs.

3. New methodology is conveniently applied in the (Q, ε) plane.

   The new assessment methodology was applied to a generic imager with annular optical aperture and square detector elements, selecting the optical factor Q and aperture obstruction ratio ε as key optical design parameters. This approach allows the computation of constant MAPE contours in the (Q, ε) plane, providing a convenient graphical view of the domain of applicability of the model under assessment.

4. Separable PSF model can lead to gross errors.

   The widespread usage of equation (1) can be traced to the low optical factors encountered in the early satellite imagers, for which it was a good approximation, although its inadequacy for some satellite imagers had already been noted (Ruiz and Lopez 2012, Ando and Tanaka 2019). Equation (1) is a useful PSF estimator within its domain of validity; our results quantify its poor performance for high optical factors.

   The same type of results obtained for the separable PSF model are expected for any spatial response model assessed: it will have low errors in some regions of the (Q, ε) plane and large errors in other regions.

5. Domain of validity of the separable PSF model is too small for lower PSF levels.

   When the PSF is modelled down to two orders of magnitude below its peak level, the domain of validity of the separable PSF model is reduced to $Q \leq 0.04$. For $Q > 0.04$, other types of models are required in this case to reconstruct the PSF from LSF measurements.

3.4.4. Limitations and future work

The results presented are valid for the generic sensor herein considered. Although this sensor is representative of many satellite imagers, different geometries or quality assumptions will yield different results. For example, if a Medium-Quality imager is assumed instead of a High-Quality imager (Valenzuela et al. 2022), the three non-separable OTFs that account for optical aberration, line of sight jitter, and detector's charge diffusion, will force a non-separable spatial response at lower optical factors. Thus, the domain of validity of equation (1) will be further reduced.

The generic sensor assumed in this work may be modified to represent other types of satellite imagers. For example, the following modifications, for which the respective OTF factors are known, may be easily performed: 1) partial pixel fill factors (Fiete 2010, equation 6.31); 2) square optical apertures Boreman 2021, equation 1.26); 3) non-square pixel geometries (Fliegel 2004); 4) pixel over-sampling (Fiete and Tatalo 1999); 5) time delay integration with pixel clock-phasing (Fiete 2010, equation 7.8); and 6) polychromatic radiation (Cota et al. 2010, equation 40).

3.5. Conclusion

This paper proposes a new methodology to assess spatial response models by assuming a generic sensor that allows the computation of the error of these models as a function of the key optical design parameters.

The underlying premise, supported by the literature, is that the actual shape of the PSF is critically dependent on the optical design of the imaging sensor, so any spatial response model may show low errors for some designs and high errors for others. Thus, the assessment of a spatial response model using a single optical design is biased; an unbiased assessment must account for a broad range of optical designs. This requirement is impractical with actual imagers as an almost endless variety of optical designs can be devised, but it can be addressed by considering a generic theoretical imager in which the key optical design parameters are treated as independent variables.

For a generic sensor with square pixels and annular optical aperture, the optical factor Q and the aperture obstruction ratio ε are selected as key optical design parameters. This new approach allows spatial response models to be conveniently assessed in the (Q, ε) plane.

The (Q, ε) plane approach was used to assess the popular separable PSF model defined by equation (1). This model is characterized by small errors for low optical factors, such as those employed in the early satellite imagers. The evolution of the instrument design and performance, and the advent of image processing techniques, has yielded many imagers with much higher optical factors for which equation (1) is not applicable.

Other spatial response models that can be assessed by using this same methodology include analytic PSF models, analytic LSF models, and the one-dimensional Hankel transform model.

This work advances the assessment and application of spatial response models for satellite imagers in two ways. Firstly, by proposing a general assessment methodology for spatial response models in which the parameters of the optical design take the role of

independent variables. Secondly, by defining the domain of validity of the model defined by equation (1), a popular model which is arbitrarily applied to all satellite imagers without considering its high errors outside this domain.

Chapter Four

A New Method to Estimate the Point Spread Function of Satellite Imagers from Edge Measurements*

* This chapter was originally published on 19th December 2023 and in its current version, with a volume number assigned, on 3rd January 2024 as:

Valenzuela AQ, Reinke K, Jones SD (2024a). A new method to estimate the point spread function of satellite imagers from edge measurements. *IEEE Geoscience and Remote Sensing Letters* **21**, 1-5. https://doi.org/10.1109/LGRS.2023.3344795.

4.1. Introduction

The spatial response of satellite imagers is characterized by their Point Spread Function (PSF), a two-dimensional (2D) function that describes how a single point source in the scene is represented in the image plane (Schowengerdt 2007, Chapter 3, Section 3). The PSF is usually estimated in orbit by imaging two edges in perpendicular directions, assuming that this function is separable (Bensebaa et al. 2004, Campagnolo and Montano 2014, Pahlevan et al. 2016, Radoux et al. 2016, Ando and Tanaka 2019, Stankevich 2021, Zhu et al. 2021). This work proposes a new three-edge method for those satellite sensors for which the two-edge method fails.

An edge measurement allows the derivation of the one-dimensional (1D) Line Spread Function (LSF) in a direction perpendicular to the edge (Pagnutti et al. 2010, Viallefont-Robiner et al. 2018). The Separable PSF model assumes that the PSF is equal to the product of two perpendicular LSFs:

$$\mathrm{PSF}(x,y) = \mathrm{LSF}_x(x) \cdot \mathrm{LSF}_y(y). \quad (1)$$

It has been recently shown that the Separable PSF model (1) is only applicable for $Q \leq 0.35$ in the case of a high-quality satellite sensor system (Valenzuela et al. 2023), where Q is the optical factor, a non-dimensional parameter that gauges the relative importance of the optics and the detector in the spatial response of the sensor (Fiete 2010, Chapter 8). Q is here defined for a sensor with an annular optical aperture of diameter D, detecting monochromatic radiation of wavelength λ, which is focused through a focal length F into a detector array of square pixels with pitch p:

$$Q = \frac{\lambda}{D}\,\frac{F}{p}. \quad (2)$$

Currently, the Separable PSF two-edge method is used for all types of satellite imagers, but now that its limitations have been established, the need for a new method to complement it arises. The objective of this work is to propose a new three-edge method to estimate the PSF of those satellite imagers for which the two-edge method fails. Both methods assume that the spatial response has quadrant symmetry.

Section 4.2 presents the methodology to assess the three-edge method. Section 4.3 shows the results of the application of the previous methodology. Section 44. discusses the relevance and limitations of our work.

4.2. Materials and Methods

4.2.1. Edge measurements

Edge targets are routinely used to measure the spatial response of satellite imagers (Pagnutti et al. 2010, Viallefont-Robiner et al. 2018). The popularity of this procedure has led to its continuing improvement (Roland 2015, Van den Bergh 2019, Nishi 2023).

Any straight boundary between a low brightness zone and a high brightness zone in the scene, can be used as an edge target. For satellite imagers either natural or manmade edge targets are employed. For Geostationary Orbit (GEO) imagers, usual targets are the Moon

(Wilson and Xiong 2019) and straight coastlines (Okuyama et al. 2015, 10). For Low Earth Orbit (LEO) imagers, special checkerboard targets and deployable tarps are preferred, although agricultural fields and canals have also been used (Pagnutti et al. 2010).

Figure 4.1 shows the steps to implement the edge procedure. The region of interest that contains the edge is identified and the edge's position and orientation are modelled. The edge should be at an angle with the orientation of the pixel array, so an oversampled version of the Edge Spread Function (ESF) - in a direction perpendicular to the edge - can be recovered. The Line Spread Function (LSF) is equal to the derivative of the ESF, and the one-dimensional Optical Transfer Function cut (OTF_{1D}) is equal to the inverse Fourier transform of the LSF.

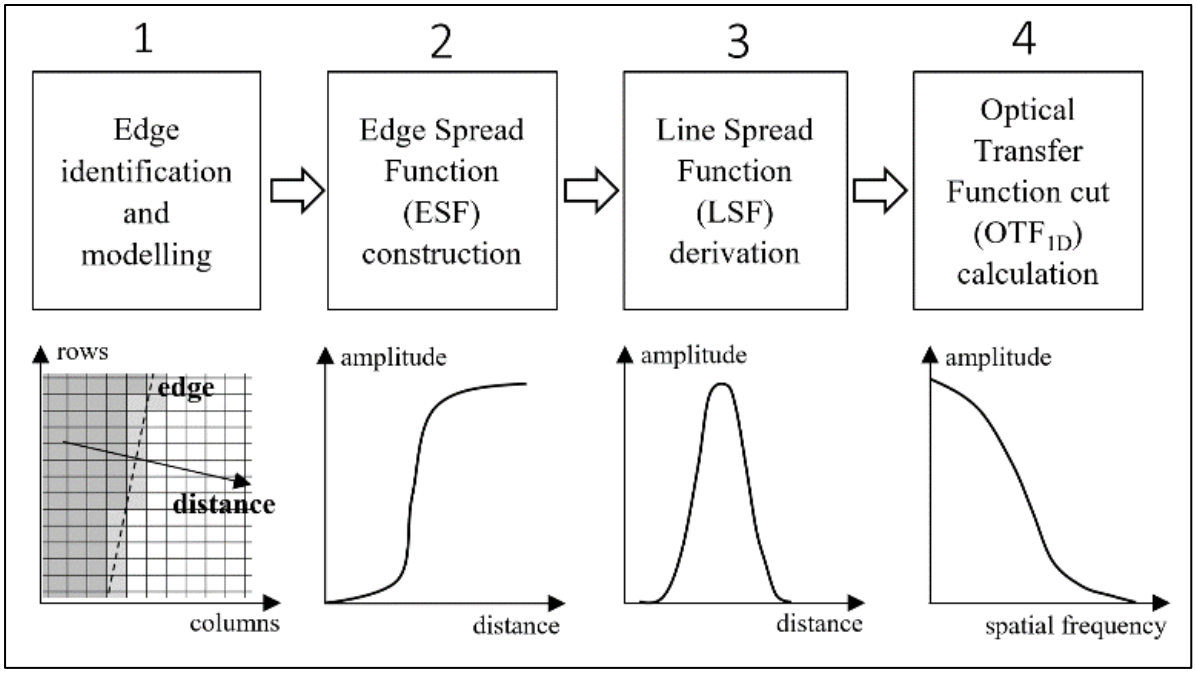

Figure 4.1: Four steps of the edge measurement procedure. Its input is an image of a straight edge, and its output is a one-dimensional cut of the Optical Transfer Function (OTF_{1D}) in a direction perpendicular to this edge. The steps are: 1) a slanted edge in the image is identified and modelled; 2) the Edge Spread Function (ESF) is found from the image pixel counts as a function of the distance to the edge; 3) the Line Spread Function (LSF) is obtained as the derivative of the ESF; and 4) the inverse Fourier transform of the LSF yields the OTF_{1D}.

Each one of these steps has its own technical problems due to aliasing and image noise, so in the pursuit of accuracy, different procedures have been developed for each one of them (Roland 2015, Van den Bergh 2019, Nishi 2023). This variety of procedures has led to conflicting results between different implementations of the edge method for satellite imagers (Viallefont-Robinet et al. 2018). The review of the different approaches to edge measurements is out of the scope of this work, for our purposes we simply assume that for each measured edge an OTF_{1D} cut is obtained as result.

Satellite imagers usually scan a narrow field of view across the scene to produce the full image. This scan can be generated by the satellite movement along its orbit as in LEO push-broom scanners, or by mechanical means as in LEO whisk-broom scanners (Schowengerdt 2007, Chapter 1) or in GEO raster scanners (Schmit et al. 2017).

The LSF and the OTF_{1D} are usually edge-measured along two perpendicular directions, Along Scan (AS) and Cross-Scan (CS), in what follows denominated *x* and *y*, respectively.

The modulus of the 2D OTF is the 2D Modulation Transfer Function (MTF) and this later term is usually employed in the satellite community instead of OTF. We use the term OTF as for satellite imagers it may take negative values (OTF < 0), so in general it cannot be replaced by the MTF.

4.2.2. Point spread function models

4.2.2.1. *Assessment procedure*

The assessment of an edge method to estimate the PSF requires knowledge of the 2D PSF and the 1D LSFs involved, but this is seldom the case for satellite imagers. Even if a sensor that satisfies this requirement was available, an edge method could only be assessed for this particular sensor. To solve this problem, a new methodology has been proposed to assess PSF models for different types of satellite imagers, using the optical design parameters of a generic sensor as independent variables (Valenzuela et al. 2023). We follow (Valenzuela et al. 2023) where *Q* and the linear obstruction ratio ε of an annular aperture (ratio between its internal and external diameters) have been selected as optical design parameters.

Figure 4.2 shows the flowchart of the method to assess a PSF model in the (*Q*, ε) plane.

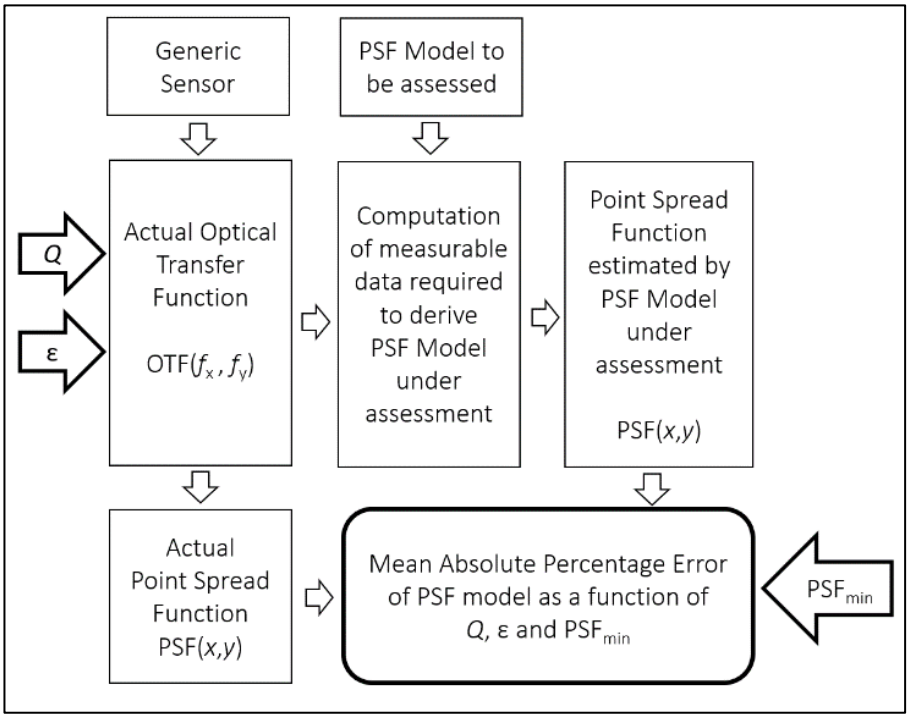

Figure 4.2: Flowchart of the procedure to assess a Point Spread Function (PSF) model. A generic sensor system is defined and used to compute the actual two-dimensional Optical Transfer Function (OTF) and the actual PSF for a given optical factor *Q* and obstruction ratio ε. The data required to build the PSF model under assessment is computed and the PSF predicted by this model is calculated as a function of *Q* and ε. The PSF predicted by the PSF model is compared with the actual PSF to compute the Mean Absolute Percentage Error (MAPE) of this model as a function of *Q* and ε. The MAPE is computed in the (*x*, *y*) plane considering all actual PSF values larger or equal than the minimum PSF level that is relevant to the application (PSF_{min}).

To assess a PSF model, a generic sensor system is defined, and the actual 2D OTF of this sensor is computed as a function of Q and ε. The actual PSF of the generic sensor is computed as the 2D inverse Fourier transform of its actual OTF. The PSF model to be assessed is defined and the measurable data required to construct this model is computed using as input the actual OTF. With this data, the PSF model is constructed and the PSF predicted by this model is computed as a function of Q and ε. Finally, the Mean Absolute Percentage Error (MAPE) of the PSF model is computed in the (x, y) plane, comparing the actual and predicted PSF for all (x, y) points where the actual PSF is larger or equal to the minimum PSF level of interest (Valenzuela et al. 2023).

We employ the same generic sensor system used to assess equation (1) (Valenzuela et al. 2023). This sensor is representative of a typical high quality satellite imager, characterized by an annular optical aperture with a linear obstruction ratio ε, square pixels with 100 % fill factor, a scan in x direction with exact sampling, a detector's charge diffusion length of Q/10 pixel and a spacecraft's induced line-of-sight jitter with a standard deviation of Q/10 pixel. Optical aberrations are modelled via Shannon's empirical OTF equation for random aberrations (Fiete 2010, equation 5-49), assuming a root mean square wavefront error of 0.1 wavelengths.

The actual and predicted PSF were computed at intervals $\delta Q = \delta\varepsilon = 0.01$ within the domain $0.01 \leq Q \leq 2$ and $0 \leq \varepsilon \leq 0.5$, totaling 10200 MAPE calculations in the (Q, ε) plane.

The domain of validity of the PSF model is defined as the region in the (Q, ε) plane where MAPE ≤ 10 %. The assessment of (1) (Valenzuela et al. 2023) shows that for the Separable PSF model this domain is roughly described by the inequality $Q \leq -0.24 \cdot \varepsilon + 0.47$, which reduces to $Q \leq 0.35$ for $\varepsilon = 0.5$.

The MAPE = 10 % value was selected as an applicability threshold considering that this figure is a mean error value and that the maximum error is usually two to five times higher than the MAPE.

4.2.2.2. *Point spread function models considered*

Table 4.1 shows the two PSF models considered in this work. The Separable PSF model requires measurements along two perpendicular edges. The new three-edge model, to be defined below, requires an additional diagonal edge measurement.

Table 4.1: Point spread function models for edge measurements.

PSF Model	Separable PSF	Quadratic Interpolation
Number of edges	2	3
Model's input data	$LSF_x(x)$ and $LSF_y(y)$	$OTF_{1D}(\rho_1)$, $OTF_{1D}(\rho_2)$ and $OTF_{1D}(\rho_3)$
Predicted PSF	Equation (1)	Equations (6) – (9)

4.2.2.3. *Quadratic Interpolation model*

A minimum number of edge measurements to estimate the PSF is desirable for satellite imagers. The Separable PSF model uses only two edges, but it fails for high Q (Valenzuela et al. 2023) so the possibility to use in this case a third edge is investigated.

The aim is to reconstruct the 2D spatial response from the three measured 1D cuts. This reconstruction must be necessarily performed in the spatial frequency domain, because for high *Q* the LSF along a given direction differs from the PSF cut in this same direction (Valenzuela et al. 2023).

Let θ be the angle in the (x, y) plane measured with respect to the x axis (AS direction). A OTF_{1D} cut is measured at a given angle θ as a function of the along-cut spatial frequency by using an edge orientated at angles θ + 90° or θ - 90°. To reconstruct the OTF from the OTF_{1D} cuts it must be considered that the pixel sampling rate depends on θ, so that each cut has a different along-cut spatial frequency (Reichenbach et al. 1991).

The OTF is a 2D function of the spatial frequencies in AS and CS directions, represented as f_x and f_y, respectively. The OTF_{1D} cuts are measured in radial direction, so to match them with the 2D OTF it is convenient to express it in polar coordinates (ρ, θ), where ρ is the along-cut spatial frequency. The conversion from rectangular to polar coordinates is well known, for our purpose the following equations are used:

$$\rho = ({f_x}^2 + {f_y}^2)^{1/2} = f_x \cdot \sec(\theta) = f_y \cdot \csc(\theta) \tag{3}$$

$$\theta = arctan(f_y/f_x). \tag{4}$$

For a given cut at an angle θ_i, the notation ρ_i represents the along-cut spatial frequency variable (not a constant radius!), computed as a function of f_x or f_y by replacing $\theta = \theta_i$ in equation (3). If three 1D cuts represented as $OTF_{1D}(\rho_1)$, $OTF_{1D}(\rho_2)$, and $OTF_{1D}(\rho_3)$ are measured at angles θ_1, θ_2, and θ_3, respectively, then the following equation must hold for i = 1, 2 and 3:

$$\mathrm{OTF}(\rho_i, \theta_i) = \mathrm{OTF}_{1\mathrm{D}}(\rho_i). \tag{5}$$

Considering that three OTF_{1D} cuts are known, we can postulate the following quadratic model for the 2D OTF:

$$\mathrm{OTF}(f_x, f_y) = \mathrm{OTF}(\rho, \theta) = A \cdot \theta^2 + B \cdot \theta + C \tag{6}$$

where *A*, *B*, *C* are three unknown two-dimensional functions, which can be found by requiring that at the three edges' angles the 2D OTF model matches the respective measured OTF_{1D} cut.

A system of three linear equations with three unknowns is obtained by replacing the right side of equation (6) in the left side of equation (5), for i = 1, 2 and 3. The straightforward solution is:

$$A(f_x, f_y) = \left(\frac{\mathrm{OTF}_{1\mathrm{D}}(\rho_1) - \mathrm{OTF}_{1\mathrm{D}}(\rho_2)}{(\theta_1 - \theta_2)(\theta_1 - \theta_3)} - \frac{\mathrm{OTF}_{1\mathrm{D}}(\rho_2) - \mathrm{OTF}_{1D}(\rho_3)}{(\theta_1 - \theta_3)(\theta_2 - \theta_3)}\right) \tag{7}$$

$$B(f_x, f_y) = \frac{\mathrm{OTF}_{1\mathrm{D}}(\rho_1) - \mathrm{OTF}_{1\mathrm{D}}(\rho_2)}{\theta_1 - \theta_2} - A(f_x, f_y) \cdot (\theta_1 + \theta_2) \tag{8}$$

$$C(f_x, f_y) = OTF_{1D}(\rho_1) - A(f_x, f_y) \cdot {\theta_1}^2 - B(f_x, f_y) \cdot \theta_1. \tag{9}$$

Once the functions *A*, *B* and *C* are found, the PSF predicted by the model is obtained as the 2D inverse Fourier transform of the right side of equation (6). In what follows we assume $\theta_1 = 0$, $\theta_2 = \pi/4$, and $\theta_3 = \pi/2$, although in practice the actual edges' angles should be considered (Van den Bergh 2019, Figure 3),

4.3. Results

Figure 4.3 shows some constant MAPE contours in the (Q, ε) plane for the Quadratic Interpolation model when it is assessed for PSF ≥ 0.1. The domain of validity (MAPE ≤ 10 %) is approximately represented by $Q \geq -0.08 \cdot \varepsilon + 0.10$.

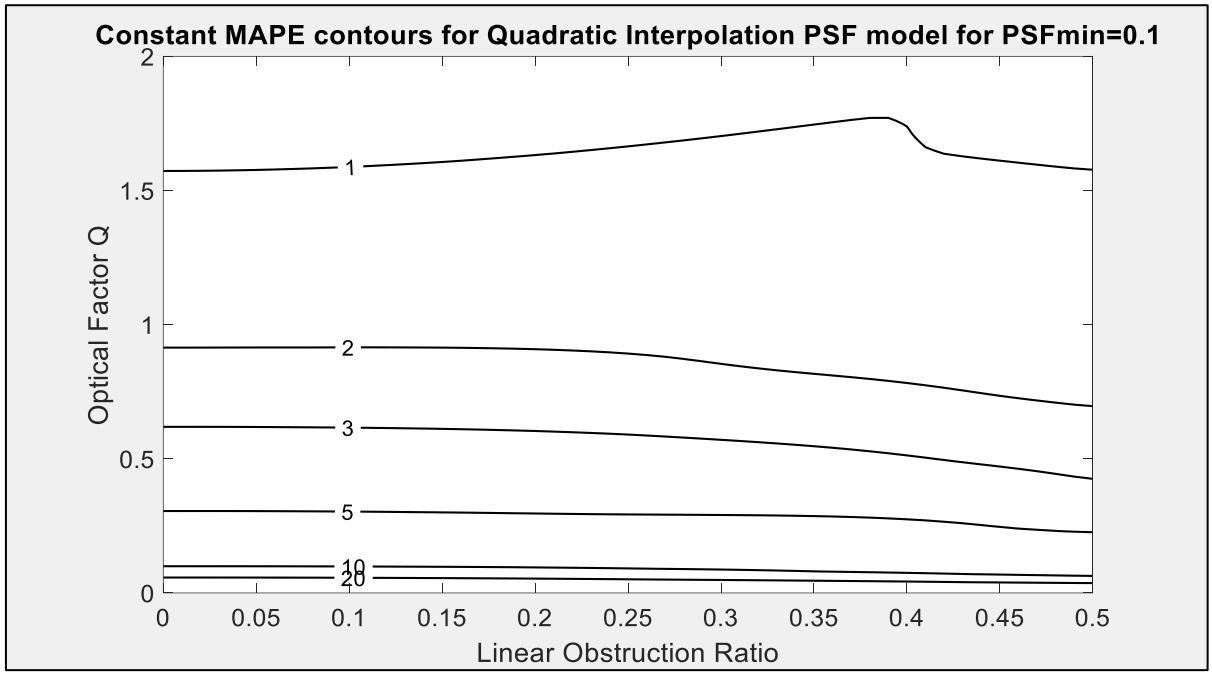

Figure 4.3: Mean Absolute Percentage Error (MAPE) of the Quadratic Interpolation Point Spread Function (PSF) model for $PSF_{min} = 0.1$. Contours of constant MAPE are drawn for the Quadratic Interpolation model in the optical factor Q - obstruction ratio ε plane, for the case of the generic sensor defined in the text. The domain where MAPE ≤ 10 % is approximately $Q \geq -0.08 \cdot \varepsilon + 0.10$.

Figure 4.4 shows some constant MAPE contours in the (Q, ε) plane for the Quadratic Interpolation model when it assessed for PSF ≥ 0.01. The domain of validity (MAPE ≤ 10 %) is approximately represented by $Q \geq -0.36 \cdot \varepsilon + 0.49$.

Table 4.2 shows the domain of validity of the two PSF models considered in this work,

For $PSF_{min} = 0.1$, both models are applicable in the domain $-0.08 \cdot \varepsilon + 0.10 \leq Q \leq -0.24 \cdot \varepsilon + 0.47$. The zone in the ($Q$, ε) plane where these two models achieve the same MAPE can be approximately represented by the equation of a straight line:

$$Q_o(\varepsilon) = -0.16 \cdot \varepsilon + 0.26 \qquad (10)$$

For a given imaging channel with known Q and ε, if $Q < Q_o(\varepsilon)$ then the model defined by equation (1) is preferable, otherwise the model defined by equation (6) is recommended. With this criterion the MAPE for $PSF_{min} = 0.1$ is less than 6 % in all the domain of interest.

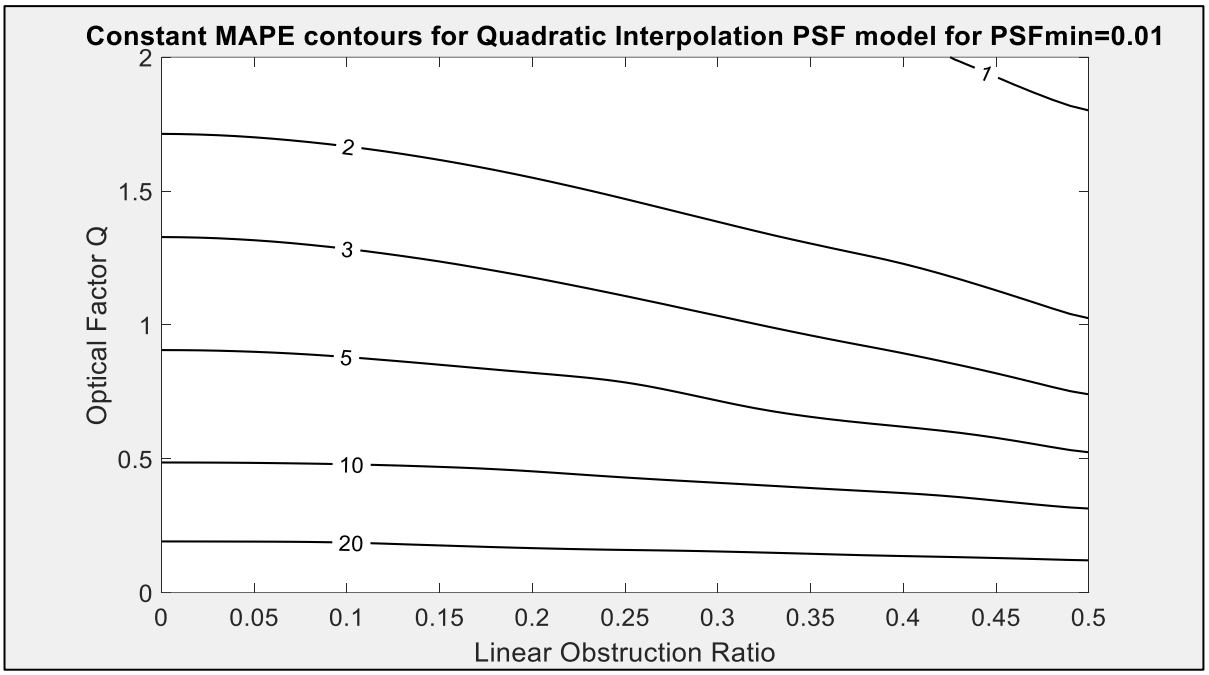

Figure 4.4: Mean Absolute Percentage Error (MAPE) of Quadratic Interpolation Point Spread Function (PSF) model for $PSF_{min} = 0.01$. Contours of constant MAPE are drawn for the Quadratic Interpolation PSF model in the optical factor Q - obstruction ratio ε plane, for the case of the generic sensor defined in the text. The domain where MAPE ≤ 10 % is approximately $Q \geq -0.36 \cdot \varepsilon + 0.49$.

Table 4.2: Domain of validity of point spread function models

PSF Model	Domain of validity (MAPE < 10 %)	
	$PSF_{min} = 0.1$	$PSF_{min} = 0.01$
Separable PSF	$Q \leq -0.24 \cdot \varepsilon + 0.47$	$Q \leq -0.04 \cdot \varepsilon + 0.07$
Quadratic Interpolation	$Q \geq -0.08 \cdot \varepsilon + 0.10$	$Q \geq -0.36 \cdot \varepsilon + 0.49$

4.4. Discussion

4.4.1. Key result

The assessment of a high-quality generic sensor system has led to the conclusion that the new three-edge Quadratic Interpolation method complements the usual two-edge Separable PSF method. This result implies that, depending on Q and the aperture obstruction ratio, two or three edges are required to estimate a PSF that displays quadrant symmetry.

Up to now, the three-edge method has not been used for satellite imagers since the two-edge method was assumed to be adequate. The use of a third edge has been proposed and used for digital cameras in a single case study, but only for the purpose of checking whether the spatial response was separable or axially symmetric (Reichenbach et al. 1991). The use of a third edge to estimate a PSF that is neither separable nor axially symmetric has not been proposed before.

With three edges, quadratic interpolation is the best option for high Q, because the constant PSF surfaces have a rounded pseudo-elliptical shape, which this later interpolation is

able to estimate with low errors, whereas linear interpolation between adjacent OTF_{1D} cuts, predicts constant PSF surfaces with a square shape, giving much larger estimation errors.

4.4.2. Interpretation of results

The new three-edge method has low errors for $Q > 1$ and high errors for $Q << 1$ because:

1. Quadratic interpolation gives perfect results for $Q \to \infty$ when the constant OTF contours take a circular shape (axially symmetric PSF and OTF). As Q decreases, the asymmetry induced by scan on these contours gets more pronounced, so the interpolation error for the OTF's main lobe increases.

2. For $Q < 1$, the OTF exhibits secondary lobes, and quadratic interpolation is not able to reconstruct the actual shape of these lobes which increase in number as Q decreases.

For a given Q, the errors of the model defined by equation (6) decrease as the obstruction ratio increases, because the constant OTF contours of the optics OTF are circles (axial symmetry), and as ε increases, the optics OTF decreases, giving a more circular shape to the constant system OTF contours.

4.4.3. Implications of results

The failure of the two-edge method for $Q > 0.5$, implies that for higher Q, at least three edges are required to reconstruct the PSF from edge measurements.

To implement the three-edge method it must be considered that the popular checkerboard targets allow only two perpendicular edges to be measured, thus, two sets of checkerboard targets orientated with a 45° difference would be required to implement this new method with this type of targets. Although the Moon's edge measurements are usually performed for only two perpendicular edges (Wilson and Xiong), the circular lunar shape allows the third diagonal edge to be readily obtained from the same image.

4.4.4. Significance of results

The use of only two-edges to reconstruct the PSF of satellite imagers is deep-rooted in the remote sensing community, because the two-edge Separable PSF model was valid for the early Landsat sensors which had $Q << 1$ (Valenzuela et al. 2023, Table I).

The generic sensor methodology allows Q to be used as an independent variable, showing that in the case of a high-quality imager with a clear aperture ($\varepsilon = 0$), at least three edges are required to estimate the PSF for $Q > 0.47$. With three edges, the new Quadratic Interpolation model achieves MAPE ≤ 10 % for $Q > 0.49$, down to two orders of magnitude below the peak response ($PSF_{min} = 0.01$), a feat that the Separable PSF model emulates for $Q < 0.07$. The current number of satellite imaging channels with $Q < 0.07$ is minimal, whereas $Q > 0.49$ is quite common (Valenzuela et al. 2023, Table I). Thus, for $PSF_{min} = 0.01$, the new three-edge model is useful for a much larger number of imaging channels than the traditional two-edge model.

The domain of applicability of edge methods depends not only on Q but also on the obstruction ratio ε of the optical aperture. A clear-cut boundary has been set in the (Q, ε) plane

to define this domain for the edge methods of Table 4.2. Thus, end users can readily select the appropriate method depending on the optical parameters of their sensors.

4.4.5. Limitations and future work

The results obtained are valid for the specific type of generic sensor considered. Although this sensor is representative of a variety of high-quality satellite imagers, different geometries or quality assumptions will yield different results (Valenzuela et al. 2022).

The quadrant symmetry assumption for the spatial response is not valid for some satellite imagers, so in this case more edges and different models will be required to reconstruct the PSF from edge measurements.

The generic sensor system model assumed in this work may be modified to represent other types of satellite imagers (Cota et al. 2010).

The same procedure used to assess the models defined by equations (1) and (6) can be employed to assess other analytic functions used in edge measurements (Li et al. 2009). If none of these functions covers the huge gap between the Separable PSF and the Quadratic Interpolation models for PSF ≥ 0.01, and if levels down to PSF ≈ 0.01 are of interest, then a new model for intermediate values of Q must be proposed.

4.5. Conclusion

A new method defined by equation (6) to estimate the Point Spread Function (PSF) of a satellite imager from three edge measurements is proposed. This method is assessed by assuming a high-quality generic sensor system with square pixels and an annular optical aperture, which generates the image by moving its line of sight in the Along Scan (AS) direction. The results are presented as contours of constant Mean Absolute Percentage Error (MAPE) in the (Q, ε) plane, where Q is the imager's optical factor and ε is the linear obstruction ratio of the optical aperture.

This new method defined by equation (6) is applicable (MAPE ≤ 10 %) for high Q so it complements the two-edge Separable PSF method (1) that is applicable for low Q. With these two methods the PSF can be estimated from edge measurements down to one order of magnitude below the peak spatial response (PSF ≥ 0.1), for any Q and obstruction ratios of interest. For PSF ≥ 0.01 a huge performance gap in the (Q, ε) plane is observed between these two methods, so further work is required to close it.

Chapter Five

A New procedure to Find the Optimum Deconvolution Kernel to Deblur Satellite Images*

* This chapter was p published on 16th October 2024 as:

Valenzuela A, Reinke K, Jones S (2024c). A new procedure to find the optimum deconvolution kernel to deblur satellite images. *International Journal of Remote Sensing* **45**(24) 9513-9537. https://doi.org/10.1080/01431161.2024.2412801

5.1. Introduction

5.1.1. Basic concept of deblurring

Deblurring is an image processing technique, also known as restoration, that attempts to reduce the undesired blur induced on the image by the different elements in the imaging chain (Gonzalez and Woods 2017). All imaging sensors are susceptible to blurring due to diffraction effects, optical aberrations, pixel sampling and pixel crosstalk. Satellite imaging sensors must deal with additional blurring induced by atmospheric transmission, line of sight scanning, spacecraft micro vibrations and image resampling, thus, specialized deblurring techniques have been developed for them (Rasti et al. 2021, Singh et al. 2022).

With the advent of deep learning techniques and the widespread availability of satellite imagery, research on deblurring has acquired an impressive momentum depicted by the number of recent publications in the subject (Rasti et al. 2021) and the plethora of restoration techniques that are currently available (Wali et al. 2023).

The key technique for image restoration is deconvolution with a kernel derived from the sensor's Point Spread Function (PSF), thus the accurate estimation of this function has become a fundamental cornerstone in the deblurring of modern satellite imagery (Llaveria et al. 2020, Ngo et al. 2021, Ji et al. 2024).

The basic idea behind restoration is that in an ideal unblurred satellite image each pixel should measure only the radiance originating from the ground area represented by this pixel, whereas in the actual blurred "raw" image a pixel also measures radiance originating from the surrounding ground areas that are represented by adjacent pixels. Thus, unblurring is a technique that attempts to reduce the adjacency effect (Huang et al. 2002).

The key objective of restoration is to process the raw image with the purpose to reduce its difference with the ideal image, but as the ideal image is not usually available, there is no unique way to assess the improvement obtained by restoration. A critical survey of image restoration metrics concluded that although numerous metrics to assess image restoration algorithms have been developed, the robustness of these metrics needs to be improved. A reason behind the wide diversity of restoration metrics, is the usual absence of an ideal reference image to gauge the effectiveness of the restoration process, so objective metrics must rely on different image databases which are scenario dependent (Hu et al. 2020).

5.1.2. Usual approach to image deblurring

The most simple and usual approach to image restoration is to assume a linear shift-invariant imaging system model. This simplified model assumes that the raw image is continuous function $\imath(x, y)$ equal to the two-dimensional convolution ($**$) between the radiance of the scene $s(x, y)$ and the Point Spread Function (PSF) $\mathrm{PSF}(x, y)$ of the imaging system, plus some additive noise $\eta(x, y)$ (Gonzalez and Woods 2017; Hu et al. 2020; Rasti et al. 2021; Wali et al. 2023):

$$\imath(x, y) = s(x, y) **(\mathrm{PSF}(x, y)) + \eta(x, y) \quad (1)$$

The imaging system PSF is named here as "sensor's PSF" for short. This is the pre-sampled PSF that is usually measured using edge targets (Viallefont-Robinet et al. 2018,

Valenzuela et al. 2024a). The sensor's PSF considers not only the image degradation due to the imperfections of the instrument (optics, detector, scanning) but also those induced by the space platform (line of sight micro vibrations) and by the transmission media (atmospheric turbulence and aerosols).

Under the shift-invariant and continuous-image assumptions, the restored image $r(x, y)$ is obtained as the two-dimensional deconvolution ($\otimes\otimes$) between the raw image and the sensor's PSF:

$$r(x, y) = \imath(x, y) \otimes\otimes (\mathrm{PSF}(x, y)) \tag{2}$$

So, in the absence of noise ($\eta(x, y) = 0$), deconvolution with the sensor's PSF allows the scene to be perfectly restored:

$$r(x, y) = \{s(x, y) ** (\mathrm{PSF}(x, y))\} \otimes\otimes (\mathrm{PSF}(x, y)) = s(x, y) \tag{3}$$

Under the shift-invariant and continuous-image assumptions, perfect deblurring is possible with a noise-free image, and the optimum deconvolution kernel is obviously the sensor's PSF, so the search for the optimum deconvolution kernel is not an issue. Thus, unblurring is usually considered a trivial exercise if noise is negligible (Scharr et al. 2021) and in some works restoration is identified exclusively with denoising instead of deblurring. In this work, the term "restoration" is used as a synonym of deblurring and so it does not consider denoising.

5.1.3. Need for an optimum deconvolution kernel

Pixel sampling is usually neglected in the deblurring of modern satellite imagery, so the continuous form of the imaging equation (1) is assumed (Llaveria et al. 2020, Ngo et al. 2021, Ji et al. 2024). This assumption implies that the optimum deconvolution kernel is the sensor's PSF.

When pixel sampling is considered, equation (1) is no longer applicable, and the image equation takes the form (Wu and Schowengerdt 1993, Valenzuela et al. 2022):

$$\boldsymbol{\imath}[n, m] = comb\{s(x, y) ** (\mathrm{PSF}(x, y)) + \eta(x, y)\} \tag{4}$$

Where $\boldsymbol{\imath}[n,m]$ is the sampled raw image, n and m are the row and column numbers of the pixel in the image plane, respectively, $s(x, y)$ is the radiance of the scene, $\mathrm{PSF}(x, y)$ is the sensor's PSF, and *comb* is the two-dimensional sampling function. The nomenclature $\boldsymbol{\imath}[n, m]$ indicates that the actual image is a matrix instead of a continuous function. The restored image $\boldsymbol{r}[n, m]$ is obtained as the two-dimensional deconvolution between the actual image $\boldsymbol{\imath}[n, m]$ and the deconvolution kernel $\boldsymbol{K}[n, m]$:

$$\boldsymbol{r}[n, m] = \boldsymbol{\imath}[n, m] \otimes\otimes \boldsymbol{K}[n, m] \tag{5}$$

Due to pixel sampling the scene cannot be perfectly restored because the image is a discrete function. To gauge the effectiveness of deconvolution kernels, the ideal noise-free unblurred image $\boldsymbol{u}[n, m]$ is defined as (Wu and Schowengerdt 1993):

$$\boldsymbol{u}[n, m] = comb\{s(x, y) ** b(x, y)\} \tag{6}$$

Where $b(x, y)$ is the box function that represents the ideal PSF which has unity value inside a pixel and zero value elsewhere. In the ideal unblurred image $\boldsymbol{u}[n, m]$, there is no adjacency effect, so the pixel's Digital Number (DN) only measures the radiance originating from the ground area represented by this pixel, whereas in the actual raw blurred image $\boldsymbol{\iota}[n, m]$ the pixel's DN also measures the radiance originating from the surrounding ground areas represented by adjacent pixels. Thus, restoration is an attempt to approximate the actual blurred image to the ideal unblurred image.

The optimum deconvolution kernel is the one that minimizes the difference between the ideal image $\boldsymbol{u}[n, m]$ and the restored image $\boldsymbol{r}[n, m]$. The usual approach is to *a priori* assume that the deconvolution kernel $\boldsymbol{K}[n, m]$ should be a matrix representation of the sensor's PSF. Huang et al. (2002) demonstrated that for a Gaussian PSF, the usual deconvolution kernel was about four times less effective than the optimum kernel that they derived using the procedure described below. Moreover, it will be shown that for the triangular PSF considered by Huang et al. (1998) the usual kernel severely degrades the raw image whereas the optimum kernel provides a significant improvement.

5.1.4. Higher Resolution Satellite Images procedure

In a series of three seminal works, an empirical procedure to find the optimum deconvolution kernels for satellite images was developed, with the purpose to reduce the errors of land cover characterization in the presence of mixed pixels. The authors computed the improvement provided by various deconvolution kernels for a satellite Sensor Of Interest (SOI) with a known PSF, using actual satellite images of much higher spatial resolution than the SOI, assuming that a mosaic of these higher resolution images was a good representation of the scene.

In the three real case scenarios considered, the satellite SOI was the Moderate Resolution Imaging Spectroradiometer (MODIS) and the higher spatial resolution sensor was the Landsat Thematic Mapper (TM). In the three applications of this Higher Resolution Satellite Images (HRSI) procedure, models of the ideal, raw, and restored image for the SOI were computed, and the improvement provided by the deconvolution kernels was then rigorously assessed by comparing the raw and restored images with the ideal image in a pixel-to-pixel basis (Huang et al. 1998, Townshend et al. 2000, Huang et al. 2002).

Blurring was quantified as the Mean Absolute Difference (MAD) between the Digital Numbers (DNs) of the ideal image and the DNs of the actual image considering all pixels. The "Improve" factor, herein named as deblurring factor Δ, was defined to measure the amount of blurring removed, that is, the percent decrease in MAD due to deconvolution (Huang et al. 2002). Perfect deblurring (Δ = 100 %) is obtained when the DNs of the restored image are equal to the DNs of the ideal image. If Δ is negative, deconvolution degrades the raw image.

In the first application of the HRSI procedure, a triangular sensor's PSF was assumed (Huang et al. 1998). An unexpected result was that for the six image bands considered, the optimum deconvolution kernel that maximized Δ was not the sensor's PSF but a shrunk version of it. It will be shown that in this case the Full Width at Half Maximum (FWHM) of the optimum deconvolution kernel is 0.80 times the FWHM of the sensor's PSF. Thus, for a triangular PSF the optimum PSF shrink factor for deblurring purposes is 0.80. With this shrink factor a deblurring factor of about Δ = 30 % was obtained (Huang et al. 1998). It will be shown

that in this case the usual unshrunk PSF kernel gives a negative deblurring factor; usual approach to image deblurring degrades the raw image.

In the second application of the HRSI procedure, a Gaussian sensor's PSF was assumed (Townshend et al. 2000). The same type of unexpected result was obtained; the optimum deconvolution kernel was a shrunk version of the Gaussian PSF. It will be shown that in this case the optimum shrink factor was 0.83. This same optimum shrink factor was obtained in 24 cases (six image bands over four widely different landscapes), so the need to explain this systematic deviation from the expected result was acknowledged; "*Explanation for this is still being sought*" (Townshend et al. 2000, 842).

In the final work of these series (Huang et al. 2002), the HRSI procedure was applied to the same Gaussian PSF considered by Townshend et al. (2000). The deblurring factor was computed as a function of a shrink factor parameter, demonstrating that the deblurring provided by the optimum shrunk PSF kernel was about four times larger than the deblurring provided by the usual (non-shrunk) PSF kernel. To explain this unexpected result, it was shown that if all the SOI's pixels represented a uniform portion of the landscape, then the un-shrunk PSF was the optimum kernel and a deblurring factor $\Delta = 100$ % was obtained. But, when the actual mixed pixels of the different landscapes of interest were considered, a shrunk version of the PSF maximized the deblurring factor which - in this case - achieved a peak value $\Delta = 54$ %.

In the three cases, the effectiveness of the deblurring procedure was assessed by computing the reduction of the error in land cover characterization due to deconvolution with the optimum kernel. This error was computed by comparing the predictions of the linear mixture model with ground truth data obtained by conducting field work at a test site used for training and validation purposes in Maryland, USA (Huang et al. 2002). The land cover characterization error was computed for the raw image model and for the deconvolved image model, in all cases a substantial reduction of this error due to deconvolution was obtained.

Table 5.1 describes the three scenarios where the HRSI procedure was applied, identifying the classes used in the linear mixture model, the different metrics used to gauge the land cover characterization error and the numerical factor by which this error was reduced due to optimum deconvolution.

In these three seminal works (Huang et al. 1998, Townshend et al. 2000, Huang et al. 2002) a large number of aerial and satellite images was employed, but not a single pair of images was published to display the improvement of deblurring. This was due to the fact that the deblurring factor computed in these works is an objective metric that directly quantifies the blur reduction on the raw image due to deconvolution, with respect to the ideal reference image. Thus, there is no need to qualitatively illustrate blur reduction (sharpness improvement) with a pair of images. In real-case scenarios the deblurring factor Δ is usually not employed because the ideal image is not available, unless the laborious HRSI procedure is implemented. To replace the lack of an ideal reference image, hundreds of metrics have been proposed to gauge the effectiveness of restoration techniques (Hu et al. 2020). There is no agreement on the preferred metrics to gauge deblurring, so each author uses a few of them and presents some pairs of images to qualitatively illustrate the reduction of deblurring (Llaveria et al. 2020, Ngo et al. 2021, Ji et al. 2024).

Table 5.1: Description of the three real case scenarios for which the optimum deconvolution kernel for MODIS images was found by using Landsat Thematic images. The reduction of land cover characterization errors due to optimum deconvolution, was computed by comparing the predictions of the linear mixture model for the different classes considered, with ground truth data obtained through field work conducted in Maryland, USA.

Case	1	2	3
Geographical location	Not specified. Presumably Maryland, USA	Maryland, USA Bolivia Egypt Canada	Maryland, USA Al Buhayrah, Egypt Santa Cruz, Bolivia Ontario, Canada
Satellite images	Landsat TM images for the six reflectance bands	Landsat TM images for the six reflectance bands	Landsat TM images (16.5 km x 16.5 km) for red and near infrared bands
MODIS PSF model	Triangular	Gaussian	Gaussian
Optimum PSF shrink factor (β) found	0.80 for all bands	0.83 for all bands	0.83 for all bands and landscapes
Maximum deblurring factor Δ for optimum PSF shrink factor	30 %	Not specified. Presumably similar to Case 3	Between 35 % and 54 % depending on band and landscape
Classes considered for linear mixture model	Water, forest, and grass	Water, forest, and herbaceous cover (grassland and crops)	Closed forest, open forest, woodland, non-forest land, land – water mix, water
Error metric used to assess land cover characterization	Average difference between mixture model prediction and actual land cover	Standard error of the estimate between mixture model prediction and actual land cover	Increase in root mean square error of mixture model prediction due to PSF effect
Reduction factor of land cover error due to optimum deblurring	1.5 (grass and water) 1.6 (forest)	2.2	3.8
Reference	Huang et al. 1998	Townshend et al. 2000	Huang et al. 2002

The HRSI procedure was successful in finding the optimum deconvolution kernel and in providing a robust metric to gauge the performance of image restoration (Deblurring factor Δ). Optimum restoration provided a significant reduction of the error in land cover estimation, reducing the error of a linear mixture model by a factor of two (Townshend et al. 2000) and the error of a support vector machine classifier by almost a factor of four (Huang et al. 2002). In spite of this success, the HRSI procedure did not found much application in the remote sensing community, presumably due to the following drawbacks:

1. It requires actual satellite images of a Higher Resolution Sensor (HRS) such that $GSD_{HRS} << GSD_{SOI}$. If $GSD_{SOI} < 1$ m, there is currently no HRS that can fulfill this requirement.

2. The HRS images should be acquired over a suitable landscape that is representative of the operational conditions envisaged for the SOI. The landscape should be heterogeneous at the scale of the SOI's pixels because the blurring or adjacency effect is unnoticeable over homogeneous scenes.

3. The GSD of the SOI should be an exact multiple of the GSD of the HRS; $GSD_{SOI} = M \cdot GSD_{HRS}$ as otherwise the procedure will be complicated by having to represent a SOI pixel by a fractional number of HRS pixels. To satisfy this restriction, Huang et al. (2002) assumed that the SOI had a GSD different from the actual one.

4. The ideal image model is not truly ideal as it is obtained by averaging a certain number of HRS pixels that have image noise and blurring.

5. The raw image model is not a perfect representation of the raw image as it is obtained by convolving the PSF with the HRS image, which has noise and blurring, and not with the actual noise-free unblurred scene.

5.1.5. Scope of this work

The key result of the three previous applications of the HRSI procedure (Huang et al. 1998, Townshend et al. 2000, Huang et al. 2002) is that the usual PSF deconvolution kernel for image deblurring is not the optimum one. This result was not assimilated in the remote sensing literature; although these three works have been cited altogether almost five hundred times, none of these citations has highlighted the fact that a shrunk version of the PSF is required to achieve maximum deblurring. This result is a fundamental property of the image formation process, so it is applicable to any type of imaging sensor, for example, in microscopy a computer program has been developed to find the optimum size of the PSF deconvolution kernel (Medyukhina and Figge. 2020).

This research was motivated by three facts: a) the optimum deconvolution kernels are much more effective than the usual kernels; b) the optimum kernels are scarcely applied in modern satellite imagery; and c) the current procedure to find the optimum kernels is seldom applied due to its drawbacks. As a main result of this research a new procedure to find the optimum deconvolution kernels was developed and validated. The objective of this work is to present the theoretical basis of the new Synthetic Edge Images (SEI) procedure and apply it to the same two PSFs considered by Huang et al. (1998, 2002), showing that the same results of the HRSI procedure are obtained.

This new SEI procedure does not have the drawbacks of the HRSI procedure, and it also allows a systematic study of the influence of different types and levels of image noise on the selection of the optimum deconvolution kernel, something that is not practical with the HSRI procedure, as a given high resolution image has a fixed type and level of noise.

The SEI procedure allows the selection of the optimum deconvolution kernel for any real case scenario in which the sensor's PSF is known, it is applicable to any type of imaging sensor and can be implemented by using different deconvolution filters. In this work the SEI procedure will be implemented using Wiener and regularized deconvolution filters and validated by showing that it yields the same optimum deconvolution kernel obtained by the HRSI procedure

in four real case scenarios, for six spectral bands, using 24 sets of Landsat TM images (Huang et al. 2002). The purpose of this research is to develop and validate the SEI procedure, its application to other real case scenarios is out of the scope of this work.

Section 5.2 describes the HRSI and SEI procedures, section 5.3 presents the results obtained by applying the SEI procedure to the cases previously studied with the HRSI procedure, and section 5.4 discusses the significance of the SEI procedure and the pathways that it opens for further research on image deconvolution.

5.2. Materials and Methods

5.2.1. Common stages and steps for both procedures

To describe and compare the HRSI and SEI procedures it is convenient to separate them into two common stages. In the first stage the data required to compute the deblurring factor Δ of the deconvolution kernel is prepared. In the second stage this data is used to find the optimum deconvolution kernel. The flowcharts for these two stages are presented in Figures 5.1 and 5.2, respectively.

5.2.1.1. *First stage*

The first stage is illustrated in Figure 5.1. This stage has the same steps for both procedures:

1. Select the Sensor Of Interest (SEI) whose images will be restored.

2. Measure or compute the sensor's PSF for the SEI. The pre-sampled sensor's PSF is obtained as the result of this step, either by measuring it (Viallefont-Robinet et al. 2018, Valenzuela et al. 2024) or by computing its Optical Transfer Function (OTF) using the cascade model approach (Fiete and Paul 2014). The preferred approach is a combination of in-ground (pre-flight) measurements, in-orbit measurements and an OTF cascade model that considers all the elements of the imaging chain.

3. Provide the images that will be required to compute the Ideal Image Model (IIM) and the Raw Image Model (RIM). In the HRSI procedure, actual satellite images must be procured, whereas in the SEI procedure, suitable edge images are defined.

4. Compute the Ideal Image Model (IIM). In both procedures several ideal images are used to measure the sensitivity of the optimum kernel to different scenes.

5. Compute the Raw Image Model (RIM). For each ideal image, a different raw image is obtained.

6. Compute the Mean Amplitude Difference (MAD) between the IIM and the RIM on a pixel-to-pixel basis, using the following equation:

$$\mathrm{MAD}_{\mathrm{RAW}} = \frac{1}{N}\sum_{i=1}^{N} |\,\mathrm{DN}_{i\,\mathrm{IIM}} - \mathrm{DN}_{i\,\mathrm{RIM}}| \tag{7}$$

Where MAD_{RAW} is the MAD between the ideal image and the raw image, N is the total number of pixels in the ideal and raw image models, i is an index between 1 and N that identifies each pixel in the ideal and raw images, $DN_{i\ IIM}$ is the Digital Number (DN) of pixel i in the ideal image, and $DN_{i\ RIM}$ is the DN of pixel i in the raw image.

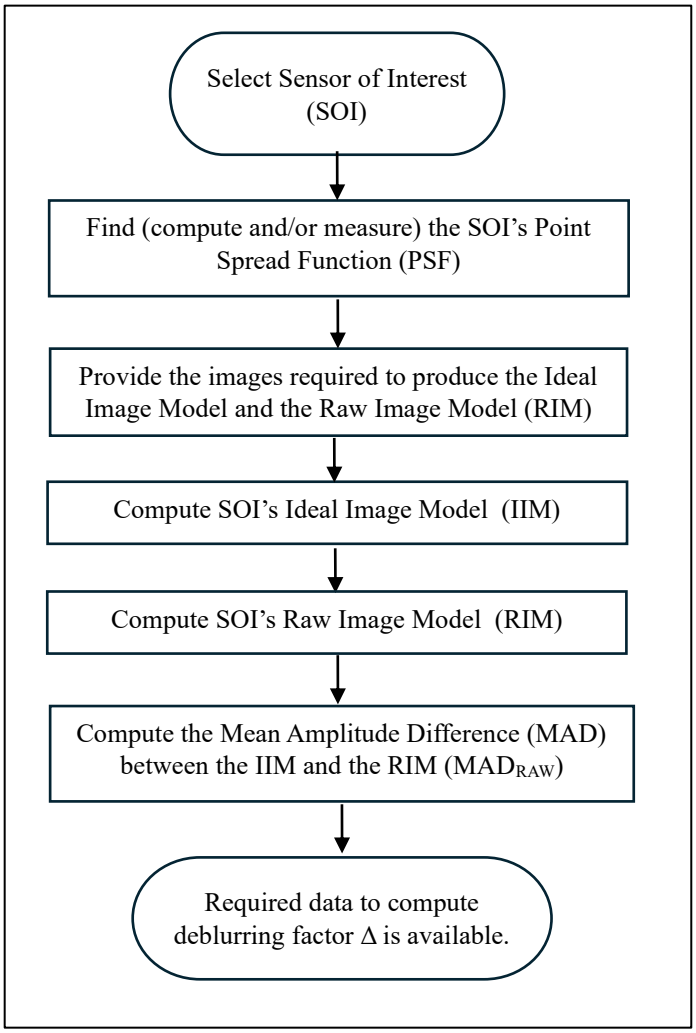

Figure 5.1: Flowchart of the first stage of the procedure to find the optimum deconvolution kernel to restore the images that will be acquired by a Sensor Of Interest (SOI). In this stage the following data required to compute the deblurring factor Δ are found: a) Pre-sampled Point Spread Function (PSF) of the SOI. b) Images required to produce the Ideal Image Model (IIM) and the Raw Image Model (RIM) of the SOI. c) Ideal Image Model of the SOI. d) Raw Image Model of the SOI. e) Mean Absolute Difference between the ideal and the raw image models (MAD_{RAW}) of the SOI.

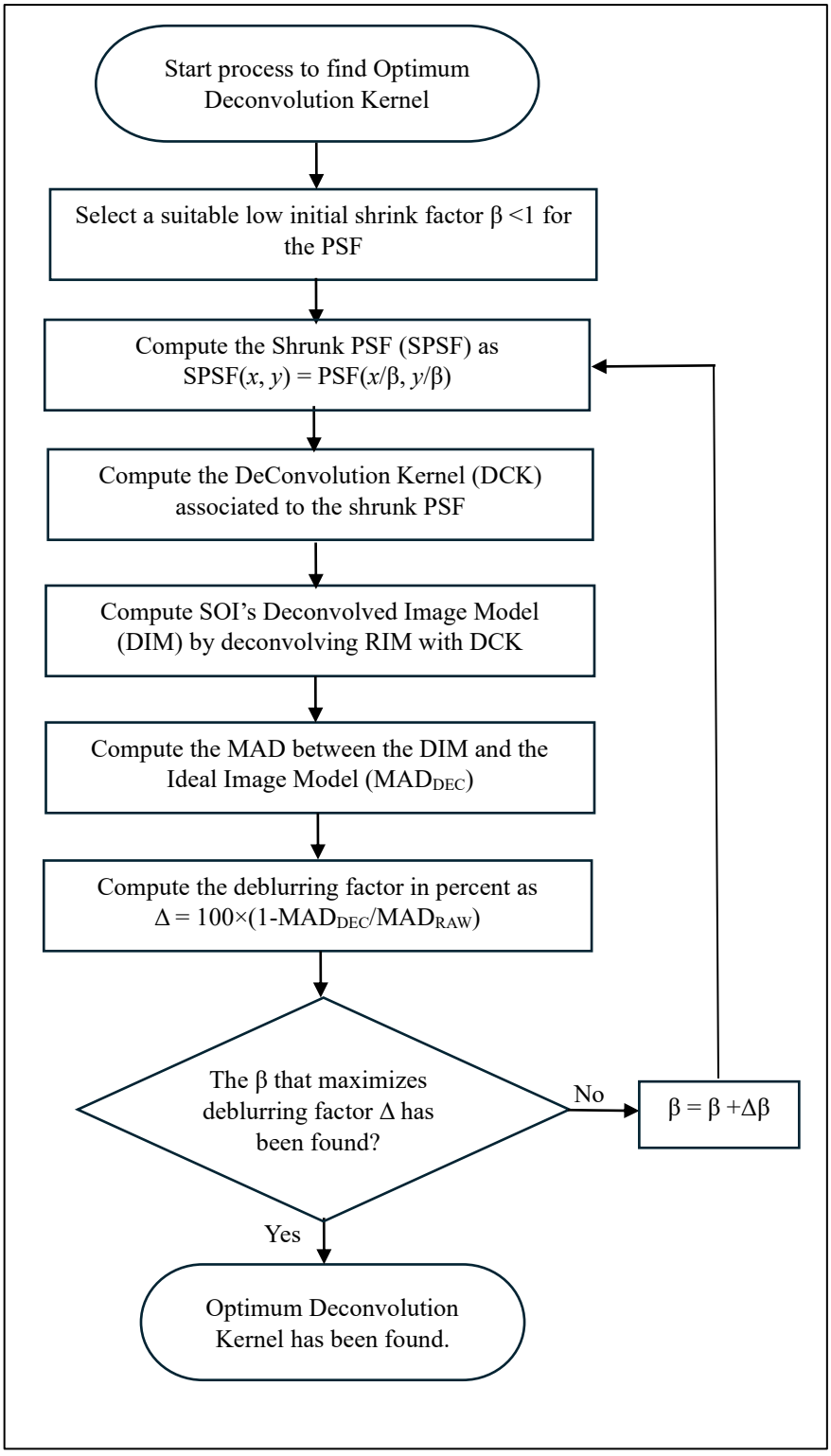

Figure 5.2: Flowchart of the second stage of the procedure to find the optimum deconvolution kernel to deblur the images that will be acquired by a Sensor Of Interest (SOI). In this stage the deblurring factor Δ is computed for different values of the PSF's shrink factor β and the shrunk deconvolution kernel ***K*** that maximizes the deblurring factor is selected as the optimum deconvolution kernel.

5.2.1.2 *Second stage*

Figure 5.2 illustrates the procedure for the second stage. This stage has the same steps for both procedures:

1. Select a suitable low value for the initial shrink factor β for the PSF. This initial value should be below the optimum β value so that the peak of the deblurring factor Δ curve versus β can be found.

   In the previous applications of the HRSI procedure the optimum shrink factor was β = 0.80 for the triangular PSF (Huang et al. 1998) and β = 0.83 for the Gaussian PSF (Huang et al. 2002). In this work an initial value β = 0.70 was used to assess the triangular PSF and an initial value β = 0.74 was used to assess the Gaussian PSF over the same range of shrink factors considered by Huang et al. (2002).

2. Compute the Shrunk PSF (SPSF) as:

$$\mathrm{SPSF}(x, y) = (\mathrm{PSF}\left(\frac{x}{\beta}, \frac{y}{\beta}\right)) \tag{8}$$

   Where β is the PSF shrink factor, that modifies by a factor β the widths of the PSF at all levels. The SPSF has the same type of shape (triangular, Gaussian, etc..) than the sensor's PSF but it is narrower if β < 1 and broader if β > 1.

3. Compute the shrunk deconvolution kernel $\boldsymbol{K}$ that is obtained with the shrunk PSF. $\boldsymbol{K}$ is a function of the shrink factor β, so for each value of β a different kernel is obtained.

   For a given PSF (un-shrunk or shrunk) there are two methods to compute the elements of the deconvolution kernel at each pixel; by point sampling the PSF at each pixel's centre (Ruiz and López 2002) or by integrating the PSF over the pixel's area (Huang et al. 1998, Huang et al. 2002). These two methods give different results, our interest is to compare the results of the HRSI procedure with those of the new SEI procedure, so we used the same analytic integrated kernels employed in the HRSI procedure; a 3×1 kernel for the triangular PSF (Huang et al. 1998), and a 3×3 kernel for the Gaussian PSF (Huang et al. 2002).

4. Obtain the Deconvolved Image Model (DIM) by deconvolving the Raw Image Model with the shrunk deconvolution kernel $\boldsymbol{K}$.

   In the application of the HRSI procedure, the authors performed deconvolution by using a computer routine to solve a sparse system of linear equations (Huang et al. 2002). For the SEI method we used the MATLAB subroutine for the classic Wiener filter.

5. Compute the Mean Amplitude Difference (MAD) between the IIM and the DIM on a pixel-to-pixel basis, using the following equation:

$$\mathrm{MAD_{DEC}} = \frac{1}{N}\sum_{i=1}^{N} |\,\mathrm{DN}_{i\ \mathrm{IIM}} - \mathrm{DN}_{i\ \mathrm{DIM}}| \tag{9}$$

Where $\mathrm{MAD_{DEC}}$ is the MAD between the ideal image and the deconvolved image, N is the total number of pixels in the ideal and deconvolved image models, i is an index between 1 and N that identifies each pixel in the ideal and deconvolved images, $\mathrm{DN}_{i\ \mathrm{IIM}}$ is the Digital Number (DN) of pixel i in the ideal image, and $\mathrm{DN}_{i\ \mathrm{DIM}}$ is the DN of pixel i in the deconvolved image.

6. Compute the deblurring factor Δ that quantifies the reduction of blur due to deconvolution, by using the following equation:

$$\Delta(\%) = 100\ \frac{\mathrm{MAD_{RAW}} - \mathrm{MAD_{DEC}}}{\mathrm{MAD_{RAW}}} \tag{10}$$

In the application of the HRSI procedure, a maximum Δ = 30 % was obtained for the triangular PSF for a single landscape (Huang et al. 1998) and maximum Δ values between 35 % and 54 % were obtained for the Gaussian PSF for the four landscapes and two spectral bands considered. The maximum deblurring factor was shown to be higher for bright images of heterogeneous landscapes and lower for dark images of homogeneous landscapes (Huang et al. 2002).

7. By examining the set of Δ values already computed as a function of the shrink factor β, decide if the range of shrink factors β considered is sufficient to find the optimum β value that maximizes the Δ factor. If the maximum value of the Δ versus β curve is evident, then the optimum kernel has been found. If the maximum value of the Δ versus β curve is not evident, then the value of β is increased by a small amount δβ.

5.2.1.3. *Relationships between shrink factor and adjacency parameter*

The procedure presented in Figure 5.2 is more general than the one used by Huang et al. (1998, 2002) because these authors did not used the concept of PSF's shrink factor, instead they computed the elements of their deconvolution kernels as analytical functions of a single numerical parameter α that represented the contribution of a pixel to its immediately adjacent pixels.

The adjacency parameter α can be expressed in terms of the shrink factor β with the following equations. For a triangular PSF as defined by Huang et al. (1998):

$$\alpha = 1 - \frac{1}{\beta} + \frac{1}{4\,\beta^2} \tag{11}$$

Where α is the adjacency parameter used by Huang et al. (1998) and β is the PSF shrink factor.

The optimum restoration kernel found by Huang et al. (1998) is α = 0.14 which according to equation (11) corresponds to a PSF shrink factor β = 0.80. For usual deconvolution with a non-shrunk PSF (β = 1), the value for the adjacency parameter is α = 0.25.

For an isotropic Gaussian PSF with a standard deviation σ as defined by Huang et al. (2002):

$$\alpha = \frac{1}{2}\left(erf\left(\frac{3\,C}{\beta}\right) \; - \; erf\left(\frac{C}{\beta}\right)\right) \tag{12}$$

Where α is the adjacency parameter used by Huang et al. (2002), *erf* is the error function, β is the PSF shrink factor, and *C* is an auxiliary variable defined as:

$$C = \frac{\mathrm{GSD_{SOI}}}{\sigma\sqrt{8}} \tag{13}$$

Where $\mathrm{GSD_{SOI}}$ is the Ground Sampling Distance of the Sensor Of Interest and σ is the standard deviation of the Gaussian function expressed in the same units as the GSD. Huang et al. (2002) considered MODIS as their Sensor Of Interest assuming $\mathrm{GSD_{SOI}}$ = 256.5 m and σ = 123.5 m, so according to equation (13), *C* = 0.734.

The optimum deconvolution kernel found by Huang et al. (2002) is α = 0.105 which according to equation (12) corresponds to a PSF shrink factor β = 0.83. For usual deconvolution with a non-shrunk PSF (β = 1), the value for the adjacency parameter is α = 0.15.

The elements of the deconvolution kernel can be written as analytic functions of an adjacency parameter α only for narrow analytical PSFs as those considered by Huang et al. (1998, 2002) in which a PSF centred in one pixel extends to no more than its eight adjacent pixels. In these cases, a 3×3 kernel in which its nine elements are function of a single adjacency parameter suffices, but in other cases, larger kernels, and more adjacency parameters to define their elements are required.

For example, if a narrow bivariate Gaussian PSF that extends to eight adjacent pixels is considered as restoration kernel (Morales-Irizarry and Vélez-Reyes 2009), then two adjacency parameters are required to define the deconvolution kernel: one for the along scan direction and other for the across scan direction. If a broader isotropic Gaussian PSF that extends to 24 adjacent pixels is considered, then at least two adjacency parameters are required to define the deconvolution kernel: one for the eight immediately adjacent pixels and other for the remaining 16 pixels.

In all possible cases, the elements of the deconvolution kernel can be numerically computed as a function of a single parameter, the shrink factor β, whereas in only very restricted cases it can be computed as function of the single parameter α used by Huang et al. (1998, 2002).

In their application of the HRSI procedure Huang et al. (1998, 2002) did not compute the shrunk PSF as the deconvolution kernel could be directly computed as a function of α. To compare the results of the HRSI procedure with those of the SEI procedure, we used the same increments of the adjacency parameter α used by Huang et al. (2002): δα = 0.005. To express the increment δβ in terms of δα, equations (11) and (12) are linearized in the range $0.7 \leq \beta \leq 1$, obtaining a coefficient of determination $R^2 > 0.999$ in both cases. For the triangular PSF an approximate linear expression is:

$$\alpha = 0.56\,\beta - 0.31 \tag{14}$$

An approximate linear expression for the Gaussian PSF is:

$$\alpha = 0.27\,\beta - 0.12 \tag{15}$$

Using these last two equations for $\delta\alpha = 0.005$, we compute $\delta\beta = 0.005/0.56 = 0.009$ for the triangular PSF and $\delta\beta = 0.005/0.27 = 0.019$ for the Gaussian PSF.

5.2.2. Higher Resolution Satellite Images procedure

In its most detailed application, the Higher Resolution Satellite Images (HRSI) procedure was implemented for the Moderate Resolution Imaging Spectroradiometer (MODIS) as the Sensor Of Interest (GSD = 250 m) using Landsat Thematic Mapper (TM) images (GSD = 28.5 m) as the Higher Resolution Sensor (Huang et al. 2002).

MODIS images were assumed to have a GSD = 9×28.5 = 256.5 m, so that exactly 9×9 = 81 TM pixels were aggregated to represent a single MODIS pixel (Huang et al. 2002). The DNs for MODIS' Ideal Image Model (IIM) were obtained by averaging the 81 corresponding DNs of the TM image. The authors acknowledged that this IIM is not truly ideal as the TM images have blurring.

MODIS's Raw Image Model (RIM) was obtained by convolving the original (non-shrunk) Gaussian PSF with the IIM. MODIS's Deconvolved Image Model (DIM) was obtained by deconvolving the RIM with the 3×3 deconvolution kernel obtained with a shrunk version of the original Gaussian PSF, varying the adjacency parameter α between 0.08 and 0.15 at intervals $\delta\alpha = 0.005$. For each value of the adjacency parameter the deblurring factor Δ was computed using equation (10).

The previous procedure was applied for the red and near infrared bands of MODIS, using TM images acquired over four different landscapes in Egypt, Maryland (USA), Bolivia and Canada. In the eight cases considered (two bands and four landscapes) the optimum adjacency parameter was in the range $\alpha = 0.105 \pm 0.005$.

Although the HRSI procedure resembles the case of image fusion, it does not fuse the TM images with MODIS images; actual TM images are used to create a model of MODIS images. Thus, actual MODIS images are not used in this procedure.

5.2.3. Synthetic Edge Images procedure

Considering that the three applications of the HRSI procedure have shown that for a given PSF the optimum deconvolution kernel does not depend on the band or the landscape, it can be assumed that this optimum kernel can also be obtained by using synthetic images which contain a variety of mixed pixels. In what follows, image noise is assumed to be negligible, although the procedure easily allows different types of noise models and levels to be considered.

For a given PSF and scene, the construction of the raw image requires an intensive computational effort (Van den Bergh 2012). A notable exception is when the scene is a straight edge that separates a dark zone from a bright zone, as in this case the DN at each pixel can be directly computed by using the Edge Spread Function (ESF). In the edge measurement method, the given raw image of a straight edge, tilted a small angle with respect to the grid of the detector array, is used to derive the unknown ESF (Viallefont-Robinet et al. 2018). In the Synthetic Edge Images (SEI) procedure, a given ESF is used to produce the unknown raw image of a scene with a straight edge.

By tilting the edge, a small angle with respect to the detecting grid, mixed pixels of different grey levels are obtained, this allows the deconvolution kernel to be tested against a variety of mixed pixels. By making the slope of the edge angle a natural number *P,* the image is periodic with a period of *P* rows, this allows only the central region of the image to be used for kernel assessment purposes, avoiding the need to consider approximations at the image borders. Figure 5.3 shows the scene for an edge angle with a slope $P = 11$.

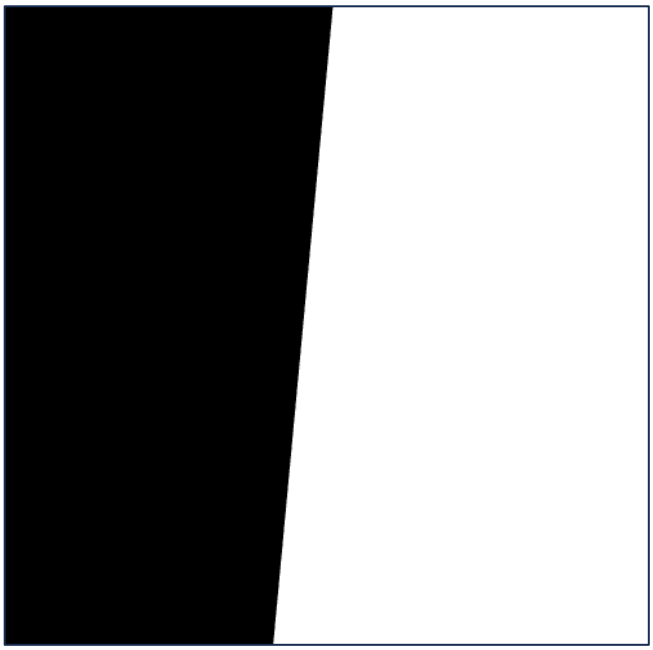

Figure 5.3: Example of a scene assumed by the Synthetic Edge Image procedure, for the case that the slope of the edge is an integer number $P = 11$. The straight edge separates a dark zone from a bright zone.

Several scenes with different values of *P* are used to consider a wider variety of mixed pixels, and the final result is obtained as the average of all the computed results. In our case five scenes with slopes and periods $P = 9, 11, 13, 15$ and 17 were considered. Odd values of *P* were used to place the central pixel of the central region at the centre of the image.

5.2.3.1. *Ideal image model*

The DNs of the ideal image are computed using the following equation:

$$\mathrm{DN_{IIM}} = B\ \varepsilon + D\ (1 - \varepsilon) \qquad (16)$$

Where $\mathrm{DN_{IIM}}$ is the Digital Number of a pixel in the ideal image model, *B* is the DN of a pure ideal pixel that represents only the bright zone, *D* is the DN of a pure ideal pixel that represents only the dark zone, and ε is the fraction of the pixel's area that is in the bright zone.

In our case square images with 61×61 pixels were considered. The left panel of Figure 5.4 shows the central part of the ideal image obtained for the scene of Figure 5.3.

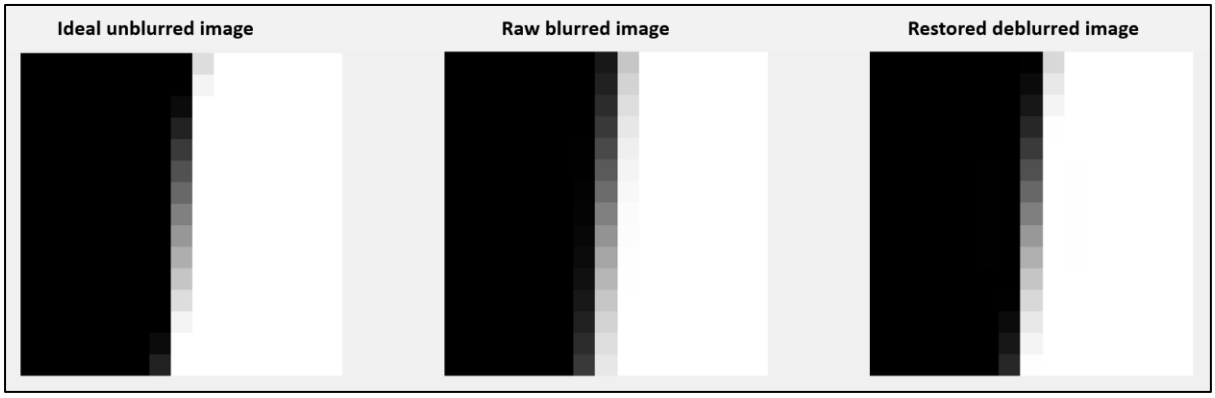

Figure 5.4: Images obtained by applying the Synthetic Edge Image procedure to the example scene depicted in Figure 5.3. The left panel shows the ideal unblurred image computed by equation (16). The centre panel shows the raw blurred image computed by equations (17) and (20). The right panel shows the restored deblurred image computed by deconvolving the raw image with the kernel defined by equation (22) for the case of optimum restoration (α = 0.105).

5.2.3.2. *Raw image model*

Assuming that the scene is a straight edge that separates a dark zone at the left of the edge from a bright zone at the right of the edge, the DNs of the raw image are exactly computed by using the following equation:

$$\mathrm{DN_{RIM}} = (B - D)\ \mathrm{ESF}(d) + D \qquad (17)$$

Where $\mathrm{DN_{RIM}}$ is the Digital Number of a pixel in the raw image model, *B* is the DN of a pure ideal pixel that represents only the bright zone, *D* is the DN of a pure ideal pixel that represents only the dark zone, ESF is the Edge Spread Function computed for the given edge angle, and *d* is the distance from the pixel centre to the edge. The distance *d* is measured positive to the right of the edge and negative to the left of the edge.

The ESF equals 0 at a large distance at the left of the edge ($\mathrm{ESF}(d \rightarrow -\infty) = 0$) and equals 1 at a large distance at the right of the edge ($\mathrm{ESF}(d \rightarrow +\infty) = 1$), so the DN of the raw image goes from *D* to *B* as the distance *d* goes from $-\infty$ to $+\infty$.

The two PSFs considered by Huang et al. (1998, 2002) are separable, so they can be written in the form:

$$\mathrm{PSF}(x,y) = \left((\mathrm{LSF})_x(x)\right)\left((\mathrm{LSF})_y(y)\right) \tag{18}$$

Where PSF(x, y) is a separable Point Spread Function, x and y are the spatial coordinates in two orthogonal directions, $\mathrm{LSF}_x(x)$ is the Line Spread Function (LSF) in x direction, and $\mathrm{LSF}_y(y)$ is the LSF in y direction. The LSF is the derivative of the ESF, so the ESF in a direction of interest is readily obtained by integrating the LSF in this same direction (Schowengerdt 2007, equation 3-22). For the triangular PSF the result is:

$$\mathrm{ESF}(d) = \begin{pmatrix} 0 & d < -\mathrm{GSD} \\ ½ + d + ½d^2 & -\mathrm{GSD} \le d < 0 \\ ½ + d - ½d^2 & 0 \le d < \mathrm{GSD} \\ 1 & d \ge \mathrm{GSD} \end{pmatrix} \tag{19}$$

Where ESF is the Edge Spread Function for a triangular PSF in the scan direction, d is the distance to the edge and GSD is the Ground Sampling Distance of the Sensor Of Interest. The triangular PSF is anisotropic, it has a triangular LSF in the scan direction and a perfect rectangular LSF in cross scan direction. For this type of PSF there is blurring only in scan direction, so the synthetic edge is assumed to be almost perpendicular to this later direction.

For the Gaussian PSF:

$$\mathrm{ESF}(d) = ½\left[1 + erf\left(\frac{d}{\sqrt{2}\,\sigma}\right)\right] \tag{20}$$

Where ESF is the Edge Spread Function for a Gaussian PSF, *erf* is the error function, d is the distance to the edge and σ is the standard deviation of the Gaussian function. The Gaussian PSF assumed by Huang et al. (2002) is isotropic, so in this case the orientation of the edge is irrelevant.

The centre panel of Figure 5.4 shows the central part of the raw blurred image computed for the scene of Figure 5.3 by using equations (17) and (20). The blurring due to the Gaussian PSF is evident by comparing the raw blurred image with the ideal unblurred image. For example, in the ideal image, the upper section of the column that separates the dark zone from the bright zone has only two pixels with different shades of grey, whereas in the raw image seven grey pixels are observed in this same section.

5.2.3.3. *Deconvolved image model*

For validation purposes, the same deconvolution kernels employed for the HRSI procedure were used to implement the SEI procedure.

For the triangular PSF (Huang et al. 1998):

$$\boldsymbol{K}(\alpha) = [½\alpha \quad 1-\alpha \quad ½\alpha] \tag{21}$$

For the Gaussian PSF (Huang et al. 2002):

$$\boldsymbol{K}(\alpha) = \begin{bmatrix} \alpha^2 & \alpha(1-2\alpha) & \alpha^2 \\ \alpha(1-2\alpha) & (1-2\alpha)^2 & \alpha(1-2\alpha) \\ \alpha^2 & \alpha(1-2\alpha) & \alpha^2 \end{bmatrix} \quad (22)$$

The deconvolved images were obtained by performing a deconvolution between the raw images and the shrunk deconvolution kernels. The deconvolution was implemented in MATLAB using the classic Wiener filter function.

The right panel of Figure 5.4 shows the central part of the deconvolved deblurred image computed for the scene of Figure 5.3, by using the optimum kernel defined by equation (22) with $\alpha = 0.105$, to deconvolve the raw blurred image presented in the centre panel of Figure 5.4. The deblurring of the raw image due to deconvolution is evident in Figure 5.4 by comparing the deconvolved and raw images with the ideal unblurred image. For example, in the deconvolved deburred image, the upper section of the column that separates the dark zone from the bright zone, has three pixels with different shades of grey, whereas in the raw blurred image seven grey pixels are observed in this same section. Deconvolution reduces from seven to three the grey pixels, giving a better approximation to the ideal unblurred image which has only two grey pixels in this same section.

5.2.3.4. *Deblurring factor computation*

If the scene is completely uniform or homogeneous, there is no difference between the ideal, raw and deconvolved images ($MAD_{RAW} = MAD_{DEC} = 0$) so no deblurring can be obtained by restoring the image.

If the scene contains homogeneous and heterogeneous landscapes, the deblurring factor Δ will diminish as the ratio of homogeneous to heterogeneous area increases, because in homogeneous landscapes deblurring is ineffective. The variation of the maximum deblurring factor with the type of landscape was observed by Huang et al. (2002); the maximum Δ fluctuated between 35 % and 54 %, as expected, the lowest values were obtained for the more uniform landscapes (Huang et al. 2002, page 211). Regardless of the maximum Δ obtained, for the four types of landscapes considered, the optimum values of the adjacency parameter for both spectral bands were $\alpha = 0.105 \pm 0.005$.

To compute Δ in the Synthetic Edge Images procedure, only raw image pixels with a DN that differs more than 1 % from the DN of the ideal image pixel, are considered. This restriction allows the pixels in the homogeneous areas far from the edge to be discarded in the computation of Δ, obtaining maximum deblurring factors similar to those obtained by Huang et al. (1998, 2002) in heterogeneous landscapes. If a higher difference between raw and ideal pixels is considered (for example 10 %), the maximum Δ increases. If a lower difference is considered (for example 0.1 %), the maximum Δ factor decreases.

The prediction of the maximum value of the deblurring factor is not relevant as in practice this value will depend on the heterogeneity of the landscape. Our objective is to predict the optimum PSF's shrink factor that allows the deblurring factor to be maximized.

5.3. Results

Figures 5.5 and 5.6 show the results predicted by the SEI procedure when it is applied to the same cases considered by Huang et al. (1998, 2002), triangular and Gaussian PSFs, respectively. In both figures, the deblurring factor Δ has been computed as a function of the adjacency parameter α, in the domain shown on the horizontal axes at intervals δα = 0.005. The blue curves represent the average of Δ obtained by the SEI procedure using five image periods (P = 9, 11, 13, 15 and 17). The minimum and maximum values computed for the deblurring factors are shown as dashed and dotted curves, respectively. The results obtained by the HRSI procedure are shown as red dots.

These results were obtained by using the MATLAB *deconvwnr* subroutine that implements the Wiener deconvolution filter. Essentially the same results were employed by using the MATLAB *deconvreg* subroutine that implements the regularized deconvolution filter. For example, for the case P = 11, the average absolute difference in the Δ values predicted by the Wiener and regularized filters is 0.14 percentage points.

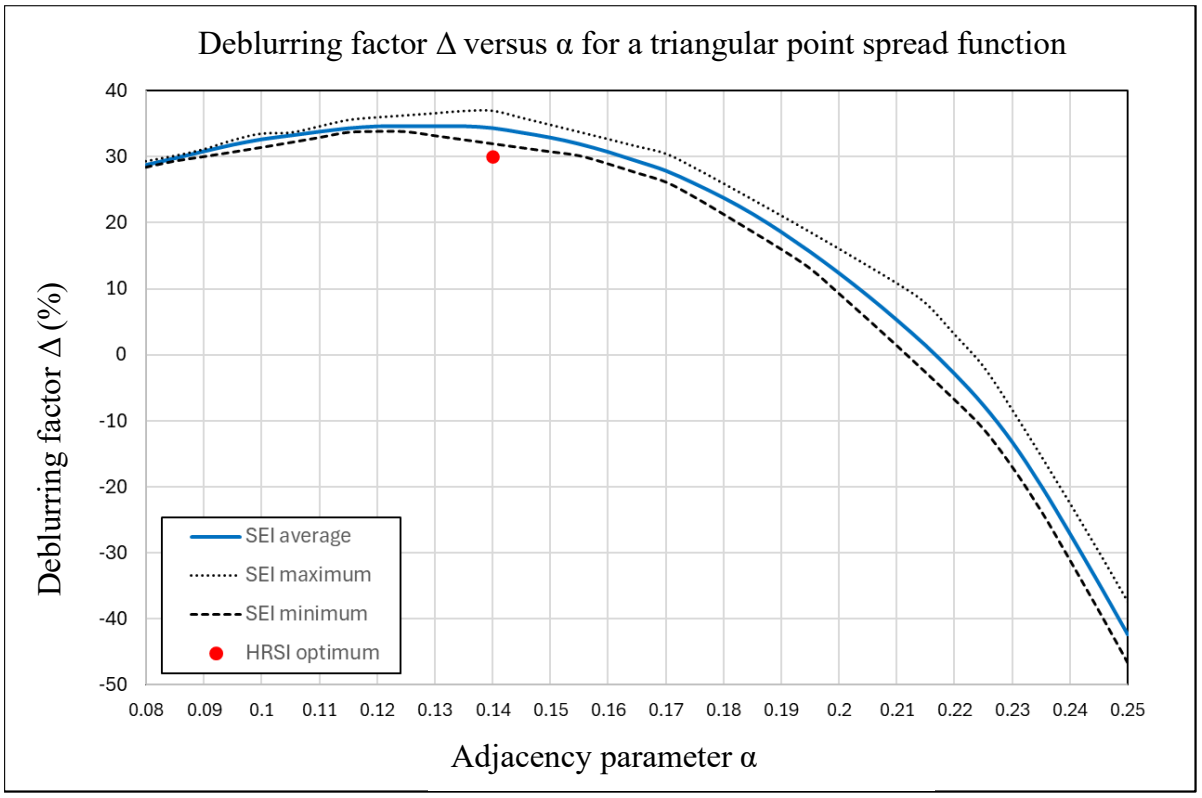

Figure 5.5: The deblurring factor Δ computed for a triangular PSF using the Synthetic Edge Images (SEI) procedure is plotted against the adjacency parameter α defined by Huang et al. (1998). The figure shows as a blue curve the average of five computations considering edges with slopes 9, 11, 13, 15 and 17. The maximum and minimum values of the deblurring factor Δ computed with these five slopes, are shown as dotted and dashed curves, respectively. The value of the maximum deblurring factor Δ and the optimum adjacency parameter obtained by Huang et al. (1998) with the Higher Resolution Satellite Images (HRSI) procedure is depicted as a red dot. The optimum adjacency parameter α predicted by the SEI procedure is in the domain 0.12 to 0.14, showing very good agreement with the optimum value α = 0.14 obtained by the HRSI procedure for six Landsat TM spectral bands.

Figure 5.5 shows the results for the triangular PSF. The optimum adjacency parameter predicted by the SEI procedure for the five image periods is within the domain $\alpha = 0.13 \pm 0.1$, showing very good agreement with the optimum value $\alpha = 0.14$ obtained with the HRSI procedure for the six MODIS' model images produced by using the respective Landsat TM images captured over six spectral bands (Huang et al.1998). A striking result is the extremely negative performance, about -40 %, predicted for the usual deconvolution procedure which assumes $\alpha = 0.25$.

Figure 5.6 shows the results for the Gaussian PSF. The optimum adjacency parameter predicted by the SEI procedure for the five image periods considered is in the range $\alpha = 0.105 \pm 0.005$, showing excellent agreement with the optimum values found with the HRSI procedure for the red and NIR Landsat TM images captured over four different landscapes. The red dots represent the deblurring factor values obtained for a landscape in Egypt using the red band images, these values are almost identical to the ones obtained for this same landscape using the NIR band (Huang et al. 2002, figure 3). The shape of the deblurring factor Δ versus adjacency parameter curve is very similar for both procedures.

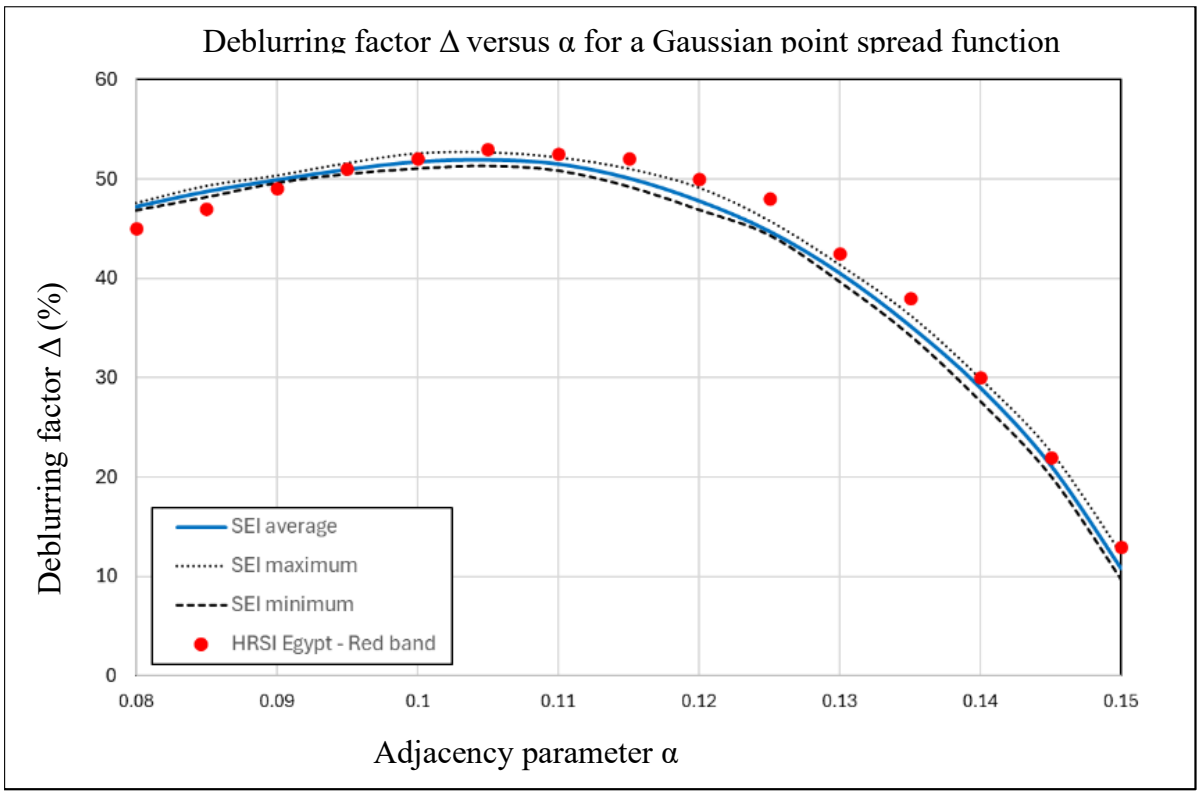

Figure 5.6: The deblurring factor Δ computed for a Gaussian PSF using the Synthetic Edge Images (SEI) procedure is plotted against the adjacency parameter α defined by Huang et al. (2002). The figure shows as a blue curve the average of five computations considering edges with slopes 9, 11, 13, 15 and 17. The maximum and minimum values of the deblurring factor Δ computed with these five slopes, are shown as dotted and dashed curves, respectively. The values of the deblurring factor Δ versus the adjacency parameter α obtained by Huang et al. (2002, figure 3.a) with the Higher Resolution Satellite Images (HRSI) procedure, for a red band image of a landscape in Egypt, are depicted as red dots. The optimum adjacency parameter α predicted by the SEI is in the domain 0.10 to 0.11, showing excellent agreement with the optimum values $\alpha = 0.105 \pm 0.005$ obtained with the HRSI procedure, for the red and near infrared bands images over four landscapes (Huang et al., 2002, figure 3).

Table 5.2 shows the increase in the average deblurring factor predicted by the SEI procedure due to the use of the optimum deconvolution kernel based on a shrunk PSF, instead of using the customary deconvolution kernel based on an unshrunk PSF.

Table 5. 2: Improvement in deblurring performance due to optimum kernel. Increase in average deblurring factor Δ according to the Synthetic Edge Images procedure implemented with Wiener filtering deconvolution, due to the use of the optimum shrunk PSF kernel as compared with the usual unshrunk PSF kernel.

Type of point spread function	Triangular	Gaussian
Average deblurring factor Δ with usual kernel (%)	- 42	11
Average deblurring factor Δ with optimum kernel (%)	34	52
Increase in average deblurring (percentage points)	76	41

5.4. Discussion

5.4.1. Key result

If the usual equation (1), that assumes a continuous image function, is used to describe the imaging process, the optimum deconvolution kernel is the sensor's PSF, and the deblurred noise-free image is equal to the scene. This noise-free image is obviously the ideal image, deblurring is a trivial exercise and so restoration focuses exclusively on denoising.

When the actual sampling occurring in the pixels of digital images is considered, equation (1) must be replaced by equation (4). The replacement of the ideal continuous image by the actual discrete image implies that the noise-free image is not equal to the scene. Moreover, the definition of an ideal noise-free unblurred image via equation (6) must be considered and it is by no means trivial which deconvolution kernel must be used in equation (5) to minimize the difference between the deblurred image and the ideal image. Thus, the quest for an optimum deconvolution kernel naturally arises.

In a series of works a procedure, herein named as the Higher Resolution Satellite Images (HRSI) procedure, was implemented to find the optimum deconvolution kernel for satellite images. A systematic and unexpected result was that, independently of the spectral band and landscape, the optimum restoration kernel was a shrunk version of the Point Spread Function (PSF) of the Sensor Of Interest (SOI) and not the original (non-shrunk) PSF as it usually assumed nowadays in the deconvolution of modern satellite imagery (Llaveria et al. 2020, Ngo et al. 2021, Ji et al. 2024).

The previous HRSI procedure has a series of drawbacks and limitations, so a new procedure using Synthetic Edge Images (SEI) was developed to replace it. The key result of this work is that the SEI procedure has been validated by showing that it predicts the same optimum deconvolution kernels of the HRSI procedure, with less effort and higher accuracy and versatility.

5.4.2. Interpretation of result

As shown by Huang et al. (2002, figure 4) the original PSF is the optimum deconvolution kernel when each pixel represents a uniform area, but when the mixed pixels of real-life satellite imagery are considered, the optimum kernel is a shrunk version of the original PSF. The optimum shrink factor depends on the shape of the PSF, so it must be found in a case-to-case basis.

The fact that the HRSI and the SEI procedures predict the same optimum restoration kernel for a given PSF can be explained by considering that both procedures have exactly the same flowchart, as shown in Figures 5.1 and 5.2, and that they both consider a variety of mixed pixels to find the optimum kernel that minimizes the statistical difference between the ideal unblurred image and the restored deblurred image.

For the Gaussian PSF, both procedures obtained the same small dispersion in the numerical value of the optimum kernel $\alpha = 0.105 \pm 0.005$. This dispersion arises in the HRSI procedure because different landscapes and bands were considered, and in the SEI procure because different edge's slopes were considered. Thus, the change of landscape and spectral band in the HRSI procedure seems to be numerically equivalent to a change of the edge's slope in the SEI procedure. The relatively small dispersion on the optimum value is reassuring as otherwise the practical utility of the deconvolution procedure would be threatened.

5.4.3. Significance of result

In its original form, the HRSI procedure was formulated in terms of a PSF's adjacency parameter, but now a new and more general formulation of this procedure based on a PSF's shrink factor has been developed. This new "shrink factor" formulation is applicable to any satellite sensor, whereas the previous "adjacency parameter" formulation is applicable only to sensors which have very restricted types of PSF.

The new SEI procedure does not have the five drawbacks indicated in section 5.1.4 for the HRSI procedure so it can be easily applied to find the optimum deconvolution kernel for any type of sensor's PSF, providing a substantial improvement of deconvolution procedures with a minimal effort. Moreover, the SEI procedure readily allows the study of the influence of the type and level of image noise in the selection of the optimum deconvolution kernels, something that cannot be done with the HRSI procedure as both noise parameters are fixed in the satellite image. Thus, a new and versatile tool is at disposal of procedures to deblur any type of digital images.

The deblurring factor curve obtained here for the triangular PSF (Figure 5.5) supplements the single point result published by Huang et al. (1998) and indicates that a substantial image degradation is obtained if the usual deconvolution kernel ($\alpha = 0.25$) is applied. The fact that deconvolution sometimes degrades the raw image instead of improving it is well-known (Hu et al. 2020, Scharr et al. 2021), this work shows that one of the reasons of these negative results may be the employment of the usual deconvolution kernel.

In other cases, such as the one depicted in Figure 5.6 for a Gaussian PSF, the usual kernel ($\alpha = 0.15$) provides only a marginal improvement, whereas the optimum kernel ($\alpha = 0.105$) increases the deblurring factor Δ by a factor of four.

The results of Figures 5.5 and 5.6 suggest that deconvolution with the sensor's PSF may have not achieved the popularity it deserves, because the usual deconvolution kernels may provide either negative or marginal improvements, respectively. The main significance of this work is that a new procedure to gauge the improvement of any type of deconvolution kernel has been developed and validated.

5.4.4. Limitations and future work

This work has considered only two simple PSFs with unidirectional (triangular PSF) and isotropic (Gaussian PSF) blurring. For these two PSFs a single synthetic edge alignment was required and small angular variations with respect to this alignment were performed by changing the edge's slope. In the general case the PSF is not isotropic so at least three edge alignments (horizontal, vertical, and diagonal) will be required and small angle variations with respect to these three alignments should be considered. The overall deblurring factor Δ can be defined as the average of all the edges' alignments considered.

The deblurring factor Δ is a useful image quality metric, but by its own it does not fully describe the impact of deblurring on image quality. The MAD between the ideal and the restored image may be smaller than the MAD between the ideal and the raw image (positive Δ), but this does not guarantee that all pixels in the image are being improved. By being a mean value, the DNs of many restored pixels may be closer to their ideal values, but the DNs of some few pixels may be farther to their ideal values. Thus, other criteria could be developed and tested, for example to minimize the maximum absolute difference between any pixel in the ideal unblurred image and the restored deblurred image.

In practice images may be corrupted by noise, this does not only limit the maximum Δ that can be obtained for the optimum kernel, but it also may impact the selection of the optimum shrink factor. The results of Huang et al. (2002) for different landscapes and bands suggest that the optimum shrink factor does not depend on the noise level, but all these results were obtained for the same isotropic Gaussian PSF, so it remains an open question how noise will impact other PSF shapes. The SEI procedure was validated here neglecting image noise, but it easily allows different type and levels of image noise to be considered.

Only the same integrated PSF type of kernel used by Huang et al. (1998, 2002) was here employed, but the sampled PSF type of kernel has also been used for satellite images (Ruiz and Lopez 2002), and other types of deconvolution kernels may be defined, for example, a linear combination between integrated and sampled PSF kernels. The SEI procedure allows different types of PSF kernels to be compared to find the one that maximizes the deblurring factor.

Finally, in this work only the Wiener and the regularized filters were employed to deconvolve the raw images, but several other methods have been used to deconvolve satellite images, for example, Lucy-Richardson and blind deconvolution (Ozan et al. 2023). The SEI procedure allows the optimum kernel obtained by different deconvolution methods to be compared.

5.5. Conclusion

Image deconvolution for blurring reduction, is a technique that improves the accuracy of various remote sensing applications in which the properties of the Earth's surface are estimated in a per-pixel basis. These applications assume that the Digital Number (DN) of each pixel

measures only the properties of the area of the Earth's surface that is represented by this pixel, neglecting the influence of adjacent pixels.

The optimum deconvolution kernel is trivial when a hypothetical continuous image is assumed, but when the actual discrete image is considered, the optimum kernel is by no means trivial and must be found in a case-to-case basis. This fact has been overlooked by the remote sensing community, as the usual trivial kernel is extensively employed, leading to a diminished performance of image deblurring.

A new procedure has been developed to find the optimum deconvolution kernels for satellite images with a known sensor Point Spread Function (PSF). This procedure uses Synthetic Edge Images (SEI) to produce the ideal, raw, and restored images required to compute the amount of deblurring provided by different deconvolution kernels.

The new procedure has been validated by applying it to the same two types of PSFs that have been previously considered to obtain optimum deconvolution kernels using the Higher Resolution Satellite Images (HRSI) procedure implemented with Landsat TM images captured over four different landscapes using six spectral bands. This later procedure employs actual satellite images with a Ground Sampling Distance (GSD) that is an exact submultiple of the GSD of the sensor of interest and has several other drawbacks that limit hits application.

Very good agreement has been obtained between the results of the HRSI and SEI procedures, confirming the little-known fact that the usual deconvolution kernel, which employs a kernel defined in terms of the system PSF, do not give optimum results, and can even degrade the raw image. Both procedures indicate that deconvolution kernels defined in terms of a shrunk version of the system PSF give optimum results.

A new and more general formulation for the SEI and HRSI procedures, based on the PSF shrink factor, has been provided, showing that the original formulation of the HRSI procedure, based on an adjacency parameter, is only applicable to very restricted types of sensor PSF.

The new SEI procedure is simpler, more accurate and more general than the original HRSI procedure, opening new research paths in satellite image deblurring.

Chapter Six

Assessing the Spatial Resolution Distance of Satellite Images: SuperDove versus Landsat 8*

* This chapter was published on 12th June 2024 as:

Valenzuela A, Reinke K, Jones S (2024b). Assessing the spatial resolution distance of satellite images: SuperDove versus Landsat 8. *International Journal of Remote Sensing* **45**(12), 4120-4159. https://doi.org/10.1080/01431161.2024.2357839.

6.1. Introduction

The definition of the Spatial Resolution Distance (SRD) of satellite images is a complex issue; the various misunderstandings that surround this concept have been a recurring topic of concern in the remote sensing literature since Landsat 1 (NASA 1973, 104).

Although many subsequent works on imaging sensors have contributed to clarify some of the confusions that surround the concept of spatial resolution (Townshend 1981, Forshaw et al. 1983, Markham 1985, Fisher 1997, Cracknell 1998, Fiete 1999, Joseph 2000, NRC 2000, Townshend et al. 2000, Ryan et al. 2003, Reulke et al. 2006, Thomson 2009, Pagnutti et al. 2010, Auelmann 2012, Verhoeven 2018, Valenzuela and Reyes 2019a) some misconceptions have not been eradicated. Among these misconceptions, currently the most prevalent is the identification of Ground Sampling Distance (GSD) with SRD (Verhoeven 2018).

The GSD is a rough approximation to the SRD of images captured by some channels of high-quality satellite sensors like Landsat and Sentinel, but it grossly underestimates the SRD (overestimates the resolution capability) of images captured by some CubeSat satellite sensors like Planet's SuperDove. For example, NASA and ESA have independently analysed SuperDove's images with GSD ≈ 3 m, concluding that their SRD is about five times larger (SRD ≈ 15 m) (NASA 2020, 12; Saunier and Cocevar 2022, 28).

The GSD describes the size of the ground pixel, it has a simple definition, it is easy to compute and has the same meaning for all users. To resolve or separate two objects in the image they must be separated at least one GSD, otherwise there would be no separating pixel between them (Lillesand et al. 2015, 224). Thus, one of the reasons why the SRD is confused with the GSD is that this later distance is the minimum possible value of the former (SRD ≥ GSD).

The SRD, also known as Ground Resolution Distance (GRD) when computed in the ground plane, has multiple definitions, it is usually much more difficult to compute than the GSD, and has different meanings for different users. The importance of the SRD is due to its threefold impact on the spatial performance of the satellite image: 1) Characterizes the minimum size of the ground area whose properties can be quantified. 2) Defines the minimum distance at which two small objects in the scene can be discerned as separate entities. 3) Determines the minimum size of the pixel-sized objects in the scene that can be identified.

A point source, much smaller than one GSD, can easily be detected by any satellite sensor provided it is strong enough. This type of source is implemented by using convex mirrors that reflect the sun towards the satellite (Conran et al. 2021). The feat that the SRD characterizes is the ability to discern how close can two of these sources be separated in the ground, so they can still be detected as two separate entities in the image (Valenzuela and Reyes 2019a).

The fact that the SRD is always larger than the GSD is due to the non-ideal spatial response of the satellite sensor, which makes the pixel's DN depend not only on the ground area it represents, but also on the surrounding area represented by adjacent pixels.

The usual and erroneous assumption that SRD = GSD implies that each pixel should represent the properties of a well-defined square area of GSD × GSD m^2. In this ideal case, the sensor has the spatial response represented in Figure 6.1(a). All the energy measured by a pixel originates from the ground area represented by this pixel, so each pixel's Digital Number (DN) represents an independent measurement of the properties of the Earth's surface. Thus, the

minimum size of the ground area whose properties can be quantified equals the GSD in this ideal case.

For some high-quality sensors such as Landsat or Sentinel 2, the SRD is roughly 1.5 times larger than their GSD, in this case about 70 % of the energy measured by a pixel originates from the ground area represented by this pixel, the remaining 30 % originates from the surrounding areas represented by adjacent pixels (Pagnutti et al. 2010, Lee et al. 2014). In this case, the sensor has the spatial response represented in Figure 6.1(b). The minimum size of the ground area whose properties can be quantified in the image is described by the SRD, which is somewhat larger than the GSD.

When the pixel's adjacency effect is neglected, the radiometric accuracy of the image is compromised, because a pixel's DN measures also the radiometric properties of the Earth's surface that surrounds the area represented by the pixel. The resultant radiometric error depends on the difference between the ground area represented by a pixel and the surrounding area; if there is no difference the error is null, if there is a large difference the error is high (Cracknell 1998). When the adjacency effect is acknowledged, some image processing techniques such as restoration are used to improve the SRD and the radiometric performance, so that each pixel measures with better accuracy the properties of the ground area represented by this pixel (Huang et al. 2002).

For some CubeSat sensors such as SuperDove, the SRD is around five times larger than the GSD, in this case about 10 % of the energy measured by a pixel originates from the ground area represented by this pixel, the remaining 90 % originates from the surrounding areas represented by adjacent pixels. In this case, the sensor has the spatial response represented in Figure 6.1(c). The minimum size of the ground area whose properties can be quantified is described by the SRD, which is much larger than the GSD.

The SRD does not only impact the spatial performance of the image, but also its radiometric performance. If the adjacency effect is very small (SRD ≈ GSD), the energy collected in the image plane due to a point source in the scene will distribute over a few pixels, so the increase of their DNs due to this source will be high. But, if the adjacency effect is very large (SRD >> GSD), this same energy will distribute over many pixels, so the increase of their DNs due to this source will be low.

One of the main reasons why the GSD is the most popular metric to gauge the SRD is that the plethora of alternative SRD metrics available, which also predict a single value for the SRD, are usually more complex to compute and give widely disparate results. These discrepancies can be traced to the fact that the SRD of a sensor should not be described by a single number (Forshaw et al. 1983, Joseph 2000). The solution to this dilemma is to acknowledge that the SRD is a function of the resolving contrast in the image that allows two objects in the scene to be distinguished as two separate entities (Stelzer 1998, Valenzuela and Reyes 2019a).

The recently developed Spatial Resolution Function (SRF) metric gives a comprehensive account of resolution phenomena by assuming two point sources in the scene and computing the SRD as a function of the actual resolving contrast in the image. The SRF allows the prediction of any single-value SRD metric to be assessed. In particular, the GSD is obtained as

a limiting case of the SRF and is shown to be applicable under very restricted circumstances (Valenzuela et al. 2022).

Another issue of interest regarding the computation of the SRD of satellite sensors is the stability of this distance in the dynamic space environment. It will be shown that a drawback of CubeSat sensors with a large SRD/GSD ratio is that the SRD of their images is highly susceptible to variations in the state of the atmosphere and spacecraft vibrations. This is one of the main reasons behind the numerous radiometric inconsistencies reported for their images (Frazier and Hemingway 2021; Anger et al. 2019; NASA 2020, 19; Saunier 2020, 27).

Considering that the SRD is one of the most important properties of a satellite image and that it is usually confused with the GSD, it is relevant to present a rigorous computation of the SRD for two different types of satellite imagers, assessing the errors and biases of some current methods to compute the SRD and, its in-orbit stability.

The objective of this work is to apply the SRF metric to the green channels of Landsat 8 and SuperDove imaging sensors, showing that the most popular single-value SRD metrics currently used are either erroneous or biased. The stability of the SRD in a space environment is studied by computing the susceptibility of the SRD to variations in the state of the atmosphere and spacecraft vibrations.

Section 6.2 summarises some technical background in spatial response functions and spatial resolution metrics, that is required to grasp the computational methods presented in section 6.3. The relevant material collected from various sources about Landsat 8 and SuperDove is presented in section 6.3, together with the different methods required to process it. Section 6.4 presents the results obtained by using different metrics to compute the SRD of Landsat 8 and SuperDove channels. Section 6.5 discusses the results obtained and outlines future work in the subject.

6.2. Background

6.2.1. Spatial response functions

6.2.1.1. *Two-dimensional functions*

The spatial response of an imaging sensor is characterized by the Point Spread Function (PSF) or, equivalently, by its Fourier transform; the Optical Transfer Function (OTF). The PSF describes the spatial response of the sensor in the spatial domain whereas the OTF describes this response in the spatial frequency domain (Fiete 2010, Boreman 2021).

The PSF is a Two-Dimensional (2D) function that describes how a single point source in the scene is represented in the image plane. It is more convenient to display the PSF in the image plane than in the ground plane because the shape of the PSF in the ground plane depends on the off-nadir view angle and the satellite height.

In the image plane the horizontal distances are measured in pixels, with respect to the origin of coordinates that represents the position of the geometrical projection of the point source. To simplify the treatment, in what follows square pixels and a nadir looking view angle are assumed, so that each pixel in the image plane represents, from a geometric (not radiometric!) point of view, a square ground pixel of size GSD×GSD m^2.

Figure 6.1 illustrates the PSF for three different sensors: (a) an ideal sensor; (b) Landsat 8's Green channel; and (c) SuperDove's Green channel. The last two PSFs are computed as explained in section 6.3. In the figure, the values of the PSFs are measured in the vertical axis normalized to a peak value of 1.

The horizontal axes of Figure 6.1 represent two orthogonal directions: along scan and cross scan. The Along Scan (AS) direction is the direction in which the satellite sensor scans its narrow field of view to form the image. The Cross Scan (CS) direction is perpendicular to the AS direction. In push broom scanners, the AS direction is the direction of the satellite track, whereas in whisk broom scanners, the AS direction is perpendicular to the satellite track.

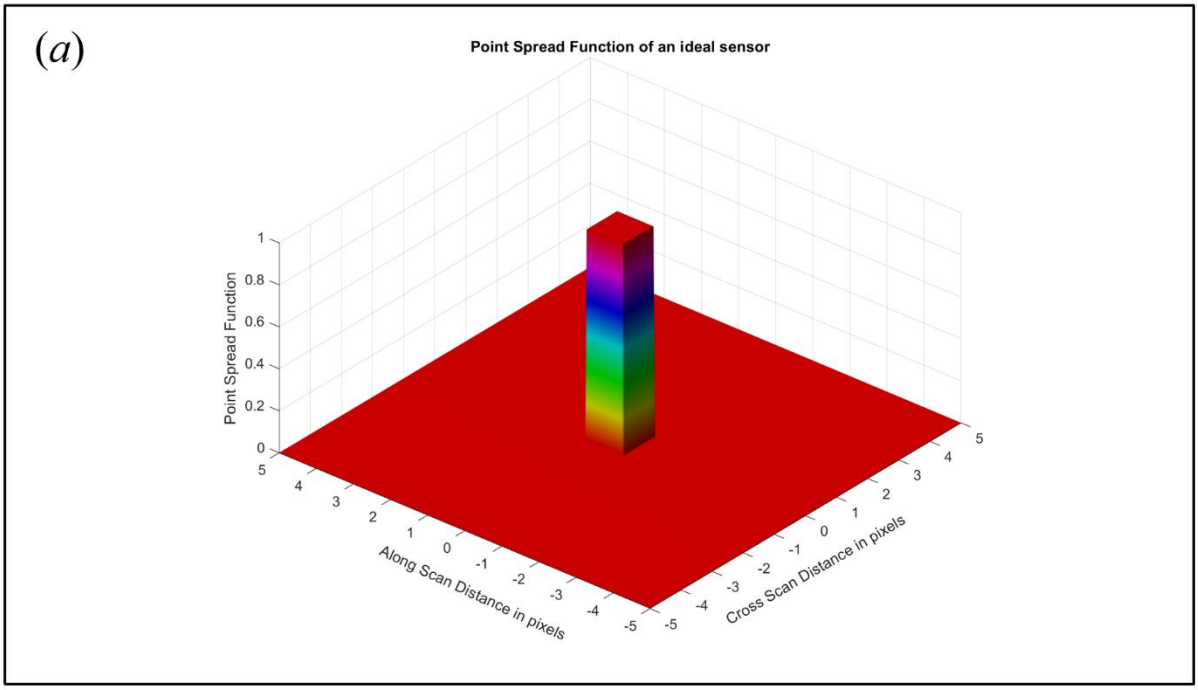

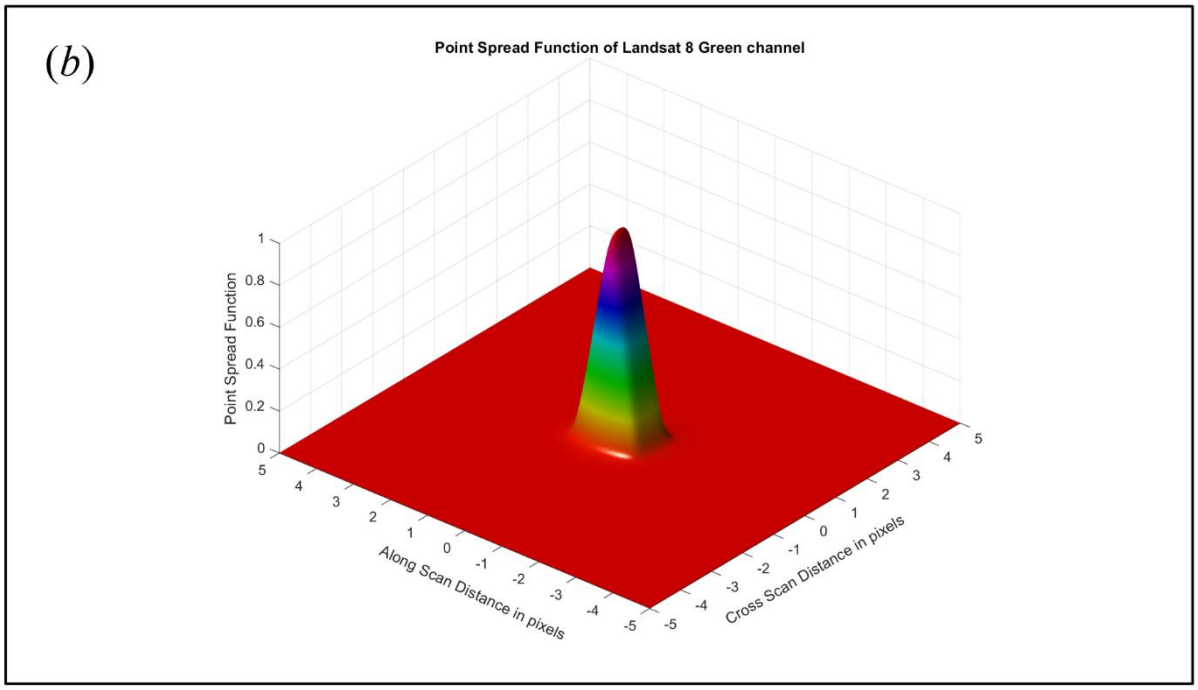

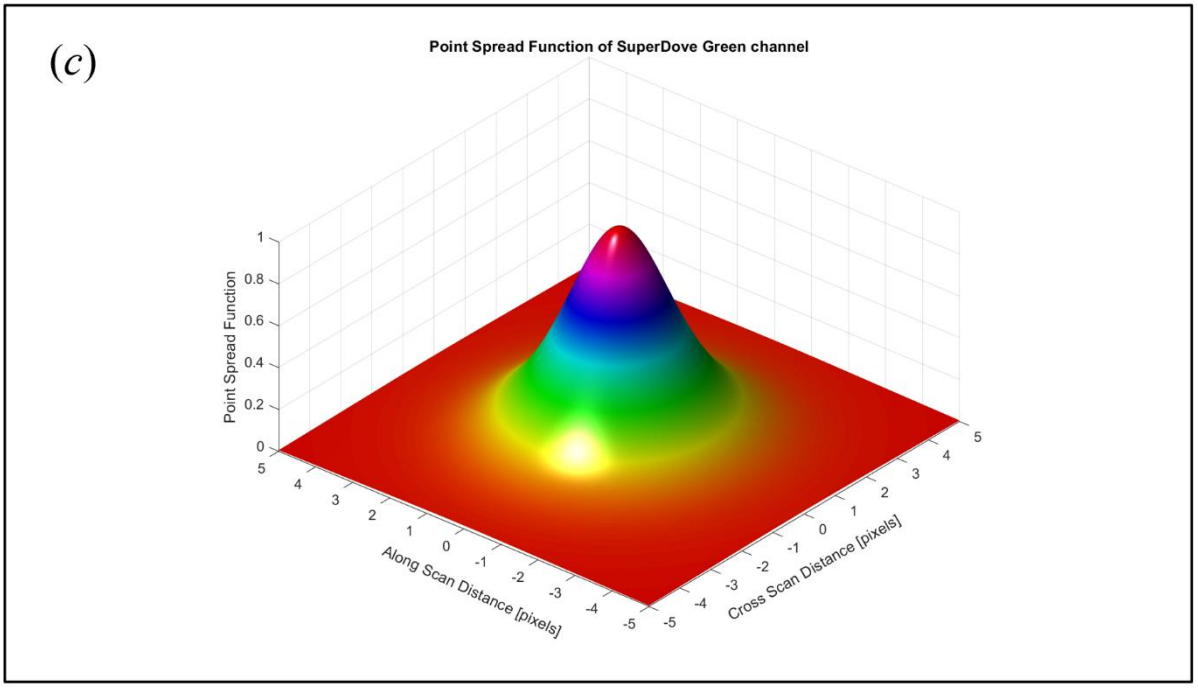

Figure 6.1: Point Spread Function (PSF) of three imaging channels. The two-dimensional PSF is represented in the image plane over an extent of 10×10 pixels, for three imaging channels: (*a*) an ideal imaging channel with no adjacency effect; (*b*) Landsat 8's Green channel; and (*c*) SuperDove's Green channel.

The PSF of an ideal imager (Figure 1(*a*)) is a rectangular parallelepiped of unitary height and square cross section with a side length of one pixel. The widths of the PSF in AS and CS directions are both exactly one pixel. The DN measured by a pixel depends only on the properties of the square ground area of size GSD×GSD that is represented by this pixel.

The PSF of Landsat's 8 Green channel (Figure 1(*b*)) has an almost rectangular cross section in CS direction and a triangular cross section in AS direction. The widths of the PSF at its base (PSF ≈ 0) in AS and CS directions are approximately 2 and 1 pixels, respectively. The DN measured by a pixel depends mainly on the properties of the square ground area of size GSD×GSD that is represented by this pixel and, to a lesser extent, on the properties of the two adjacent ground pixels in AS direction.

The PSF of SuperDove's Green channel (Figure 1(*c*)) has a bell-shaped cross section in AS and CS directions. The widths of the PSF at its base (PSF ≈ 0) in AS and CS directions are both roughly six pixels. The widths of the PSF at half its maximum value (PSF = 0.5) in AS and CS directions are both roughly three pixels. The DN measured by a pixel depends mainly on the properties of a square ground area of size 3·GSD×3·GSD centred on this pixel and, to a lesser extent, on the properties of about 48 pixels that surround this square area, and which are located up to three pixels away from its perimeter.

Once the PSF is known, all the other functions that describe the spatial response can be derived through the mathematical procedures presented in Figure 6.2. The definitions of the five spatial response functions of interest for our work are summarized in Table 6.1.

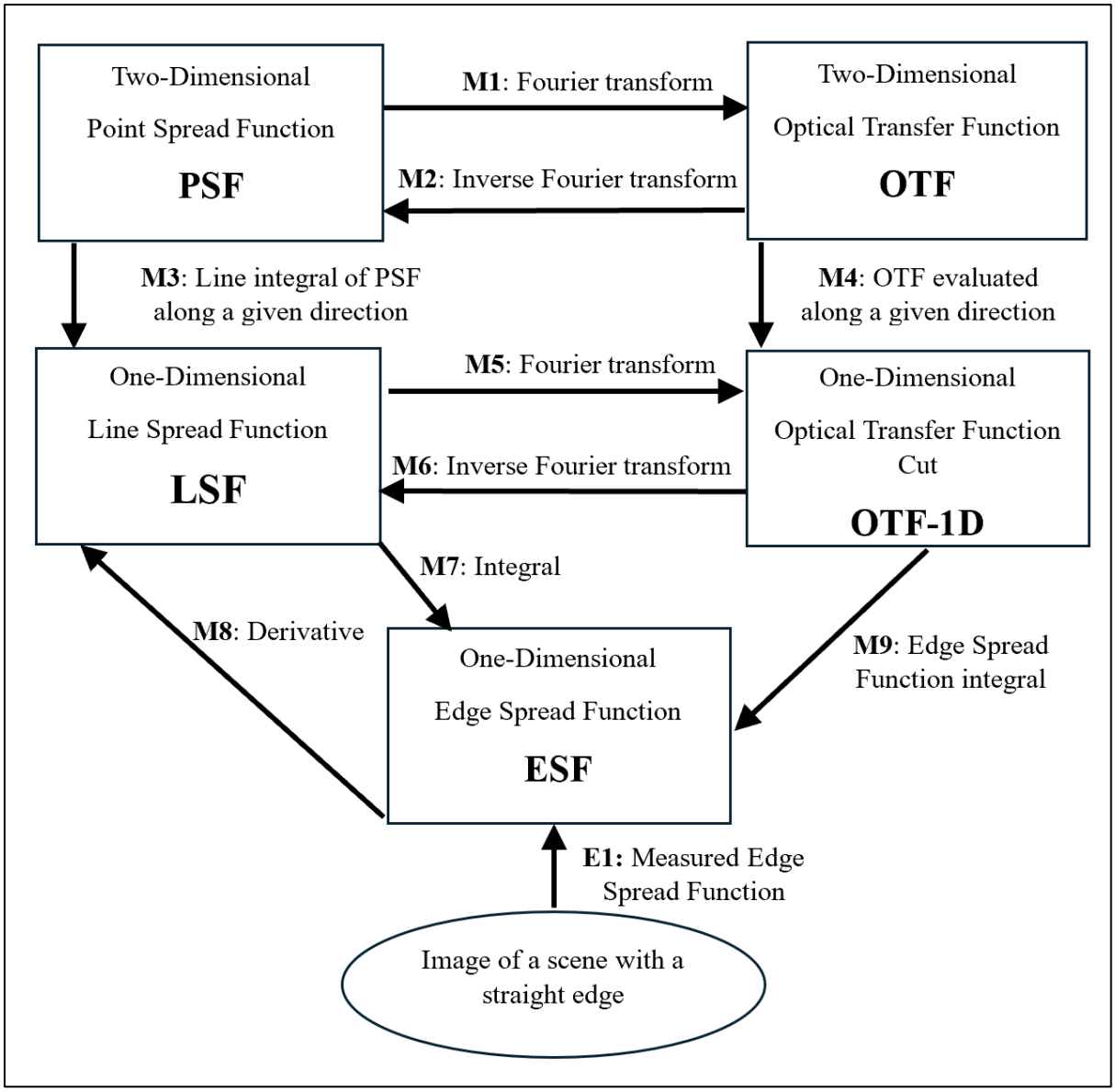

Figure 6.2: Procedures used to obtain the different spatial response functions. The five spatial response functions of interest are displayed in rectangular boxes. The mathematical procedures used to derive a spatial response function from another spatial response function are displayed as arrows that connect these two spatial response functions. These mathematical procedures are labelled with the letter "M" and a correlative number. The image used to measure the spatial response is displayed in an oval shape. The empirical procedure that uses this image to obtain the Edge Spread Function (ESF) is labelled as E1 and displayed as an arrow that connects the image with the ESF.

The 2D OTF is obtained as the 2D Fourier transform of the PSF (Gaskill 1978, equation 11.107), procedure labelled as M1 in Figure 6.2. From a mathematical viewpoint, it is much easier to compute the OTF in the spatial frequency domain than the PSF in the spatial domain. Thus, the 2D "system" OTF is usually computed using the method of multiplication of OTF components described in section 6.3.2.2. When the system OTF is known, the PSF is then obtained as its inverse 2D Fourier transform, procedure labelled as M2 in Figure 6.2. We have followed this later procedure to obtain the PSFs depicted in Figures 6.1(*b*) and 6.1(*c*).

Table 6.1: Spatial response functions considered in this work.

Spatial response function	Definition
Edge Spread Function (ESF)	One-dimensional function that defines how a scene containing a single straight edge, that separates two areas of different brightness, is represented in the image plane.
Line Spread Function (LSF)	One-dimensional function that defines how a scene containing a single line source is represented in the image plane. It is equal to the derivative of an ESF computed in the same direction than the line source.
Optical Transfer Function (OTF)	Two-dimensional function that defines the spatial response of a sensor in the spatial frequency domain. It is equal to the Fourier transform of the PSF.
Optical Transfer Function cut (OTF-1D)	One-dimensional function obtained by evaluating the two-dimensional OTF along a certain direction. It is equal to the inverse Fourier transform of the LSF in this same direction.
Point Spread Function (PSF)	Two-dimensional function that defines how a scene containing a single point source is represented in the image plane. It is equal to the inverse Fourier transform of the OTF.

6.2.1.2. *One-dimensional functions*

Once the 2D PSF and OTF are known, the one-dimensional (1D) spatial response functions of interest can be derived through the mathematical procedures indicated in Figure 6.2. If the PSF and OTF do not exhibit axial symmetry, the shapes of these three 1D functions will depend on the direction in which they are computed.

Examples of these 1D functions were computed for Landsat 8's Green channel in AS direction, using the OTF model described in sections 6.3.2.2, 6.3.2.3 and 6.3.2.5, and the results are graphically portrayed in Figure 6.3. Each one of these 1D functions has been used to derive several spatial resolution metrics (Valenzuela et al. 2022), the most popular of these metrics for each 1D function is graphically presented in Figure 6.3 and described below.

The Edge Spread Function (ESF) is a 1D function that describes how a scene that contains a single straight edge, which separates two areas of different brightness, is represented in the image plane. Figure 6.3(*a*) presents as a blue curve the ESF in AS direction for Landsat 8's Green channel.

The ESF in a certain direction can be computed as an integral of the LSF in this same direction (Schowengerdt 2007, equations 3-22), procedure labelled as M7 in Figure 6.2, or via the OTF by calculating the ESF integral of an OTF-1D cut in this same direction (Fiete 2010, equation 11.11), procedure labelled as M9 in Figure 6.2. In our case the ESF was calculated via the ESF integral.

The Relative Edge Response (RER) of the ESF, depicted with a double-headed red arrow in Figure 6.3(*a*), measures the slope of the ESF at the edge. The General Image Quality Equation (GIQE) uses the ratio GSD/RER as spatial response parameter (Leachtenauer et al. 1997), so this same ratio has been used to estimate the SRD of satellite imagers (Auelmann 2012).

To develop the OTF model of SuperDove's Green channel, we have used the average RER parameters measured by its operating agency (Planet) in AS and CS directions.

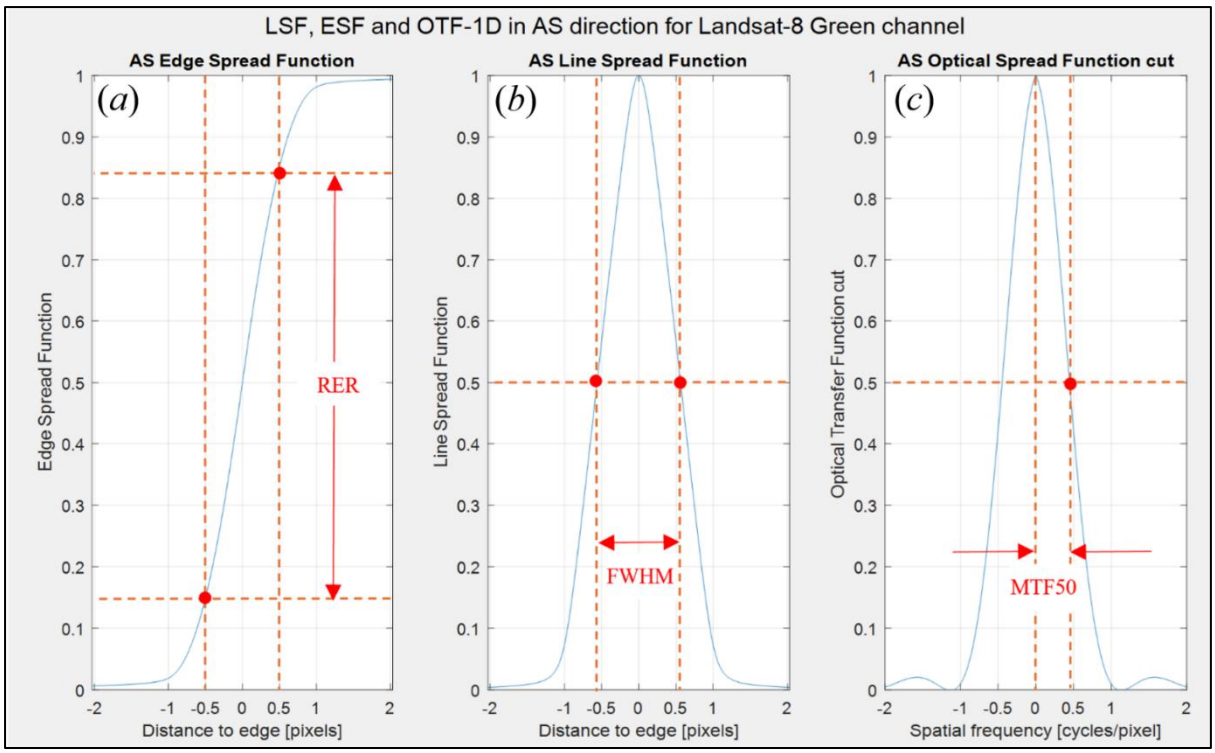

Figure 6.3: One-dimensional spatial response functions computed in this work for Landsat 8's Green channel in Along Scan (AS) direction. The spatial response functions represented as blue curves are: (*a*) the Edge Spread Function (ESF); (*b*) the Line Spread Function (LSF); and (*c*) the Optical Transfer Function cut (OTF-1D). For each function the magnitude of the parameter of interest for the respective spatial resolution metric is represented with red arrows.

The Line Spread Function (LSF) is a 1D function that describes how a single line source in the scene is represented in the image plane. Figure 6.3(*b*) presents as a blue curve the LSF in AS direction for Landsat 8's Green channel.

The LSF along a direction of interest can be obtained by three methods. The first method is to perform a line integral of the PSF in a direction perpendicular to the direction of interest (Schowengerdt 2007, equations 3-21), procedure labelled as M3 in Figure 6.2. The second method is to compute the inverse Fourier transform of a 1D cut of the OTF along the direction of interest (Gaskill 1978, equation 11.130), procedure labelled as M6 in Figure 6.2. The third method is to compute the derivative of the ESF along the direction of interest (Schowengerdt 2007, equations 3-21), procedure labelled as M8 in Figure 6.2.

In our case, we have used the second method to compute the LSF, implemented through the MATLAB Fast Fourier Transform (FFT) routines to compute the inverse Fourier transform of the 1D OTF cut. To check the accuracy of the FFT routines we have use the third method and compare its results with those obtained by the second method.

The Full Width at Half Maximum (FWHM) of the LSF, depicted with a double-headed red arrow in Figure 6.3(*b*), is a popular spatial resolution metric used to predict the SRD (Ryan et al. 2003, Pagnutti et al. 2010).

To develop the OTF model of Landsat 8's Green channel, we used the LSF measurements in AS and CS directions provided by its operating agency (Unites States Geological Survey).

To derive an OTF-1D cut from the 2D OTF, this later function is evaluated along the direction of interest. Let OTF(f_x, f_y) be the 2D OTF, f_x the spatial frequency in *x* direction, and f_y the spatial frequency in *y* direction. Then, the OTF-1D cut in *x* direction is OTF(f_x, 0) and the OTF-1D cut in *y* direction is OTF(0, f_y).

The Modulation Transfer Function (MTF) is the absolute value of the OTF. The OTF is used here instead of the MTF because when SRD ≈ GSD it must be considered that for some spatial frequencies OTF < 0 to get the correct results.

The most popular procedure to measure the spatial response of imaging sensors is the edge method (Pagnutti et al. 2010). In this empirical procedure a suitable straight edge in the scene is used to measure the ESF in a direction perpendicular to edge's direction, procedure labelled as E1 in Figure 6.2. The LSF is obtained as the derivative of the ESF (procedure M8 in Figure 6.2) and the Fourier transform of the LSF gives the OTF-1D cut in a direction perpendicular to the edge (Gaskill 1978, equation 9.166), procedure labelled as M5 in Figure 6.2. Figure 6.3(*c*) presents as a blue curve the OTF-1D cut in AS direction for Landsat 8's Green channel.

The MTF50 spatial frequency, at which the OTF-1D cut achieves a 50 % of its peak value is used to compute the Effective Instantaneous Field OF View (EIFOV), a popular spatial resolution metric (Markham 1985, Bensebaa et al. 2012). The MTF50 spatial frequency is depicted within red arrows in Figure 6.3(*c*).

6.2.2. Spatial resolution metrics

Table 6.2: Spatial resolution metrics used in this study.

Spatial resolution metric	Definition
Effective Instantaneous Field of View (EIFOV)	Half the reciprocal of the spatial frequency "MTF50" at which a one-dimensional cut of the Optical Transfer Function (OTF) achieves 50 % of its peak value.
Full Width at Half Maximum (FWHM) of the LSF	Width of the Line Spread Function (LSF) measured at 50 % of its peak value.
Generalized Rayleigh Criterion (GRC)	Separation distance between two point sources in the scene, that allows them to be distinguished in the image as two separate objects, with an image's resolving contrast of 25 %.
Ground Sampling Distance (GSD)	Projection of the Instantaneous Field Of View (IFOV) of the detector on the ground plane.
Ground Spot Size (GSS)	Projection of the Optical Field Of View (OFOV) of the optical aperture on the ground plane.
Rayleigh Diffraction Limit (RDL)	1.22 times the projection of the Optical Field Of View (OFOV) of the optical aperture on the ground plane.
Relative Edge Response (RER)	Slope of the Edge Spread Function (ESF) measured at two points separated half a pixel pitch from the edge (± 0.5 pixels).
Spatial Resolution Function (SRF)	Separation distance between two point sources in the scene, that allows them to be distinguished in the image as two separate objects, computed as a function of the image's resolving contrast.

There is consensus that either the PSF or the OTF fully describe the spatial response of an imaging sensor, but for a given PSF or OTF, there is no agreement on how the SRD should be measured or computed. This lack of agreement is reflected in the fact that more than thirty different spatial resolution metrics have been used to compute the SRD of satellite images. These metrics differ on the way that the spatial response of the imaging sensor is considered in

the computation of the SRD and so they predict widely different results (Valenzuela et al. 2022). The metrics considered in this work are summarized in Table 6.2.

A general taxonomy to classify spatial resolution metrics considers the following three types (Valenzuela et al. 2022):

6.2.2.1. *Theoretic metrics*

As their name indicates, these metrics are based on theoretical assumptions, without considering the actual spatial response of the imaging sensor. These metrics assume that the SRD is a single value that can be computed as a function of some sensor parameters. The most common sensor parameters used by Theoretic metrics are the pixel pitch p of the detector array, the focal length F of the optics, the diameter D of the optical aperture and the wavelength λ of the detected radiation.

From these four parameters, two angular parameters are derived. The Instantaneous Field Of View (IFOV) of the detector is defined as the pixel pitch to focal length ratio (IFOV = p/F) and the Optical Field of View (OFOV) of the optical aperture is defined as the wavelength to aperture's diameter ratio (OFOV = λ/D). The GSD and the Ground Spot Size (GSS) are the projections of the IFOV and OFOV, respectively, on the ground plane. For a nadir-looking satellite sensor at an orbital height H, GSD = IFOV$\cdot H$ and GSS = OFOV$\cdot H$ (Fiete 1999). These parameters are illustrated in Figure 6.4.

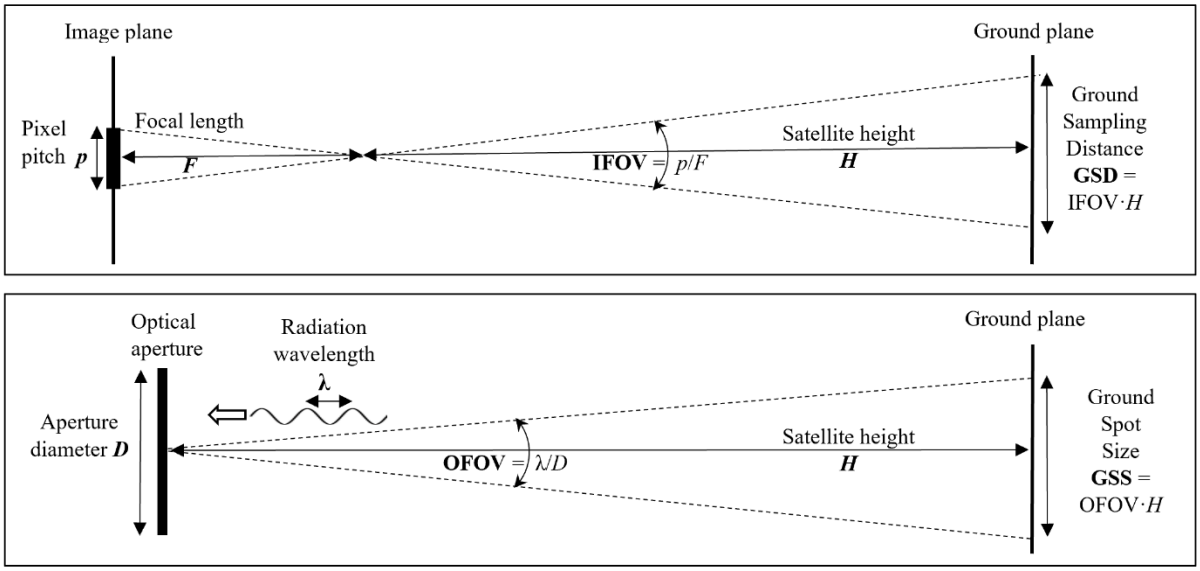

Figure 6.4: Pictorial representation of the parameters involved in the definition of Ground Sampling Distance (GSD) and Ground Spot Size (GSS) for a satellite imaging sensor. The upper figure represents the GSD as the projection of the Instantaneous Field Of View (IFOV) on the ground plane. The lower figure represents the GSS as the projection of the Optical Field Of View (OFOV) on the ground plane.

The Optical factor Q can be defined as the ratio between the GSS and the GSD, or equivalently as the ratio between the OFOV and the IFOV (Fiete 1999):

$$Q = \frac{(\text{GSS})}{(\text{GSD})} = \frac{\frac{\lambda}{D}H}{\frac{p}{F}H} = \frac{\lambda}{D}\frac{F}{p} = \frac{(\text{OFOV})}{(\text{IFOV})} \quad (1)$$

For high-quality imagers, if $Q << 1$, the response of the detector predominates, so in this case the angular width of the PSF, measured at half power points, is approximately equal to the IFOV, and, if $Q >> 1$, the response of the optics predominates, so in this case the later width is approximately equal to the OFOV. The quality an imager will be quantified through the Resolution Degradation Index to be defined in section 6.3.4. This index measures the degradation of the SRD due to sensor's imperfections, if this degradation is small the sensor is considered high-quality, otherwise it is considered low-quality.

Theoretic metrics usually assume that the SRD is proportional to the GSD ("detector" metrics), proportional to the GSS ("optics" metrics) or a simple function of the GSD and the GSS ("system" metrics).

The most popular of all Theoretic metrics simply assumes that SRD = GSD, this is a rough approximation for high-quality imagers with $Q << 1$, but it grossly underestimates the SRD for imagers with $Q >> 1$ or for low-quality imagers.

Another popular Theoretic metric is the Rayleigh Diffraction Limit (RDL) which assumes that SRD = 1.22·GSS (Fiete 2010, 109), this is a rough approximation for high-quality imagers with $Q > 1$, but it grossly underestimates the SRD for imagers with $Q << 1$ or for low quality imagers.

The SRD can be measured on the ground plane in units of distance or equivalently on the image plane in pixel pitch units. A distance of one GSD in the ground plane corresponds to one pixel pitch in the image plane, so for example, if SRD = 3·GSD m in the ground plane (Verhoeven 2018), then SRD = 3 pixels in the image plane. Pixel pitch units are convenient because they remove the dependency of the SRD on satellite height.

6.2.2.2. *Spatial Response metrics*

Spatial Response metrics assume that the SRD is a single value equal to a certain property of the PSF or OTF of the imaging sensor. These metrics are usually much more accurate than Theoretic metrics because they consider the actual spatial response of the imaging channel to compute the SRD. The most popular Spatial Response metrics are:

1. Relative Edge Response (RER). The RER is the slope of the ESF, measured at ± 0.5 pixels from the edge: RER= ESF(+0.5) – ESF(0.5) (Fiete 2010, 183). GSD/RER is the spatial resolution metric used in the General Image Quality Equation (Leachtenauer et al. 1997), so when the RER is used as a spatial resolution metric, it predicts SRD = 1/RER pixels (Auelmann 2012, 13). Figure 6.3(*a*) illustrates the computation of the RER.

2. Full Width at Half Maximum (FWHM) of the Line Spread Function (LSF). This width is a basic characteristic of the LSF curve. When the LSF's FWHM is used as a spatial resolution metric it predicts SRD = FWHM pixels (Ryan et al. 2003, Pagnutti et al. 2010). Figure 6.3(*b*) illustrates the computation of the LSF's FWHM.

3. Effective Instantaneous Field Of View (EIFOV). The EIFOV is defined as half the reciprocal of the spatial frequency "MTF50" (in cycles per pixel) at which the system MTF achieves a 50 % of its peak response. This metric predicts SRD = 1/(2·MTF50) pixels (Markham 1985, Bensebaa et al. 2012). Figure 6.3(*c*) illustrates the computation of the MTF50 spatial frequency.

The main limitation of Spatial Response metrics is that they assume that the SRD is a single value, without considering the fact that in practice the SRD is a function of the resolving contrast in the image (Stelzer 1998). Regarding this issue, Forshaw et al. (1983, 499) had already stated that "*one of the greatest obstacles to clear understanding is the insistence on a single-valued measure for spatial resolution*" while Stelzer (1998, 16) concluded that "it *does not make any sense to discuss contrast and resolution as if they were independent terms*".

6.2.2.3. *Two-point source metrics*

One of the most practical, rigorous, and general approaches to define the SRD of a sensor is the two-point source criterion. Under this criterion the SRD is defined as the smallest distance between two closely spaced point sources of equal intensity in the scene, that allows them to be detected as two separate objects in the image. This definition has been adopted for astronomy (Den Dekker and Van den Bos 1997), microscopy (Cremer 2012, 373), human and robotic vision (Calvo et al. 1996), medical imaging (Kouame and Ploquin 2009), airborne sensors (Reulke et al. 2006), digital cameras (Fiete 2010, 109) and satellite sensors (Valenzuela et al. 2022).

The use of convex-mirrors as virtual point-sources for in-orbit spatial resolution measurements has allowed the two-point source criterion to achieve a solid empirical foundation, being the preferred approach for a direct measurement of the in-orbit SRD satellite of imagers (Conran et al. 2021).

Both "Spatial Response" and "Two-point Source" metrics consider the actual spatial response of the sensor. But whereas Spatial Response metrics attempt to define SRD as single number which represents a property of the spatial response, Two-point Source metrics use this later response to compute the actual resolving contrast that allows the sources to be separated in the image. These later metrics are subclassified as "Single-Value" metrics, when a given value of resolving contrast is of interest, or as "Contrast-Function" metrics, when the full range of contrast values of interest is considered.

Two closely spaced point sources of equal strength in the scene, are considered to be resolved or separated in the image, when a certain resolving contrast C is achieved between them, as illustrated in Figure 6.5. In this figure, the projections of the two sources in the image plane are located near the centres of pixels 4 and 6, and the signals due to these two sources extend from pixel 2 to 8 due to the adjacency effect. The maximum signal I_{max} occurs at pixels 4 and 6 and the minimum signal I_{min} in between these two pixels occurs at pixel 5. The resolving contrast is defined as:

$$C = (I_{max} - I_{min})/I_{max} \quad (2)$$

Where I_{max} is the maximum DN measured at the two signal peaks and I_{min} is the minimum DN between these two peaks.

The Generalized Rayleigh Criterion (GRC) is a Single-Value (Two-point Source) metric that removes the fundamental limitations of the (Theoretic) Rayleigh Diffraction Limit metric, by defining the SRD as the distance required to achieve a given resolving contrast in the image (Den Dekker and Van den Bos 1997). The GRC has been successfully used to compute the SRD of airborne cameras using $C = 0.25$ as resolution criterion (Reulke et al. 2006).

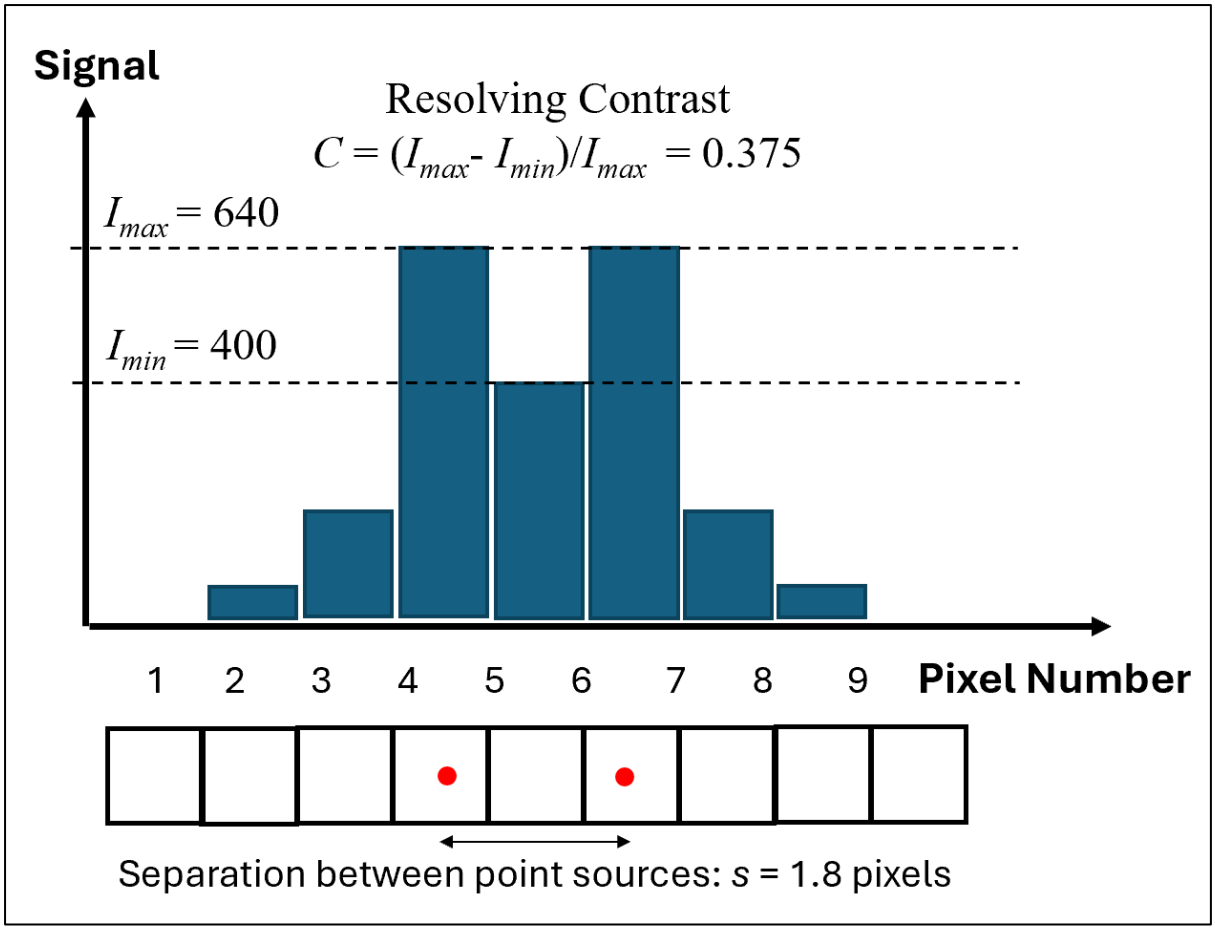

Figure 6.5: Example of resolving contrast computation. Two point sources of identical strength in the scene are projected in the image plane on pixels 4 and 6, being separated in this plane at a distance of 1.8 pixels. The maximum signal level I_{max} is produced in pixels 4 and 6, where the projections of the sources are located. Due to the adjacency effect, signal is generated in pixels 2 to 8. The minimum signal level I_{min} between the two pixels with maximum signal occurs at pixel N° 5. The resolving contrast is defined as the difference between I_{max} and I_{min} divided by I_{max}.

For a given source separation, the resolving contrast is maximized when the two sources are located symmetrically with respect to a pixel centre as shown in Figure 6.5. The relevance of the central symmetry condition will be now illustrated by using the two-point source criterion to conceptually deduct the SRD of an ideal sensor, which has the spatial response presented in Figure 6.1(*a*).

For an ideal sensor only the two "signal" pixels where the projections of the sources are located will have a signal I_{max} and, as there is no adjacency effect, there will be no signal in adjacent pixels. Under the central symmetry condition, if the two sources are separated at a distance of one pixel (plus an infinitesimal distance) there will be no signal in the pixel between the two signal pixels, so $I_{min} = 0$, that is $C = 1$. In this ideal condition, the GSD metric that predicts SRD = 1 pixel is exact as 100 % contrast is generated with a separation of 1 pixel between sources. For smaller separations, resolution is not physically possible as there is no pixel between the two signal pixels; this fact has already been noted by Lillesand et al. (2015, 224). But, if the sources are now located symmetrically with respect to a pixel edge, then the sources will have to be separated at a minimum distance of two pixels (plus an infinitesimal

distance) to achieve 100 % contrast. In the edge symmetry condition SRD = 2 pixels, because for any separation smaller than two pixels there are no pixels in between the two signal pixels.

The fact that the ideal sensor has SRD = 1 pixel for central symmetry and SRD = 2 pixels for edge symmetry, shows that the GSD metric (SRD = 1 pixel) can be used as an approximation to the SRD of actual sensors, only if central symmetry is assumed.

The SRF is a Contrast-Function (Two-Point Source) metric that assumes central symmetry and uses the two-point source criterion to compute the SRD as a function of the resolving contrast *C*. The computation of the SRF has the following three stages, whose details and steps are discussed further in section 6.3.3:

1. Set computational framework

Assume a scene with only two point sources of equal strength separated at a given distance of *s* pixels. Specify an adequate phasing between the scene and the detector grid so that the sources can be resolved at the minimum possible distance. Set the framework required to compute the resulting image resolving contrast *C* as a function of the separation distance.

2. Compute contrast versus separation

Gradually vary the separation *s* between sources, starting from *s* slightly less than one pixel, computing the contrast *C* for each separation until the maximum resolving contrast of interest $C = C_{max}$ is obtained. For actual sensors, 100% contrast requires in theory an infinite separation distance, so in our case C_{max} = 0.99 was considered adequate as the maximum contrast of interest.

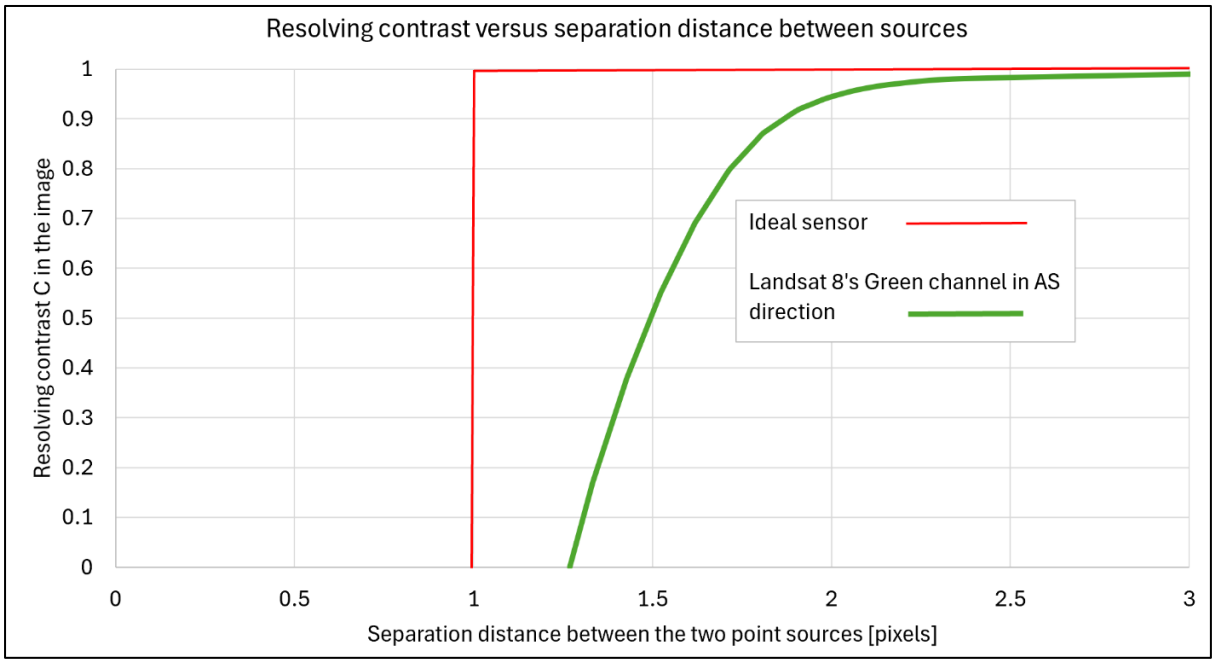

Figure 6.6: Two examples of the computation of image resolving contrast *C* versus separation distance *s* between two-point sources. The red lines show the *C*(*s*) function for the ideal imager, which changes from *C* = 0 to *C* = 1 at *s* = 1 pixel. The green curve shows the *C*(*s*) function for Landsat 8's Green channel in AS direction, in which the contrast starts to gradually increase from *C* = 0 when the separation *s* is greater than 1.27 pixels.

3. Compute resolution distance versus contrast

Invert the $C(s)$ function and define the function $s(C)$ over the domain $0 \leq C \leq C_{max}$ as the Spatial Resolution Function: $SRF(C) = s(C)$. This function gives the SRD as a function of image contrast: $SRD(C) = SRF(C)$.

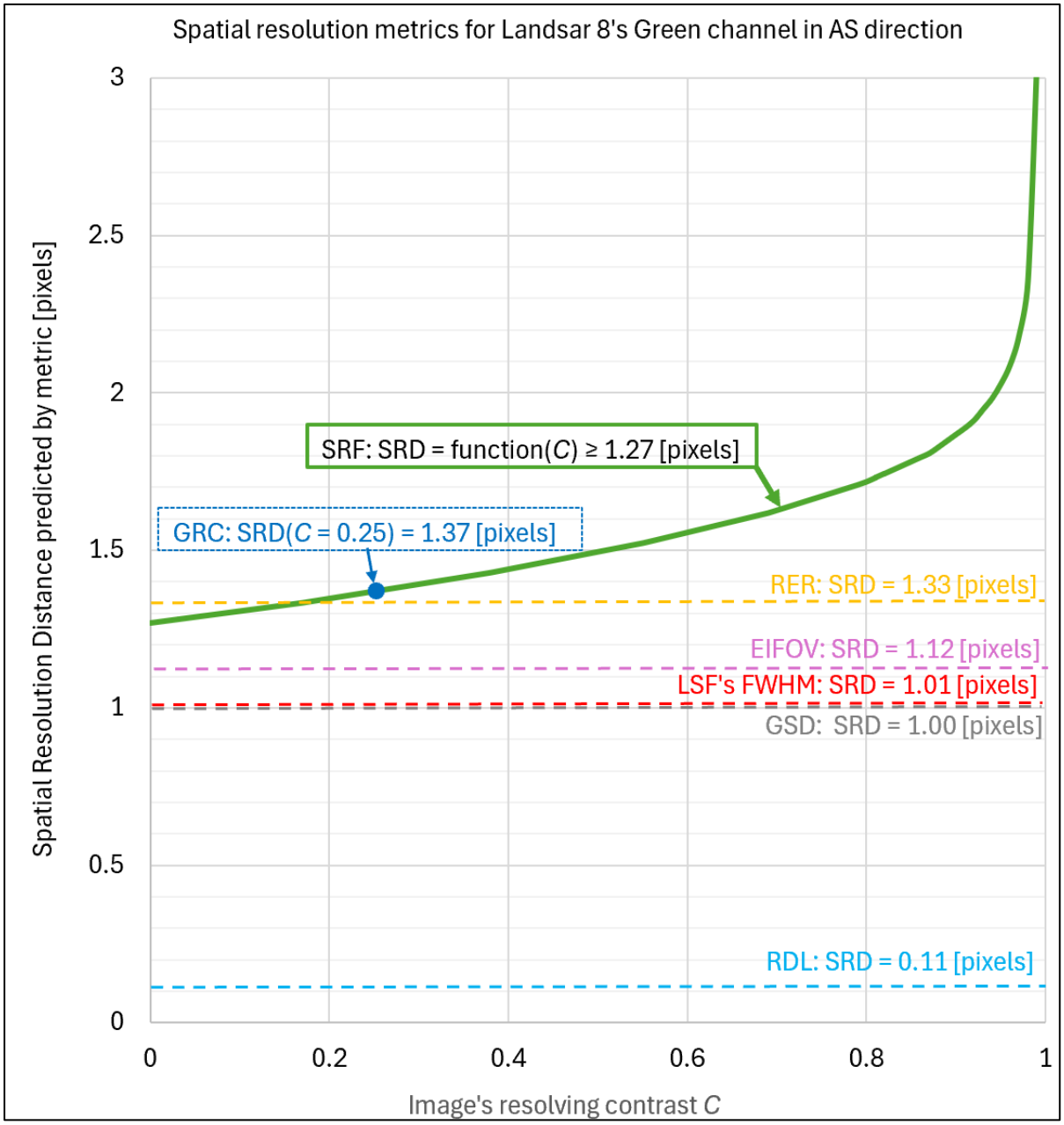

Figure 6.7: Example of the computation of spatial resolution metrics for Landsat 8's Green channel in AS direction. The green curve shows the Spatial resolution Function (SRF), the blue dot on this curve at $C = 0.25$ represents the prediction of the Generalized Rayleigh Criterion (GRC) which is identical to the SRD predicted by the SRF for this same value of contrast. The dashed horizontal lines show, from bottom to top, the SRD predicted by the following metrics: Rayleigh Diffraction Limit (RDL); Ground Sampling Distance (GSD); Full Width at Half Maximum (FWHM) of the Line Spread Function (LSF); Effective Instantaneous Field Of View (EIFOV); and Relative Edge Response (RER). Only the RER metric predicts an SRD that allows some resolving contrast to be obtained in the image, the RDL, GSD, LSF's FWHM and EIFOV metric fail because they predict an SRD at which it is not possible to resolve the two sources.

Figure 6.6 shows an example of the results of the previous stage 2, displaying as a green curve the $C(s)$ function for Landsat 8's Green channel in AS direction. This figure also displays the $C(s)$ function for an ideal sensor using red straight lines. Whereas the resolving contrast for the Green channel increases gradually from zero after a minimum separation of 1.27 pixels, the resolving contrast for the ideal sensor changes abruptly from zero to 100 % when the separation exceeds 1.0 pixel by an infinitesimal amount.

Figure 6.7 shows an example of the results of stage 3, displaying as a green curve the SRF function for Landsat 8's Green channel in AS direction. The SRD predicted by the GRC for $C = 0.25$ is represented by a single blue dot on the SRF curve.

The minimum value of the SRF always occurs for $C = 0$, in this example it is SRF($C = 0$) =1.27 pixels. This minimum no-contrast value is named as Sparrow's limit in analogy with the optical case in which no resolving contrast is obtained (Verhoeven 2019). A small separation distance above Sparrow's limit will give a small contrast, but in practice larger values of contrast may be required to resolve the two sources. The minimum value of contrast will depend on the application at hand and the Signal to Noise Ratio (SNR) of the image (Valenzuela et al. 2022). In any case, it is not possible to resolve two point sources separated at a distance smaller than Sparrow's limit.

The SRDs predicted by some Theoretic and Spatial Response spatial resolution metrics for Landsat 8's Green channel, have been presented in Figure 6.7 as dashed horizontal lines. From the two-point source criterion perspective, most of these metrics fail, as they predict an SRD smaller than 1.27 pixels, which does not allow the sources to be resolved. This is the case of the RDL (SRD = 0.11 pixels), the GSD (SRD = 1.00 pixels), the LSF's FWHM (SRD =1.01 pixels), and the EIFOV (SRD =1.12 pixels). Only the RER metric (SRD =1.33 pixels) provides an SRD prediction for which the sources may be detected as two separate objects in the image.

6.3. Materials and Methods

6.3.1. Selection of imaging sensors and channels

CubeSats have established themselves as one of the most versatile versions of small satellites, allowing an unprecedented temporal resolution in remote sensing from Low Earth Orbit (LEO). The Planet constellation is one of the most successful innovations in CubeSat technology, comprising more than two hundred 3U* ~ 6 kg "SuperDove" satellites in orbit, allowing daily revisit of almost any point of interest over the Earth's surface. This constellation challenges the traditional space agency deployed remote sensing satellites by matching their spectral resolution and attempting to surpass their spatial resolution (Safyan 2015).

SuperDove has been selected as a representative of CubeSat remote sensing satellites because the widespread availability of its images has triggered multiple studies to measure its spatial response (Anger et al. 2019, Gabr et al. 2020, NASA 2020, Saunier 2020, Kim et al. 2021, Bahloul et al. 2021, Saunier and Cocevar 2022). Thus, the spatial response of SuperDove can be assessed more thoroughly than the spatial response of other CubeSat imagers.

Landsat 8 was selected as a representative of traditional remote sensing satellites, because 80 spatial response parameters are available for each one of its channels (USGS 2019). For

* A "U" is the CubeSat unit for mass and volume, which amounts to a cubic volume of one litre (10 ×10 ×10 cm^3) and a weight between 1 and 2 kilograms.

other traditional satellites like Sentinel 2, only two parameters are usually available (Gascon et al. 2017). Thus, Landsat 8 allows a much more accurate spatial response's study than other traditional remote sensing satellites.

To select the channels, it was considered that Planet regularly delivers the average RER for SuperDove in AS and CS directions, but only for its "Green ii" channel (Bahloul et al. 2021). Consequently, the Green ii channel was selected for this study.

The effect of atmospheric turbulence in the spatial response of satellite imagers is heavily dependent on wavelength. Thus, to compare this effect on an equal basis for SuperDove and Landsat 8, the green channel of Landsat 8 that has almost the same wavelength that SuperDoves's Green ii channel was selected.

Therefore, the selection of the imaging channels was conditioned by the RER data released by Planet, and the need to consider two channels of similar wavelengths. The relevant parameters of the selected channels, their sensors and their satellite platforms are presented in Table 6.3. These parameters will be considered for the computation of the spatial response of the channels and in the computation of the SRD predicted by the different spatial resolution metrics.

Table 6.3: Parameters of SuperDove and Landsat-8 satellites, their remote sensing instruments, and their green channels.

Parameter	SuperDove	Landsat 8
Satellite mass (kg)	5.8	2623 (at launch)
Orbital height (km)	475	705
Sensor	PSBlue / PSB.SD	OLI
Optical aperture's diameter (mm)	90	135 (equivalent; non-circular)
Linear obstruction ratio ε	0.43 (estimated)	0 (clear aperture)
Pixel pitch p (μm)	5.5	36
Focal length F (mm)	700	886
Channel number – name	4 – Green ii	3 – Green
Centre wavelength λ (nm)	565	562
Channel bandwidth (nm)	36	59
Nadir looking GSD (m)	3.7 (native) / 3 (L3B)	30
IFOV = p/F (μrad)	7.9 (native) / 5.6 (L3B)	41
Optical factor Q	0.80 (native) / 1.12 (L3B)	0.10
Along scan oversampling factor	1.0 (assumed)	0.85
References	Safyan 2015, Bahloul et al. 2021, Fernandez-Saldivar et al. 2020.	Figoski et al. 2009, USGS (n.d.).

6.3.2. Computation of the Spatial Response

6.3.2.1. *General procedure*

The spatial response of the green channels of SuperDove and Landsat-8 will be computed using the OTF methodology, applying the following six-step procedure for each channel:

1. Collect data about the channel's sensor.

2. Collect data about the channel's spatial response measurements and select the key measurements that the OTF model must match.

3. Build an OTF model of the channel using the sensor's data collected in step 1.

4. Use the OTF model to compute the channel's spatial response functions required to match the key measurements selected in step 2 (Figure 6.2).

5. Adjust the unknown parameters of the OTF model so that the spatial response predicted by the model matches the key measurements.

6. The OTF model that best matches the key measurements is selected to describe the spatial response of the channel.

As shown in Figure 6.2, once the 2D OTF is known all the other spatial response functions can be found by using the required mathematical procedures. For SuperDove, the RER in AS and CS directions were selected as key measurements. As illustrated in Figure 6.3(*a*), the RER is a property of the ESF, so the ESF in AS and CS directions are the spatial response functions required to match these measurements. For Landsat 8, the set of LSF measurements in AS and CS directions were selected as key measurements, so the LSF in AS and CS directions are the spatial response function required to match these measurements.

6.3.2.2. *Optical Transfer Function model*

The basic assumption of the OTF methodology is that the system OTF is equal to the product of the OTF of all the system's components that contribute to the spatial response. A wide variety of components can be considered, and for a given component, many different OTF models may be available (Cota et al. 2010, Fiete 2010, Fiete and Paul 2014, Boreman 2021).

To build the OTF models for the Green channels of SuperDove and Landsat 8, the following OTF components have been selected (the specific OTF equation used to model each one of these components is indicated within parenthesis):

1. Ideal square detectors with partial fill factor (Fiete and Paul 2014, equation 21).

2. Ideal annular optical aperture (Fiete 2010, equation 5.35).

3. Ideal scan in the Along Scan (AS) direction considering the possibility of oversampling (Fiete and Paul 2014, equation 14).

4. Random optical aberrations characterized by their Root Mean Square (RMS) wavefront error using Shannon's parabolic OTF model (Fiete 2010, equation 5.49).

5. LOS jitter characterized by the standard deviation of the Gaussian OTF model (Fiete 2010, equation 7.11).

6. Charge diffusion in detectors characterized by their equivalent charge diffusion length using a Lorentzian OTF model (Davis et al. 1998).

7. Charge transfer inefficiency (Fiete 2010, equation 6.34).

8. Atmospheric turbulence (Li et al. 2012, equation 8).

The first three OTF components model the three basic elements of an ideal satellite imager: detector, optics, and scan. Component 4 models the degradation of the optical system, component 5 models the degradation of the scan movement, components 6 and 7 model the degradations of the detectors, and component 8 models the degradation of the whole system due to an imperfect transmission media between the scene and the sensor.

A more rigorous OTF model should consider the computation of the polychromatic OTF, which must be calculated in terms of the spectral response of the channels (Cota et al. 2010). But, as shown in Table 6.3, for the two Green channels of interest the spectral bandwidth is much smaller than the centre wavelength, so the monochromatic OTF is a good approximation to the polychromatic OTF. Therefore, a monochromatic OTF will be assumed. This assumption allows a considerable simplification as there is no need to consider the spectral response of the channels, and to compute the OTF at each wavelength within this response, only the computation of the OTF at the centre wavelength is required.

It will be assumed that the key spatial response measurements, that the OTF model will match, have been performed in a "baseline" condition, named Case 1. This baseline case has negligible atmospheric turbulence (OTF component 8) and a low level of jitter (OTF component 5). To study the stability of the spatial response, two other cases will be considered: strong turbulence and high jitter. Thus, the OTF will be computed for the Green channels of SuperDove and Landsat 8, in the three following cases:

Case 1: Baseline case with low jitter and negligible turbulence.

Case 2: Turbulent case with low jitter and strong turbulence.

Case 3: Jitter case with high jitter and negligible turbulence.

6.3.2.3. *General overview of the Green channels' OTF models*

The OTF models of the Green channels were initially built by considering the parameters of Table 6.3. For SuperDove, the OTF model of the Level 3 B (L3B) image was built using the methods described in section 6.3.2.4. For Landsat 8, the OTF model was built using the methods described in section 6.3.2.5.

The unknown parameters of both OTF models were adjusted so that the predicted spatial response matches the key spatial response measurements. These key measurements are shown in Table 6.4 (second and third lines) and Figure 6.8 (red dots), for SuperDove and Landsat 8, respectively. The final values assumed for these unknown parameters are presented in Table 6.5.

Table 6.4: Spatial response parameters measured for SuperDove's L3B Green ii channel images.

Parameter	Value	References
Average RER in along-track direction	0.234	Bahloul et al. 2021, 21
Average RER in cross-track direction	0.224	
RER (Unspecified direction)	0.25	Kim et al. 2021,16
LSF's FWHM (Unspecified direction)	3.7 pixels	
LSF's FWHM (Unspecified direction)	6 pixels	Saunier and Cocevar 2022, 28

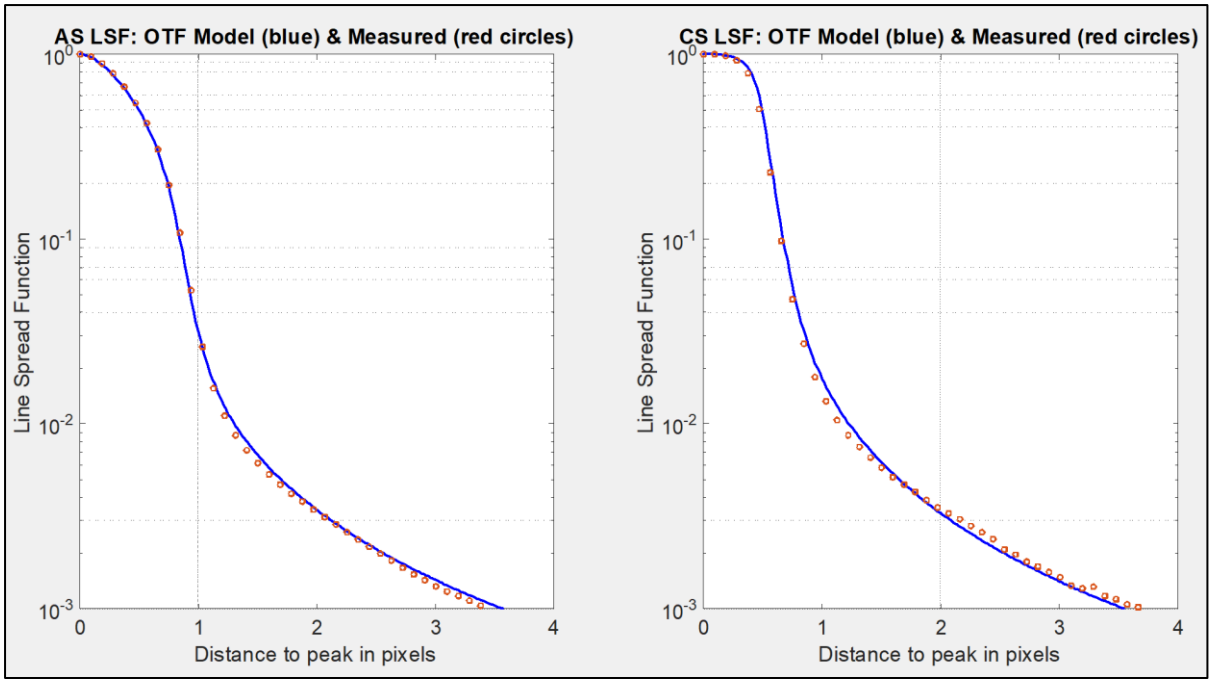

Figure 6.8: Line Spread Functions for Landsat 8's Green Channel in Along Scan (AS) and Cross Scan (CS) directions. The Line Spread Function (LSF) predicted by the OTF model is presented as a blue line, the values measured for the LSF are presented as red circles. The unknown parameters of the OTF model were adjusted to provide the best possible match in both directions.

Table 6.5: Values assumed for the unknown OTF parameters of the Green channels. The jitter parameter σ represents low jitter, so it is not applicable to Case 3.

Parameter	SuperDove	Landsat 8
Along scan (AS) pixel fill factor	1.00	0.92
Cross scan (CS) pixel fill factor	1.00	1.00
RMS wavefront error (wavelengths)	0.13	0.095
Standard deviation of LOS jitter σ (pixels)	0.53	0.02
Equivalent charge diffusion length (pixels)	0.45	0.07
Charge transfer inefficiency (percent)	0.012	0.00
Number of charge transfers	8800	N/A

The values assumed for the unknown parameters of Table 6.5 are not necessarily representative of the actual values, as the channel's spatial response is defined by the product of its OTF components. Thus, different combinations of parameters at the component level can be used to match the key measurements.

Furthermore, different models for some OTF components or even different OTF components could have also been used to match the key measurements. For example, the OTF component that describes the defocus issues of SuperDove (Fernandez-Saldivar et al. 2020) has not been considered in the model of section 6.3.2.2, so in our model some actual (unknown) defocus may have been indirectly considered by assuming a jitter deviation larger than the actual deviation.

For our purposes, the modelling differences between the actual and the assumed OTF components are not critical, providing the system's spatial response predicted by the OTF model is similar to the actual spatial response.

6.3.2.4. *SuperDove's Green channel model*

The computation of the PSF of Planet's Dove satellites has been considered unfeasible due to the complex image processing that is performed to deliver the final product and the limited design data available about the optics, detectors, and resampling kernels (Saunier 2020, 28). This consideration may have also been conditioned by the inconsistencies of image quality measurements between different Dove satellites (Saunier 2020, 27).

Although these same considerations apply to SuperDove, we have developed an approximate OTF model that matches the average RER values in AS and CS directions, delivered by Planet for SuperDove's L3B orthorectified image (GSD = 3 m). These RER values are presented in the second and third lines of Table 6.4, being roughly similar to the RER value measured by Kim et al. (2021), which is shown in the fourth line of this later table.

Planet computes the RER of the resampled 3-meter L3B image by multiplying the RER of the native image by a constant factor equal to the ratio between the resampled GSD (3 m) and the average native GSD. This constant is calculated by Planet using several edge targets around the world and a large number of images, it is disseminated four times a year being relatively stable with time, for this study the value 0.717 employed by Bahloul et al. (2021, 21) will be used.

Planet assumes that the RERs of the L3B image can be calculated from the native image RERs by considering that the effective L3B pixel pitch is 0.717 times the actual pixel pitch (Bahloul et al. 2021, 21). We use this same assumption to obtain the L3B values for $Q = 0.80/0.717 = 1.12$ and IFOV = $7.86 \times 0.717 = 5.6$ μrad.

In satellite imagers the Along Scan (AS) RER is usually smaller than the Cross Scan (CS) RER, because the scan movement degrades the spatial response only in AS direction. SuperDove uses a push-frame mode to capture its images, so the scan direction is given by the track direction. The RER values disseminated by Planet, consistently indicate that the cross-track (CS) response is more degraded than the along-track (AS) response. To account for this issue in the OTF model, we assume that the relative excess in CS degradation is due to charge transfer inefficiency, an OTF component which does not degrade the spatial response in AS direction (Fiete 2010, equation 6.34).

With this additional CS OTF component, the unknown parameters of the OTF model can be adjusted to match Planet's L3B average RER values within the three significant figures given in Table 6.4. The resultant values for unknown parameters are shown in the second column of Table 6.5.

The final result is a rough OTF model for the Green ii channel, which uses the effective pixel pitch to consider the image reconstruction process required to deliver a 3 m GSD using native images with GSD ≥ 3.7 m. A more accurate model should consider the polychromatic OTF, an additional defocus OTF component, the native image parameters, and the additional OTF components that are required to describe the image resampling and reconstruction processes.

6.3.2.5. *Landsat-8's Green channel model*

The LSFs of Landsat 8 were measured before launch for all channels in AS and CS directions, so that their in-orbit spatial response could be accurately characterized (USGS 2019). The unknown OTF parameters of the Green channel model were adjusted to match the measured LSFs in both directions. Figure 6.8 shows the LSFs predicted by the OTF model against the measurements; a good match is obtained even down to three orders of magnitude

below the peak response. The values assumed for the unknown parameters are shown in the third column of Table 6.5.

The final result is an approximate OTF model that uses an equivalent circular aperture to consider a non-circular optical aperture of undisclosed shape (Bergstrom and Dissly 2012, 4). A more accurate OTF model should consider the polychromatic OTF, the actual shape of the optical aperture, and the corresponding difference of the optical factors in AS and CS directions.

6.3.3. Computation of Spatial Response Function

Once the OTF model is built, the computation of the SRD predicted by the RER, LSF's FWHM, and EIFOV metrics is straightforward. The ESF, LSF, and OTF-1D are computed in AS and CS directions using the procedures indicated in Figure 6.2, and then the parameters required to compute the SRD predicted by these metrics are found as illustrated in Figure 6.3.

The computation of the SRF is more involved. Once the PSF is known, the SRF can be computed in AS and CS directions using the following procedure (Valenzuela et al. 2022):

1. Set Computational Framework.

   a. Compute the PSF of the channel of interest. Assume that the PSF(x, y) is computed at a set of discrete points such that $x = n \cdot \delta x$ and $y = n \cdot \delta y$, where PSF(0, 0) = 1 is the peak PSF, $\delta x = \delta y$, and $n = 0, 1, 2, 3, \ldots$

   b. Consider an ideal scene with only two point sources of equal intensity separated at a distance $s \cdot$GSD m. Thus, the separation between the geometrical projections of the two point sources in the image plane is s pixels.

   c. Assume that the projections of the two sources in the image plane are symmetrical with respect to a pixel centre named Pixel 0, as is illustrated in Figure 6.9. In this figure, these projections are represented as black dots, and the centre of Pixel 0 is represented by the symbol "⊕". As discussed in section 6.2.2.3, and illustrated in Figure 6.6 with red lines, the centre symmetry assumption allows SRD = SRF = GSD for an ideal imager.

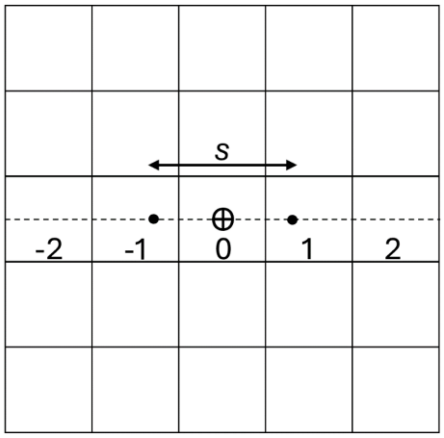

Figure 6.9: Conditions required to compute the Spatial Resolutions Function (SRF) in horizontal direction. The projections of the two point sources in the image plane are represented as black dots. These two projections are symmetrical with respect to the centre of Pixel 0 depicted by the symbol "⊕". The two point sources are separated at a variable distance "s" by moving along the dashed horizontal straight line that passes through the centre of Pixel 0.

d. Assume that the separation distance s is varied by moving the two point sources along a straight line, orientated in the direction of interest (AS or CS), passing through the centre of Pixel 0. In Figure 6.9 this line is represented as a dashed line orientated in horizontal direction. This assumption maximizes the signal I_{max} and provides an additional symmetry condition in the image plane that simplifies the search for the pixel with I_{max}.

e. The separation s must be an integer multiple of $2 \cdot \delta x$ so that the SRF can be computed without the need of interpolation, with a resolution $\delta s = 2 \cdot \delta x$.

f. For a given separation s, neglect noise and compute the signal for all the pixels of the image by considering the superposition of two identical Point Spread Functions (PSFs) whose peak values in the image plane are located at the projection of the two sources. The signal in any pixel is computed as the sum of the two PSFs evaluated at the centre of this pixel.

g. For each separation distance s find the signal I_0 at Pixel 0 and the maximum signal value I_{max} elsewhere, different from I_0.

h. Compute the resolving contrast in the image plane as $C(s) = (I_{max} - I_0)/I_{max}$.

i. If $I_{max} < I_0$ then consider that $C(s) < 0$.

2. Compute contrast versus separation.

a. Assume an initial separation s slightly less than one pixel.

b. Compute the resolving contrast $C(s)$ for this separation, it should be negative.

c. Increase the separation distance by an amount $\delta s = 2 \cdot \delta x$ and compute the resolving contrast $C(s)$ for this new separation.

d. Repeat previous step "c" until $C(s) > C_{max}$ where C_{max} is the maximum resolving contrast of practical interest. A value $C_{max} = 0.99$ was used in our computations.

e. Interpolate between negative and positive $C(s)$ values to find the separation s_o such that $C(s_o) = 0$ and $C(s > s_o) > 0$. This separation is named the Sparrow limit of the digital sensor. The restriction $C(s > s_o) > 0$ is necessary because some channels with obstructed optical apertures may have more than one root for $C(s) = 0$.

3. Compute resolution distance versus contrast.

a. Invert $C(s)$ to present $s(C)$ between $C = 0$ and $C = C_{max}$.

b. Define SRF = $s(C)$ as the function that yields the SRD as a function of the resolving contrast in the image plane.

c. Designate the SRF in pixel units as SRF = $R(C)$.

d. Compute the SRD in the ground plane as SRD = $R(C) \cdot$GSD.

6.3.4. Computation of Resolution Degradation Index

An ideal sensor has the spatial response presented in Figure 6.1(*a*). This response requires a null optical factor ($Q = 0$) which is impossible to achieve in practice as it requires either an infinite diameter for the optical aperture ($D \rightarrow \infty$) or an infinite pixel pitch ($p \rightarrow \infty$).

We define a "perfect" sensor as a hypothetical sensor that has identical parameters to the actual sensor, except for those parameters that describe the imperfections of the imaging system which are assumed to be null.

In our case, the spatial response of a perfect sensor can be found by using the same OTF model of Table 6.5, assuming null values for the four parameters which quantify sensor's imperfections (wavefront error, jitter deviation, diffusion length and transfer inefficiency).

The Resolution Degradation Index of an imager is defined as the percent increase in the mean SRF of a perfect sensor due to the imperfections of the actual sensor. This index will be computed for SuperDove and Landsat 8 Green channels in their baseline condition (Case 1) to gauge how much they deviate from a perfect imaging channel.

If the index is a few percent the sensor is considered to be of high quality, if the index is high the sensor is considered to be of low quality. This index measures degradations with respect to a perfect (not ideal!) performance, so it does not penalize sensors for having a high *Q* and consequently a high SRD/GSD ratio; it penalizes sensors for having high degradations.

6.3.5. Instability of the spatial response

6.3.5.1. *Evidence of instability*

The instability of the spatial response is present in any imaging sensor which must operate in the space environment. For example, by using convex mirrors as point-sources to achieve accurate in-orbit measurements of the spatial response for the panchromatic channel of Ikonos, a minor instability in its spatial response could be observed on different images taken during the same overpass. This instability was tentatively attributed to jitter or atmospheric variations (Schiller et al. 2012, 13).

The Full Width at Half Maximum (FWHM) of the Line Spread Function (LSF) of SuperDove's channels has been measured to be 3.65 ± 0.05 pixels (Kim et al. 2021) and 6.0 pixels (Saunier and Cocevar 2022). This large difference between FWHM measurement results was also observed for the channels of SkySat, the newest member of PlanetScope constellation, its measured LSF's FWHM were 2.4 ± 0.4 pixels (Saunier et al. 2020) and 4.0 ± 0.3 pixels (Kim et al. 2022).

These large differences on the width of the spatial response have a huge impact on the radiometric performance. For example, if the PSF has axial symmetry and its diameter changes from 3.65 to 6.0 pixels, this means that in the image, the energy detected due to one point source in the scene, which was initially distributed over $(\pi/4)\cdot 3.65\times 3.65 \approx 10$ pixels, will now be distributed over $(\pi/4)\cdot 6\times 6 \approx 28$ pixels. So, a variation of $6.0/3.65 \approx 1.6$ times in the width of the spatial response will create a variation of $(6.0/3.65)^2 \approx 2.7$ times in the radiometric performance. This means, that for the same scene, small features that were detected with a narrow response may be undetected with a broader response; the two images are essentially different.

The high discrepancies between the two sets of LSF's FWHM measurements for SuperDove (Kim et al. 2021, Saunier and Cocevar 2022) are coherent with the following findings regarding the instability of the spatial and radiometric performance of Planet's images:

1. Large differences between two SuperDove images of the same scene (Frazier and Hemingway 2021).

2. Large standard deviation measured for the image sharpness of any given satellite within the Planet constellation (Anger et al. 2019).

3. Significant differences in average image sharpness between different satellites of the Planet constellation (Anger et al. 2019).

4. Low utility of Planet images for time series analysis (NASA 2020, 19).

5. Large inconsistencies of image quality measurements between different Dove satellites (Saunier 2020, 27).

One of the factors that explains the difference in the spatial response between two SuperDove satellites is their wide manufacturing tolerances; to pass the pre-launch test, the EIFOV of a SuperDove imager can be anywhere between 3.3 and 5.0 pixels (Fernandez-Saldivar et al. 2020, 19).

The instability of the spatial response for the same SuperDove satellite can be attributed to dynamic factors that fluctuate markedly over time, such as Line Of Sight (LOS) micro vibrations (jitter) during integration time (Shields et al. 2017) and atmospheric turbulence (Li et al. 2017). The relevant material regarding atmospheric turbulence and spacecraft jitter is presented in what follows.

6.3.5.2. *Atmospheric turbulence*

The spatial response of Earth observing satellites depends on the atmospheric parameters, among others, on the intensity of air turbulence and the distribution of aerosols in the optical path. We consider here only turbulence which is due to random variations in the atmospheric refraction index. The exponential model that accounts for the OTF component due to turbulence is well known (Li et al. 2012, equation 8). For short integration times, such as those employed in SuperDove and Landsat 8, this model can be written in the form:

$$OTF_{turbulence} = \exp\{ - 57.53 \cdot K \cdot (\lambda)^{-1/3} \cdot (f/(IFOV))^{5/3} \cdot [1 - 0.5 \cdot (f \cdot Q)^{1/3}] \} \quad (3)$$

Where K is the turbulence strength parameter in $m^{-2/3}$, λ is the wavelength in meters, f is the spatial frequency in cycles per pixel, IFOV is the Instantaneous Field Of View in radians, and Q is the optical factor. The parameter K fluctuates typically between $5 \cdot 10^{-13}$ $m^{-2/3}$ and $5 \cdot 10^{-11}$ $m^{-2/3}$ for weak and strong turbulence, respectively (Li et al. 2012). For our purposes, we assume $K = 2 \cdot 10^{-11}$ $m^{-2/3}$ for Case 2 and neglect atmospheric effects in Cases 1 and 3 ($K = 0$).

6.3.5.3. *Line of sight jitter*

Spacecraft jitter is a high frequency vibration of small amplitude generated by onboard devices with rotating or moving mechanisms, such as reaction wheels, momentum wheels, cryocoolers, cryopumps, filter wheels and scanning mirrors (Dennehy and Alvarez-Salazar

2019). Jitter induces a vibration on the line of sight of the satellite sensor during its integration time. This vibration may be more detrimental for sensors on board small satellites, due to their proximity to the jitter source, the size limitations for jitter damping mechanisms and the low inertia of the spacecraft (NRC 2000, 32).

An inverse proportion between satellite launch mass and pointing stability (measured in angular units) has been suggested (Pong 2018, figure 1). If this rule of thumb would apply to the high frequency jitter, then, according to the masses indicated in Table 6.3, SuperDove's jitter should be more than two orders of magnitude larger than Landsat 8's jitter.

For attitude control, SuperDove uses reaction wheels which change their speed due to manoeuvres and external disturbances (Safyan 2015). Certain wheel speeds can excite structural modes of the satellite, generating a peak jitter much larger than the baseline jitter. For example, the peak jitter of a 6U Cubesat was estimated to be 39 μrad, a value 80 times larger than its baseline jitter (Shields et al. 2017). This later value exemplifies the large jitter fluctuations that can be expected in a CubeSat due to variations in the speed of its reaction wheels.

No information was found about the LOS jitter for SuperDove. For a 3U Cubesat with three reaction wheels, the 1 sigma jitter values were between 42 and 107 μrad for an integration time of 10 seconds (Mason et al. 2017); much smaller values may be expected for SuperDove's integration time which is about 0.5 ms (Bahloul et al. 2021, 8). In the Green channel's model of Table 6.5, the 1 sigma baseline jitter for SuperDove was arbitrarily assumed to be $\sigma = 2.97$ μrad to match the measured average RERs of Table 6.4. This value must be divided by the L3B IFOV of Table 6.3 to be converted to the pixel units of Table 6.5.

In Landsat 8 the main jitter source for the OLI sensor was the cryocooler of the TIRS instrument. In the worst simulated scenario, OLI's OTF at Nyquist frequency was reduced by a factor 0.977 due to jitter (Schott et al. 2012, figure 2.6). In this later study the following Gaussian jitter model assumed in section 6.3.2.2 was validated (Schott et al. 2012, 2485):

$$OTF_{jitter} = \exp[- 2\cdot(\pi\cdot\sigma\cdot f /(IFOV))^2] \quad (4)$$

Where σ is the 1 sigma LOS jitter in radians, f is the spatial frequency in cycles per pixel, and IFOV is the Instantaneous Field Of View in radians. If $OTF_{jitter} = 0.977$ at Nyquist frequency ($f = 0.5$) then $\sigma = 2.8$ μrad. This jitter level was considered a potential problem for OLI, so a sophisticated vibration isolation system was designed and implemented (Robinson and Tonn 2015). In the Green channel's model of Table 6.5, $\sigma = 0.82$ μrad was arbitrarily assumed for Landsat 8 to match the measured spatial responses of Figure 6.8. This value must be divided by the Landsat 8's IFOV of Table 6.3 to be converted to the pixel units of Table 6.5.

Considering the limited information available, a peak jitter $\sigma = 10$ μrad was tentatively assumed to quantify the effect of a worst-case jitter due to changes in the speed of the reaction wheels. The evidence indicates that although this jitter level is feasible for a 3U CubeSat it is highly unlikely for Landsat 8, nevertheless – for the sake of comparison – the same peak jitter will be assumed in Case 3 for both satellites.

6.4. Results

6.4.1. SuperDove

Figure 6.10 presents the SRF for SuperDove's Green ii channel and for Landsat 8's Green channel for the three cases defined in section 6.3.2.2. The spatial response metrics for these same channels and cases are presented in Table 6.6. These results are analysed in what follows.

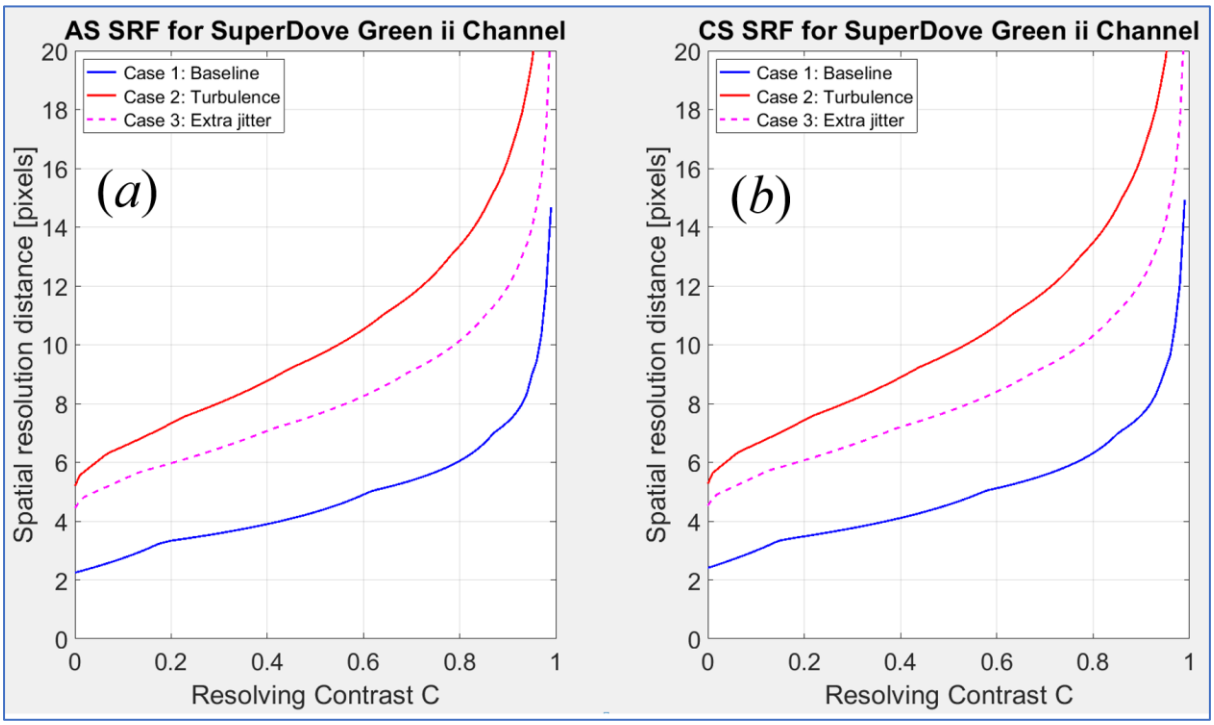

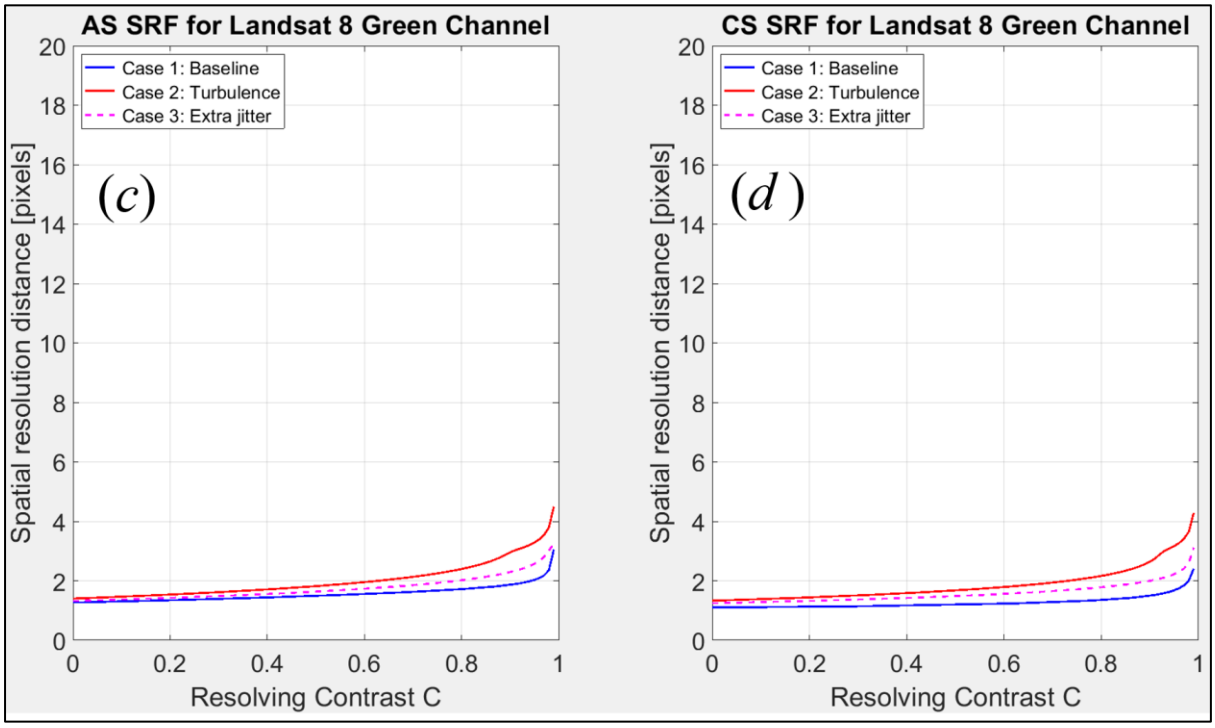

Figure 6.10: Spatial Resolution Function of SuperDove's Green ii channel (upper figures *a* and *b*) and Landsat 8's Green channel (lower figures *c* and *d*) in Along Scan (AS) direction (left figures *a* and *c*) and Cross Scan (CS) direction (right figures *b* and *d*) for three cases. Case 1 (blue line) has moderate jitter and no turbulence. Case 2 (red line) has moderate jitter and strong turbulence. Case 3 (slashed magenta line) has high jitter and no turbulence.

Table 6.6: Spatial resolution metrics for (*a*) SuperDove's Green ii channel and (*b*) Landsat 8's Green channel, in three different cases.

Channel	Spatial resolution metric	Along Scan (AS)			Cross Scan (CS)		
		Case 1	Case 2	Case 3	Case 1	Case 2	Case 3
(*a*) SuperDove's Green ii channel	Sparrow's limit $R(0)$ (pixels)	2.25	5.19	4.45	2.41	5.27	4.53
	Mean SRF $\langle R \rangle$ (pixels)	4.81	10.7	8.24	5.03	10.8	8.38
	EIFOV (pixels)	4.94	10.3	7.31	5.14	10.4	7.42
	PSF's FWHM (pixels)	2.83	6.57	5.32	3.02	6.65	5.41
	LSF's FWHM (pixels)	3.21	7.15	5.54	3.41	7.24	5.64
	1/RER (pixels)	4.27	8.92	6.65	4.47	9.02	6.76
(*b*) Landsat 8's Green channel	Sparrow's limit $R(0)$ (pixels)	1.27	1.40	1.32	1.10	1.33	1.25
	Mean SRF $\langle R \rangle$ (pixels)	1.55	2.01	1.74	1.26	1.86	1.58
	EIFOV (pixels)	1.12	1.62	1.17	0.95	1.49	0.96
	PSF's FWHM (pixels)	1.00	1.29	1.06	1.00	1.19	1.01
	LSF's FWHM (pixels)	1.01	1.33	1.07	1.01	1.22	1.01
	1/RER (pixels)	1.33	1.69	1.37	1.17	1.59	1.18

6.4.1.1. *Case 1 (Baseline)*

Case 1 for SuperDove has been tailored to match Planet's RER measurement; 0.22 and 0.23 in AS and CS directions, respectively. These values are similar to the RER = 0.25 measured for SuperDove by Kim et al. (2021, 16).

The LSF's FWHMs predicted by the OTF model are 3.2 and 3.4 pixels in AS and CS directions, respectively. These values are similar to the FWHM = 3.7 pixels measured for SuperDove by Kim et al. (2021, 16).

The mean values of the SRF are 4.8 and 5.0 pixels in AS and CS directions, respectively. These values agree with the SRD = 15 m measured by NASA (2020, 12) for the retrieval of aerosol optical depth using Planet's images. For SuperDove (GSD = 3 m) so SRD = 15 m is equivalent to SRD = 5.0 pixels.

The SRF increases by a factor of about six when the resolving contrast increases from 0 % to 99 %. For example, the SRD predicted by the SRF metric in AS direction increases from 2.3 to 14.7 pixels. Thus, the SRD is strongly dependent on the minimum level of resolving contrast that can be detected in the image. This minimum level depends on the SNR (Valenzuela et al. 2022), so a strong dependency between SRD and SNR is expected for SuperDove.

These results indicate that the baseline case is representative of the conditions in which the images used for the measurements of Planet (Bahloul et al. 2021), Kim et al. (2021) and NASA (2020, 12) were obtained.

6.4.1.2. *Case 2 (Turbulence)*

Case 2 is representative of conditions of strong turbulence. As expected, the difference between the spatial responses in AS and CS directions is reduced, because turbulence is an isotropic OTF component that becomes predominant.

The OTF model predicts LSF's FWHM ≈ 7.2 pixels for AS and CS directions; more than two times larger than the baseline case. The predicted FWHM is somewhat larger than the LSF's FWHM = 6 pixels measured for SuperDove by Saunier and Covecar (2022, 28). For weaker conditions of turbulence an exact match with this later measurement can be obtained.

Just like in Case 1, the SRF increases by a factor of six when the resolving contrast increases from 0 % to 99 %, increasing from about 5 to 30 pixels in both directions. The mean SRF is roughly eleven pixels in both directions. With respect to Case 1, strong turbulence degrades SuperDove's SRD by a factor of two.

These results indicate that fluctuations of atmospheric turbulence can induce in SuperDove's images variations by a factor of two, on its SRD and on the width of its spatial response.

6.4.1.3. *Case 3 (Extra jitter)*

Case 3 is representative of conditions of peak spacecraft jitter. The results obtained are intermediate between Case1 and Case 3, being more near to the later.

The OTF model predicts LSF's FWHM ≈ 5.6 pixels for AS and CS directions. This value is near the LSF's FWHM = 6 pixels measured for SuperDove by Saunier and Covecar (2022, 28).

These results indicate that the images used in the measurements of Saunier and Cocevar (2022, 28) could have been obtained under conditions degraded by atmospheric turbulence and/or spacecraft jitter.

6.4.1.4. *Resolution Degradation Index*

The Resolution Degradation Index for the Green ii channel of SuperDove was computed for Case 1, by comparing the mean SRFs of Table 6.6(*a*) with the ones obtained by assuming a "perfect" SuperDove imager with null values for the four parameters of Table 6.5 which gauge sensor imperfections (wavefront error, jitter deviation, diffusion length and transfer inefficiency).

Due to sensor imperfections, the mean SRF is degraded 97 % and 134 % for AS and CS directions, respectively. This means that the mean SRD of this channel is degraded by a factor of roughly two, due to sensor and platform imperfections. Higher degradations are obtained due to extra jitter and turbulence.

6.4.1.5. *Conclusion*

The overall conclusion is that the SRF metric predicts that the mean SRD of SuperDove is about five pixels in baseline conditions and about eleven pixels under strong atmospheric turbulence. This conclusion is coherent with:

1. The SRD reported by NASA (2020, 12) for the measurement of aerosol optical depth

2. The discrepancies between the spatial response measurements of SuperDove performed by the United States Geological Survey (Kim et al. 2021) and the European Space Agency (Saunier and Cocevar 2022).

3. The instabilities reported about the spatial and radiometric performance of Planet's images (Anger et al. 2019, NASA 2020, Saunier 2020, Frazier and Hemingway 2021).

4. The SRD values predicted by the EIFOV and RER metrics.

6.4.2. Landsat 8

Figures 6.10(*c*) and 6.10(*d*) presents the SRF for Landsat 8's Green channel in the three cases defined in section 6.3.2.2, for AS and CS directions, respectively. The spatial response metrics for these same cases are presented in Table 6.6(*b*).

In the baseline condition (Case 1) the SRD predicted by the SRF metric increases by a factor of 2.4 when the resolving contrast increases from 0 % to 99 %, for example, the SRF in AS direction increases from 1.3 to 3.1 pixels. This later increase factor was 6.4 for SuperDove, thus, a dependency between SRD and SNR is also expected for Landsat 8, but 6.4/2.4 = 2.7 times weaker than the one expected for SuperDove.

The SRF in AS direction increases from 1.4 to 4.5 pixels in Case 2. Thus, strong turbulence degrades Landsat 8's spatial resolution, very slightly at low contrasts but notably at high contrasts. Turbulence degrades the mean SRF by a factor of 1.3 and 1.5 in AS and CS directions, respectively. This same degradation factor was 2.2 for SuperDove, so Landsat 8's SRD is less susceptible to turbulence fluctuations.

Case 3 is intermediate between Cases 1 and 2. It must be stressed that the jitter assumed for Case 3 (10 μrad) is representative of CubeSats, but it is not representative of Landsat 8. If instead, the maximum level of jitter (2.8 μrad) considered in Landsat 8 study (Schott et al. 2012) – before jitter damping devices were implemented – is assumed for Case 3, then this case would be almost identical to Case 1. Thus, with the implementation of the damping devices, jitter is not expected to be an issue for Landsat 8.

The Resolution Degradation Index for the Green channel of Landsat 8 was computed for Case 1. The mean SRF is degraded 4 % and 13 % for AS and CS directions, respectively. This means that the SRD of this channel is only slightly degraded due to sensor imperfections. A higher degradation is obtained in the presence of turbulence.

The SRF metric predicts that the average SRD of Landsat 8, computed as the average of the mean SRF values in AS and CS directions, is 1.4 pixels for baseline conditions and 1.9 pixels under strong atmospheric turbulence.

The overall conclusion is that the SRD of Landsat 8 is almost insensitive to jitter fluctuations and that is moderately affected by strong atmospheric turbulence. This conclusion is coherent with the stringent radiometric stability requirements established for Landsat 8 (Knight and Kvaran 2014, table 1).

6.4.3. Assessment of spatial resolution metrics

The axes of Figures 6.10(*a*), 6.10 (*b*), 6.10(*c*) and 6.10(*d*) have the same scales to illustrate the very large difference in SRD between SuperDove and Landsat 8. For SuperDove the SRD predicted by the SRF fluctuates between 2 and more than 20 times the GSD (Figures 6.10(*a*) and 6.10(*b*)). For Landsat 8 the SRD predicted by the SRF fluctuates between one and three GSDs (Figures 10(*c*) and 10(*d*)). The first conclusion is that the GSD is a convenient unit

to measure the SRD in the ground plane, but that it should not be confused with the SRD, as SRD > GSD in all practical cases.

Figure 6.10 illustrates that to specify the SRD without defining the resolving contrast can be highly misleading. For example, for Case 1 in AS direction it could be specified that the SRD of SuperDove is 2.25 pixels because $R(0) = 2.25$, and that the SRD of Landsat 8 is 3.05 pixels because $R(0.99) = 3.05$. The specification is correct but incomplete and biased as the specified distances are for contrasts of 0 % and 99 %, respectively. From this biased specification it may be erroneously concluded that SuperDove has an SRD advantage of 3.05 - 2.25 = 0.8 pixels. An unbiased comparison can be made if 0 % or 99 % contrast is simultaneously considered for both channels, concluding that Landsat 8 has a resolution advantage over SuperDove of 1.0 or 11.6 pixels, respectively. The second conclusion is that is meaningless to specify the SRD without indicating the resolving contrast.

The third conclusion is that the EIFOV metric fails for low optical factors. This is evident from Table 6.6(*b*); in Cases 1 and 3 it predicts an SRD smaller than Sparrow's limit. But, for $Q > 1$, the EIFOV could be suitable as it shows for SuperDove a very good agreement with the mean SRF value (Table 6.6(*a*)).

The fourth conclusion is that the PSF's FWHM and LSF's FWHM metrics fail for low optical factors. This is evident from Table 6.6(*b*); in all cases these metrics predict an SRD below Sparrow's limit. Moreover, for Cases 1 and 3 the PSF and LSF FWHM metrics predict similar resolution distances for AS and CS directions, being unable to gauge the actual difference in resolution due to scan. The failure of the FWHM metrics was already expected, as it has been shown that spatial resolution metrics based on the PSF's width measured at a level larger than the 33 % of the peak response, will fail for low optical factors (Valenzuela et al. 2022). Thus, a FWHM metric, based on the PSF's width measured at 50 % of the peak response, must fail.

The RER metric predicts in Cases 1 and 2 an SRD larger than Sparrow's limit, so it can be assessed against the SRF, as an example it will be assessed for Case 1 in AS direction. For SuperDove, Table 6.6(*a*) shows that 1/RER = 4.27 pixels and Figure 6.10 (blue curve in left figure) indicates that this SRD is obtained for a contrast $C = 49$ %. For Landsat 8, Table 6.6(*b*) shows that 1/RER = 1.33 pixels and Figure 6.10(*c*) (blue curve) indicates that this SRD is obtained for a contrast $C = 15$ %.

If the RER metric is used to compare the resolution distances of the two Green channels the conclusion is that Landsat 8 has a resolution advantage of 4.27 - 1.33 = 2.94 pixels over SuperDove. But this comparison is biased because different resolving contrasts are being considered for Landsat 8 and SuperDove channels. If 15 % ($C = 0.15$) contrast is considered for both channels, then from Figure 6.10(*a*), $R(0.15) = 3.06$ pixels for SuperDove, so the actual resolution advantage for Landsat 8 at this contrast is 3.06 – 1.33 = 1.73 pixels. In this example the RER metric has a bias error of (2.94 -1.73)/1.73 = 39 %.

Thus, the fifth conclusion is that the RER metric displays a bias when it is used to compare the resolution distance of two imagers with different optical factors.

Although the RER is a biased resolution metric, the metric $RER^2 = RER_{AS} \times RER_{CS}$ is useful to estimate the magnitude of the pixel's adjacency effect, that is, the percentage of energy collected in a pixel, that actually comes from radiance originated in the ground area represented by this pixel (Pagnutti et al. 2010, equation 8). For example, consider Case 1 for the Green channels, the actual percentages of energy (computed via the respective PSF) are 6.4 % and 66.5 % for SuperDove and Landsat 8, respectively, while the RER^2 metric yields

estimates of 5.2 % and 64.6 %, respectively. Thus, the RER^2 metric provides a fair estimate of the pixel's adjacency effect for both imagers without the need to compute their PSFs.

The overall conclusion is that any spatial resolution metric which defines a single SRD based on a specific value of the spatial response can be either erroneous or biased. It errs when it predicts an SRD smaller than Sparrow's limit. It is biased when it is used to compare two images captured by sensors with different optical factors while predicting SRDs that generate different resolving contrasts in each image.

6.5. Discussion

6.5.1. Key Findings

The key findings are summarised as:

1. Spatial Resolution Distance

   a. The assumption that the GSD is equal to the SRD is a mistake prevalent in the remote sensing community.

   b. Regardless of the satellite's size, an unbiased spatial resolution metric should compute the SRD considering the resolving contrast produced in the image by two point sources in the scene.

   c. The SRD of SuperDove is much higher than its GSD.

   d. The SRD of Landsat 8 is slightly higher than its GSD.

2. Stability of the Spatial Response

   a. For a given satellite and orbital height, a reduction of the GSD reduces the stability of the spatial response.

   b. The spatial response of SuperDove's imaging sensors is very unstable.

   c. The spatial response of Landsat 8's imaging sensors is quite stable.

These findings and their impacts are discussed in what follows.

6.5.2. Spatial Resolution Distance

6.5.2.1. *Confusion of GSD with SRD*

Considering that nowadays most users of satellite images incorrectly assume that SRD = GSD, it is convenient to understand why this error became encroached within the remote sensing community.

Early satellite imagers had very low optical factors ($Q << 1$) and near perfect performance due to small sensor imperfections. According to the two-point source criterion, a perfect sensor with $Q << 1$ has, in the most favourable condition (depicted in Figure 6.9), an SRD in CS direction only slightly larger than its GSD. Thus, it became common to identify GSD with SRD as this was a fair approximation for these low-Q imagers.

Moreover, for these early imagers, spatial resolution metrics like the EIFOV and the LSF's FWHM yielded SRDs roughly similar to the GSD (Markham 1985, 868). This

congruence between these three spatial resolution metrics is also observed for the Green channel of Landsat 8 as illustrated in Table 6.6(*b*). Thus, for these high-quality low-*Q* imagers, the GSD metric gave roughly the same results than other more elaborate metrics, justifying its use as a measure of SRD.

But, when a satellite's scan is considered, or when a low quality (substantially degraded due to sensor imperfections) imager is assumed, the GSD metric fails, even with $Q << 1$. The errors of the GSD metric increase with *Q*, so many different metrics have been proposed to replace it (Valenzuela et al. 2022). All these metrics predicted different SRDs for the same sensor and none of them was widely accepted, so the mainstream users of satellite imagers continued using the GSD metric as a synonym of SRD despite of the numerous warnings of its inadequacy (Townshend 1981, Forshaw et al. 1983, Markham 1985, Fisher 1997, Cracknell 1998, Joseph 2000, NRC 2000, Townshend at al. 2000, Ryan et al. 2003, Thomson 2009. Auelmann 2012, Verhoeven 2018, Valenzuela and Reyes 2019a).

In short, the SRD is currently identified with the GSD because it was a fair approximation for the first generation of satellite imagers.

6.5.2.2. *Erroneous, biased and unbiased spatial resolution metrics*

The GSD, or ground pixel size, should not be confused with the SRD which is always larger than the GSD. The GSD should not be used to compare the SRD of two satellite imagers, as a Sensor A with a larger GSD may have a smaller (better) SRD than a Sensor B with a smaller GSD. This may occur when Sensor A has $Q << 1$ and Sensor B has $Q > 1$.

For a given imager, metrics like the EIFOV or the PSF's FWHM are suitable to measure the width of the spatial response in the spatial frequency or spatial domain, respectively, but should not be employed as spatial resolution metrics, because the SRD must be measured at a given resolving contrast in the image plane, not at a given width of the spatial response.

The General Image Quality Equation (GIQE) uses the RER as a spatial resolution metric (Leachtenauer et al. 1997). We have shown that this metric has a bias because the SRDs predicted will generate different resolving contrasts for different optical factors. Thus, this equation should not be used to compare imagers with quite different optical factors. This recommendation is consistent with the observation that version 3 of the GIQE "*may not be valid*" for $Q > 1$ (Leachtenauer et al. 1997, 8328).

To measure or predict the actual SRD under an unbiased framework, the two-point source criterion must be employed, considering the actual resolving contrast. Suitable point source targets are available and have been used for in-orbit resolution measurements (Conran et al. 2021). An unbiased prediction of SRD requires any metric of the so called "Two-Point Source" type (Valenzuela et al. 2022). Among this type, the SRF metric is preferred when the full range of resolving contrasts is of interest, but simpler single-contrast metrics like the Generalized Rayleigh Criterion may also be used (Jahn and Reulke 2000).

In short, SRD measures the capability of separating in the image two closely spaced point sources, so to avoid errors or bias it must be defined considering the resolving contrast that allows these sources to be identified as separate objects.

6.5.2.3. *SuperDove's SRD is much larger than its GSD*

A high temporal resolution from Low Earth Orbit (LEO) is only possible with a constellation that has a high number of satellites. Due to their small size, CubeSats are cheap enough to make such a constellation commercially feasible. But this small size has a drawback,

because it severely restricts the maximum diameter of the optical aperture, for example, it must be smaller than 10 cm for a 3U CubeSat. Thus, for a given wavelength the OFOV is fixed. Then, at a given orbital height H, if the GSD is reduced by a certain factor, $Q = H \cdot \text{OFOV}/\text{GSD}$ will increase by this same factor. Therefore, the first reason why the SRD of SuperDove is much larger than its GSD is its high optical factor Q, which inevitably leads to a high ratio between the mean SRF and the GSD (Valenzuela et al. 2022, figure 6).

In addition, sensor imperfections further degrade (broaden) the imager's spatial resolution. To quantify this degradation, a comparison was conducted between the actual sensor and a perfect sensor, i.e., one that is free from any imperfections. We computed this degradation for the Green channels of SuperDove and Landsat 8, our results for Case 1 show that the average degradation, considering AS and CS directions, was 115 % and 8 %, respectively. Therefore, the second reason behind of SuperDove's high SRD/GSD ratio are its relatively large imperfections.

The high imperfections of SuperDove's Green channel are evident in Table 6.5 (lines 4 to 7) when compared with those of Landsat 8 and can be tentatively attributed to the high jitter of small satellites (Pong 2018, figure 1), to the pronounced charge diffusion effects in the small pixels (Davis et al. 1998) required to achieve a small GSD, and to the wide manufacturing tolerances of SuperDove's telescopes (Fernandez-Saldivar 2020, 19). Defocus was not explicitly considered in our OTF model, so its effect at system level, may have been accounted by an equivalent jitter deviation or charge diffusion length that are larger than their actual values.

In short, the SRD of SuperDove's sensor is much higher than its GSD because it has a high optical factor and relatively large imperfections.

6.5.2.4. *Impact of results*

The first impact of the previous results is that the GSD is not suitable as a spatial resolution metric, because it systematically errs by predicting an SRD smaller than Sparrow's limit $R(0)$. A rigorous specification of the SRD must consider that this distance is a function of the resolving contrast, but this specification requires knowledge of the PSF and the computation of the SRF. A shortcut is to use the reciprocal of the RER as a rough estimate of the SRD. Although the RER is biased as a spatial resolution metric (Valenzuela et al. 2022) it is the simplest metric that can be derived from edge measurements and does not err by predicting $\text{SRD} < R(0)$.

The second impact of SRD > GSD is that if the DN measured by a pixel is not only due to the radiance originating from the ground area represented by this pixel, but that it is also due to radiance originating from the surrounding ground area represented by adjacent pixels. This adjacency effect generates errors in all image processing techniques that assume that neglect this adjacency effect. These errors can be reduced by spatial aggregation and deconvolution (Huang et al. 2002).

6.5.3. Stability of the spatial response

6.5.3.1. *Drawbacks of reducing the GSD*

Once the GSD was identified with SRD, the two possible measures to reduce the GSD gained popularity: lower the orbital height or narrow down the IFOV. The reduction of orbital height has a limit due to the increase of atmospheric drag which restricts the spacecraft lifetime,

especially for CubeSats as there is not much room for the thrusters and fuel required to maintain the orbit.

The reduction of the GSD by narrowing the IFOV is attractive, especially if the customer identifies GSD with SRD, regardless of the actual SRD achieved. But if the IFOV decreases, as equations 3 and 4 show, the susceptibility of the spatial response to variations of turbulence and jitter, respectively, increases.

A CubeSat can have a stable spatial response in spite of its relatively high jitter, if its IFOV is much larger than its jitter's standard deviation. But, in a market that identifies GSD with SRD, these stable images may not be attractive.

In short, if the GSD is reduced by decreasing the IFOV, the susceptibility of the spatial response to variations of spacecraft jitter or atmospheric turbulence increases.

6.5.3.2. *Stability of SuperDove's images*

Due to their small size and inertia, CubeSats may experience large jitter fluctuations due to variations in the speed of their reaction wheels (Shields et al. 2017).

In the effort to reduce the GSD of SuperDove, its effective IFOV is 7.3 times smaller than the one of Landsat 8. From the perspective of the stability of the spatial response, a decrease of the IFOV by a factor 7.3 is equivalent to:

1. An increase of the turbulence parameter K by a factor $(7.3)^{5/3} \approx 28$ (Equation (3)).

2. An increase in the jitter standard deviation by a factor 7.3 (Equation (4)).

In short, the small size of SuperDove makes it susceptible to jitter fluctuations due to changes in the speed of its reaction wheels. The small IFOV of SuperDove's images makes them susceptible to variations in their spatial response when the jitter or turbulence changes.

6.5.3.3. *Impact of results*

The main impact of an unstable spatial response is the radiometric inconsistencies of the image product, these inconsistencies are well documented for SuperDove (Anger et al. 2019, NASA 2020, Saunier 2020, Frazier and Hemingway 2021). To reduce these inconsistencies, the PSF can be estimated from edge measurements and images with a similar PSF should be used for time series analysis.

If the instability of the spatial response is an issue, remote sensing users can apply the same procedures outlined in this work to estimate how a given variation in atmospheric turbulence will affect the PSF of a satellite sensor. With this knowledge they can select images that meet the minimum stability requirements.

6.5.4. Limitations and future work

The limitations of the OTF models for the Green channels of SuperDove and Landsat 8, and the measures proposed to improve these models, have already been discussed at the end of sections 6.3.2.4 and 6.3.2.5, respectively. Although more accurate models are of interest, they are expected to have only a minor effect on the key results presented here.

This study has been limited to the comparison of only one small and one large satellite, other small and large satellites like SkySat and Sentinel 2, respectively, are also of interest to the remote sensing community and can be compared by using the same methodology in a future study.

In practice the SRD is constrained by noise. The SRF formulation allows noise to be considered in terms of the image's SNR (Valenzuela et al. 2022), but this issue requires additional materials, methods, and results that will considerably extend the length of this paper. Therefore, the consideration of image noise has been left aside as future work.

Regarding CubeSats' imagers, future work to assess their SRD, should develop more accurate models to characterize the spatial response fluctuations caused by spacecraft jitter and atmospheric effects. Jitter models should consider the actual LOS's jitter standard deviation versus reaction wheels' speed, while atmospheric modelling should account for both turbulence and aerosol effects. If spatial response fluctuations could be characterised in real time, image processing methods to compensate them could be explored, to optimize the radiometric stability of the final product.

6.6. Conclusion

The Spatial Resolution Distance (SRD) of CubeSat's imagers with high optical factors and large imperfections, such as SuperDove, is much larger than their Ground Sampling Distance (GSD). To rigorously compute the SRD of any satellite image, the classical two-point source resolution criterion should be applied, considering the Point Spread Function (PSF) of the sensor to find how this distance varies as a function of the resolving contrast in the image.

Metrics based on a single property of the spatial response, such as the Full Width at Half Maximum of the Line Spread Function, the Effective Instantaneous Field Of View and the Relative Edge Response, are useful tools to characterize the width of the spatial response, the width of the spatial frequency response, and the influence of adjacent pixels, respectively. However, these metrics should not be used as spatial resolution metrics since they give erroneous and/or biased predictions for the SRD. Instead, Two-point Source metrics that compute the SRD as a function of the resolving contrast should be employed.

Among these later metrics, the Spatial Resolution Function (SRF) is convenient as it: 1) considers all possible values of resolving contrasts; 2) reduces to the GSD in a limiting case; 3) allows Signal to Noise Ratio effects to be considered; and 4) allows other spatial resolution metrics to be assessed (Valenzuela et al. 2022).

Efforts to reduce the GSD in CubeSat's images, are effective to promote the resultant images in a market that incorrectly identifies GSD with SRD but are ineffective to improve the actual SRD when it is already limited by the optical aperture, defocus, spacecraft jitter and charge diffusion. Some users of SuperDove images have concluded that their SRD is five times the GSD (NASA 2020, 12), this conclusion is coherent with the computed SRF and with the spatial response measurements of SuperDove obtained by Planet (Bahloul et al. 2021, 21) and the United States Geological Survey (Kim et al. 2021, 16).

Previous assessments of Planet's images have identified inconsistencies on their spatial and radiometric performance (Anger et al. 2019, NASA 2020, Saunier 2020, Frazier and Hemingway 2021). In this work these inconsistencies have been traced to the intrinsic instability of SuperDove's spatial response, concluding that its width can increase by a factor of two under strong atmospheric turbulence. This conclusion explains the previous inconsistencies and the large differences between the spatial response's widths measured by the European Space Agency (Saunier and Cocevar 2022, 28) and the United States Geological Survey (Kim et al. 2021, 16).

CubeSat's imaging sensors can be designed to achieve a stable spatial response, but at the cost of a much larger GSD, losing their attractiveness in a market that confuses GSD with SRD.

If remote sensing users are aware of the actual SRD and stability of image products, they are likely to make better use of them, taking informed decisions about their fitness-for-purpose. If image providers characterize and exploit the actual spatial response of their imaging sensors, during all the stages of the image processing chain, they are likely to deliver better products.

Chapter Seven

Conclusion

7.1. Overview

Section 7.2 summarizes the results of the work performed to answer the four research questions.

Section 7.3 provides a synthesis of the research, focusing on its overall significance and suggesting how the different results can be synergistically integrated in a practical case.

Section 7.4 introduces the results obtained through some supplementary research lines that have achieved a preliminary state of maturity. These results are presented in detail in the Appendices sections, and these can be topics of future publications.

Section 7.5 discusses some fundamental limitations of the optical transfer function methodology employed to answer all the research questions and suggests some research lines that could be conducted to explore them.

Section 7.6 outlines the three topics of future work that are envisaged as the more pressing research issues due to their impact on the remote sensing community.

Finally, section 7.7 presents some closing remarks about the overall characteristics of the research conducted.

7.2. Summary of results

The overall aim of this research was to advance our knowledge of the assessment of the spatial response of satellite imagers. To achieve this aim, the four research questions presented in section 1.3.3 were posed to develop new metrics, models and procedures that could fill some of the gaps detected during my literature review. My answer to these questions is summarized as follows.

7.2.1. How can we assess and improve current spatial resolution metrics for satellite imagers?

A new classification scheme of spatial resolution metrics was developed by extending the three-type taxonomy proposed by Valenzuela and Reyes (2019a) for satellite imagers. This extension allows a more precise and comprehensive classification of spatial resolution metrics by 1) defining two or more subtypes under each type; 2) including spatial frequency domain metrics; and 3) incorporating empirical metrics.

A new spatial resolution metric, named the Spatial Resolution Function (SRF), was developed by applying the classical two-point source resolution criterion to the case of digital (pixel-sampled) satellite imagers. An optimum phasing was assumed between the two-point source scene and the pixel grid, so that under the conditions that minimize the Spatial Resolution Distance (SRD), the SRF is equal to the Ground Sampling Distance (GSD).

Unlike other well-known metrics which assume that the SRD is a single value, the SRF metric considers that the SRD is a function of the resolving contrast C in the image plane. This is the contrast that allows the two-point sources to be resolved, that is, to be detected in the image as two separate objects instead of a single object.

The SRF was computed in terms of the sensor's Point Spread Function (PSF), for values of resolving contrast C between 0 and 1. The value SRF($C = 0$), named Sparrow's limit, is the

absolute threshold of resolution. At this limit there is no resolving contrast, but any separation between sources greater than this limit will allow some contrast to be obtained.

To illustrate the computation of the SRF, the PSF was calculated for the case of a generic sensor by using the Optical Transfer Function methodology. The generic sensor assumed has a circular optical aperture, a detecting array of square pixels, a uniform scan of its line-of-sight, and representative values for optical aberrations, line-of-sight micro vibrations and pixel crosstalk. This formulation allowed the SRF to be computed as a two-dimensional function in terms of the image resolving contrast C and the sensor's optical factor Q.

In practice, the minimum resolving contrast that can be observed is limited by image noise. Rose's criterion estimates the minimum contrast C_{min} that can be observed in the presence of image noise, the application of this criterion to the SRF allowed an estimation of the ultimate SRD = SRF($C = C_{min}$) > SRF($C = 0$) that can be obtained in the presence of image noise.

Once the SRF is computed, other spatial resolution metrics can be readily assessed. Metrics that yield SRD < SRF($C = 0$) are considered flawed, as there is no possibility to resolve two-point sources at a distance below Sparrow's limit. Spatial resolution metrics that predict SRD > SRF($C = 0$) are assessed in terms of the bias that they introduce when they are used to compare the SRD of two sensors with different optical factors.

The SRF allows the predicted SRDs to be associated to a certain resolving contrast $C > 0$, if both SRDs are associated to the same contrast there is no bias, as the two sensors are gauged under the same conditions. But if the two associated contrasts are different, the metric is favouring the sensor with smallest associated contrast because this sensor is being gauged under a more favourable condition.

It was shown that the most popular spatial resolution metrics are either erroneous or biased, stressing the need to consider the SRF to obtain an unbiased prediction of SRD.

The results of this research are published in the International Journal of Applied Earth Observation and Geoinformation (Valenzuela et al. 2022).

7.2.2. How can we assess current spatial response models for satellite imagers?

The plethora of models used to describe the spatial response of imaging sensors, was illustrated by classifying them in four types. Twelve references, which use different spatial response models, were cited in section 3.1 to illustrate the diversity of models available.

The bias inherent in the current methodology to assess spatial response models was demonstrated by showing that five comparative assessments of analytic function models have selected a different function as the best model. This bias was traced to the use of a specific sensor as a benchmark of spatial response, whereas in practice a variety of sensors and spatial responses are encountered. A model that is suitable for a certain sensor may be unsuitable for another sensor.

In response to this bias, a new assessment methodology that uses the optical design parameters of a generic sensor as independent variables was developed. The basic idea is that the shape of the spatial response of a generic sensor depends on a few key optical design parameters, so if two of these parameters are used as independent variables in a plane of

possible optical designs, then each point in this plane will represent a different shape for the spatial response. By computing the error of the model under assessment at each point in the optical design plane, the regions of this plane where the model is valid can be readily established.

The spatial response is defined by the Point Spread Function (PSF), so to develop the methodology, an equation was derived to define the minimum PSF level that is of interest for practical purposes (PSF_{min}), assuming a scene with a single point source on a homogeneous background. The equation derived allows PSF_{min} to be computed as a function of two parameters: the peak-signal to background-signal ratio R and the background Signal to Noise Ratio SNR_B. Using this equation as a basis, a comparative study of different types of satellite imagers was performed, concluding that PSF_{min} levels of 0.1 and 0.01 were representative of most practical cases.

A generic sensor with square pixels and an annular optical aperture was selected as representative of several types of satellite imagers. The optical factor Q and the linear obstruction ratio ε of the optical aperture were selected as the key parameters of the optical design. These two key parameters were varied over a wide range that is representative of the whole variety of satellite imagers. Each point in the optical design plane (Q, ε) has a different PSF shape, more than ten thousand of these points were considered to assess the spatial response models.

The previous methodology was applied to assess the accuracy of the popular separable PSF model, which uses two perpendicular edge measurements to estimate the PSF of a satellite imager. The errors of this model were computed in the optical design plane (Q, ε) showing that the separable model is only applicable to low optical factors, creating the need for a new model that – by using edge measurements - can estimate the spatial response for medium and high optical factors.

The results of this research are published in the IEEE Transactions on Geoscience and Remote Sensing (Valenzuela et al. 2023).

7.2.3. How can we improve current spatial response models derived from edge measurements?

The new methodology to assess a spatial response model demonstrated that the separable PSF model – which estimates the PSF from only two edge measurements - is only valid for low optical factors ($Q < 0.4$). Currently, most satellite imagers have medium ($0.4 < Q < 1$) to high ($Q > 1$) optical factors and edge measurements are the most common method to estimate their PSF. Thus, the need arose to develop a model that uses edge measurements to estimate the PSF for imagers with medium and high optical factors.

The separable PSF model uses only two perpendicular edges to estimate the PSF. The recommendation to measure a third diagonal edge to verify if the PSF is separable or axially symmetric was proposed by Reichenbach et al. (1991) in their seminal paper on edge measurements for imaging sensors, but this recommendation was not followed by the remote sensing community, which usually measures only two perpendicular edges to estimate the PSF of satellite imagers.

The new model uses the third diagonal edge measurement to reconstruct the three-dimensional (3D) Optical Transfer Function (OTF) in the spatial frequency domain. Each edge measurement yields a one-dimensional (1D) cut of the two-dimensional (2D) OTF in a direction perpendicular to the edge. It was shown that for medium and high optical factors, the 2D OTF can be estimated by performing quadratic interpolation between three 1D OTF cuts (two perpendicular cuts and one diagonal cut in between). Once the 2D OTF is reconstructed by quadratic interpolation, the PSF is obtained as its inverse Fourier transform.

The three-edge quadratic interpolation model was assessed in the plane (Q, ε) of optical designs, by employing the same methodology used to assess the separable PSF model. The results show that the quadratic model works where the separable model fails and vice versa, so that for $PSF_{min} = 0.1$ both models allow the estimation of the PSF for any optical factor of interest. For $PSF_{min} = 0.01$ there is performance gap for low and medium optical factors, as neither the quadratic nor the separable model achieves low errors for $0.07 < Q < 0.49$; further research is needed to close this gap.

The results of this research are published in the IEEE Geoscience and Remote Sensing Letters (Valenzuela et al. 2024a).

7.2.4. How can we exploit our knowledge on the spatial response of satellite imagers to upgrade current image processing algorithms?

The remote sensing community assumes that the Digital Number (DN) measured by a pixel in a satellite imager is proportional to the average radiance originated on the ground area represented by this pixel. This assumption is only valid for an ideal satellite sensor with a null optical factor ($Q = 0$), but all satellite sensors have $Q > 0$. The fact that the DN is also due to the radiance originated in the surrounding areas represented by adjacent pixels is usually overlooked, generating errors in image processing algorithms that estimate Earth's surface parameters in a pixel-to-pixel basis.

Restoration, also known as deblurring, is an image processing technique to reduce the adjacency effect, so that the DN measured by each pixel approximates as closely as possible the DN measured by the ideal satellite sensor. The usual approach to restoration is deconvolution of the raw image with a kernel defined in terms of the PSF of the imaging sensor. This approach is based on the fact that if pixel sampling is neglected, the PSF kernel yields optimum results. When pixel sampling is considered, the optimum restoration kernel is not trivial and so it must be found on a case-to-case basis (Huang et al. 1998, Huang et al. 2002).

The current procedure to find the optimum restoration kernel is quite involved as it requires auxiliary satellite images captured by a sensor that has much higher spatial resolution than the sensor of interest. In particular, the Ground Sampling Distance (GSD) of the auxiliary sensor must be equal to the GSD of the sensor of interest divided by an integer number much greater than one (Huang et al. 2002). The restrictions of this procedure have inhibited its application, the existence of an optimum kernel different from the PSF kernel is usually overlooked, and currently the PSF kernel is usually employed for image restoration.

A new procedure to find the optimum restoration kernel was developed by using synthetic edge images. This new procedure is much simpler and accurate that the current procedure. It was shown that the new procedure predicts the same optimum kernels that were obtained by Huang et al. (1998, 2002) using the current procedure with auxiliary satellite images.

The results of this research are published in the International Journal of Remote Sensing (Valenzuela et al. 2024c).

7. 3. Synthesis

7.3.1. Overall significance of results

The current knowledge about the spatial response of imaging sensors in the remote sensing community is conditioned by the legacy of the early satellite imagers. These early imagers had very low optical factors, so some simple spatial response metrics, methods and models that were developed to handle them, proved to be useful. The small errors of these low-Q metrics, methods, and models were masked by the relatively high noise of the early images and thus considering their success, were adopted as axioms.

Satellite imagers have currently evolved to higher optical factors, and the errors of the early low-Q metrics, methods, and models has increased significantly. Moreover, these larger errors are no longer masked by the relatively low noise of the current satellite images.

This research developed new spatial response metrics, methods and models that are applicable to all types of satellite imagers. To gauge the significance of these innovations in spatial response assessment, the errors of the low-Q metrics, methods, and models have been computed.

Regarding these errors, the most prominent error in the remote sensing community is the widespread identification of Ground Sampling Distance (GSD) with Spatial Resolution Distance (SRD). This identification is a rough approximation for low-Q imagers, but it is a gross error for high-Q imagers. To address this issue, Chapter 2 developed the Spatial Resolution Function (SRF), a new unbiased spatial resolution metric, and, assuming a generic sensor, used this metric to assess the errors of the GSD and other current spatial resolution metrics. The discovery that the well-known Relative Edge Response (RER) metric has a bias error, is particularly significant, because the RER is the cornerstone of the General Image Quality Equation (Leachtenauer et al. 1997).

In Chapter 2 the spatial response was assumed to be given, instead, in the following two chapters the procedures to find this response are considered. Specifically, Chapters 3 and 4 assess empirical procedures to estimate the two-dimensional spatial response from a set of one-dimensional edge measurements. To comprehensively assess these estimation procedures a new methodology had to be developed.

This new assessment methodology, developed in Chapter 3, considers the whole range of optical factors. In Chapter 3 the new methodology was used to assess the separable PSF model, showing that it performs well for low optical factors, and that it fails for high optical factors. The assessment of the separable PSF model is significant because currently it is indiscriminately applied to any sensor, regardless of its optical factor.

In Chapter 4 the new methodology was used to assess the new three-edge quadratic interpolation PSF model, showing that it works where the two-edge separable model fails. As shown in Chapter 4, if the separable model fails, then quadratic interpolation using the results of the three edges can give a much better estimation of the PSF. The significance of this three-edge innovation is that edge measurements are the most usual type of spatial response measurements and high-Q sensors are the most common type of imagers in orbit, so now a

much more accurate estimate of their spatial response can be obtained with only a moderate increase in workload (third edge). This third edge measurement is also convenient to implement the original recommendation of Reichenbach et al. (1991) to test the separable model: measure a third diagonal edge and verify that the result agrees with the prediction of the separable model.

The new methodology presented in Chapter 3 allows the assessment of spatial response models for different types of applications. In Chapters 3 and 4 it was used to assess PSF models which are derived from edge measurements, but it can also be used to assess response models employed in the following types of applications:

- Assess the analytic Edge Spread Function (ESF) models that are used in edge measurements to estimate the position of the straight edge with sub-pixel accuracy.

- Assess the ESF models that are used in edge measurements to reduce the errors due to image noise by fitting the ESF measurements to a one-dimensional analytic function.

- Assess the analytic PSF models that are used in point-source measurements to fit the PSF measurements to a two-dimensional analytic function.

The overall significance of Chapters 3 and 4 is that their innovations allow the popular edge measurement procedures to provide a more accurate knowledge of the spatial response of the sensors under test. Once the spatial response is known it can be used for a variety of purposes, some remote sensing tasks that benefit from an improvement in the accuracy of the sensor's spatial response knowledge are shown in Table 7.1.

Table 7.1: Remote sensing tasks that benefit by improving the accuracy of the sensor's spatial response data. The execution of these tasks requires previous knowledge of the sensor's Point Spread Function (PSF) and their final result will improve if this PSF is known with greater accuracy.

Type of remote sensing task	References
Imager's calibration	Du and Voss 2004
Imager's spatial resolution assessment	Valenzuela et al. 2022
Image's blur correction	Hajlaoiu et al. 2010, Ngo et al. 2021
Estimation of true radiance from measured radiance	Meister et al. 2008
Reduction of spatial correlation in hyperspectral images	Inamdar et al. 2020
Image fusing and registration	Zhou et al. 2020
Land cover characterization	Huang et al. 2002
Subpixel mapping	Wang and Atkinson 2017
Downscaling continua	Wang et al. 2020
Spectral unmixing	Wang et al. 2018
Estimation of fire temperature and burning area	Calle et al. 2009
Super resolution	Lv et al. 2017

The key innovation of Chapter 5 is a new procedure to find the optimum restoration (blur-correction) algorithm. This innovation is significant due to the following facts:

- The remote sensing community usually assumes that there is no need to find the optimum restoration algorithm and usually employs an algorithm based on the sensor's PSF.

- As shown in Chapter 5, the improvement in image quality provided by the usual restoration algorithm based on the sensor's PSF is much lower than the improvement provided by the optimum algorithm.

- Moreover, in some cases the usual restoration algorithm may even degrade image quality.

Once blur is corrected, other remote sensing tasks will benefit from this correction, specifically, land cover characterization, spectral unmixing and estimation of fire temperature and burning area.

The procedure used in Chapter 5 to generate ideal, raw, and restored synthetic edge images has revived the significance and utility of the Deblurring factor as an image quality metric. The Deblurring factor was originally defined to assess the effectiveness of restoration (blur-correction) algorithms that are applied to a raw image with the purpose to approximate it to the ideal image. This same factor can be used to assess the effectiveness of any type of image processing algorithm that is applied to a raw image with the purpose to improve some of its features, supplementing the assessment provided by the SRF metric.

Finally, the publication of Chapter 6 applied the same SRF metric of Chapter 2 to two popular satellite imagers: a low-Q imager and a high-Q imager. For the high-Q CubeSat imager, the predictions of the SRF metric agree with the measurements performed by NASA and the European Space Agency: the SRD is about five times larger than the GSD. It is expected that this agreement and the gross difference between SRD and GSD, raises the awareness of the remote sensing community on the limitations of the most common spatial resolution metrics.

Although Chapter 6 is mainly an application of the metric derived in Chapter 3 (it does not answer a specific research question) it has also contributed with two innovations to the spatial response assessment of satellite imagers:

- A new procedure to estimate the two-dimensional spatial response model for a sensor whose relevant technical parameters are only partially known (Section 6.3.2.1).

- A new metric, named Resolution Degradation Index, to gauge the degradation of the spatial resolution distance due to sensor imperfections (Section 6.3.4).

The previous discussion illustrates the wide-reaching impact and significance of the innovations developed in this research, the four key innovations which give an answer to their respective research question are schematically illustrated in Figure 7.1.

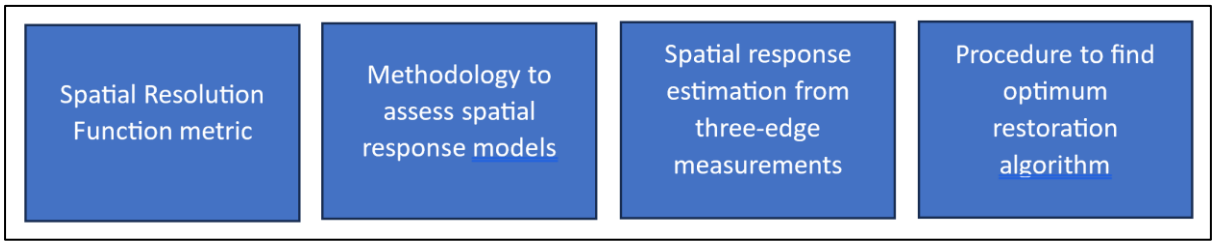

Figure 7.1: Innovations developed in this thesis to answer the four research questions. From left to right, these innovations are described in Chapters 2, 3, 4 and 5, respectively.

These four innovations can be used by their own, as previously described in the respective chapter, or they can be synergistically combined as explained in what follows.

7.3.2. A synergistic perspective

The innovations and concepts developed in this research can be combined to perform more complex tasks. An illustrative example where the four innovations are used is an imaging sensor whose in-orbit spatial response must be first estimated by edge measurements and then improved by image processing. This example has the following steps:

- Natural or artificial edges found in the sensor's raw images are used for edge measurements.
- To improve the accuracy edge measurements, the known parameters of the sensor are used to build a first-cut model of its Edge Spread Function (ESF) using the Optical Transfer Function (OTF) methodology.
- The assessment methodology of Chapter 3 is used to select the best analytic function to model its ESF along different directions. This analytic ESF model will allow the undesired impact of image noise to be reduced, allowing a more accurate measurement of the one-dimensional (1D) OTF cut in each direction.
- Once three 1D OTF cuts are available, the method of Chapter 4 is used to estimate the two-dimensional PSF.
- The estimated PSF is employed to assess the spatial resolution distance of the raw image, using the SRF metric as detailed in Chapters 2 and 6.
- The estimated PSF is also employed to find the optimum restoration algorithm as described in Chapter 5.
- Once the raw image is restored, the same edges used to estimate the PSF of the raw image are used to estimate the PSF of the restored image.
- The SRF is computed for the restored image to assess the improvement in spatial resolution distance achieved by restoration.

7.4. Other results presented in the Appendices

The innovations of Figure 7.1 are of general nature so they can be applied to other cases that were not considered in the respective chapter. The following illustrative examples are presented in the Appendices in the form of short papers.

1. Appendix 1: Spatial Resolution Function of obstructed apertures.

   This appendix shows the results obtained when the SRF of Chapter 2 is computed for an obstructed optical aperture, for one low and one high values of contrast, in the same (Q. ε) plane considered in Chapters 3 and 4.

2. Appendix 2: Impact of Modulation Transfer Function Compensation on the Spatial Resolution Function.

This appendix shows the results obtained when the SRF of Chapter 2 is computed for an imager with and without Modulation Transfer Function Compensation, a technique that is used to boost image contrast.

3. Appendix 3: Assessment of the bivariate Gaussian Point Spread Function model

This appendix shows the results obtained when the assessment methodology of Chapter 3 is applied to the bivariate Gaussian PSF model, assuming that the two unknown parameters of this model are estimated by two different methods:

a) Through the widths of the Line Spread Functions in along scan and cross scan directions.

b) Through the widths of the Point Spread Function in along scan and cross scan directions.

7.5. Limitations of the Optical Transfer Function methodology

The specific limitations of each innovation are discussed in detail at the end of the respective chapter; in this section, two limitations of more fundamental character are outlined. Both limitations point to some possible weaknesses of the Optical Transfer Function (OTF) methodology that has been used in Chapters 2, 3, 4, 5 and 6.

The first limitation is that the OTF methodology assumes that the overall system OTF is equal to the product of the different components of the spatial response, that is, the OTF components are separable. Although the great majority of the works that discuss OTF methodology take separability for granted, the separability of certain OTF components has been questioned in a few authors, two of these works deserve to be mentioned.

Feltz and Karim (1990) have questioned the separability of scan OTF from the detector OTF, stating that this is only possible in some special cases. Stevens (1992) has questioned the separability of the detector OTF from the charge diffusion OTF, for partial fill factors (active pixel area smaller than total pixel area). In both cases the authors provide a more complex OTF equation that is intended to replace the product of the two simpler and usual OTF equations.

Further research is required to properly assess the claims of the two works cited in the previous paragraph. It may be expected that the accuracy of the separability assumption will become an issue that will draw more attention as the precision and accuracy of OTF measurements are improved.

The second fundamental limitation is that - in general - transfer function analysis requires shift invariance, but this is not the case for imaging sensors. Thus, the OTF currently being computed is a pre-sampled OTF that represents the best possible performance of the imaging sensor, so it does not consider all the possible phasings between the scene and the image plane (Park et al. 1984). To compute the average sampled OTF, the pre-sampled OTF is sensibly reduced by the product of a sampling OTF (Boreman 2022, equation 2.13), but this average sampled OTF does not quantify the worst possible performance. Further research is needed to assess the impact of the worst-case sampling on satellite imagers.

7.6. Future work

Future work has already been described at the end of each chapter and two lines of fundamental research regarding OTF methodology have been outlined in the previous section

7.5. In this section I identify three specific topics of interest that could be more pressing due to their impact on the remote sensing community.

1. Universal Image Quality Equation.

   The three known versions of General Image Quality Equation (GIQE) are based on the use of the Relative Edge Response (RER) metric as spatial resolution estimator (Valenzuela and Reyes 2019b). In Chapters 2 and 6 this metric has shown to be biased when a wide range of optical factors is considered, a finding that is coherent with the restriction of version 4 of the GIQE to optical factors below 1 ($Q < 1$) (Leachtenauer 1997, 8328).

   The SRF metric allows an unbiased spatial resolution estimator to be defined, and the consideration of the image Signal to Noise ratio in this definition, paving the way to a "universal" form of the GIQE which can be employed over the whole range of optical factors encountered in satellite imagers.

2. Replacement of Gaussian PSF model

   The overwhelming popularity of the Gaussian Point Spread Function model is not congruent with its huge errors, which are described in Appendix 3.

   It is relatively straightforward to demonstrate the shortcomings of the bivariate Gaussian model, and to reveal the misconceptions that surround its use, but it is not an easy task to propose a new model to replace it. If found, this new model could also be used to close the performance gap noted at the end of section 7.2.3.

3. Comprehensive assessment of Modulation Transfer Function Compensation (MTFC)

   Modulation Transfer Function Compensation is a technique that is used to boost the OTF at high spatial frequencies, increasing the image contrast near the edges. This technique has been promoted of improving the spatial resolution distance by a factor of two (Blonski 2002, 325; Blonski 2003, 7; Ryan et al. 2003, 46).

   As described in Appendix 2, the application of the SRF metric to MTFC, shows that the Spatial Resolution Distance (SRD) is not reduced at the lowest observable contrasts, thus the ultimate SRD is not improved by MTFC.

   The SRF metric also shows that MTFC substantially improves (reduces) the SRD at high contrasts, but this metric does not quantify the associated degradation in radiometric accuracy. The use of the Deblurring factor metric considered in Chapter 6 allows this degradation to be exposed, so that when this factor is used together with the SRF metric, a comprehensive appraisal of the benefits and shortcomings of this image processing technique could be obtained.

7.7. Final remarks

The assessment of the spatial response of satellite imagers is critical to satellite earth observation. In this thesis I have presented a rigorous theoretical approach that allows a critical examination of the underlying assumptions of the commonly applied metrics, models, and methods.

To innovate it must be considered that even if the great majority of works provide a common type of solution to a certain problem, this is not a guarantee that this solution is the correct one or the best one, unless this can be rigorously demonstrated from first principles.

Although satellite imagers have been the focus of this work, all the innovations herein developed are applicable to any type of imaging sensors, thus, the impact of this research is much broader than the title may suggest.

The research conducted for this thesis has been mainly theoretical, its findings being supported by several measurements performed by other researchers. To strengthen these lines of research further, it would be ideal to support the theoretical findings with additional measurements specifically designed and executed for demonstrating these findings.

Bibliography

Andersen TB (2015). Accurate calculation of diffraction-limited encircled and ensquared energy. *Applied Optics* **54**(25), 7525-7533. https://doi.org/10.1364/AO.54.007525.

Ando S, Tanaka K (2019). In-orbit straylight characterization and correction of optical radiometer using the moon image. *Mechanical Engineering Journal* **6**(6). https://doi.org/10.1299/mej.19-00098.

Anger J, Franchis C, Facciolo G (2019). Assessing the Sharpness of Satellite Images: Study of the PlanetScope Constellation. *IGARSS 2019 - 2019 IEEE International Geoscience and Remote Sensing Symposium* 389-392. https://doi.org/10.1109/IGARSS.2019.8900526.

Auelmann RR (2012). Image Quality Metrics. [Accessed 8th July 2024] https://www.cis.rit.edu/~rlepci/Image%20Quality%20Metrics.pdf.

Barnes WL, Pagano TS, Salomonson VV (1998). Prelaunch characteristics of the Moderate Resolution Imaging Spectroradiometer (MODIS) on EOS-AM1. *IEEE Transactions on Geoscience and Remote Sensing* **36**(4), 1088-1100. https://doi.org/10.1109/36.700993.

Bahloul S, Jumpasut A, Fritzler A (2021). *Planet L1 Data Quality Q2 2021 report: Status of Calibration and Data Quality for the PlanetScope Constellation*. San Francisco, CA: Planet Labs. [Accessed 9th August 2023] https://support.planet.com/hc/en-us/article_attachments/4407707085073/2021-Q2_Planet_L1_Data_Quality_Report_PlanetScope.pdf.

Bendinelli O, Parmeggiani G, Zavatti F (1988). CCD star images: On the determination of Moffat's PSF shape parameters. *Journal of Astrophysics and Astronomy* **9,**17-24. https://doi.org/10.1007/BF02715053.

Bensebaa K, Banon GJ, Fonseca LG (2004). On orbit spatial resolution estimation of CBERS-I CCD camera. In: *Third International Conference on Image and Graphics* (ICIG'04) pp. 576-579. IEEE. https://doi.org/10.1109/ICIG.2004.109.

Bergstrom J, Dissly R (2012). High-performance pushbroom imagers for planetary missions. In: *International Workshop on Instrumentation for Planetary Missions*. [Accessed 1st August 2024] https://ssed.gsfc.nasa.gov/IPM/IPM2012/PDF/Revised_Orals/Bergstrom-1149.pdf.

Blonski S, Pagnutti MA, Ryan R, Zanoni V (2002). In-flight edge response measurements for high-spatial-resolution remote sensing systems. *Proceedings of the SPIE* **4814**, 317-326. https://doi.org/10.1117/12.452197.

Blonski S (2003). QuickBird panchromatic imagery: Spatial resolution evaluation. In: *Joint Agency for Commercial Imagery Evaluation Workshop (1 Jan 2003).* [Accessed 5th August 2024] https://ntrs.nasa.gov/api/citations/20060028257/downloads/20060028257.pdf.

Blonski S (2004). Spatial resolution characterization for QuickBird image products 2003-2004 Season. In: *Proceedings of the 2004 High Spatial Resolution Commercial Imagery Workshop (30 Jan 2006)*. [Accessed 5th August 2024] https://ntrs.nasa.gov/api/citations/20080021630/downloads/20080021630.pdf.

Boreman GD, Yang S (1995). Modulation transfer function measurement using three-and four-bar targets. *Applied Optics* **34**(34), 8050-8052. https://doi.org/10.1364/AO.34.008050.

Boreman GD (2001). *Modulation transfer function in optical and electro-optical systems*. SPIE Press, Bellingham, WA, USA.

Boreman GD (2021). *Modulation transfer function in optical and electro-optical systems*. 2nd edition. SPIE Press, Bellingham, WA, USA.

Bugby SL, Lees JE, Perkins AC (2016). Characterisation and quality assurance protocols for SFOV gamma cameras. In: *Gamma Cameras for Interventional and Intraoperative Imaging.* CRC Press. Boca Raton, FL, USA, pp. 171-188.

Burgess AE (1999). The Rose model, revisited. *Journal of the Optical Society of America A* **16**(3), 633-646. https://doi.org/10.1364/JOSAA.16.000633.

Calle A, Casanova JL, Gonzalez-Alonso F (2009). Impact of point spread function of MSG SEVIRI on active fire detection. *International Journal of Remote Sensing* **30**(17), 4567–4579. https://doi.org/10.1080/01431160802609726.

Calvo ML, Chevalier M, Lakshminarayanan V, Mondal PK (1996). Resolution Criteria and Modulation Transfer Function (MTF) / Line Spread Function (LSF) Relationship in Diffraction Limited Systems. *Journal of Optics* **25**, 1–21. https://doi.org/10.1007/BF03549299.

Campagnolo ML, Montano EL (2014). Estimation of effective resolution for daily MODIS gridded surface reflectance products. *IEEE Transactions on Geoscience and Remote Sensing* **52**(9), 5622-5632. https://doi.org/10.1109/TGRS.2013.2291496.

Campbell JB, Wynne RH (2011). *Introduction to Remote Sensing*. 5th edition. Guilford Publications, New York.

Chapel J, Stancliffe D, Bevacqua T, Winkler S, Clapp B, Rood T, Gaylor D, Freesland D, Krimchansky A (2015). Guidance, navigation, and control performance for the GOES-R spacecraft. *CEAS Space Journal* **7**, 87-104. https://doi.org/10.1007/s12567-015-0077-1.

Chen F, Ma JL, Chan JC, Yan DM (2011). Quantitative measurement of the homogeneity and contrast of step edges in the estimation of the point spread function of a satellite image. *International Journal of Remote Sensing* **32**(22), 7179-7201. https://doi.org/10.1080/01431161.2010.519007.

Cheng Y, Jin S, Wang M, Zhu Y, Dong Z (2017). Image mosaicking approach for a double-camera system in the GaoFen2 optical remote sensing satellite based on the big virtual camera. *Sensors* **17**(6),1441. https://doi.org/10.3390/s17061441.

Chesley B, Lutz R, Brodsky RF (1999). *Space payload design and sizing*. In: Larson, J.W., Wertz, J.R. (Eds.), *Space mission analysis and design*. 3rd edition. Kluwer Academic Publishers, Dordrecht. pp. 241-300.

Choi T, Helder D.L. (2005). Generic sensor modeling for modulation transfer function (MTF) estimation. *Proceedings ASPRS Annual Conference*, Sioux Falls, SD, USA. [Accessed 7th July 2024] https://www.asprs.org/a/publications/proceedings/pecora16/Choi_T.pdf.

Claxton CD, Staunton RC (2008). Measurement of the point-spread function of a noisy imaging system. *Journal of the Optical Society of America A* **25**(1), 159-169. https://doi.org/10.1364/JOSAA.25.000159.

CNES (Centre National d'Etudes Spatiales) (2013). *SPOT Image Quality Performances*. CNES, Paris, France, Reference: C443-NT-0-296-CN, 2 avril 2013.

Conran D, Ientilucci EJ, Schiller S, Russell B, Holt J, Durell C, Arnold W (2021). A new technique to define the spatial resolution of imaging sensors. *IGARSS 2021- 2021 IEEE International Geoscience and Remote Sensing Symposium,* 8158-8161. https://doi.org/10.1109/IGARSS47720.2021.9554436.

Coppo P, Brandani F, Faraci M, Sarti F, Dami M, Chiarantini L, Ponticelli B, Giunti L, Fossati E, Cosi M (2020). Leonardo spaceborne infrared payloads for Earth observation: SLSTRs for Copernicus Sentinel 3 and PRISMA hyperspectral camera for PRISMA satellite. *Applied Optics* **59**(23), 6888-6901. https://doi.org/10.1364/AO.389485.

Cota SA, Bell JT, Boucher RH, Dutton TE, Florio CJ, Franz GA, Grycewicz TJ, Kalman LS, Keller RA, Lomheim TS, Paulson DB, Wilkinson TS (2010). PICASSO: An end-to-end image simulation tool for space and airborne imaging systems. *Journal of Applied Remote Sensing* **4**, 1-36. https://doi.org/10.1117/1.3457476.

Cracknell AP (1998). Review article: Synergy in remote sensing - What's in a pixel? *International Journal of Remote Sensing* **19**, 2025 -2047. https://doi.org/10.1080/014311698214848.

Cremer JT (2012). *Advances in imaging and electron physics*. Volume 172. Neutron and X-ray Microscopy - Part 1. Academic Press, Amsterdam.

Davis M, Greiner ME, Sanders JG, Wimmers JT (1998). Resolution issues in InSb focal plane array system design. *Proceedings of the SPIE* **3379**, 288-299. https://doi.org/10.1117/12.317596.

Den Dekker AJ, Van den Bos A (1997). Resolution: A Survey. *Journal of the Optical Society of America A* **14**(3), 547-557. https://doi.org/10.1364/JOSAA.14.000547.

Dennehy C, Alvarez-Salazar OS (2019). A survey of the spacecraft line of sight jitter problem. In: *American Astronautical Society Annual Guidance and Control Conference*. [Accessed 2nd August 2024] https://ntrs.nasa.gov/api/citations/20200002690/downloads/20200002690.pdf.

Dial G, Bowen H, Gerlach F, Grodecki J, Oleszczuk R (2003). IKONOS satellite, imagery, and products. *Remote sensing of Environment* **88**(1-2), 23-36. https://doi.org/10.1016/j.rse.2003.08.014.

Du H, Voss KJ (2004). Effects of point-spread function on calibration and radiometric accuracy of CCD camera. *Applied Optics* **43**(3), 665-670. https://doi.org/10.1364/AO.43.000665.

ESA (European Space Agency) Earth Online (2024). PlanetScope. [Accessed 7th July 2024] https://earth.esa.int/eogateway/missions/planetscope.

Engel CB, Jones SD, Reinke KJ (2021). Real-time detection of daytime and night-time fire hotspots from geostationary satellites. *Remote Sensing* **13**(9), 1627. https://doi.org/10.3390/rs13091627.

Feltz JC, Karim MA (1990). Modulation transfer function of charge-coupled devices. *Applied Optics* **29**(5),717-722. https://doi.org/10.1364/AO.29.000717.

Fernandez-Saldivar J, Pritchett C, Ozawa K, Zuleta I (2020). Focus characterization of SuperDoves: On-ground and on-orbit first light. *Conference on Characterization and Radiometric Calibration for Remote Sensing (CALCON)*. [Accessed 30th July 2024] https://digitalcommons.usu.edu/calcon/CALCON2020/all2020content/34.

Fiete RD (1999). Image Quality and λFN/p for Remote Sensing Systems. *Optical Engineering* **38**, 1229-1240. https://doi.org/10.1117/1.602169.

Fiete RD, Tantalo TA (1999). Image quality of increased along-scan sampling for remote sensing systems. *Optical Engineering* **38**(5), 815-820. https://doi.org/10.1117/1.602053.

Fiete RD, Tantalo TA (2001). Comparison of SNR image quality metrics for remote sensing systems. *Optical Engineering* **40**(4), 574-585. https://doi.org/10.1117/1.1355251.

Fiete RD (2007). Image chain analysis for space imaging systems. *Journal of Imaging Science and Technology* **51**(2), 103-109. https://doi.org/10.2352/J.ImagingSci.Technol.

Fiete RD (2010). *Modeling the imaging chain of digital cameras*. SPIE Press, Bellingham, WA, USA.

Fiete RD, Paul BD (2014). Modeling the Optical Transfer Function in the Imaging Chain. *Optical Engineering* **53**(8), 1-29. https://doi.org/10.1117/1.OE.53.8.083103.

Figoski JW, Zaun N, Mooney T (2009). Performance results for the Landsat OLI spectral filters. *Proceedings of the SPIE* **7452**, 256-267. https://doi.org/10.1117/12.823601.

Fisher P (1997). The pixel: A snare and a delusion. *International Journal of Remote Sensing* **18**, 679-685. https://doi.org/10.1080/014311697219015.

Fliegel K (2004). Modeling and measurement of image sensor characteristics. *Radioengineering* **13**(4), 27-34.

Forshaw MR, Haskell A, Miller PF, Stanley DJ, Townshend JR (1983). Spatial resolution of remotely sensed imagery: A review paper. *International Journal of Remote Sensing* **4**(3), 497-520. https://doi.org/10.1080/01431168308948568.

Forster BC, Best P (1994). Estimation of SPOT P-mode point spread function and derivation of a deconvolution filter. *ISPRS Journal of Photogrammetry and Remote Sensing* **49**(6), 32-42. https://doi.org/10.1016/0924-2716(94)90013-2.

Frazier AE, Hemingway BL (2021). A technical *review* of Planet Smallsat data: Practical considerations for processing and using PlanetScope imagery. *Remote Sensing* **13**(3930), 1-12. https://doi.org/10.3390/rs13193930.

Gabr B, Ahmed M, Marmoush Y (2020). PlanetScope and Landsat 8 Imageries for Bathymetry Mapping. *Journal of Marine Science and Engineering* **8**(13), 1-17. https://doi.org/10.3390/jmse8020143.

Gascon F, Bouzinac C, Thépaut O, Jung M, Francesconi B, Louis J, Lonjou V, Lafrance B, Massera S, Gaudel-Vacaresse A, Languille F et al. (2017). Copernicus Sentinel-2A calibration and products validation status. *Remote Sensing* **9**(6), 584. https://doi.org/10.3390/rs9060584.

Gaskill JD (1978). *Linear Systems, Fourier Transforms, and Optics*. J. Wiley & Sons, New York, NY, USA.

Geo-Kompsat-2 (2024). Geo-Kompsat-2. ESA Earth Observation Portal. [Accessed 12th July 2024] https://www.eoportal.org/satellite-missions/geo-kompsat-2#space--hardware-components.

Gonzalez R, Woods R (2017). *Digital Image Processing*. 4th edition. Global Edition: Pearson Education.

Goodman JW (1996). *Introduction to Fourier optics*. 2nd edition. McGraw Hill, New York.

Greslou D, De Lussy F, Delvit JM, Dechoz C, Amberg V (2012). Pleiades-HR innovative techniques for geometric image quality commissioning. *The International Archives of the Photogrammetry, Remote Sensing and Spatial Information Sciences* **39**(B1), 543-547. https://doi.org/10.5194/isprsarchives-XXXIX-B1-543-2012.

Guo Q, Yang C, Wei C (2010). A new approach to the on-orbit evaluation of point spread function of thermal infrared images with applications to FY-2 satellite products. *IEEE Transactions on Geoscience and Remote Sensing* **48**(3), 1598-1612. https://doi.org/10.1109/TGRS.2009.2030330.

Hajlaoui N, Chaux C, Perrin G, Falzon F, Benazza-Benyahia A (2010). Satellite image restoration in the context of a spatially varying point spread function. *Journal of the Optical Society of America A* **27**(6), 1473-1481. https://doi.org/10.1364/JOSAA.27.001473.

Helder D, Choi T, Rangaswamy M (2005). In-flight characterization of spatial quality using point spread functions. In: *Post-Launch Calibration of Satellite Sensors* – ISPRS Book Series, Leiden, Netherlands, A. A. Balkema Pub., pp. 151-170.

Helder D, Choi J, Anderson C (2006). On-orbit modulation transfer function (MTF) measurements for IKONOS and QuickBird. In: *Proceedings of the 2006 Civil Commercial Imagery Evaluation Workshop (1 Jan 2007)*. [Accessed 12th July 2024] https://ntrs.nasa.gov/api/citations/20070038252/downloads/20070038252.pdf.

Helstrom CW (1969). Detection and resolution of incoherent objects by a background-limited optical system. *Journal of the Optical Society of America* **59**(2), 164-175. https://doi.org/10.1364/JOSA.59.000164.

Holts GC (2007). Imaging system performance based upon Fλ/d. *Optical Engineering* **46**(10), 103204. https://doi.org/0.1117/1.2790066.

Hu B, Li L, Wu J, Qian J (2020). Subjective and objective quality assessment for image restoration: A critical survey. *Signal Processing: Image Communication* **85**, 1-19. https://doi.org/10.1016/j.image.2020.115839.

Huang C, Kalluri SN, Townshend JR, Yang K (1998). Assessing and deconvolving the impacts of the point spread function on satellite remote sensing. In: *IGARSS'98. Sensing and Managing the Environment. 1998 IEEE International Geoscience and Remote Sensing. Symposium Proceedings*. (Cat. No. 98CH36174) Vol. 4, pp. 2035-2037. https://doi.org/10.1109/IGARSS.1998.703732.

Huang C, Townshend JR, Liang S, Kalluri SN, DeFries RS (2002). Impact of sensor's point spread function on land cover characterization: assessment and deconvolution. *Remote Sensing of Environment* **80**(2), 203-212. https://doi.org/10.1016/S0034-4257(01)00298-X.

Huang W, Sun S, Jiang H, Gao C, Zong X (2018). GF-2 satellite 1m/4m camera design and in-orbit commissioning. *Chinese Journal of Electronics* **27**(6), 1316-1321. https://doi.org/10.1049/cje.2018.09.018.

Inamdar D, Kalacska M, Leblanc G, Arroyo-Mora JP (2020). Characterizing and mitigating sensor generated spatial correlations in airborne hyperspectral imaging data. *Remote Sensing* **12**(4), 641. https://doi.org/10.3390/rs1204064.

Irons JR, Dwyer JL, Barsi JA (2012). The next Landsat satellite: the Landsat data continuity mission. *Remote Sensing of Environment* **122**, 11-21, 2012. https://doi.org/10.1016/j.rse.2011.08.026

Jacobsen K (2011). Characteristics of very high resolution optical satellites for topographic mapping. *International Archives of the Photogrammetry, Remote Sensing and Spatial Information Sciences* **38**(Part 4), 14-17. https://doi.org/10.5194/isprsarchives-XXXVIII-4-W19-137-2011.

Jahn H, Reulke R (2000). Staggered line arrays in pushbroom cameras: Theory and application. *International Archives of Photogrammetry and Remote Sensing* **33**(B1), 164–172 [Accessed July 8th 2024] https://www.isprs.org/proceedings/xxxiii/congress/part1/164_XXXIII-part1.pdf.

Ji F, Wang J, Cui S, Li J, Tang X, Xu F (2024). Physics-Guided Optical Simulation and PSF Analysis for Remote Sensing Images Deblurring. *IEEE Transactions on Geoscience and Remote Sensing* **62**, 1-15. https://doi.org/10.1109/TGRS.2024.3426094.

Joseph G (2000). How well do we understand Earth observation electro-optical sensor parameters? *ISPRS Journal of Photogrammetry and Remote Sensing* **55**, 9–12. https://doi.org/10.1016/S0924-2716(00)00004-6.

Joseph G (2015). *Building Earth Observation Cameras*. Taylor & Francis Group. CRC Press, Boca Raton, FL, USA.

Just D (2000). SEVIRI level 1.5 data. *Proceedings of the First MSG RAO Workshop*. ESA SP-452, pp. 29-37. [Accessed 8th July 2024] https://earth.esa.int/eogateway/documents/20142/37627/1st%20MSG%20RAO%20Workshop.

Kerekes JP (2009). Optical sensor technology. *The SAGE Handbook of Remote Sensing*. SAGE Publications Ltd. London. pp. 95-107.

Khetkeeree S, Liangrocapart S (2018). Satellite image restoration using adaptive high boost filter based on in-flight point spread function. *Asian Journal of Geoinformatics* **18**(1), 15-27. [Accessed 14th July 2024] https://aars-ajg.org/archives/374-176176271-1-PB.pdf.

Kim M, Park S, Anderson C, Stensaas GL (2021). *System Characterization Report on Planet's SuperDove*. U.S. Geological Survey. Reston, VA, USA. https://doi.org/10.3133/ofr20211030F.

Kim M, Park S, Sampath A, Anderson C, Stensaas GL (2022). *System Characterization Report on Planet SkySat*. U.S. Geological Survey. Reston, VA, USA. https://doi.org/10.3133/ofr20211030E.

Knight EJ, Kvaran G (2014). Landsat-8 Operational Land Imager design, characterization and performance. *Remote Sensing* **6**, 10286–10305. https://doi.org/10.3390/rs61110286.

Kompsat-3 (2024). KOMPSAT-3 (Korea Multi-Purpose Satellite-3). ESA Earth Observation Portal. [Accessed 15th July 2024] https://www.eoportal.org/satellite-missions/kompsat-3.

Koksal S, Canarslan I, Coskun OD (2019). Image quality characterization of earth observation electro-optic imagers through PSF and MTF analysis. In: *9th International Conference on Recent Advances in Space Technologies (RAST)* pp. 429-434). IEEE. https://doi.org/10.1109/RAST.2019.8767852.

Koretsky GM, Nicoll JF, Taylor MS (2022). *Tutorial on Electro-Optical/Infrared (EO/IR) Theory and Systems*. Institute for Defense Analyses. IDA Document D-4642, Alexandria, VA, USA. [Accessed 11th July 2024] https://www.ida.org/-/media/feature/publications/a/at/a-tutorial-on-e-lectro--opticalinfrared-eoir-theory-and-systems/ida-document-d-4642.ashx.

Kouame D, Ploquin M (2009). Super-Resolution in Medical Imaging: An Illustrative Approach Through Ultrasound. *2009 IEEE International Symposium on Biomedical Imaging: From Nano to Macro* 249-252. https://doi.org/10.1109/ISBI.2009.5193030.

Kubik P, Pascal V (2004). AMETHIST: A Method for Equalization Thanks to HISTograms. *Proceedings of the SPIE* **5570**, 256-267. https://doi.org/10.1117/12.565091.

Lamard JL, Gaudin-Delrieu C, Valentini D, Renard C, Tournier T, Laherrere JM (2004). Design of the high resolution optical instrument for the Pleiades HR Earth observation satellites. *Proceedings of the SPIE* **10568**, 138-146. https://doi.org/10.1117/12.2307995.

Leachtenauer JC, Malila W, Irvine J, Colburn L, Salvaggio N (1997). General Image-Quality Equation: GIQE. *Applied Optics* **36**(32), 8322-8328. https://doi.org/10.1364/AO.36.008322.

Lee D, Helder D, Christopherson J, Stensaas G (2014). Spatial Quality for Satellite Image Data and Landsat8 OLI Lunar Data. *38th CEOS Working Group Calibration Validation Plenary*, College Park, MD, USA. [Accessed 29h July 2024] https://ceos.org/document_management/Working_Groups/WGCV/Meetings/WGCV-38/WGCV_38_DongHan_1002.pdf.

Li T, Feng H, Xu Z, Li X, Cen Z, Li Q (2009). Comparison of different analytical edge spread function models for MTF calculation using curve-fitting. *Proceedings of the SPIE* **7498**. https://doi.org/10.1117/12.832793.

Li T, Feng H, Xu Z (2011). A new analytical edge spread function fitting model for modulation transfer function measurement. *Chinese Optics Letters* **9**(3). https://doi.org/10.3788/COL201109.031101.

Li X, Gu X, Yu T, Cheng T, Li J, Gao H, Wang Z (2012). Atmospheric scattering and turbulence modulation transfer function for CCD cameras on CBERS-02b and HJ-1A/1B. *International Journal of Remote Sensing* **33**(7), 2130-2151. https://doi.org/10.1080/01431161.2011.606242.

Lifshin E, Kandel YP, Moore RL (2013). Improving scanning electron microscope resolution for near planar samples through the use of image restoration. *Microscopy and Microanalysis* **20**(1), 78-89. https://doi.org/10.1017/S1431927613013688.

Light D (2004). A basis for estimating digital camera parameters. *Photogrammetric Engineering & Remote Sensing* **70**(3), 297–300. https://doi.org/10.14358/PERS.70.3.297.

Lillesand TM, Kiefer RW, Chipman JW (2015). *Remote Sensing and Image Interpretation*. 7th edition. John Wiley & Sons. USA.

Lin G, Tilton JC, Wolfe RE, Tewari KP, Nishihama M (2013). SNPP VIIRS spectral bands co-registration and spatial response characterization. *Proceedings of the SPIE* **8866**, 446-460. https://doi.org/10.1117/12.2023367.

Lin SF, Chen CH, Huang YK (2020). Optimal F-number of Ritchey–Chrétien telescope based on tolerance analysis of mirror components. *Applied Sciences* **10**(15), 5038. https://doi.org/10.3390/app10155038.

Llaveria D, Camps A, Park H (2020). Correcting the ADCS jitter induced blurring in small satellite imagery. *IEEE Journal on Miniaturization for Air and Space Systems* **1**(2), 130-137. https://doi.org/10.1109/JMASS.2020.3013440.

Lomheim TS, Kalman LS (1992). Analytical modeling and digital simulation of scanning charged-coupled device imaging systems. In: Karim, M. (Ed.), *Electro-Optical Displays*. Taylor & Francis Group. CRC Press, Boca Raton, FL, USA, pp. 513-584.

Luca L, Cardonne G (1991). Modulation transfer function cascade model for a sampled IR imaging system. *Applied Optics* **30**(13), 1659 -1664. https://doi.org/10.1364/AO.30.001659.

Luo Q, Wang L, Yang H, Zhang S, Shao X (2014). MTF compensation method utilizing the curved edge for high-resolution satellite image recovery. *Proceedings of the SPIE* **9124**, 84-94. https://doi.org/10.1117/12.2051573.

Luquet P, Chikouche A, Benbouzid AB, Arnoux JJ, Chinal E, Massol C, Rouchit P, De Zotti S (2008). NAOMI instrument: a product line of compact and versatile cameras designed for high resolution missions in Earth observation. *Proceedings of the SPIE* **10566**, 24-128. https://doi.org/10.1117/12.2308229.

Lv Z, Jia Y, Zhang Q (2017). Joint image registration and point spread function estimation for the super-resolution of satellite images. *Signal Processing: Image Communication* **58**, 199–211. https://doi.org/10.1016/j.image.2017.08.006.

Maidment ADA (2014). Measures of image quality. Chapter 4. In: Dance, D.R. et al. (Eds.), *Diagnostic Radiology Physics: A Handbook for Teachers and Students*. International Atomic Energy Agency, Vienna, pp. 55-88. [Accessed 5th August 2024] https://www-pub.iaea.org/MTCD/Publications/PDF/Pub1564webNew-74666420.pdf.

Marchand EW (1965). From line to point spread function: The general case. *Journal of the Optical Society of America* **65**(4), 352-354. https://doi.org/10.1364/JOSA.55.000352.

Markham BL (1985). The Landsat sensors' spatial responses. *IEEE Transactions on Geoscience and Remote Sensing*, **GE-23**(6), 864-875. https://doi.org/10.1109/TGRS.1985.289472.

Mason JP, Baumgart M, Rogler B, Downs C, Williams M, Woods TN, Palo S, Chamberlin PC, Solomon S, Jones A, Li X (2017). MinXSS-1 CubeSat on-orbit pointing and power performance: The first flight of the Blue Canyon technologies XACT 3-axis attitude determination and control system. *Journal of Small Satellites* **6**(3), 651–662. [Accessed 2nd August 2024] https://jossonline.com/wp-content/uploads/2018/01/Mason-Final-MinXSS-1-CubeSat-On-Orbit-Pointing-and-Power-Performance.pdf.

McLean IS (2008). *Electronic imaging in astronomy - Detectors and instrumentation*. 2nd edition. Springer, Praxis Publishing, Chichester, UK.

Medyukhina A, Figge MT (2020). DeconvTest: Simulation framework for quantifying errors and selecting optimal parameters of image deconvolution. *Journal of Biophotonics* **13**(4), e201960079. https://doi.org/10.1002/jbio.201960079.

Meister G, Zong Y, McClain CR (2008). Derivation of the MODIS Aqua Point-Spread Function ocean color bands. *Proceedings of the SPIE* **7081**, 413-424. https://doi.org/10.1117/12.796980.

Mika AM (1997). Three decades of Landsat instruments. *Photogrammetric Engineering & Remote Sensing* **63**(7), 839-852. [Accessed 15th July 2024] https://www.asprs.org/wp-content/uploads/pers/1997journal/jul/1997_jul_839-852.pdf.

Morales-Irizarry EV, Vélez-Reyes M (2009). Effects of image restoration in classification and visual analysis of LANDSAT imagery over Puerto Rico. *Proceedings of the SPIE* **7334**, 727-736. https://doi.org/10.1117/12.823753.

Morfitt R, Barsi J, Levy R, Markham B, Micijevic E, Ong L, Scaramuzza P, Vanderwerff K (2015). Landsat-8 Operational Land Imager (OLI) radiometric performance on-orbit. *Remote Sensing* **7**(2), 2208-2237. https://doi.org/10.3390/rs70202208.

Mori H, Miyazawa T, Awaki H, Matsumoto H, Babazaki Y, Bandai A, Demoto T, Furuzawa A, Haba Y, Hayashi T, Iizuka R (2018). On-ground calibration of the Hitomi hard X-ray telescopes. *Journal of Astronomical Telescopes, Instruments, and Systems* **4**(1), 011210. https://doi.org/10.1117/1.JATIS.4.1.011210.

NASA (National Aeronautics and Space Administration) SP-335 (1973). *Advanced Scanners and Imaging Systems for Earth Observation: Report of a Working Group Meeting at Cocoa Beach, Florida, December 11-15, 1972*. Washington, DC: National Aeronautics and Space Administration. [Accessed July 8th 2024] https://ntrs.nasa.gov/api/citations/19740003174/downloads/19740003174.pdf.

NASA (National Aeronautics and Space Administration) (2019). *GOES-R series data book*. Goddard Space Flight Center. Greenbelt, MD. [Accessed July 12th 2024] https://www.goes-r.gov/downloads/resources/documents/GOES-RSeriesDataBook.pdf.

NASA (National Aeronautics and Space Administration) (2020). *Commercial SmallSat Data Acquisition Program Pilot: Evaluation Report*. Mountain View, CA. NASA Earth Science Division. NASA Ames Research Center. [Accessed July 7th 2024] https://www.earthdata.nasa.gov/s3fs-public/imported/CSDAPReport0420.pdf.

Ngo TD, Bui TT, Pham TM, Thai HTB, Nguyen GL, Nguyen TN (2021). Image deconvolution for optical small satellite with deep learning and real-time GPU acceleration. *Journal of Real-Time Image Processing* **18**, 1697–1710. https://doi.org/10.1007/s11554-021-01113-y.

Nieke J, Mavrocordatos C (2017). Sentinel-3a: Commissioning phase results of its optical payload. *Proceedings of the SPIE* **10562**. https://doi.org/10.1117/12.2296174.

Nishi K (2023). Does the slanted-edge method provide the true value of spatial frequency response? *Journal of the Optical Society of America A* **40**(2), 259-269. https://doi.org/10.1364/JOSAA.478864.

NRC (National Research Council) (2000). *The role of small satellites in NASA and NOAA Earth observation programs*. Washington, DC: The National Academies Press. https://doi.org/10.17226/9819.

Okuyama A, Andou A, Date K, Hoasaka K, Mori N, Murata H, Tabata T, Takahashi M, Yoshino R, Bessho K (2015). Preliminary validation of Himawari-8/AHI navigation and calibration. *Proceedings of the SPIE* **9607**, 663-672. https://doi.org/10.1117/12.2188978.

Orych A (2015). Review of methods for determining the spatial resolution of UAV sensors. *International Archives of the Photogrammetry, Remote Sensing and Spatial Information Sciences* **40**(1), 391-395. https://doi.org/10.5194/isprsarchives-XL-1-W4-391-2015.

Ozan O, Kaya G, Tarhan G, Doğan M, Kasapoğlu NG (2023). Performance Comparison of Deblurring Techniques for Optical Satellite Imagery Using MTF. In: *2023 10th International Conference on Recent Advances in Air and Space Technologies (RAST)*1-5. IEEE. https://doi.org/10.1109/RAST57548.2023.10197925.

Pagnutti M, Blonski S, Cramer M, Helder D, Holekamp K, Honkavaara E, Ryan R (2010). Targets, methods, and sites for assessing the in-flight spatial resolution of electro-optical data products. *Canadian Journal of Remote Sensing* **36**(5), 583-601. https://doi.org/10.5589/m10-078.

Pahlevan N, Sarkar S, Franz BA (2016). Uncertainties in coastal ocean color products; impacts of spatial sampling. *Remote Sensing of Environment* **181**, 14-26. https://doi.org/10.1016/j.rse.2016.03.022.

Park SK, Schowengerdt R, Kaczynski M (1984). Modulation-transfer-function analysis for sampled image systems. *Applied Optics* **23**(15), 2572-2582. https://doi.org/10.1364/AO.23.002572.

Peng J, Liu Q, Wang L, Liu Q, Fan W, Lu M, Wen J (2015). Characterizing the pixel footprint of satellite albedo products derived from MODIS reflectance in the Heihe River basin, China. *Remote Sensing* **7**(6), 6886-6907. https://doi.org/10.3390/rs70606886.

Pleiades (2024). Pleiades 1 Satellite. Apollo Mapping. [Accessed 12th July 2024] https://apollomapping.com/pleiades-1-satellite-imagery.

Pleiades-HR (2024). Pleiades-HR (High-Resolution Optical Imaging Constellation of CNES) ESA Earth Observation Portal. [Accessed 15th July 2024] https://www.eoportal.org/satellite-missions/pleiades#pleiades-hr-high-resolution-optical-imaging-constellation-of-cnes.

Pleiades Neo (2024). Pleiades Neo Satellite. Apollo Mapping. [Accessed 12th July 2024] https://apollomapping.com/pleiades-neo-satellite.

Pong CM (2018). "On-orbit performance & operation of the attitude & pointing control subsystems on ASTERIA. In: *32nd Annual AIAA/USU Conference on Small Satellites*. [Accessed 2nd August 2024] https://digitalcommons.usu.edu/cgi/viewcontent.cgi?article=4173&context=smallsat.

Radoux J, Chomé G, Jacques DC, Waldner F, Bellemans N, Matton N, Lamarche C, d'Andrimont R, Defourny P (2016). Sentinel-2's potential for sub-pixel landscape feature detection. *Remote Sensing* **8**(6), 488. https://doi.org/10.3390/rs8060488.

Rafol B, Gunapala SD, Keo SA, Ting DZ, Soibel A, Khoshakhlagh A, Hill CJ, Luong E, Fisher AM, Mumolo JM, Liu JK, Pepper B (2019). Modulation transfer function measurements of type-II mid-wavelength and long-wavelength infrared superlattice focal plane arrays. *Infrared Physics & Technology* **96**, 251-261. https://doi.org/10.1016/j.infrared.2018.11.006.

Ramsay BP, Cleveland EL, Koppius OT (1941). Criteria and the intensity-epoch slope. *Journal of the Optical Society of America* **31**(1), 26-33. https://doi.org/10.1364/JOSA.31.000026.

Rasti B, Chang Y, Dalsasso E, Denis L, Ghamisi P (2021). Image restoration for remote sensing: Overview and toolbox. *IEEE Geoscience and Remote Sensing Magazine* **10**(2), 201-230. https://doi.org/10.1109/MGRS.2021.3121761.

Reichenbach SE, Park SK, Narayanswamy R (1991). Characterizing digital image acquisition devices. *Optical Engineering* **30**(2), 170-177. https://doi.org/10.1117/12.55783.

Ren H, Du C, Liu R, Qin Q, Yan G, Li ZL, Meng J (2014). Noise evaluation of early images for Landsat 8 Operational Land Imager. *Optics Express* **22**(22), 27270-27280. https://doi.org/10.1364/OE.22.027270.

Reulke R, Becker S, Haala N, Tempelmann U (2006). Determination and improvement of spatial resolution of the CCD-line-scanner system ADS40. *ISPRS Journal of Photogrammetry and Remote Sensing* **60**(2), 81-90. https://doi.org/10.1016/j.isprsjprs.2005.10.007.

Reulke R, Sebastian I, Williges C, Hohn R (2017). MTF determination of Sentinel-4 detector arrays. *The International Archives of the Photogrammetry, Remote Sensing and Spatial Information Sciences* **42**, 559-565. https://doi.org/10.5194/isprs-archives-XLII-1-W1-559-2017.

Reuter DC, Richardson CM, Pellerano FA, Irons JR, Allen RG, Anderson M, Jhabvala MD, Lunsford AW, Montanaro M, Smith RL, Tesfaye Z (2015). The Thermal Infrared Sensor (TIRS) on Landsat 8: Design overview and pre-launch characterization. *Remote Sensing* **7**(1),1135-1153. https://doi.org/10.3390/rs70101135.

Roland JKM (2015). A study of slanted-edge MTF stability and repeatability. *Proceedings of the SPIE* **9396**, 181-189. https://doi.org/10.1117/12.2077755.

Rongjun Q, Jianya G (2011). A robust method of calculating point spread function from knife-edge without angular constraint in remote sensing images. *Journal of Remote Sensing (Chinese)* **15**(5), 897–909. https://doi.org/10.11834/jrs.20110171.

Rosak A, Latry C, Pascal V, Laubier D (2004). From SPOT 5 to Pleiades HR—Evolution of the instrumental specifications. *Proceedings of the SPIE* **554**,141-148. https://doi.org/10.1117/12.2307974.

Ruiz CP, Lopez FA (2002). Restoring SPOT images using PSF-derived deconvolution filters. *International Journal of Remote Sensing* **23**(12), 2379-2391. https://doi.org/10.1080/01431160110075857.

Ryan R, Baldridge B, Schowengerdt RA, Choi T, Helder DL, Blonski S (2003). IKONOS spatial resolution and image interpretability characterization. *Remote Sensing of Environment*. **88**(1-2), 37-52. https://doi.org/10.1016/j.rse.2003.07.006.

Safyan M (2015). Overview of the Planet Labs constellation of Earth imaging satellites: In: *Space to Help Life on Earth*. Presented at the ITU Symposium and Workshop on Small Satellite Regulation and Communication Systems. [Accessed 30th July 2024] https://www.itu.int/en/ITU-R/space/workshops/2015-prague-small-sat/Presentations/Planet-Labs-Safyan.pdf.

Salomonson VV, Nickeson JE, Bodechtel J, Zilger J. Comparative point-spread function calculations for the MOMS-1, thematic mapper and SPOT-HRV instruments. In: *Spectral Signatures of Objects in Remote Sensing 1988* (Vol. 287, p. 407-412).

Satellogic (2024). Satellite Imaging Corporation. Satellogic MicroSatellite Constellation. [Accessed 15th July 2024] https://www.satimagingcorp.com/satellite-sensors/satellogic-07m/

Saunier S (2020). TN on quality assessment for PlanetScope (Dove): Issue 1.3. *European Space Agency Earthnet Data Assessment Pilot* (EDAP). [Accessed 29th July 2024] https://earth.esa.int/eogateway/documents/20142/37627/Technical+Note+on+Quality+Assessment+for+PlanetScope+%28DOVE%29.pdf/518ec6d2-d0bd-87ae-5a59-39e9dd7cc25f.

Saunier S (2021). *Technical note on quality assessment for BlackSky.* European Space Agency Earthnet Data Assessment Pilot (EDAP) [Accessed 15th July 2024] https://earth.esa.int/eogateway/documents/20142/37627/Technical%20Note%20on%20Quality%20Assessment%20for%20BlackSky.

Saunier S, Karakas G, Yalcin I, Done F, Mannan R, Albinet C, Goryl P, Kocaman S (2020). SkySat Data Quality Assessment within the EDAP Framework. *Remote Sensing* **14**(1646), 1-26. https://doi.org/10.3390/rs14071646.

Saunier S, Cocevar P (2022). *Technical note on quality assessment for SuperDove: Issue 1.0*. European Space Agency Earthnet Data Assessment Pilot (EDAP) [Accessed 7th July 2024] https://dragon3.esa.int/documents/d/earth-online/technical-note-on-quality-assessment-for-superdove-

Scharr H, Rademske P, Alonso L, Cogliati S, Rascher U (2021). Spatio-spectral deconvolution for high resolution spectral imaging with an application to the estimation of sun-induced fluorescence. *Remote Sensing of Environment* **267**, 112718. https://doi.org/10.1016/j.rse.2021.112718.

Schiller S, Silny J, Taylor MM (2012). In-Flight performance assessment of imaging systems using the Specular Array Radiometric Calibration (SPARC) method. In: *11th Joint Agency Commercial Imagery Evaluation (JACIE) Workshop*. [Accessed 2nd August 2024] https://calval.cr.usgs.gov/apps/sites/default/files/jacie/Schiller_JACIE-2012_-Image_Assesment_Using_SPARC_V2.pdf.

Schiller SJ (2016). Application of the specular array radiometric calibration (SPARC) method for the vicarious calibration of Landsat sensors. In: *Joint Agency Commercial Imagery Evaluation (JACIE) Workshop*, Fort Worth, TX, USA. [Accessed 5th August 2024] https://calval.cr.usgs.gov/apps/sites/default/files/jacie/SLI-SPARC-JACIE-2016_schiller.pdf.

Schmetz J, Pili P, Tjemkes S, Just D, Kerkmann J, Rota S, Ratier A (2002). An introduction to Meteosat second generation (MSG). *Bulletin of the American Meteorological Society* **83**(7), 977-992. https://doi.org/10.1175/1520-0477(2002)083<0977:AITMSG>2.3.CO;2.

Schmid J (2000). The SEVIRI instrument. In: *Proceedings of the 2000 EUMETSAT meteorological satellite data user's conference* **29**, 13-32. [Accessed 12th July 2024] https://www-cdn.eumetsat.int/files/2020-04/pdf_ten_msg_seviri_instrument.pdf.

Schmit TJ, Griffith P, Gunshor MM, Daniels JM, Goodman SJ, Lebair WJ (2017). A closer look at the ABI on the GOES-R series. *Bulletin of the American Meteorological Society* **98**(4), 681-698. https://doi.org/10.1175/BAMS-D-15-00230.1.

Schneider W, Fink W (1976). Integral sampling in optics. *Optica Acta: International Journal of Optics* **23**(12), 1011-1028. https://doi.org/10.1080/713819199.

Schott J, Gerace A, Brown S, Gartley M, Montanaro M, Reuter DC (2012). Simulation of image performance characteristics of the Landsat Data Continuity Mission (LDCM) Thermal Infrared Sensor (TIRS). *Remote Sensing* **4**(8), 2477–2491. https://doi.org/10.3390/rs4082477.

Schowengerdt RA (2007). *Remote sensing: Models and methods for image processing*. 3rd edition. Academic Press. Burlington, MA, USA.

SESO 2024. KompSat 3 Korsch telescope. [Accessed 15th July 2024] http://www.seso.com/new-services/space/kompsat-3-telescope/

Sentinel-2 (2024). European Space Agency. [Accessed 12th July 2024] https://sentiwiki.copernicus.eu/web/sentinel-2.

Shannon RR (2010). Optical specifications. In: Bass, M. et al. (Eds.) *Handbook of optics – Volume II*. 3rd edition. Optical Society of America, McGraw Hill, New York, Chapter 4.

Shea JJ (1999). Lunar limb knife-edge optical transfer function measurements. *Journal of Electronic Imaging* **8**(2), 196-208. https://doi.org/10.1117/1.482697.

Shields J, Pong C, Lo K, Jones L, Mohan S, Marom C, McKinley I, Wilson W, Andrade L (2017) Characterization of CubeSat reaction wheel assemblies. *Journal of Small Satellites* **6**(1), 565-580. [Accessed 2nd August 2024]. https://jossonline.com/wp-content/uploads/2017/05/Shields-Final-Characterization-of-CubeSat-Reaction-Wheel-Assemblies.pdf.

Silverfast 2024. SilverFast Resolution Target (USAF 1951) by LaserSoft Imaging. [Accessed 11th July 2024] https://www.silverfast.com/show/resolution-target/en.html.

Singh D, Kaur M, Jabarulla MY, Kumar V, Lee HN (2022). Evolving fusion-based visibility restoration model for hazy remote sensing images using dynamic differential evolution. *IEEE Transactions on Geoscience and Remote Sensing* **60**,1-4. https://doi.org/10.1109/TGRS.2022.3155765.

Skauli T, Torkildsen HE (2019). Simplified measurement of point spread functions of hyperspectral cameras for assessment of spatial coregistration. *Proceedings of the SPIE* **10986**, 95-102. https://doi.org/10.1117/12.2520219.

Slater PN (1979). A re-examination of the Landsat MSS. *Photogrammetric Engineering and Remote Sensing* **45**(11), 1479-1485. [Accessed 15th July 2024] https://www.asprs.org/wp-content/uploads/pers/1979journal/nov/1979_nov_1479-1485.pdf.

Smith EHB (2006). PSF Estimation by gradient descent fit to the ESF. *Proceedings of the SPIE* **6059**, 192-137. https://doi.org/10.1117/12.643071.

SpaceView (2024). L3 Harris. SpaceView. Small satellites imaging solutions. [Accessed 12th July 2024] https://www.l3harris.com/sites/default/files/2021-06/l3harris-spaceview-brochure-sas.pdf

Stankevich SA (2021). Evaluation of the spatial resolution of digital aerospace image by the bidirectional point spread function parameterization. In: *Mathematical modeling and simulation of systems*, New York, NY, USA, Springer Cham, 2021, pp. 317-327, https://doi.org/10.1007/978-3-030-58124-4_31.

Stelzer EHK (1998). Contrast, resolution, pixelation, dynamic range and signal-to-noise ratio: Fundamental limits to resolution in fluorescence light microscopy. *Journal of Microscopy* **189**(1), 15-24. https://doi.org/10.1046/j.1365-2818.1998.00290.x.

Stevens EG (1992). A unified model of carrier diffusion and sampling aperture effects on MTF in solid-state image sensors. *IEEE Transactions on Electron Devices* **39**(11), 2621-2623. https://doi.org/10.1109/16.163473.

S3MPC (Sentinel 3 Mission Performance Centre) (2021). *S3MPC OPT Annual Performance Report - Year 2021*. ACRI-ST. [Accessed 5th July 2024] https://sentinels.copernicus.eu/documents/247904/3519647/S3MPC.ACR.APR.009+-+i1r0+-+OPT+Annual+Performance+Report+-+Year+2021.pdf/c6f22e03-7f9e-b3f2-6f7c-e83d0c53f954?t=1641920772437.

Thomson GH (2009). A note on spatial resolution measurement and its implications for image radiometry. *International Journal of Remote Sensing*, **30**, 1-8. https://doi.org/10.1080/01431160802339480.

Thomson GH (2010). Digital camera performance where spatial resolution is determined by the optical component. *The Photogrammetric Record* **25**(129), 42-46. https://doi.org/10.1111/j.1477-9730.2009.00566.x.

Torshina IP, Yakushenkov YG (2015). Determination of the spatial resolution of electro-optical measuring system using the criterion of O. Schade. *Measurement Techniques* **57**(12), 1361-1364. https://doi.org/10.1007/s11018-015-0635-0.

Townshend JRG (1981). The spatial resolving power of earth resources satellites. *Progress in Physical Geography: Earth and Environment*, **5**(1), 32-55. https://doi.org/10.1177/030913338100500102.

Townshend JRG, Huang C, Kalluri SNV, Defries RS, Liang S, Yang K (2000). Beware of per-pixel characterization of land cover. *International Journal of Remote Sensing* **21**, 839–843. https://doi.org/10.1080/014311600210641.

Tschunko HFA (1974). Imaging performance of annular apertures. *Applied Optics*, **13**, 1820-1823. https://doi.org/10.1364/AO.13.001820.

Tschunko HFA (1978). Imaging performance of annular apertures. Part 2: Line spread functions. *Applied Optics* **17**(7), 1075-1078. https://doi.org/10.1364/AO.17.001075.

USGS (United States Geological Survey) (n.d.). *Spatial Performance of Landsat 8 Instruments*. United States Geological Survey. [Accessed 30th July 2024] https://www.usgs.gov/landsat-missions/spatial-performance-landsat-8-instruments.

USGS (United States Geological Survey) (2019). *Landsat 8 Prelaunch Point Spread Functions*. United States Geological Survey. [Accessed 1st August 2024] https://www.usgs.gov/media/files/landsat-8-prelaunch-point-spread-functions.

Valenzuela AQ, Reyes JCG (2019a). Basic spatial resolution metrics for satellite imagers. *IEEE Sensors Journal* **19**(13), 1-9. https://doi.org/10.1109/JSEN.2019.2902512.

Valenzuela AQ, Reyes JCG (2019b). Comparative study of the different versions of the general image quality equation. *ISPRS Annals of the Photogrammetry, Remote Sensing and Spatial Information Sciences* **4**, 493-500. https://doi.org/10.5194/isprs-annals-iv-2-w5-493-2019.

Valenzuela A, Reinke K, Jones S (2022). A new metric for the assessment of spatial resolution in satellite imagers. *International Journal of Applied Earth Observation and Geoinformation* **114**, 1-19. https://doi.org/10.1016/j.jag.2022.103051.

Valenzuela A, Reinke K, Jones S (2023). A new methodology to assess spatial response models for satellite imagers using the optical design parameters of a generic sensor as independent variables. *IEEE Transactions on Geoscience and Remote Sensing* **61**, 1-10. https://doi.org/10.1109/TGRS.2023.3270433.

Valenzuela A, Reinke K, Jones S (2024a). A new method to estimate the point spread function of satellite imagers from edge measurements. *IEEE Geoscience and Remote Sensing Letters* **21**, 1-5. https://doi.org/10.1109/LGRS.2023.3344795.

Valenzuela A, Reinke K, Jones S (2024b). Assessing the spatial resolution distance of satellite images: SuperDove versus Landsat 8. *International Journal of Remote Sensing* **45**(12), 4120-4159. https://doi.org/10.1080/01431161.2024.2357839.

Valenzuela A, Reinke K, Jones S (2024c). A new procedure to find the optimum deconvolution kernel to deblur satellite images. *International Journal of Remote Sensing* **45**(24), 9513-9537. https://doi.org/10.1080/01431161.2024.2412801.

Van den Bergh F (2012). On the rendering of synthetic images with specific point spread functions. In: *Proceedings of the Twenty-Third Annual Symposium of the Pattern Recognition Association of South Africa* 75-82. Pretoria, South Africa, November 2012. [Accessed 27th July 2024] https://researchspace.csir.co.za/dspace/handle/10204/6409.

Van den Bergh F (2019), Robust edge-spread function construction methods to counter poor sample spacing uniformity in the slanted-edge method. *Journal of the Optical Society of America A* **36**(7), 1126 -1136. https://doi.org/10.1364/JOSAA.36.001126.

Verhoeven G (2018). Resolving some spatial resolution issues – Part 1: Between line pairs and sampling distance. *Aerial Archaeology Research Group AARGnews* **57**, 25-34.

Verhoeven G (2019). Resolving some spatial resolution issues - Part 2: When diffraction takes over. *Aerial Archaeology Research Group AARGnews* **59**, 12-23.

Viallefont-Robinet F, Helder D, Fraisse R, Newbury A, van den Bergh F, Lee D, Saunier S (2018). Comparison of MTF measurements using edge method: towards reference data set. *Optics Express* **26**(26):33625-33648. https://doi.org/10.1364/OE.26.033625.

Vollmerhausen RH, Driggers RG (2000). *Analysis of Sampled Imaging Systems*. SPIE Press, Bellingham, WA, USA. Chapter 2, section 3, pp. 28-31.

Wali A, Naseer A, Tamoor M, Gilani SA (2023). Recent progress in digital image restoration techniques: a review. *Digital Signal Processing* **141**(104187), 1-16. https://doi.org/10.1016/j.dsp.2023.104187.

Wang G, Li Y (1999). Axiomatic approach for quantification of image resolution. *IEEE Signal Processing Letters* **6**(10), 257-258. https://doi.org/10.1109/97.789603.

Wang Q, Atkinson PM (2017). The effect of the point spread function on sub-pixel mapping. *Remote Sensing of Environment* **193**,127-137. https://doi.org/10.1016/j.rse.2017.03.002.

Wang Q, Shi W, Atkinson PM (2018). Enhancing spectral unmixing by considering the point spread function effect. *Spatial statistics* **28**, 271-283. https://doi.org/10.1016/j.spasta.2018.03.003.

Wang Q, Tang Y, Atkinson PM (2020). The effect of the point spread function on downscaling continua. *ISPRS Journal of Photogrammetry and Remote Sensing* **168**, 251-267. https://doi.org/10.1016/j.isprsjprs.2020.08.016.

Wetherell WB (1980). The calculation of image quality. In: Shannon, R.R., Wyant, J.C. (Eds.) *Applied Optics and Optical Engineering*, Volume VIII. Academic Press, New York, pp. 171-315.

Williams CS, Becklund OA (2002). *Introduction to the Optical Transfer Function*, SPIE Press, Bellingham, WA, USA.

Wilson T, Xiong X (2019). Modulation transfer function characterization for GOES-16 Advanced Baseline Imager using lunar observations. *Proceedings of the SPIE* **11127**, 460-467. https://doi.org/10.1117/12.2528138.

Wittenstein W, Fontanella JC, Newbery AR, Baars J (1982). The definition of the OTF and the measurement of aliasing for sampled imaging systems. *Optica Acta: International Journal of Optics* **29**(1), 41-50. https://doi.org/10.1080/713820741.

Wu HH, Schowengerdt RA (1993). Improved estimation of fraction images using partial image restoration. *IEEE Transactions on Geoscience and Remote Sensing* **31**(4), 771-778. https://doi.org/10.1109/36.239899.

Wu X, Schmidt C, Yu F, Wang Z (2020). Investigation of GOES-R ABI cold pixels around fire. *Proceedings of the SPIE* **11501**, 1150118. https://doi.org/10.1117/12.2571067.

Ye G, Pan J, Zhu Y, Jin S (2020). A jitter detection method based on the integration imaging model. *ISPRS Annals of the Photogrammetry, Remote Sensing and Spatial Information Sciences* **V**(3), 709-715. https://doi.org/10.5194/isprs-annals-V-3-2020-709-2020.

Zhang P, Li J, Olson E, Schmit TJ, Li J, Menzel WP (2006). Impact of point spread function on infrared radiances from geostationary satellites. *IEEE Transactions on Geoscience and Remote Sensing* **44**(8), 2176-2183. https://doi.org/10.1109/TGRS.2006.872096.

Zhang S, Wang L, Shi X, Wang X, Shao X (2014). High-resolution remote sensing image restoration based on double-knife-edge method. *Proceedings of the SPIE* **9124**, 25, 34. https://doi.org/10.1117/12.2053281.

Zhou Y, Rangarajan A, Gader PD (2020). An integrated approach to registration and fusion of hyperspectral and multispectral images. *IEEE Transactions on Geoscience and Remote Sensing* **58**(5), 3020-3033. https://doi.org/10.1109/TGRS.2019.2946803.

Zhu Z, Gao G, Wu Q, Dou Z (2021). On-orbit MTF test method of GEO optical satellite based on random phase sampling of critical linear targets. *Proceedings of the SPIE* **11763**, 2172-2187. https://doi.org/10.1117/12.2587568.

Appendix 1:
Spatial Resolution Function of obstructed apertures

1. Introduction

For satellite imagers, the most common geometries for the optical apertures are the circle and the annulus. The annular geometry is representative of the "folded optics" telescope configurations like the Cassegrain, Ritchey-Chrétien and Newtonian designs, in which the undesirable central aperture blockage due to a secondary mirror is accepted to reduce the telescope volume required to achieve a given focal length. The annulus approximates the actual optical aperture as it does not consider the struts or "spider" required to hold the secondary mirror in place.

For the generic satellite imager to be considered in this Appendix, the same Optical Transfer Function (OTF) approach used by Valenzuela et al. (2022) to characterize a high and a medium quality scanner with square pixels will be applied, with the innovation that instead of assuming a circular unobstructed aperture, the more general case of an annular aperture characterized by its linear obstruction ratio ε will be considered.

The objective of this appendix is to investigate the properties of the Spatial Resolution Function, developed in Chapter 3, for the case of an annular optical aperture,

2. Materials and Methods

The OTF of an annular aperture is well known (Fiete 2010, Eq. 5.35). The numerical parameters used to compute the Point Spread Function (PSF) of the generic imager are presented in Table 1 in terms of the sensor's optical factor *Q*.

Table 1: Parameters to compute the PSF of a generic satellite imager with square pixels and annular optical aperture.

Parameter	High-Quality Scanner	Medium-Quality Scanner
Optical factor Q computational range	$0.01 \leq Q \leq 2$	
Obstruction ratio ε computational range	$0.0 \leq \varepsilon \leq 0.5$	
Q computational interval δQ	0.01	
ε computational interval δε	0.01	
Along scan (AS) pixel fill factor	1.00	
Cross scan (CS) pixel fill factor	1.00	
Along scan oversampling factor	1.00	
RMS wavefront error (wavelengths)	0.1	0.2
Standard deviation of LOS jitter (pixels)	$Q/10$	$Q/2$
Equivalent charge diffusion length (pixels)	$Q/10$	$3 \cdot Q/10$

The OTF components considered for the generic imagers are: 1) ideal square detector with 100 % fill-factor; 2) ideal annular optical aperture; 3) ideal scan in the Along Scan (CS) direction with exact sampling; 4) random optical aberrations characterized by their RMS wavefront error using Shannon's parabolic OTF model (Fiete 2010, Eq. 5.49); 5) LOS jitter characterized by its standard deviation using the Gaussian OTF model (Fiete 2010, Eq. 7.11);

and 6) charge diffusion in detectors characterized by its equivalent charge diffusion length using the Lorentzian OTF model (Rafol et al. 2018).

The first three OTF components model the three basic elements of an ideal satellite imager: detector, optics, and scan. The last three OTF components model the performance degradations of the former elements. To avoid a loss of generality the numerical factors that quantify degradations are measured in units of pixels or wavelengths. It is assumed that the wavelength, the diameter of the optical aperture and the focal length are fixed, so the optical factor is varied by changing the pixel pitch.

To consider that high Q sensors are more susceptible to motion blur (Fiete 2010, p. 122), the platform jitter is assumed to be constant so its standard deviation in pixel units is proportional to the optical factor. To consider that smaller pixels are more affected by diffusion effects (Davis et al. 1998), the diffusion length is assumed to be constant so in pixels units it is proportional to the optical factor.

Regarding the symmetry of the spatial response, the OTF components with axial symmetry are those of the optical aperture, the optical aberrations, the LOS jitter, and charge diffusion. These four OTFs are independent of direction, in particular they have the same form in Along Scan (AS) and Cross Scan (CS) directions. The detector's OTF has the same form in AS and CS directions because the pixel has a square active area with a 100 % fill factor, but it has a different form in diagonal directions. The scan's OTF is the only component that has a different form in AS and CS directions.

Once the two-dimensional OTF is found, the PSF is readily obtained as its inverse Fourier transform. The PSF can then be used to compute the Spatial Resolution Function using the method presented in Section 2.3.2.2 of Chapter 2 and Section 6.3.3 of Chapter 6.

3. Results

Figure 1 shows the constant *SRF* curves for a High-Quality Scanner in the (Q, ε) plane for a resolving contrast $C = 0.1$ and $C = 0.9$, in AS and CS directions.

When the Ground Sampling Distance (GSD) is used as a spatial resolution metric, it assumes $R = 1$ pixel. It is expected that this metric gives its best estimation for low optical factors in CS direction. Observing the CS curves for $C = 0.1$ (lower left graph of Figure 1) it can be seen that the GSD is a good approximation to the SRF for $Q < 0.1$, as Q increases this approximation deteriorates until for $Q > 1.5$ the *SRF* is about twice the *GSD*. For $C = 0.9$ (lower right graph of Figure 1) the error of the *GSD* metric is much higher even for low optical factors.

In the four sets of curves of Figure 1, an increase in Q always implies an increase in the SRF. This is to be expected as a higher optical factor implies a more extended spatial response, so a higher separation distance is required to achieve a certain resolving contrast.

Regarding the obstruction ratio, an increase in ε may increase or decrease the *SRF* depending on the contrast level and the optical factor. The obstruction distorts the shape of the optics' PSF decreasing its width near its peak and increasing its width at lower levels. For low

values of contrast, resolution depends on the PSF's width near its peak whereas for high values of contrast, resolution depends on the PSF's width at lower levels.

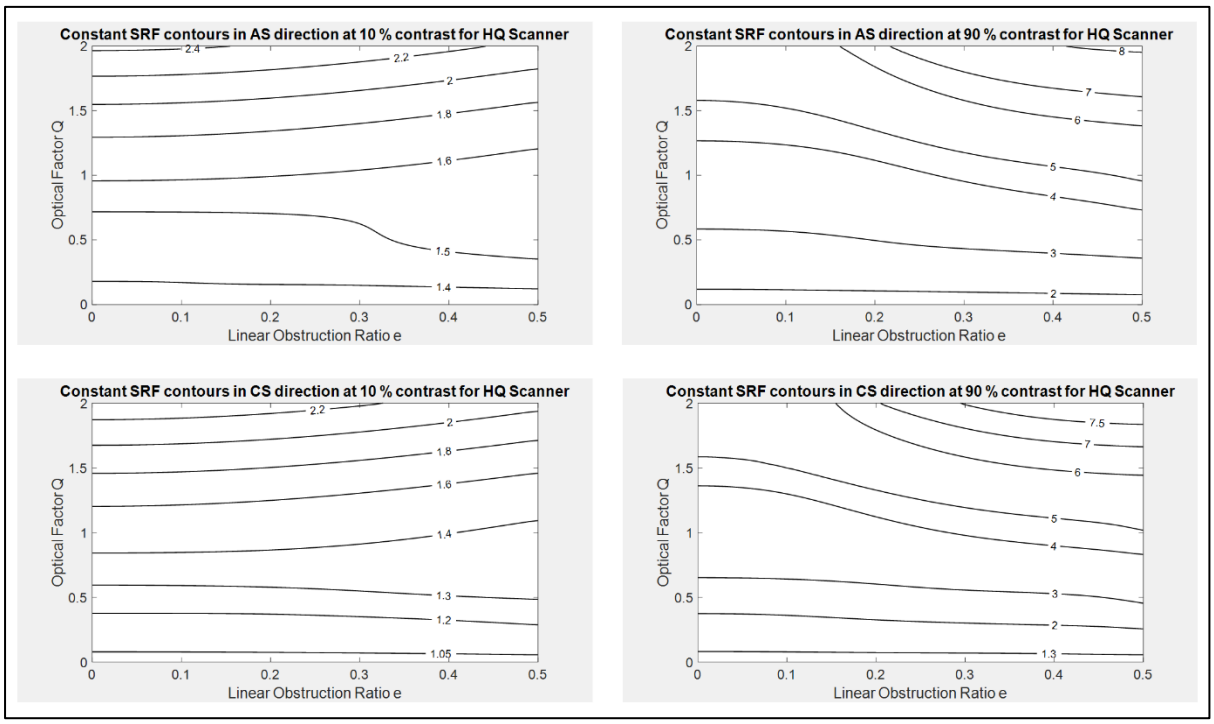

Figure 1: Contours of constant Spatial Resolution Function for a High-Quality (HQ) Scanner in Along Scan (AS) direction (upper figures) and Cross Scan (CS) direction (lower figures) for image contrasts of 10 % (left figures) and 90 % (right figures).

The effect of the obstruction is clearly visible in Figure 1 for the higher range of optical actors in which the optics' PSF predominates over the detector's PSF. For $Q > 1$ an increase in ε decreases the SRF for $C = 0.1$ (improves resolution at low contrasts) and increases the SRF for $C = 0.9$ (degrades resolution at high contrasts).

The difference between the SRF in AS direction (upper graphs of Figure 1) and the SRF in CS direction (lower graphs of Figure 1) is due to the scan which manifests as a degradation of resolution (an increase of the SRF) in AS direction. This effect is most evident for low optical factors as in this case the detector and the scan are the main contributors to the spatial response. For the higher optical factors, the optics is the main contributor to the spatial response and due to its axial symmetry, the scan asymmetry is less evident.

Figure 2 shows the constant SRF curves for a Medium-Quality Scanner in the (Q, ε) plane for $C = 0.1$ and $C = 0.9$. For medium quality there is very little difference between the SRF in AS and CS directions because the axially symmetric OTF components predominate over the scan asymmetry.

As expected, for a given values of Q and ε, the SRF of the Medium-Quality Scanner is always larger than the SRF of the High-Quality Scanner. The increase of SRF when passing from high to medium quality is strongly dependent on the optical factor; Figure 3 shows this increase in percent on the (Q, ε) plane for the four cases considered in Figures 1 and 2.

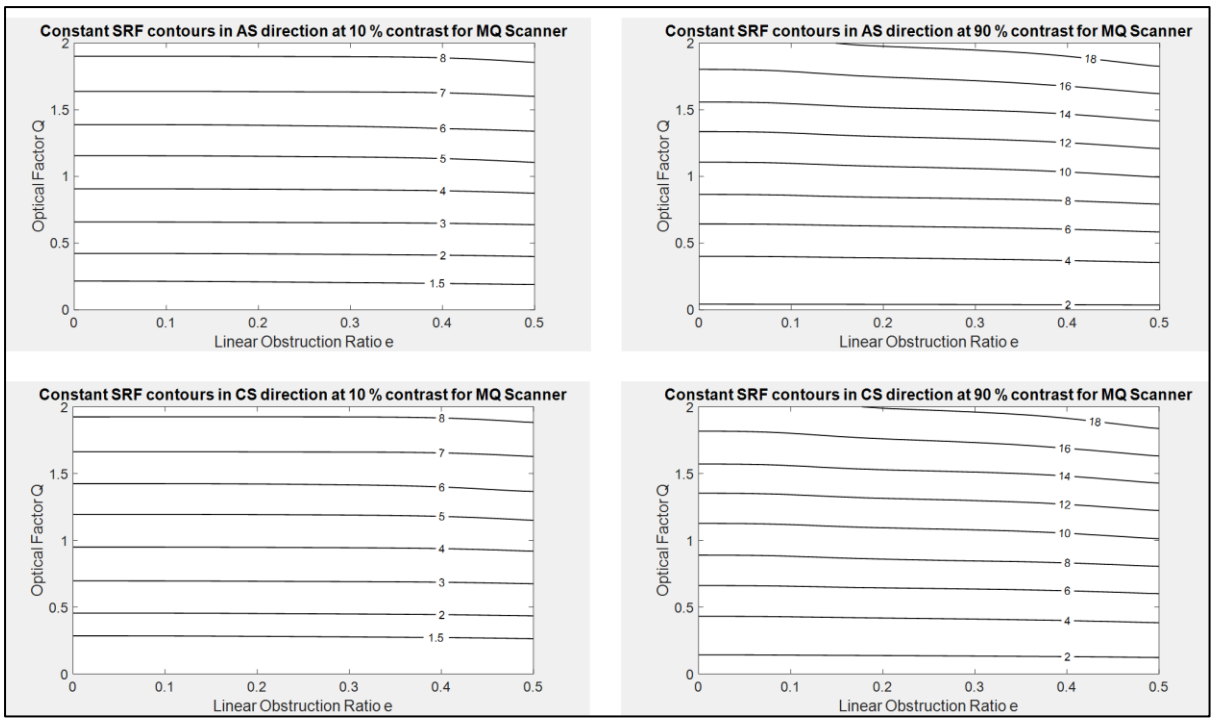

Figure 2: Contours of constant Spatial Resolution Function for a Medium-Quality (MQ) Scanner in Along Scan (AS) direction (upper figures) and Cross Scan (CS) direction (lower figures) for image contrasts of 10 % (left figures) and 90 % (right figures).

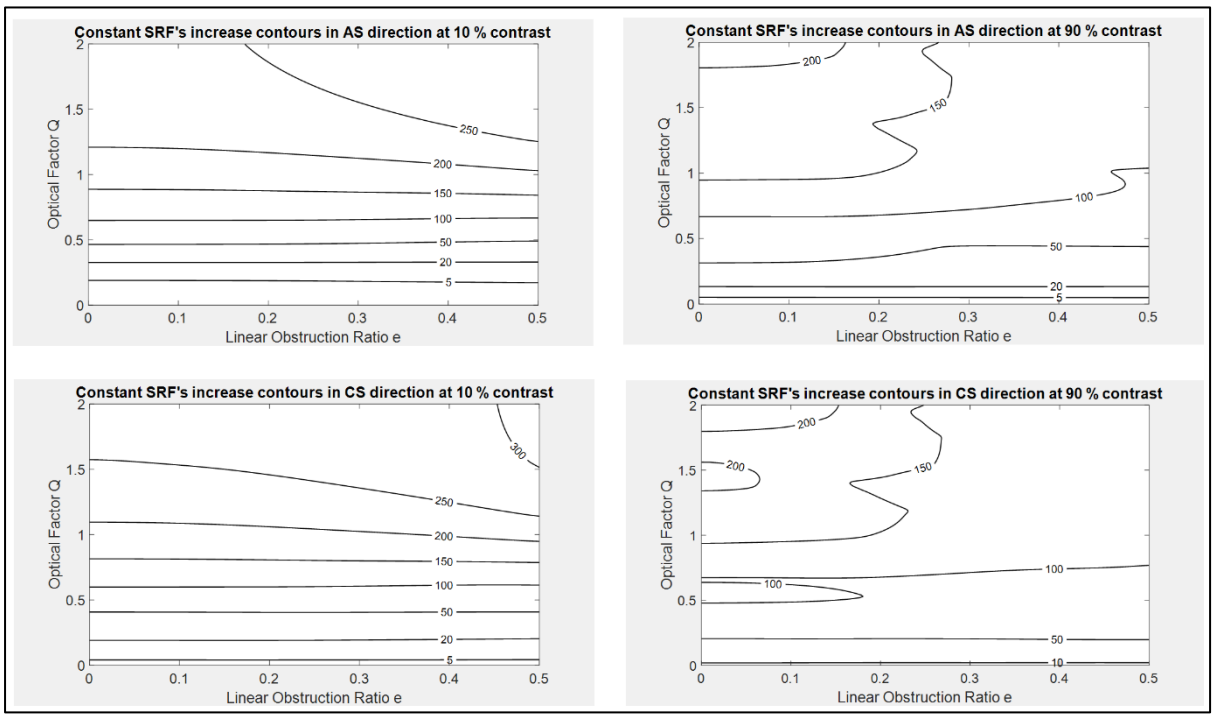

Figure 3: Contours of constant increase in Spatial Resolution Function when passing from a High-Quality (HQ) Scanner to a Medium-Quality (MQ) Scanner in Along Scan (AS) direction (upper figures) and Cross Scan (CS) direction (lower figures) for image contrasts of 10 % (left figures) and 90 % (right figures).

Regarding Figure 3, it can be observed that in all cases the increase of the SRF is small (< 7 %) for $Q = 0.01$ and high (> 137 %) for $Q = 2$. This shows that under the stated assumptions (constant jitter and diffusion length) low Q sensors are much less susceptible to a degradation of system parameters than high Q sensors.

4. Conclusion

The central obstruction of the optical aperture improves (decreases) the spatial resolution distance at low values of resolving contrast but degrades (increases) the spatial resolution distance at low values of resolving contrast.

For satellite imagers, the difference on the spatial resolution distance in along scan and cross scan directions is much more pronounced in a High-Quality imager than in Medium-Quality imager.

If the line-of-sight jitter due to spacecraft micro vibrations and the charge diffusion length are assumed to be constant, imagers with low optical factors are less susceptible to image quality degradations due to sensor imperfections, than imagers with high optical factors.

Appendix 2:
Impact of Modulation Transfer Function Compensation on the Spatial Resolution Function

1. Introduction

Modulation Transfer Function Compensation (MTFC) is a resampling technique that enhances contrast in the image at expense of increasing noise by a factor equal to the noise gain, and the appearance of undesired overshoot artifacts (Fiete 2010, 37-156; Schowengerdt 2007, 309-315).

MTFC was explicitly considered in versions 3 and 4 of the GIQE, which gauged image quality using restored image parameters (Leachtenauer 1997) but is now implicit with other resampling techniques in GIQE version 5, which gauges quality of a "well-enhanced" image using raw image parameters (Valenzuela and Reyes 2019b).

In-orbit spatial response measurements of satellite images resampled with MTFC, exhibit oscillations of the Edge Spread Function (ESF) and the corresponding negative sidelobes of the Line Spread Function (LSF) (Ryan et al. 2003, figure 14; Blonski 2004, 11-12; Helder et al. 2006, 22).

MTFC reduces the sensor's LSF's Full Width at Half Maximum (FWHM) by a certain factor with respect to unrestored image. Adopting this width as a resolution metric (Ryan et al. 2003, 46) it has been claimed for Ikonos (Blonski 2002, 325) and QuickBird (Blonski 2003, 7) satellites, that MTFC improves the spatial resolution distance of their images by this same factor.

The objective of this appendix is to investigate the validity of this claim using the Spatial Resolution Function developed in Chapter 2.

2. Materials and Methods

To assess the previous claim regarding the improvement of spatial resolution distance due to MTFC, in this appendix a representative model of MTFC applied to Ikonos PAN images will be developed and assessed.

To develop Ikonos' model, I consider the Ikonos' LSF measurements in Cross Scan (CS) direction, obtained by Helder et al. (2006, 18) during a five-year period, which yielded LSF's FWHMs of 1.08 ± 0.10 and 1.61 ± 0.08 pixels, with and without MTFC, respectively. As expected MTFC decreases the width of the LSF.

I further consider that Ikonos MTFC convolution kernel had a 4.16 noise gain providing an MTF boost greater than 6 at Nyquist frequency (Ryan et al. 2003, 39).

A 3×3 MTFC quadrant symmetric kernel that has the same noise gain and Nyquist frequency boost is found by using the previous works on this type of boosting kernel (Fiete 2010, equation 9-32; Auelmann 2012, 35; Valenzuela and Reyes 2019b, equations 12-17; Koksal 2019, equations 31-34). The required MTFC kernel that emulates Ikonos' MTFC performance is:

$$\text{Kernel} = \begin{bmatrix} c & d & c \\ b & a & b \\ c & d & c \end{bmatrix} \qquad \text{With} \quad a = 3.997 \qquad b = d = -0.2141 \qquad c = -0.5352$$

The OTF with MTFC (MTFC On: Condition 2) is equal to product of the OTF without MTFC (MTFC Off: Condition 1) and the following contrast boosting function defined in terms of the elements of the previous kernel*:

$$OTF_{MTFC}(\eta_x,\eta_y) = a + 2b \cdot cos(2\pi\eta_x) + 4c \cdot cos(2\pi\eta_x) cos(2\pi\eta_y) + 2d \cdot cos(2\pi\eta_y)$$

I assume a "medium" value of the optical factor $Q = 0.86$, as previously published for Ikonos PAN channel (Valenzuela and Reyes 2019a, table II).

I now use the same generic sensor model defined in Chapter 2. To obtain without MTFC (Condition 1) an LSF's $FWHM_1 = 1.61$ pixels, I assume the following values for the three model's parameters defined in section 2.3.1.2, that consider the sensor's imperfections:

- Wave Front Error WFE = 0.15 wavelengths.
- Spacecraft jitter σ = 0.1 pixels.
- Charge diffusion length $L = 0.1$ pixels.

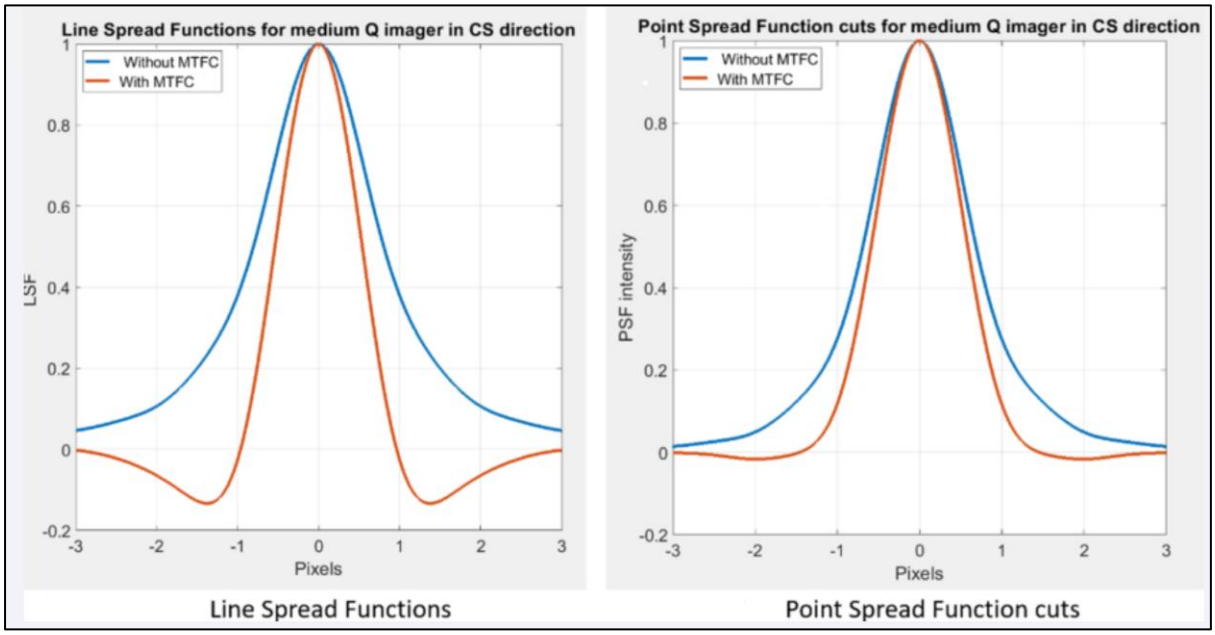

Figure 1: Spatial response functions in Cross Scan (CS) direction for the Optical Transfer Function (OTF) model of an imager with a medium value of the optical factor *Q* that emulates the performance of Ikonos imaging sensor with (red curves) and without (blue curves) Modulation Transfer Function Compensation (MTFC). The left panel represents the Line Spread Function (LSF) in CS direction with MTFC (red curve) and without MTFC (blue curve). The right panel represents a cut of the Point Spread Function (PSF) in CS direction with MTFC (red curve) and without MTFC (blue curve). The OTF model used to compute the LSF and the PSF without MTFC (blue curves) has been tailored to match the Full Width at Half Maximum (FWHM) of the LSF in CS direction measured by Helder et al. (2006) for Ikonos without MTFC. The model of the MTFC kernel has been tailored to match the specifications published for Ikonos MTFC kernel by Ryan et al. (2003). The model predicts the same LSF's FWHM with MTFC measured for Ikonos by Helder et al. (2006), validating the model of the MTFC kernel and showing the coherence between the LSF's measurements of Helder et al. (2006) with the MTFC kernel's specifications of Ryan et al. (2003).

* In the work of Koksal et al. (2019) there is typo in the last term of equation 31.

With these assumptions, when the boosting kernel previously defined is applied I obtain with MTF (Condition 2) an LSF's $FWHM_2$ = 1.08 pixels, just like in Ikonos case, validating my MTFC kernel. Figure 1 presents resultant the LSFs and PSFs cuts in CS direction. Negative sidelobes and FWHM reduction are less pronounced in the PSF than in the LSF.

The Spatial Resolution Function (SRF) without MTFC is computed by using the procedure indicated in Section 2.3.2.2 of Chapter 2 and Section 6.3.3 of Chapter 6. The SRF with MTFC is computed as follows:

- Compute the raw sampled image applying steps 1, 2 and 3 of section 6.3.2.2.
- For each separation between point sources, obtain MTFC image applying the previously defined 3×3 kernel to the raw sampled image.
- Compute resolution function of the image with MTFC using steps 4, 5 and 6 of section 6.3.2.2.

2. Results

Figure 2 shows the SRF with and without MTFC for Ikonos' model..

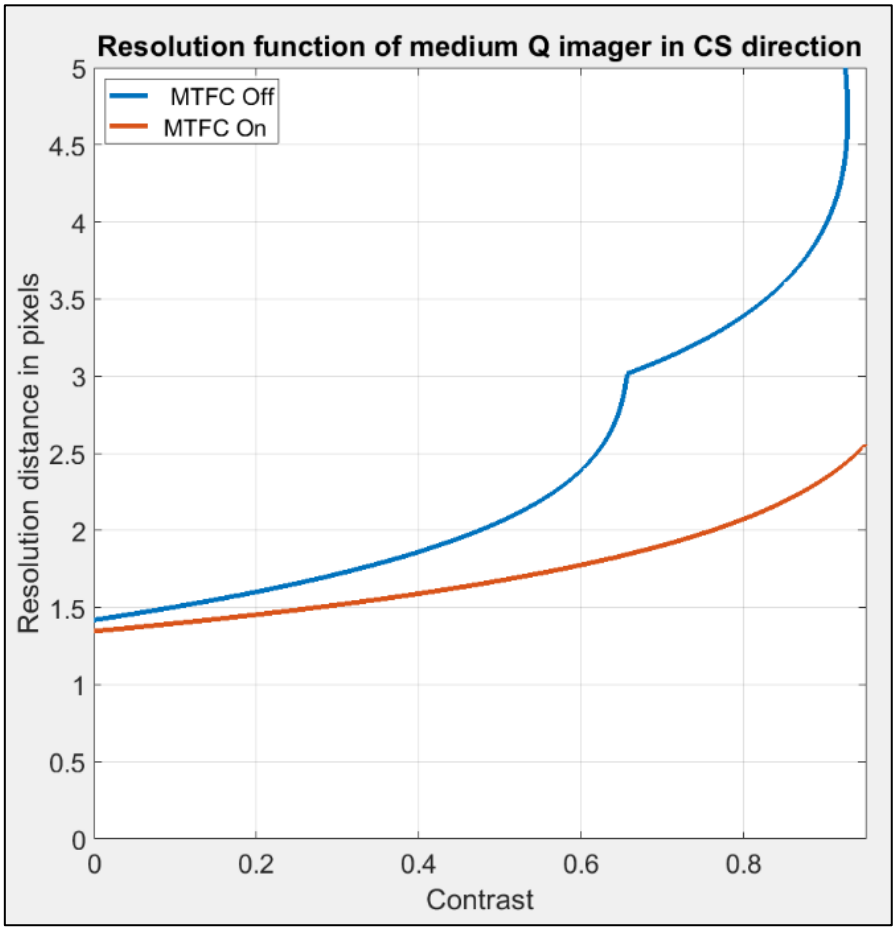

Figure 2: Spatial Resolution Function (SRF) in Cross Scan (CS) for the model of an imager with a medium value of the optical factor *Q* that emulates the performance of Ikonos imaging sensor with (red curve) and without (blue curve) Modulation Transfer Function Compensation (MTFC). The SRF is computed as a function of the resolving contrast *C* in the image.

As expected, at high contrast levels the spatial resolution distance is significantly improved (reduced) by MTFC. This improvement increases by 0.4 points the image quality rating computed by the version 4 of the General Image Quality Equation (Ryan 2003 p. 50).

I now assess the claim that resolution is improved by the same factor by which the LSF's FWHM is reduced. To assess this claim, the ultimate resolution distance R_{min} is computed according to the procedure of Section 2.3.2.3. Assuming that the maximum Signal to Noise Ratio is $SNR_{max} = 89$, as measured in Ikonos PAN channel acceptance tests (Dial 2003, table II), I obtain the following values for the minimum detectable contrast C_{min} and its corresponding ultimate (minimum) spatial resolution distance R_{min}:

Without MTFC: $C_{min\_1} = 5/89 = 0.056 \quad \rightarrow \quad R_{min\_1} = R_1(0.056) \approx 1.47$ pixels.

With MTFC: $C_{min\_2} = 4.16 \cdot 0.056 = 0.23 \quad \rightarrow \quad R_{min\_2} = R_2(0.23) \approx 1.47$ pixels.

Where R_1 and R_2 are the SRFs computed without and with MTFC, respectively.

The MTFC kernel of Ikonos increases noise by a factor 4.16, thus MTFC does not improve (reduce) R_{min}. Thus, both LSF's FWHM and PSF's FWHM metrics are unsuitable to gauge resolution improvement at the minimum useful contrast.

4. Conclusion

Modulation Transfer Function Compensation (MTFC) increases the noise in the image, so it does not improve the ultimate spatial resolution distance obtained at the minimum detectable value of contrast.

MTFC improves the spatial resolution distance at medium and high level of contrasts, being this the reason why it improves the image quality rating computed by the version 4 of the General Image Quality Equation.

This improvement in image quality is associated to the generation of artifacts that increase image the blurring, so a more comprehensive assessment of MTFC must consider the Deblurring factor defined in Chapter 5.

Appendix 3:
Assessment of the bivariate Gaussian Point Spread Function model

1. Introduction

A study of 91 remote sensing publications where analytic Point Spread Function (PSF) models were employed, indicated that the most popular models were the Gaussian and Fermi functions used in 59 and 29 of these works, respectively.

The objective of this appendix is to use the methodology developed in Chapter 3 to assess the most popular PSF model, the Gaussian function, which in its bivariate form is defined as (Bensebaa et al. 2004, Campagnolo and Montano 2014, Stankevich 2021):

$$\mathrm{PSF}(x,y) = exp\left[-½\left(\frac{x}{\sigma_x}\right)^2 - ½\left(\frac{y}{\sigma_y}\right)^2 \right] \quad (1)$$

Where *exp* is the exponential function, and σ_x and σ_y are the standard deviations in *x* and *y* directions, respectively. In this appendix, as in Equation (1), the PSF is normalized to a peak value of 1.0.

2. Materials and Methods

There are several approaches to estimate the σ_x and σ_y of the Gaussian model from spatial response measurements. I note here three of them.

The first approach is to measure the Edge Spread Function (ESF) in *x* and *y* directions using two straight edges in the scene orientated at *y* and *x* directions, respectively. The derivate of the ESF in one direction yields the Line Spread Function (LSF) in this same direction. The Full Width at Half Maximum (FWHM) of the LSFs can be used to compute the standard deviations (Campagnolo and Montano 2014, 5625; Radoux et al. 2016, 12):

$$\sigma_x = \frac{FWHM_x}{2.355} \qquad \sigma_y = \frac{FWHM_y}{2.355} \quad (2)$$

Where $FWHM_x$ and $FWHM_y$ are the full widths at half maximum of the LSFs in *x* and *y* directions respectively.

The second approach is to directly measure the Point Spread Function using a set of point sources (Schiller 2016). If the FWHMs of the PSF in *x* and *y* directions are known, then Equation (2) can also be used, but in this case $FWHM_x$ and $FWHM_y$ are the full widths at half maximum of the PSF in *x* and *y* directions respectively.

The third approach is to assume that the standard deviations are equal to the Effective Instantaneous Field Of View (Morales-Irizarry and Velez-Reyes 2009).

When the standard deviations are defined, the assessment of the resultant model in the optical factor (Q) versus aperture obstruction ratio (ε) plane is straightforward by using the methodology developed in Chapter 3. The same generic sensor used in Chapter 3 and Chapter 4 will be here employed.

It is out of the scope of this Appendix to assess these three approaches, only the first and second approaches will be here considered for the same generic high-quality imager defined in Chapters 2, 3, and 4.

3. Results

3.1. Model defined in terms of the Line Spread Functions

Figure 1 shows some constant Mean Average Percentage Error (MAPE) contours in the (Q, ε) plane for the Bivariate Gaussian Model assessed for PSF ≥ 0.1, assuming that the standard deviations are computed through the LSFs' FWHMs.

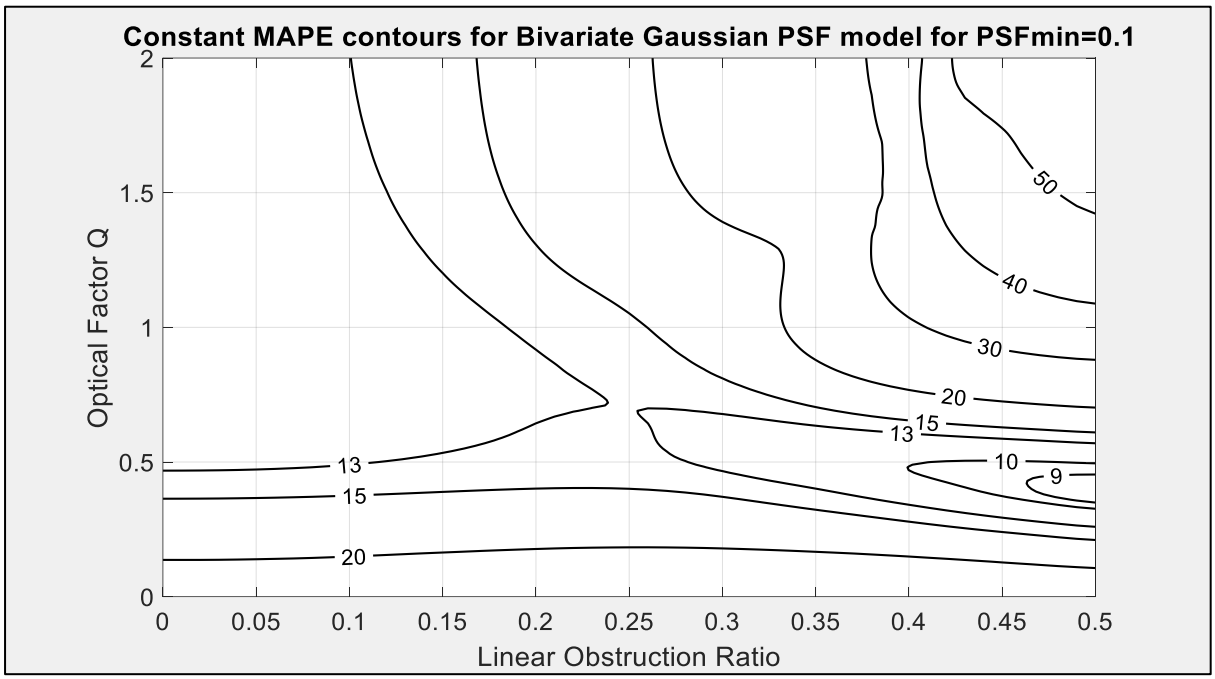

Figure 1: Mean Absolute Percentage Error (MAPE) of Bivariate Gaussian PSF model for PSF_{min} = 0.1 when adjusted to the Line Spread Function's Full Width at Half Maximums in Along Scan and Cross Scan directions. Contours of constant MAPE are drawn for the Bivariate Gaussian Point Spread Function model in the optical factor Q - obstruction ratio ε plane, for the case of the high-quality Generic Sensor defined in Chapters 2, 3 and 4.

The minimum MAPE is 8 % for Q = 0.38 and ε = 0.5. The maximum MAPE is 59 % for Q = 2 and ε = 0.5. The oval shaped domain of validity inside the 10 % contour is only useful for highly obstructed apertures (ε ≥ 0.4) being too narrow to be of practical utility.,

Figure 2 shows some constant MAPE contours in the (Q, ε) plane for the Bivariate Gaussian Model assessed for PSF ≥ 0.01. The minimum MAPE is 28 % for Q = 0.23 and ε =0.5. The maximum MAPE is 230 % for Q = 0.04 and ε = 0.05. Thus, the Gaussian model has no domain of validity (MAPE is always higher than 10 %) when it is assessed two orders of magnitude below the peak response.

The Gaussian model has high errors for Q << 1 because in this case the PSF has a triangular shape in AS direction and a square shape in CS direction (Schowendgert 2007, 88-89), thus, in neither direction this model matches the PSF shape.

For Q > 1, although the upper part of the PSF approximates a Gaussian shape, when the Gaussian model is adjusted to the LSF's FWHM it has high errors because the LSF deviates from a PSF cut. This deviation is characteristic of circular apertures being more pronounced for obstructed apertures (Tschunko 1978).

The highest errors occur for $Q > 1$ and $\varepsilon > 0.4$, because the monotonic Gaussian function is unable to reproduce the secondary lobes that appear due to the aperture obstruction. These secondary lobes are not relevant for $Q < 0.5$.

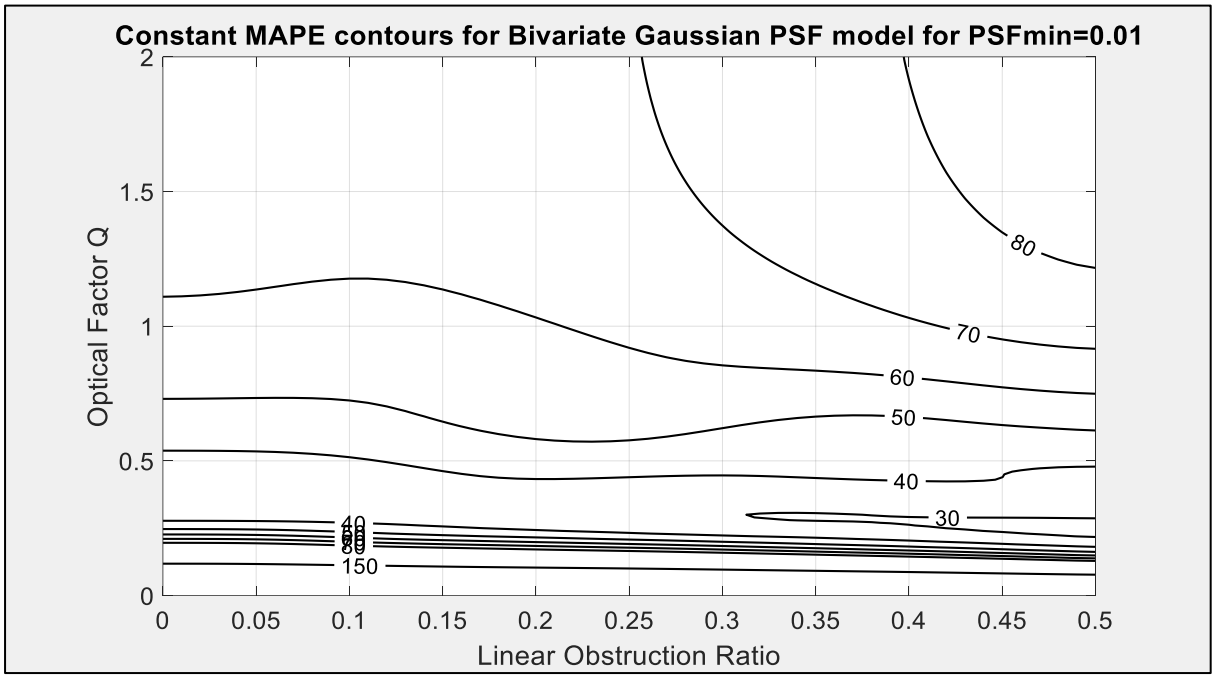

Figure 2: Mean Absolute Percentage Error (MAPE) of Bivariate Gaussian PSF model for $PSF_{min} = 0.01$ when adjusted to the Line Spread Function's Full Width at Half Maximums in Along Scan and Cross Scan directions. Contours of constant MAPE are drawn for the Bivariate Gaussian Point Spread Function model in the optical factor Q - obstruction ratio ε plane, for the case of the high-quality Generic Sensor defined in Chapters 2, 3 and 4.

Thus, the failure of the Gaussian PSF model when it is defined in terms of the LSF is due to three factors:

- For $Q << 1$ the LSF approximates a PSF cut, but the shape of the PSF deviates from Gaussian.
- For $Q > 1$ the upper part of the PSF approximates a Gaussian shape, but the LSF deviates from a PSF cut.
- For $Q > 1$ and $\varepsilon > 0.4$ the PSF shape deviates from Gaussian due to the appearance of secondary lobes.

3.2. Model defined in terms of the Point Spread Function

If the standard deviations of the Gaussian model are computed in terms of the PSF's FWHMs instead of the LSF's FWHMs, then its domain of validity for PSF ≥ 0.1 is much larger, as illustrated in Figure 3 which must be compared with Figure 1.

The domain of validity for PSF ≥ 0.1 increases substantially, achieving very low errors for unobstructed apertures and high optical factors. This domain vanishes for PSF ≥ 0.01 as the minimum MAPE in the (Q, ε) plane is now 26 %. Thus, although the Bivariate Gaussian model is not useful to model the PSF when it is based in the LSF's FWHMs, it has a large domain of

validity for PSF ≥ 0.1 if the PSF's FWHMs are used to define its standard deviations. It is not applicable when the range PSF ≥ 0.01 must be modelled.

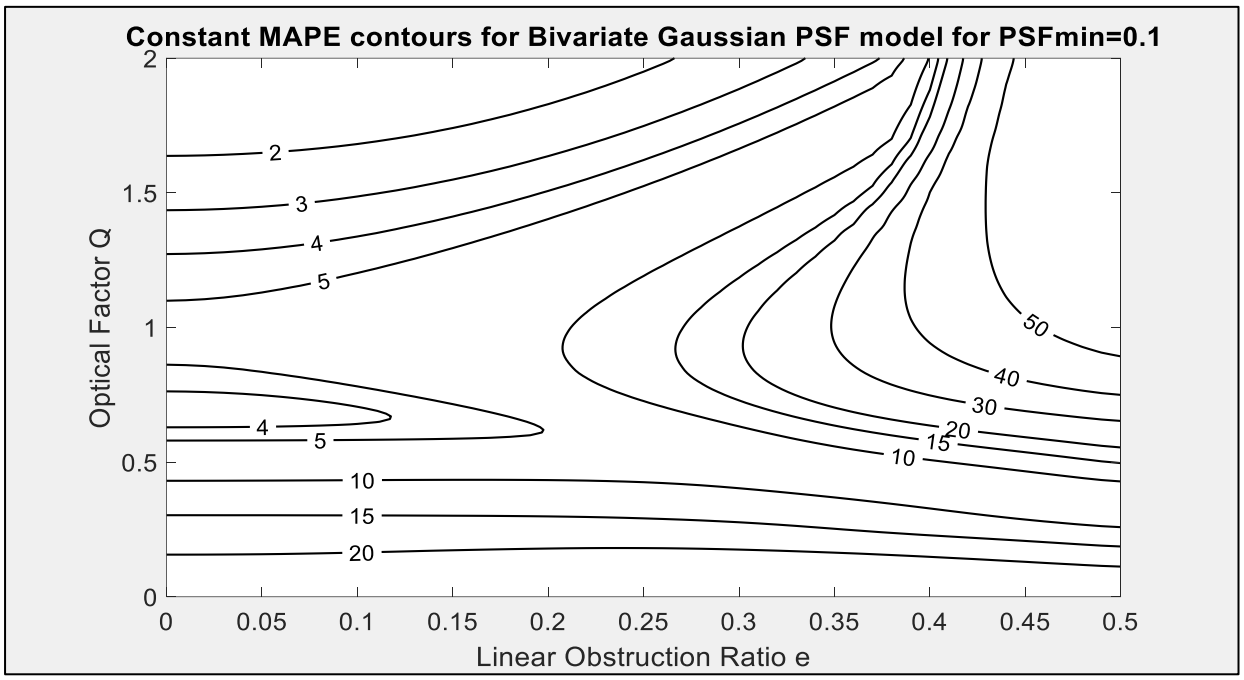

Figure 3: Mean Absolute Percentage Error (MAPE) of Bivariate Gaussian PSF model for PSF_{min} = 0.1 when adjusted to the Point Spread Function's Full Width at Half Maximums in Along Scan and Cross Scan directions. Contours of constant MAPE are drawn for the Bivariate Gaussian Point Spread Function model in the optical factor *Q* - obstruction ratio ε plane, for the case of the Generic Sensor defined in Chapters 2, 3, and 4.

3.3. Other cases in which the model is valid

3.3.1. Low quality imagers

The Gaussian model can be useful for some types of low-quality imagers, two cases are here considered.

In the first case, if a sufficiently large number of OTF components of different shapes degrade the system PSF, then according to the central limit theorem of statistics this PSF should be Gaussian (Chen 2011, 7181-7182).

In the second case any satellite imager with a spatial response dominated by a Gaussian jitter with a sufficiently high standard deviation will also have a Gaussian system PSF.

In both cases, the spatial resolution of the satellite imager is much larger than its Ground Sampling Distance (Valenzuela et al. 2022).

Thus, these two cases in which the Gaussian PSF is valid are representative of low-quality imagers with heavily degraded performance due to a large number of OTF components or Gaussian line of sight jitter.

3.3.2. High quality imagers

For some high-quality imagers with optical factors $Q > 0.4$ and aperture obstruction ratios $\varepsilon < 0.2$, the Gaussian function is useful to model the PSF in the range PSF > 0.1, as

illustrated in Figure 3. The Gaussian model fails in the range PSF < 0.1 regardless of the optical factor and obstruction ratio.

The failure of the Gaussian model for high quality imagers when PSF < 0.1 is in contradiction with the positive assessment published by Schiller (2016) for this model due to its application to the panchromatic channel of Landsat 8. This positive assessment is based on the fact that negligible residuals are obtained with a Gaussian fit to the PSF measurements of this channel (Schiller 2016, 30).

The following procedure shows that very small residuals do not guarantee a small error:

1. Assume that the PSF of Landsat 8's panchromatic channel is a bivariate Gaussian function. Then, due to the definition of LSF, for the special case of a bivariate Gaussian PSF, the LSF in Along Scan (AS) and Cross Scan (CS) directions should be a one-dimensional Gaussian function with a standard deviation equal to the standard deviation of the PSF in AS and CS directions, respectively (Marchand 1965).

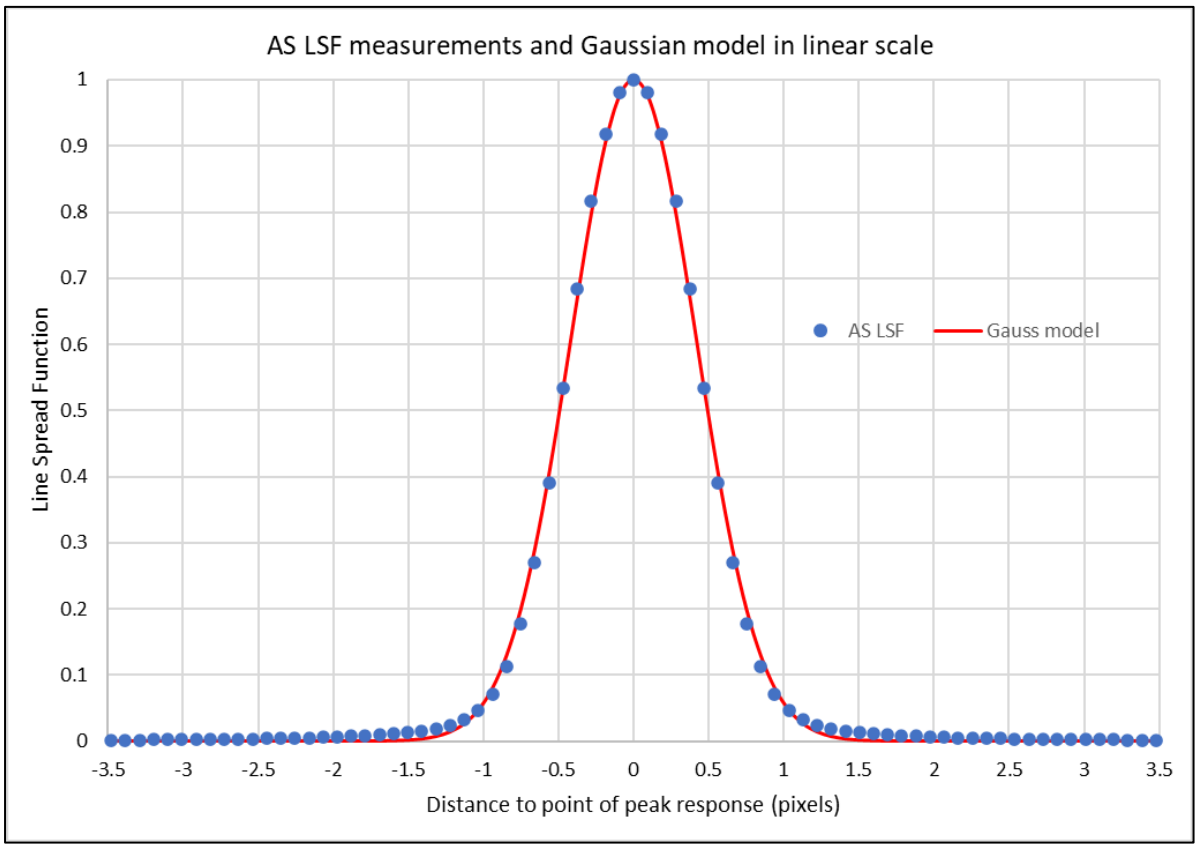

Figure 4: Line Spread Function measurements for Landsat 8's panchromatic channel (blue dots) and their Gaussian model fitted to the Full Width at Half Maximum (red curve), presented in linear scale.

2. Download the LSF measurements versus ground distance published for Landsat 8's panchromatic channel (OLI Band 8) in AS and CS directions (USGS 2019). These LSF measurements are normalized to a maximum value of 1 and the distance is normalized to pixel units dividing the ground distance by the Ground Sampling Distance (GSD) of the panchromatic channel (GSD = 15 m). The normalized LSF measurements in a direction are presented as blue dots in Figure 4 and Figure 5.

3. Compute the Full Width at Half Maximum (FWHM) in AS and CS directions from the correspondent LSF measurements, by using linear interpolation between the two measurements that are adjacent to the LSF = 0.5 value. The following values are obtained:

$$FWHM_{AS} = 0.985 \text{ (pixels)} \qquad FWHM_{CS} = 0.920 \text{ (pixels)}$$

4. Compute the standard deviation of the LSF Gaussian model in AS and CS directions from the correspondent FWHM using Equation (2). The following results are obtained:

$$\sigma_{AS} = 0.418 \text{ (pixels)} \qquad \sigma_{CS} = 0.391 \text{ (pixels)}$$

5. Compute the LSFs predicted by the Gaussian model using the following equations:

$$LSF_{AS}(x) = exp\left[-\tfrac{1}{2}\left(\frac{x}{\sigma_{AS}}\right)^2\right] \quad (3)$$

$$LSF_{CS}(y) = exp\left[-\tfrac{1}{2}\left(\frac{y}{\sigma_{CS}}\right)^2\right] \quad (4)$$

Where x and y are the distances (measured in pixel units) to the point of peak response in AS and CS directions, respectively. The LSF in AS direction, predicted by Equation (3) is shown as a red curve in Figures 4 and 5.

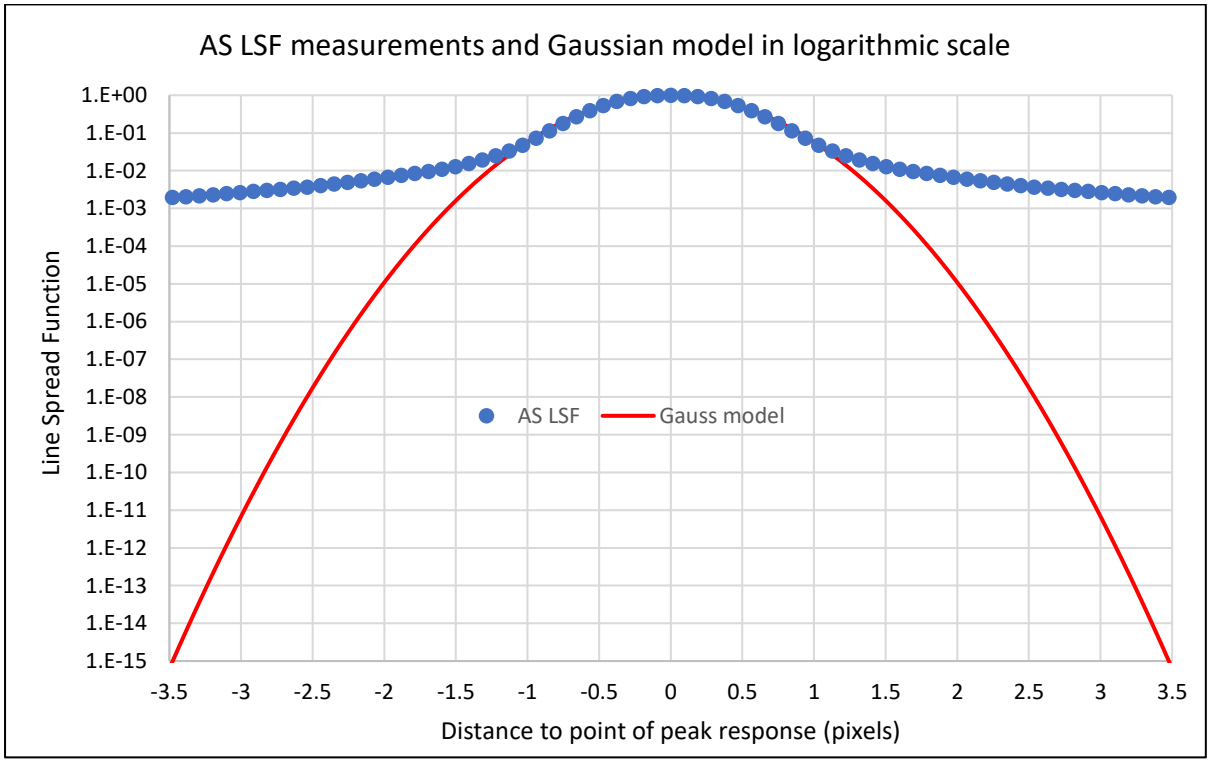

Figure 5: Line Spread Function measurements for Landsat 8's panchromatic channel (blue dots) and their Gaussian model fitted to the Full Width at Half Maximum (red curve), presented in logarithmic scale.

The residuals of the Gaussian model are the difference between the LSF values predicted by the model and the actual model. These residuals are quite small; the maximum values in AS and CS direction are 0.02 and 0.05, respectively. But, as illustrated in Figure 5 using logarithmic scale, this does not mean that the errors of the Gaussian model are small; this model underestimates the LSF by more than twelve orders of magnitude at a distance of 3.5 pixels

from the peak response. This conclusion is coherent with the results of the high-quality Generic sensor illustrated in Figures 1 and 2 which indicate that the Gaussian model may be valid (MAPE < 10 %) for PSF > 0.1 but that it is not valid (MAPE > 10 %) for PSF > 0.01.

To illustrate the impact of the Gaussian model errors, I consider an example in which a strong point source in the scene is projected in the image plane at the centre of a pixel "A". Assume that it is required to find the effect of this point source at a nearby pixel "B" that is separated by one pixel from pixel "A". The centre of pixel "B" is located two pixels from the centre of pixel "A", so from the LSF measurements (blue dots of Figure 4 and 5) it can be concluded that the signal induced by the point source at pixel "B" is about 150 times smaller than the signal induced by this source at pixel "A".

But, if the Gaussian model is used to estimate this effect, it is erroneously concluded that the signal induced by the point source at pixel "B" is about 68 thousand times smaller than the signal induced by this source at pixel "A". Thus, the Gaussian model errs by about three orders of magnitude in this task.

4. Conclusion

For the case of a high-quality Generic sensor the bivariate Gaussian Point Spread Function (PSF) model is practically useless when based on the Full Width at Half Maximum (FWHM) of the Line Spread Function (LSF) in Along Scan (AS) and Cross Scan (CS) directions.

For this same case, in the upper PSF range (PSF > 0.1), the Gaussian PSF model is valid, that is it has a Mean Absolute Percentage Error (MAPE) smaller than 10 %, for optical factors greater than 0.4 ($Q > 0.4$) and optical obstruction ratios smaller than 0.2 ($\varepsilon < 0.2$). When values of PSF > 0.01 are of interest the model is not valid (MAPE > 10 % for all values of Q and ε).

The Gaussian Point Spread Function model is useful for low quality satellite imagers that have a Gaussian Optical Transfer Function (OTF), due to the predominance of an OTF component that has a Gaussian response (for example Gaussian spacecraft jitter) or due to the existence of a very large number of OTF components that give a Gaussian shape to the final system OTF.

The fact that the Gaussian model has low residuals for some high-quality imagers does not mean that it has small errors; it has been shown that with residuals not larger than 0.02 (2 % of the LSF) the model underestimates the LSF by many orders of magnitude at a few pixels away from the peak response.